APPLIED COMPUTATIONAL ELECTROMAGNETICS SOCIETY JOURNAL

December 2020
Vol. 35 No. 12
ISSN 1054-4887

The ACES Journal is abstracted in INSPEC, in Engineering Index, DTIC, Science Citation Index Expanded, the Research Alert, and to Current Contents/Engineering, Computing & Technology.

The illustrations on the front cover have been obtained from the research groups at the Department of Electrical Engineering, The University of Mississippi.

THE APPLIED COMPUTATIONAL ELECTROMAGNETICS SOCIETY
http://aces-society.org

EDITORS-IN-CHIEF

Atef Elsherbeni
Colorado School of Mines, EE Dept.
Golden, CO 80401, USA

Sami Barmada
University of Pisa, ESE Dept.
56122 Pisa, Italy

ASSOCIATE EDITORS

Mohammed Hadi
Kuwait University, EE Dept.
Safat, Kuwait

Alistair Duffy
De Montfort University
Leicester, UK

Wenxing Li
Harbin Engineering University
Harbin 150001, China

Maokun Li
Tsinghua University
Beijing 100084, China

Mauro Parise
University Campus Bio-Medico of Rome
00128 Rome, Italy

Yingsong Li
Harbin Engineering University
Harbin 150001, China

Riyadh Mansoor
Al-Muthanna University
Samawa, Al-Muthanna, Iraq

Lijun Jiang
University of Hong Kong, EEE Dept.
Hong, Kong

Shinichiro Ohnuki
Nihon University
Tokyo, Japan

Kubilay Sertel
The Ohio State University
Columbus, OH 43210, USA

Antonio Musolino
University of Pisa
56126 Pisa, Italy

Abdul A. Arkadan
Colorado School of Mines, EE Dept.
Golden, CO 80401, USA

Salvatore Campione
Sandia National Laboratories
Albuquerque, NM 87185, USA

Wei-Chung Weng
National Chi Nan University, EE Dept.
Puli, Nantou 54561, Taiwan

Alessandro Formisano
Seconda Universita di Napoli
81031 CE, Italy

Piotr Gas
AGH University of Science and Technology
30-059 Krakow, Poland

Long Li
Xidian University
Shaanxa, 710071, China

Steve J. Weiss
US Army Research Laboratory
Adelphi Laboratory Center (RDRL-SER-M)
Adelphi, MD 20783, USA

Jiming Song
Iowa State University, ECE Dept.
Ames, IA 50011, USA

Maokun Li
Tsinghua University, EE Dept.
Beijing 100084, China

Marco Arjona López
La Laguna Institute of Technology
Torreon, Coahuila 27266, Mexico

Paolo Mezzanotte
University of Perugia
I-06125 Perugia, Italy

Luca Di Rienzo
Politecnico di Milano
20133 Milano, Italy

Lei Zhao
Jiangsu Normal University
Jiangsu 221116, China

Sima Noghanian
University of North Dakota
Grand Forks, ND 58202, USA

Qiang Ren
Beihang University
Beijing 100191, China

Nunzia Fontana
University of Pisa
56122 Pisa, Italy

Stefano Selleri
DINFO – University of Florence
50139 Florence, Italy

Amedeo Capozzoli
Univerita di Napoli Federico II, DIETI
I-80125 Napoli, Italy

Yu Mao Wu
Fudan University
Shanghai 200433, China

Atif Shamim
King Abdullah University of Science and Technology (KAUST)
Thuwal 23955, Saudi Arabia

EDITORIAL ASSISTANTS

Matthew J. Inman
University of Mississippi, EE Dept.
University, MS 38677, USA

Shanell Lopez
Colorado School of Mines, EE Dept.
Golden, CO 80401, USA

Madison Le
Colorado School of Mines, EE Dept.
Golden, CO 80401, USA

Allison Tanner
Colorado School of Mines, EE Dept.
Golden, CO 80401, USA

EMERITUS EDITORS-IN-CHIEF

Duncan C. Baker
EE Dept. U. of Pretoria
0002 Pretoria, South Africa

Allen Glisson
University of Mississippi, EE Dept.
University, MS 38677, USA

Ahmed Kishk
Concordia University, ECS Dept.
Montreal, QC H3G 1M8, Canada

Robert M. Bevensee
Box 812
Alamo, CA 94507-0516, USA

Ozlem Kilic
Catholic University of America
Washington, DC 20064, USA

David E. Stein
USAF Scientific Advisory Board
Washington, DC 20330, USA

EMERITUS ASSOCIATE EDITORS

Yasushi Kanai
Niigata Inst. of Technology
Kashiwazaki, Japan

Alexander Yakovlev
University of Mississippi, EE Dept.
University, MS 38677, USA

Levent Gurel
Bilkent University
Ankara, Turkey

Mohamed Abouzahra
MIT Lincoln Laboratory
Lexington, MA, USA

Ozlem Kilic
Catholic University of America
Washington, DC 20064, USA

Erdem Topsakal
Mississippi State University, EE Dept.
Mississippi State, MS 39762, USA

Sami Barmada
University of Pisa, ESE Dept.
56122 Pisa, Italy

Fan Yang
Tsinghua University, EE Dept.
Beijing 100084, China

Rocco Rizzo
University of Pisa
56123 Pisa, Italy

William O'Keefe Coburn
US Army Research Laboratory
Adelphi, MD 20783, USA

EMERITUS EDITORIAL ASSISTANTS

Khaled ElMaghoub
Trimble Navigation/MIT
Boston, MA 02125, USA

Christina Bonnington
University of Mississippi, EE Dept.
University, MS 38677, USA

Kyle Patel
Colorado School of Mines, EE Dept.
Golden, CO 80401, USA

Anne Graham
University of Mississippi, EE Dept.
University, MS 38677, USA

Mohamed Al Sharkawy
Arab Academy for Science and Technology, ECE Dept.
Alexandria, Egypt

DECEMBER 2020 REVIEWERS

Galip Orkun Arican
Guan-Yu Chen
Jie Chen
Arkaprovo Das
Timothy Garner
Piotr Gas
Tianqi Jiao
Darko Kajfez
Robin Kalyan
P. Kumar
Ali Lalbakhsh
Yingsong Li
Wen-Jiao Liao
Guizhen Lu
Paulo Mendes
Yang Meng
Ali Mir
Felix Miranda
Abdullahi Mohammed
Antonio Orlandi
Xiaotian Pan
Anyong Qing
Rengasamy Rajkumar
Paul Record
Alain Reineix
Imaculate Rosaline
Remi Sarkis
Jiming Song
Aathmanesan T.
Wanchun Tang
Yasuhiro Tsunemitsu
Heming Yao
Kedi Zhang
Lei Zhao
Yujuan Zhao
Bessem Zitouna

THE APPLIED COMPUTATIONAL ELECTROMAGNETICS SOCIETY JOURNAL

Vol. 35 No. 12 December 2020

TABLE OF CONTENTS

A Comparative Study of the Computation Efficiency of a GPU-Based Ray Launching Algorithm for UAV-Assisted Wireless Communications
Maximilian J. Arpaio, Enrico M. Vitucci, and Franco Fuschini 1456

Constitutive Parameter Optimization Method of Obliquely Incident Reflectivity for Conformal PML
Yongjie Zhang, Xiaofeng Deng, and Xiaohu Zhang 1463

Optimization Design of Electromagnetic Devices Using an Enhanced Salp Swarm Algorithm
Houssem R.E.H. Bouchekara, Mostafa K. Smail, Mohamed S. Javaid, and Sami Ibn Shamsah 1471

Approach for CM/DM Current Extraction and Crosstalk Analysis of Twisted-Wire Pairs with Random Non-uniform Twisting
Chao Huang, Yan Zhao, Wei Yan, Yanxing Ji, Qiangqiang Liu, Shijin Li, and Yi Cao 1477

Antenna Resonant Frequency Modeling based on AdaBoost Gaussian Process Ensemble
Tianliang Zhang, Yubo Tian, Xuezhi Chen, and Jing Gao 1485

Circularly Polarized Jute Textile Antenna for Wi-MAX, WLAN and ISM Band Sensing Applications
Ram Sandeep Duvvada, Prabakaran Narayanaswamy, Madhav Boddapati Taraka Phani, and Narayana Kavuluru Lakshmi 1493

Wideband Octagonal Dual Circularly Polarized Sub-array Antenna for Ku-Satellite Systems
Khalid. M. Ibrahim, Walaa. M. Hassan, Esmat A. Abdallah, and Ahmed M. Attiya 1500

A Broadband Dual-polarized Antenna with CRR-EBG Structure for 5G Applications
Peng Chen, Lihua Wang, and Tongyu Ding 1507

Design and Analysis of Reflectarray Compound Unit Cell for 5G Communication
Tahir Bashir, Han Xiong, Abdul Aziz, Muhammad Ali Qureshi, Haroon Ahmed, Abdul Wahab, and Muhammad Umaid 1513

Electromagnetic Response Prediction of Reflectarray Antenna Elements Based on Support Vector Regression
Liping Shi, Qinghe Zhang, Shihui Zhang, Chao Yi, and Guangxu Liu 1519

© 2021, The Applied Computational Electromagnetics Society

Performance and Analysis of UWB Aesthetic Pattern Textile Antenna for WBAN Applications
Thillaigovindhan Annalakshmi and Subramaniam Ramesh 1525

Design of Frequency Reconfigurable Patch Antenna for Sensing and Tracking Communications
Priya Anumuthu, Kaja Mohideen Sultan, Manavalan Saravanan, Mohd Tarmizi Ali, Manikandan Kandadai Venkatesh, Mohammad Ghouse Khaderbasha Saleem, and Imaduddeen Valathoor Nizamuddeen 1532

A Metamaterial Inspired Compact Miniaturized Triple-band Near Field Resonant Parasitic Antenna for WLAN/WiMAX Applications
Si Li, Atef Z. Elsherbeni, Zhenfeng Ding, and Yunlong Mao 1539

A Third-Order Bandpass Three-Dimensional Frequency Selective Surface with Multiple Transmission Zeros
Zhengyong Yu and Wanchun Tang..... 1548

Radiated Susceptibility Analysis of Multiconductor Transmission Lines Based on Polynomial Chaos
Tianhao Wang, Quanyi Yu, Xianli Yu, Le Gao, and Huanyu Zhao 1556

© 2021, The Applied Computational Electromagnetics Society

A Comparative Study of the Computation Efficiency of a GPU-Based Ray Launching Algorithm for UAV-Assisted Wireless Communications

Maximilian J. Arpaio, Enrico M. Vitucci, and Franco Fuschini

Department of Electrical, Electronic and Information Engineering "G. Marconi"
Alma Mater Studiorum University of Bologna, Bologna, 40136, Italy
{maximilian.arpaio, enricomaria.vitucci, franco.fuschini}@unibo.it

Abstract ─ Graphics Processing Units (GPU), have opened up new opportunities for speeding up general-purpose parallel computing applications. In this paper, we present the computation efficiency in terms of time performances of a novel ray launching field prediction algorithm which relies on NVIDIA GPUs and its Compute Unified Device Architecture (CUDA). The software tool assesses the propagation losses between a wireless transmitter - carried by an Unmanned Air Vehicle (UAV) - over a 3D urban environment. Together with other effective features, the software tool is shown to reduce by several orders of magnitude the computation time of simulations. Performances and cost-benefit analysis of three different NVIDIA GPU configurations are thus investigated over three different urban scenarios, taken as test-cases for Air-to-Ground (A2G) communications for 5G applications and beyond.

Index Terms ─ 5G, Air-To-Ground (A2G) propagation, GPU, NVIDIA, ray launching, UAV.

I. INTRODUCTION

Deterministic wave propagation modelling represents a state-of-the-art technique for RF channel analysis. The accuracy of site-specific propagation models, like ray tracing or ray launching, has seen great improvements in the last few decades thanks to better characterization of propagation mechanisms [1]. Although the compute capability of modern processors is constantly increasing, deterministic models still require significant runtimes to achieve accurate results, which has motivated the research community to extensive look for optimized and efficient acceleration methods [2]. Unfortunately, the complex mechanisms of electromagnetic waves as well as the huge amount of geometric calculations can make Central Processing Unit (CPU) computation inefficient. It has been argued that standard models - lacking of any speeding-up expedient - take more than an hour to retrieve channel characteristics across a kilometre-scale scenario with a single radio source [3]. Parallel computing – on the contrary - is a process of decomposing a large serial task into smaller sub-tasks, which can be calculated concurrently. Multi-core processors are currently the most commonly available and exploited parallel computing platform, allowing much faster computations compared to a single core, as long as the computer code is optimized to take advantage from the multiple cores [4]. Furthermore, interest has grown rapidly in recent years towards harnessing the power of graphic hardware to perform general-purpose parallel computing. This alternative approach has become widespread and is based on the use of the GPU—in addition to the CPU—for general purpose computing.

Having effectively reached a limit in the improvement of the single-core frequency of CPUs, GPU computing has become the method of choice for applications with high computational demands. Although GPUs have been known in the computing industry for over 40 years, they haven't represented a breakthrough until programmable and general purpose (GPGPU) have been developed. Since then, the computation potential has gained increasing acknowledgement, and GPUs have become far more than an embedded device for display operations: their special design allows us to perform many operations simultaneously and to perform computation-heavy tasks that would otherwise require a large computer cluster. Moreover, modern GPUs are equipped for double-precision mathematical operations in parallel configuration, which extends the range of applications even further. It is anyway important to note that even if parallelisation is not always guaranteed by simply having installed a GPU card and using CUDA language, it can be potentially achieved at a high- or low-level scale for many applications [5].

By means of a comparative study of the computation efficiency in terms of calculation time, this paper aims at shedding light on the crucial benefits that GPU computing can bring to the characterization of electromagnetic propagation between an UAV flying over an urban area and users roaming at street level. To the best of the authors' knowledge, no papers have been published so far with comparative, detailed, cost-benefit analyses of GPU architectures applied to electromagnetic computation problems. This represents the main novel contribution of

Submitted On: April 26, 2020
Accepted On: October 20, 2020
https://doi.org/10.47037/2020.ACES.J.351201

1054-4887 © ACES

this paper; surprisingly, high-end, more powerful GPU card might not always provide the greatest computation efficiency as it will be shown in the next sections.

As a matter of fact, while UAV assisted wireless communications are currently envisaged in the framework of 5G and beyond [6], experimental investigations of the A2G link are extremely challenging and complex due to the limited payload, the problem in powering up flying transceivers and the regulations to comply with at national/international level especially within inhabited areas. Therefore, ray-launching simulations can represent an easier and cheaper way to improve awareness about A2G propagation properties, as long as the corresponding computation effort is worth it. In this regard, a key characteristic of the ray launching approach is that rays do not interact each other along their own propagation paths. From departure to arrival, ray paths can be independently traced, which is of great advantage for GPU-based computation thanks to the intrinsic parallelisation degree within the whole propagation process.

This document is structured as follows: in Section II we provide general details of the ray-launching software while in Section III we introduce the hardware and software configurations, with a particular focus on the NVIDIA GPU cards. In Section IV we go through the main results in terms of computation time and speed-up factors, both for isotropic and directive antennas. The final Section V summarises the results while briefly drawing the main conclusions.

II. PRINCIPLES OF RAY-LAUNCHING ACCELERATION

Due to the increase in the computational demands of modern applications, many developers are currently looking for different ways to accelerate their applications beyond the – limited – speed that conventional CPUs can provide. Among all the possible solutions, the baseline for the GPU-based A2G propagation assessment proposed within this paper is the Discrete Environment-Driven Ray Launching model (DED-RL), which has been introduced for the first time in [7] together with the related computational theory. As with all RL algorithms, DED-RL is suitable for prediction over large areas or volumes. More specifically, it has been designed to perform fast deterministic propagation prediction on 3-D outdoor surfaces of all buildings and streets in a given target area, to enable multi frequency RF coverage design and optimization.

The software relies on a digitalised 3D urban model where each building is a polygon prism with a defined shape, material, position and height. The model is totally discrete, i.e., the building walls are properly discretized into "tiles" with a predetermined size. DED-RL has also inherited some advanced features from a pre-existing RT model developed at the University of Bologna, such as the Effective Roughness (ER) diffuse-scattering model. In addition to the environment discretization, the algorithm is also "environment-driven", meaning that ray tubes are launched only towards the tiles that are visible from the transmitter, and these ray tubes are then bounced toward tiles that are visible to each other. Another advantage of the discretization is that all the visibility relations among the tiles can be pre-computed and properly stored into a "visibility matrix" since the tile centres can be assumed as fixed points. This visibility pre-processing takes advantage of GPU parallelization and must be done only one time for a single simulation scenario. Once the pre-processing is done, ray bouncing can be performed very efficiently for any transmitter location in the same environment. All these features are implemented in DED-RL through the CUDA C++ language for NVIDIA GPUs. Using the combination of the above-mentioned techniques in addition to GPU parallelization, DED-RL is thus able to achieve very high levels of computational efficiency – up to four orders of magnitude compared to a conventional ray-tracing algorithm – while retaining a good level of accuracy, despite the intrinsic error introduced by the environment discretization [8].

All the main features of DED-RL algorithm described above — visibility pre-processing, launching of ray tubes, ray bouncing, and field computation — are suitable for code parallelization via GPU acceleration and thus may benefit significantly from GPU-based computation due to its ability to process vectors or matrices with extreme efficiency, as it will be shown in the following sections.

III. HARDWARE CONFIGURATION AND SIMULATION MODELLING

In order to investigate the computation time for UAV A2G propagation, we performed worst-case ray-launching simulations of a full three-dimensional (3D) scenario. DED-RL simulations were run by means of dedicated scripts within a MATLAB R2017B (Update 9) environment. The purpose of the scripts was to automate in a simple and efficient way the different runs concerning UAV positions and flight levels, as well as its transmitting frequencies.

Table 1: NVIDIA GPUs configurations under investigation

GPU Card	Architecture	Streaming Processors	Core Clock	Memory Clock	Bus Width	VRAM	Single Precision	Double Precision
Tesla K40c	Kepler, GK180	2880	745 MHz	6 GHz GDDR5	384-bit	12GB	5.04 TFLOPS	1.68 TFLOPS
Titan XP	Pascal, GP102	3840	1405 MHz	11.4 GHz DDR5X	384-bit	12GB	12.15 TFLOPS	0.38 TFLOPS
Tesla P100	Pascal, GP100	3584	1190 MHz	1.4 GHz HBM2	4096-bit	12GB	9.32 TFLOPS	4.73 TFLOPS

To freeze the hardware configuration throughout the different runs, all simulations were set-up on a commercial workstation, equipped with an Intel(R) Xeon(R) CPU E5-2620 v4 @ 2.10 GHz [8c/16t] and 48 GB DDR4 RAM.

As listed and described in Table 1, three different NVIDIA GPU cards were set-up: two cards belonging to the professional business sector (Tesla series), namely Tesla K40c (medium end) and Tesla P100 (high end), while the last one belonging to the gaming business one (GTX series), namely Titan Xp (high end). Although an extensive description of hardware details and specific mechanism of NVIDIA GPUs is out of the scope of this paper, the reader can find interesting details in [9] for Kepler and in [10] for Pascal architectures.

Regardless of the specific business sector they have been designed for, GPU processing capabilities can be measured in terms of SP and Video RAM (VRAM), together with floating point operations per second, either single or double precision. It can be seen from Table 1 that the three NVIDIA GPU cards show the same VRAM but they differentiate from each other for specific features. The Tesla series cards, as expected for professional business purposes, show better performances in terms of double precision TFlops, while the GTX card, gaming-oriented, really lacks. Conversely, the GTX card outperforms the Tesla series concerning single precision TFlops and memory clock, as expected from a card that must react promptly in tough gaming sessions. The number of SP is comparable between the two high-end GTX and Tesla cards, being instead slightly lower in the medium-end Tesla card. It should be remarked that performance improvements are an increasing function of the number of available computing cores; the more cores are available, the higher the speedups that can be achieved compared to sequential counterpart versions.

Together with the complexity of device architectures, it is seen that computational power of GPUs is rapidly growing with many new features proposed to developers, to the researchers or to the gaming community, like the very recent Ray Tracing (RT) cores for real time ray-tracing calculations [11]. Nevertheless, we must not be inebriated by the multiple features and capabilities: one of the most important aspects when comparing performances in terms of computation times, is to get a fair and balanced set of output metrics for proper accelerator comparison. In this regards Table 2 summarises the main DED-RL parameters set-up during the different simulation runs. In fact, it was important to fine-tune the DED-RL parameters - among those related to the addressed GPU memory and the number of rays launched per cycle - with a set of commonly acceptable values for all the involved GPUs and to get comparable results among the different scenarios.

For benchmarking purposes, the DED-RL software was configured assuming a single UAV hovering over a 3D urban city environment at different positions in space.

Table 2: Ray launching main simulation parameters

Parameter	Values
Frequency	0.7, 3.5, 26 and 70 GHz
UAV heights	30, 50, 75, 150, 300, 450 m AGL
UAV hovering positions	8 circular positions
Number of Interactions	5 bounces, 5 reflections, 2 diffractions and 1 scatter
Number of Combined Interactions	3 reflections/diffractions (max), 3 diffractions/scatters (max)
GPU Memory Allocation Heap Size	1536 MB
Maximum LOS Rays Per Cycle	100000
Amount of GPU Memory for Packets	40%

Table 3: Urban model environments

Parameter	Bologna	Munich	San Francisco
No. Tiles	170931	148584	268868
Area [Km^2]	6.5	8.8	10.2
Building/Area	30.5%	37.8%	40.5%

Three different urban models were investigated, with a special focus on their city centres: Bologna (Italy), Munich (Germany) and San Francisco (USA). This was done to explore how much a specific urban map was affecting the computation time. Coverage predictions were performed on a whole urban area with a single tile resolution of 10x10 m and general details as further specified in Table 3.

By means of *tic* and *toc* Matlab commands [12], it

was possible to measure - and to focus only on - the elapsed time before and after the call to the executable DED-RL file.

Although, on one hand, this is the most straightforward way to measure the computation time in a coherent way among the different GPU cards, on the other hand it may be objected that the CPU processing affects this measurement as part of the whole RL code execution. We can say not only that this part is negligible, but we must also emphasise that this part is common – and the same – for any simulation run on the same workstation, thus returning a set of comparable results.

IV. RESULTS

Simulation results shown in the following subsections represent the combined outcomes of multiple aggregated runs corresponding to different UAV spatial hovering positions (i.e., lat-long UTM coordinates and height above ground level,) or transmitting frequencies, over the three different test-referenced scenarios. This strategy was agreed to make available significant data samples and a clear breakdown of run parameters and characteristics.

A. Computation time for isotropic antennas

In this specific subsection, the UAV was equipped with an isotropic antenna. Although this type of antenna does not have any physical meaning, it allowed us to run a worst-case scenario where rays were launched in all directions, thus increasing the computation effort of calculating multiple interactions at 360° spherical degrees. Furthermore, it is worth noting that the isotropic case can somehow represent real situations where the radiation lobe of the antenna is wide enough to illuminate the whole urban area below the UAV frame.

To get the representative graphs in Fig. 1, runs have been averaged over the UAV spatial positions, as it turned out to slightly affect the computation time. According to Fig. 1, this time is generally longer at lower frequencies and shorter at higher frequencies. Differently from "Image" Ray Tracing techniques, where the intensity of a ray can be computed only after the whole ray path - from the transmitter to the receiver - is traced, Ray Launching can take note instead of the ray intensity while it is being traced. Therefore, rays with negligible intensity can be stopped and discarded, thus saving computation time. As propagation losses increase with frequency and distance, many rays are therefore dismissed by the DED-RL algorithm, thus explaining the achieved results.

At the same time, the Tesla P100 GPU card tends to be the fastest one at lower frequencies, with an average speed up factor of ~4x vs. Tesla K40c and ~2x vs. Titan Xp. This speed-up factor is seen to increase with the complexity of the environment. In the most challenging case (San Francisco, according to the parameters listed in Table 3), the Tesla P100 shows a simulation time which is ~3x and ~7x lower compared to the Titan Xp and the Tesla K40 cards respectively, whereas the three GPU cards show similar performances from 26 GHz onwards. On one hand, these results are reasonable and proportional to the number of rays vs. computed interactions. On the other hand, this sounds like a surprising result: it might be expected the high end Tesla P100 card to always be somehow the first of the class due to its technical specs and economical value, while actually the gap with the Titan Xp is indeed minor.

In agreement with CUDA programming best practices [13] and literature [14], this behaviour is likely related to the additional overhead the Tesla P100 brings in connection to its intrinsic complexity. This can limit the computation speed when there is no good balance among the different thread blocks scheduled onto the GPU Streaming Multiprocessors (SM). However, this imbalance is more likely to happen in less challenging cases, i.e. the higher frequencies, due to the selective discarding of those rays whose intensity falls below the minimum power threshold, as previously mentioned.

B. Computation time for directive antennas

Following the interesting results of the previous subsection, the UAV was then equipped with a directional antenna of fixed aperture angle α, placed under the UAV fuselage and pointing downwards.

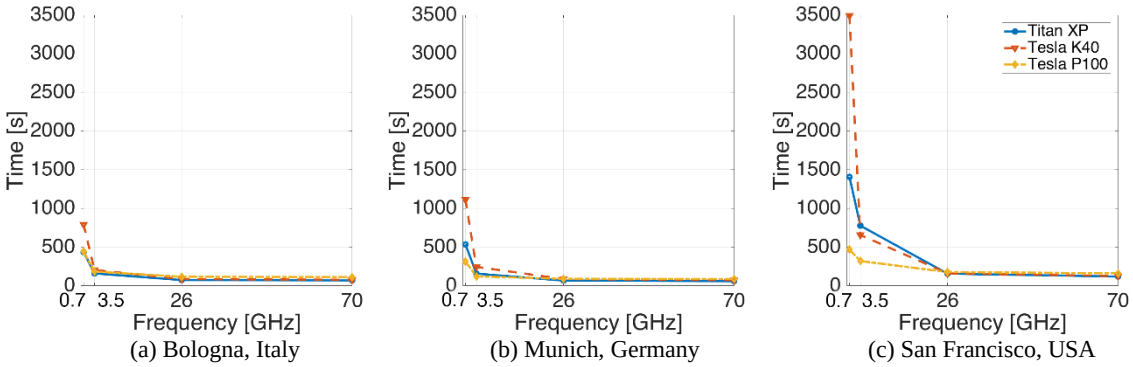

(a) Bologna, Italy (b) Munich, Germany (c) San Francisco, USA

Fig. 1. Computation time [s] over frequency [GHz] for different Nvidia cards and environments.

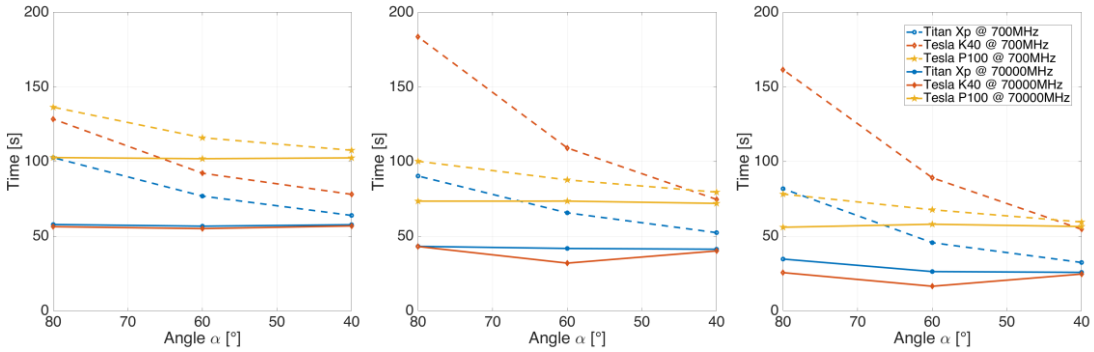

(a) Bologna, Italy (b) Munich, Germany (c) San Francisco, USA

Fig. 2. Computation time [s] over antenna aperture angle [°] for different NVIDIA cards and environments.

This can be seen as a best-case scenario where rays are launched only within a specific cone, thus drastically reducing the computation effort of calculating additional interactions. In this regard, please note that angle α is simply the ideal radiation cone aperture, i.e., we assumed a simplified 0 dB constant gain inside and instead an –Inf dB constant gain outside.

To get the representative graphs in Fig. 2, runs have been averaged in terms of spatial positions and results split into low and high frequency samples, 700 MHz and 70GHz respectively. On that note, it is seen that at 70GHz the simulation time are flat all over the α angle span, with the Tesla P100 now the slowest among the card.

As the limited number of rays to be traced at high frequency is further reduced by the antenna directive pattern, the simulation time is simply dominated by the specific overhead of the GPU, which is likely to be heavier for the Tesla P100. This is not completely true at 700MHz, where plots are no longer flat and simulation time logically decreases as a function of the angle α, (i.e., it increases as a function of antenna directivity).

Generally speaking, the use of directive antennas in our test-case brings out the way in which GPU overhead represents an important factor for any evaluation of the computation time. From these plots, it is possible to see the Titan XP card to better perform out of the other two cards, which is not always true in case of an isotropic antenna.

V. CONCLUSION

We have investigated the performance of a Discrete Environment-Driven Ray Launching Algorithm in terms of computation time and the related speed-ups among different NVIDIA GPU cards.

We have demonstrated the benefit of GPU parallelization as a means to accelerate ray launching field computation, with typical computation times for complete predictions over all building surfaces ranging from seconds to few tens of minutes, depending on the size of the urban scenario, the hardware used for simulation runs and the characteristics of RF propagation. This shows the potential benefit of GPUs for electromagnetic simulations, and especially for deterministic field strength predictions, in fair agreement with the main outcomes of previous works in [15-17].

It was seen how computation time decreases with frequencies and the use of different directive antennas could affect simulation time. As it can be expected, the wider the antenna radiation cone, the longer the simulation time, although remarkable only at lower frequencies. It was also seen that both professional and gaming GPGPU provide reasonable and consistent results in terms of computation time, the former having better performances at lower frequencies due to the higher number of rays to be processed. On the other hand, performance can be degraded when using the high-end Tesla GPUs in less demanding environments, due to their additional overhead. This shows that NVIDIA gaming GTX cards should not be automatically dismissed and they can be a good choice under specific simulation cases, instead of more expensive Tesla cards.

Future works will focus on more demanding simulation environments, i.e., densely urban as well as on different and more recent Nvidia GPU architectures, especially those with RT cores, like Turing and Ampere.

ACKNOWLEDGMENT

The authors wish to express their gratitude to NVIDIA Corporation with the donation of the Titan XP GPU used for this research.

REFERENCES

[1] Z. Yun, M. F. Iskander, “Ray tracing for radio propagation modelling: Principles and applications,” *IEEE Access*, vol. 3, pp. 1089-1100, July 2015.

[2] N. Kinayman, “Parallel programming with GPUs: Parallel programming using graphics processing units with numerical examples for microwave engineering,” *IEEE Microwave Magazine*, vol. 14,

iss. 4, pp. 102-115, June 2013.

[3] J. D. Owens, D. Luebke, N. Govindaraju, M. Harris, J. Kruger, A. E. Lefohn, and T. J. Purcell, "A survey of general-purpose computation on graphics hardware," *Proc. Eur. Assoc. Comput. Graph*., pp. 21-51, Aug. 2005.

[4] A. Hidic, D. Zubanovic, A. Hajdarevic, A. Huseinovic, and N. Nosovic, "Attempt of unbiased comparison of GPU and CPU performance in common scientific computing," *2012 IX International Symposium on Telecommunications (BIHTEL)*, Sarajevo, Bosnia & Herzegovina, Oct. 25-27, 2012.

[5] S. W. Keckler, W. J. Dally, B. Khailany, M. Garland, and D. Glasco, "GPUs and the future of parallel computing," *IEEE Micro*., vol. 31, iss. 5, Sept.-Oct. 2011.

[6] US Dept. of Transportation. "Unmanned Aircraft System (UAS) Service Demand 2015-2035: Literature Review and Projections of Future Usage," Technical Report, v. 1.0, Feb. 2014.

[7] J. S. Lu, E. M. Vitucci, V. Degli-Esposti, F. Fuschini, M. Barbiroli, J. A. Blaha, and H. L. Bertoni, "A discrete environment-driven GPU-based ray launching algorithm," *IEEE Transactions on Antennas and Propagation*, vol. 67, iss. 2, pp. 1180-1192, Feb. 2019.

[8] E. M. Vitucci, V. Degli-Esposti, F. Fuschini, J. S. Lu, M. Barbiroli, J. N. Wu, M. Zoli, J. J. Zhu, and H. L. Bertoni, "Ray tracing RF field prediction: An unforgiving validation," *International Journal of Antennas and Propagation*, Hindawi, vol. 2015, pp. 1-11, Aug. 2015.

[9] NVIDIA Corporation Whitepaper, "NVIDIA's Next Generation, CUDA Compute Architecture: Kepler GK110/210 Family," 2012.

[10] NVIDIA Corporation Whitepaper, "NVIDIA's Next Generation, CUDA Compute Architecture: Pascal GP100 Family," 2017.

[11] NVIDIA Corporation Whitepaper, "NVIDIA's NVIDIA Turing GPU Architecture: Graphics Reinvented," 2019.

[12] The MathWorks, Inc., "Matlab 2017B User Guide: On-line Help," referenced resources, 2016.

[13] NVIDIA Corporation, Developer's zone, "NVIDIA CUDA Toolkit 10.2.89: CUDA Toolkit Documentation," Nov. 2019.

[14] N. Matloff, "Parallel Computing for Data Science: With Examples in R, C++ and CUDA," June 4, 2015 Chapman and Hall/CRC Pub., June 2015.

[15] C. Reaño and F. Silla, "Performance evaluation of the NVIDIA Pascal GPU architecture: Early experiences," *2016 IEEE 18th International Conference on High Performance Computing and Communications*, Sydney, Australia, Dec. 12-14, 2016.

[16] Z. Dai and R. J. Watson, "Accelerating a ray launching model using GPU with CUDA," *12th European Conference on Antennas and Propagation (EuCAP 2018)*, London, UK, Apr. 9-13, 2018.

[17] M. Ujaldon, "Using GPUs for accelerating electromagnetic simulations," *Applied Computational Electromagnetics Society Journal*, vol. 25, no. 4, 2010.

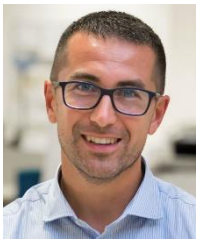

Maximilian James Arpaio received the Master degree in Telecommunications Engineering from the University of Parma in 2005 and a specialization in wind engineering and aerodynamics from the Polytechnic University of Milan in 2007. He received a Postgraduate Master in Project Management from the University of Verona in 2012. Since 2006, he has been collaborating with various Italian universities by promoting technical seminars and scientific collaborations. His current interests are on antennas and RF propagation within different environments, especially those related to next generation mobile systems (5G) for UAVs assisted wireless networks. He is a member of the IEEE and the Antennas & Propagation Society since 2018.

Enrico Maria Vitucci received the M.Sc. degree in Telecommunication Engineering and the Ph.D. degree in Electrical Engineering from the University of Bologna, Italy. He is currently a tenure-track Assistant Professor in electromagnetic fields at the Department of Electrical, Electronic and Information Engineering "G. Marconi" (DEI) of the University of Bologna. From 2011 to 2016, he was a Research Associate at the Center for Industrial Research on ICT of the University of Bologna. In 2015, he was a Visiting Researcher at Polaris Wireless, Inc., Mountain View, USA. His research interests are in deterministic wireless propagation models and multi-dimensional radio channel characterization. He is author or co-author of about 80 technical papers on international journals and conferences, and co-inventor of 4 international patents. He is a Senior Member of IEEE, and a member of the Editorial Board of the journal "Wireless Communications and Mobile Computing".

Franco Fuschini graduated with honours in Telecommunication Engineering and received the Ph.D. degree in Electronics and Computer Science from the University of Bologna in March 1999 and in July 2003, respectively. In April 1999 he received the 'Marconi Foundation Young Scientist Prize' in the context of the XXV Marconi International Fellowship Award. He is now Research Associate at the Department of Electrical, Electronic and Information Engineering "G. Marconi" of the University of Bologna. His main research interests are in the area of radio systems design and radio propagation channel theoretical modelling and experimental investigation. Franco Fuschini is author or co-author of about 20 papers on IEEE journals about radio propagation and wireless system design.

Constitutive Parameter Optimization Method of Obliquely Incident Reflectivity for Conformal PML

Y. J. Zhang*, X. F. Deng, and X. H. Zhang

School of Civil Aviation, Northwestern Polytechnical University, Xi'an, 710072, P.R. China
zyj19191@nwpu.edu.cn

Abstract ─ The conformal perfectly matched layer (PML), i.e., an efficient absorbing boundary condition, is commonly employed to address the open-field scattering problem of electromagnetic wave. To develope a conformal PML exhibiting a significant absorption effect and small reflection error, the present study proposes the constitutive parameter optimization method of obliquely incident reflectivity in terms of the conformal PML. First, the recurrence formula of obliquely incident reflectivity is derived. Subsequently, by the sensitivity analysis of constitutive parameters, the major optimal design variables are determined for the conformal PML. Lastly, with the reflectivity of the conformal PML as the optimization target, this study adopts the genetic algorithm (GA), simulated annealing algorithm (SA) and particle swarm optimization algorithm (PSO) to optimize the constitutive parameters of the conformal PML. As revealed from the results, the optimization method is capable of significantly reducing the reflection error and applying to the parameter design of conformal PML.

Index Terms ─ Conformal PML, obliquely incident reflectivity, parameter optimization, sensitivity analysis.

I. INTRODUCTION

The concept of the perfectly matched layer (PML) was initially proposed by Berenger [1] in 1994. The PML refers to an artificial truncation boundary condition, applying to electromagnetic scattering computation as a local boundary condition that exhibit excellent performance [2-7]. Subsequently, the conformal PML was introduced by Kuzuoglu and Mittra, which can be developed as the similar shell to the geometry of cylindrical and spherical scatterer to save spatial scattering elements [8]. Figure 1 illustrates the construction of a conformal PML.

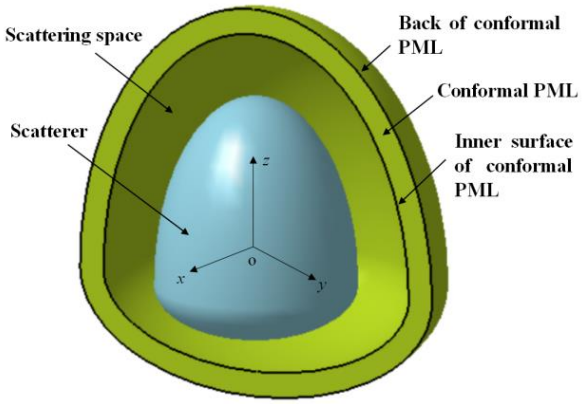

Fig. 1. The construction of a conformal PML.

Theoretically, the absorbing efficiency of conformal PML [9-13] is not determined by the incident angle and frequency of the incident electromagnetic wave, while it is only dependent of the thickness of the absorbing boundary layer. Compared with the conventional boundary conditions [14-16], the conformal PML can more easily fit the complex shape scatterers since it can maintain the consistent geometry with the scatterers. Furthermore, the conformal PML [17,18] can be formed in the space close to the surface of scatterers. Thus, the number of elements meshed in scattering space can be down-regulated maximally, thereby considerably saving the computational memory and time. Thus, the conformal PML is considered one of the most excellent local boundary conditions over the recent few years. To design a conformal PML that exhibits a significant absorption effect and small reflection error, the present study proposes a constitutive parameter optimization method given the derivation of obliquely incident reflectivity. The optimization method is expected as a basic method to design high-performance conformal PML.

Submitted On: March 20, 2020
Accepted On: October 20, 2020

https://doi.org/10.47037/2020.ACES.J.351202

1054-4887 © ACES

II. FUNDAMENTAL PARAMETERS OF CONFORMAL PML

The three-dimensional electromagnetic scattering field with a conformal PML is expressed as:

$$\nabla\times\left(\frac{1}{\mu_r}\overline{\overline{\Lambda}}^{-1}\bullet\nabla\times\boldsymbol{E}^s\right)-\omega^2\varepsilon_r\overline{\overline{\Lambda}}\boldsymbol{E}^s=0\,, \tag{1}$$

where $\boldsymbol{E}^s$ denotes the scattering electric field. μ_r and ε_r respectively represent the relative permeability and relative dielectric constant. Λ indicates the constitutive parameter of conformal PML in tensor.

Given the literature [11,19,20], the components of relative permeability $\overline{\overline{\mu}}=\mu_r\overline{\overline{\Lambda}}$ and relative dielectric constant $\overline{\overline{\varepsilon}}=\varepsilon_r\overline{\overline{\Lambda}}$ for conformal PML are respectively written as follows:

$$\begin{cases}\overline{\overline{\mu}}_1=\dfrac{s_2s_3}{s_1}\mu_r & \overline{\overline{\varepsilon}}_1=\dfrac{s_2s_3}{s_1}\varepsilon_r\\ \overline{\overline{\mu}}_2=\dfrac{s_1s_3}{s_2}\mu_r & \overline{\overline{\varepsilon}}_2=\dfrac{s_1s_3}{s_2}\varepsilon_r\\ \overline{\overline{\mu}}_3=\dfrac{s_1s_2}{s_3}\mu_r & \overline{\overline{\varepsilon}}_3=\dfrac{s_1s_2}{s_3}\varepsilon_r\end{cases}, \tag{2}$$

where subscripts 1 and 2 denote two tangential components; subscript 3 represents the normal component in local coordinate system of conformal PML; *s* indicates the complex extension variable following a certain direction.

When the electromagnetic wave is obliquely incident from infinity, it can be approximately considered that the local coordinate system complies with the global coordinate system. If an arbitrarily polarized planar electromagnetic wave is obliquely incident to the interface (Fig. 2), the *xoy* plane acts as the interface, and the *xoz* plane refers to the reflective surface. The incident plane is defined as the incident wave propagation direction $\boldsymbol{k}_i$ and normal direction $\hat{n}$ of the interface. In terms of the incident wave, the electric field $\boldsymbol{E}_i$ and magnetic field $\boldsymbol{H}_i$ are in a plane perpendicular to the propagation direction $\boldsymbol{k}_i$, and the orientation of $\boldsymbol{E}_i$ in this plane may be arbitrary. On the whole, the propagation direction of the uniform plane wave is not constantly perpendicular to the incident surface, and the arbitrary wave incident can fall into two components [20].

The electromagnetic wave is assumed to be decomposed into the vertical polarization and horizontal polarization plane wave, defined as $\boldsymbol{E}_i^{\perp}$ and $\boldsymbol{E}_i^{\parallel}$ respectively, the uniform plane wave is expressed as $\boldsymbol{E}_i=\boldsymbol{E}_i^{\perp}+\boldsymbol{E}_i^{\parallel}$. Under the available reflectivity $R^{\perp}$ and $R^{\parallel}$ of the vertical polarization and horizontal polarization plane wave, the reflected wave is expressed as $\boldsymbol{E}_r=R^{\perp}\boldsymbol{E}_i^{\perp}+R^{\parallel}\boldsymbol{E}_i^{\parallel}$. Thus, the reflectivity of the plane wave is defined as:

$$R=\sqrt{\left(R^{\perp}\cos\alpha\right)^2+\left(R^{\parallel}\sin\alpha\right)^2}\,, \tag{3}$$

where α denotes the polarization angle of the incident electromagnetic wave.

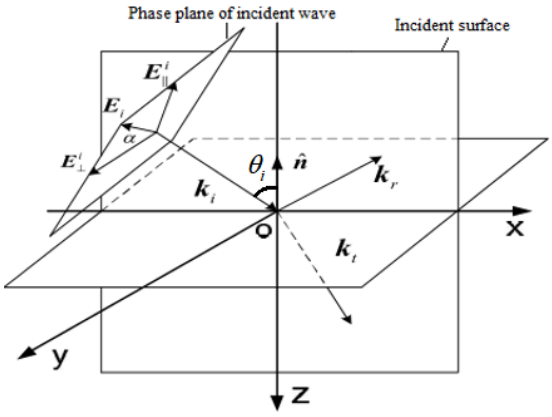

Fig. 2. Obliquely incident electromagnetic wave at arbitrarily polarized direction.

Overall, the conformal PML is utilized in multiple layers. Suppose that the physical space located by the conformal PML is vacuum or air, the relative permeability and relative dielectric constant of conformal PML are $\mu_r=\varepsilon_r=1$. According to the expressions of relative permittivity and permeability in (1) and (2), the wave number k_i and impedance η_i of the *i*th layer of conformal PML can be written as:

$$\begin{cases}k_i=\omega\left(\dfrac{s_2s_3}{s_1}\right)\sqrt{\mu_0\mu_{ir}\varepsilon_0\varepsilon_{ir}}=\left(\dfrac{s_2s_3}{s_1}\right)k_0\\ \eta_i=\sqrt{\dfrac{\mu_r}{\varepsilon_r}}=\sqrt{\dfrac{\mu_0}{\varepsilon_0}}\bullet\sqrt{\dfrac{\mu_{ir}}{\varepsilon_{ir}}}=\eta_0\sqrt{\dfrac{\mu_{ir}}{\varepsilon_{ir}}}=\eta_0\end{cases}, \tag{4}$$

where $\mu_{ir}=1$ and $\varepsilon_{ir}=1$ respectively denote the relative permeability and relative dielectric constant of the *i*th layer for conformal PML; $k_0=\omega\sqrt{\mu_0\varepsilon_0}$ and $\eta_0=\sqrt{\mu_0/\varepsilon_0}$ respectively represent the wave number and impedance of vacuum or air.

III. OBLIQUELY INCIDENT REFLECTIVITY OF MULTILAYER CONFORMAL PML

Under the sufficiently far source, the incident electromagnetic wave may be approximated as a uniform plane wave. For the multiple shell of the conformal PML, the case of vertical polarization at the incident point or

local area exhibiting small curvature is illustrated in Fig. 3. The angle between the incident wave and interface of the ith layer refers to the incident angle θ_i. If xoz indicates the reflective surface, and the electric field is vertical polarization, the propagation of electric and magnetic fields in the ith and the $(i+1)$th layers is presented in Fig. 3.

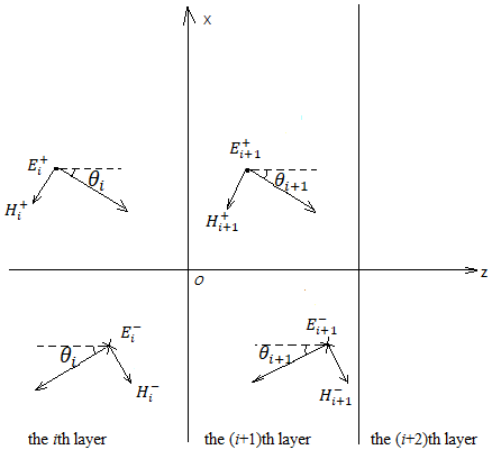

Fig. 3. Propagation of obliquely incident vertical polarization wave in multilayer conformal PML.

If the oblique incidence is vertical polarization, the electric field only covers the z-component. Hence, the electric and magnetic fields in the ith layer of the conformal PML are expressed as:

$$\begin{cases} \boldsymbol{E}_i = \left[E_i^i e^{-jk_i\left(x\sin\theta_i + z\cos\theta_i\right)} + E_i^r e^{-jk_i\left(x\sin\theta_i - z\cos\theta_i\right)} \right] \hat{\boldsymbol{e}}_y \\ \boldsymbol{H}_i = \dfrac{1}{\eta_i}\left[E_i^i \left(-\cos\theta_i \hat{\boldsymbol{e}}_x + \sin\theta_i \hat{\boldsymbol{e}}_z\right) e^{-jk_i z\cos\theta_i} \right. \\ \qquad \left. + E_i^r \left(\cos\theta_i \hat{\boldsymbol{e}}_x + \sin\theta_i \hat{\boldsymbol{e}}_z\right) e^{-jk_i z\cos\theta_i} \right] e^{-jk_i x\sin\theta_i} \end{cases}, \quad (5)$$

where θ_i respectively denotes the incident angle of the ith layer. E_i^i and E_i^r respectively represent the electric field amplitude of incident and reflected waves of the ith layer.

Likewise, the electric and magnetic fields in the (i+1) th layer of conformal PML can be expressed as:

$$\begin{cases} \boldsymbol{E}_{i+1} = \left[E_{i+1}^i e^{-jk_{i+1}\left(x\sin\theta_{i+1} + z\cos\theta_{i+1}\right)} + E_{i+1}^r e^{-jk_{i+1}\left(x\sin\theta_{i+1} - z\cos\theta_{i+1}\right)} \right] \hat{\boldsymbol{e}}_y \\ \boldsymbol{H}_{i+1} = \dfrac{1}{\eta_{i+1}}\left[E_{i+1}^i \left(-\cos\theta_{i+1} \hat{\boldsymbol{e}}_x + \sin\theta_{i+1} \hat{\boldsymbol{e}}_z\right) e^{-jk_{i+1} z\cos\theta_{i+1}} \right. \\ \qquad \left. + E_{i+1}^r \left(\cos\theta_{i+1} \hat{\boldsymbol{e}}_x + \sin\theta_{i+1} \hat{\boldsymbol{e}}_z\right) e^{-jk_{i+1} z\cos\theta_{i+1}} \right] e^{-jk_{i+1} x\sin\theta_{i+1}} \end{cases}. \quad (6)$$

The continuity condition of tangential components of electric and magnetic field at the interface (z=0) is written as:

$$\begin{cases} E_{iy} = E_{(i+1)y} \\ H_{ix} = H_{(i+1)x} \end{cases}. \quad (7)$$

By combining (6) and (7), it yields:

$$\begin{cases} E_{iy} = E_i^i e^{-jk_i\left(x\sin\theta_i + z\cos\theta_i\right)} + E_i^r e^{-jk_i\left(x\sin\theta_i - z\cos\theta_i\right)} \\ H_{ix} = \dfrac{\cos\theta_i}{\eta_i}\left(-E_i^i e^{-jk_i z\cos\theta_i} + E_i^r e^{-jk_i z\cos\theta_i}\right) e^{-jk_i x\sin\theta_i} \end{cases}. \quad (8)$$

Likewise, $E_{(i+1)y}$ and $H_{(i+1)x}$ can be written as:

$$\begin{cases} E_{(i+1)y} = E_{i+1}^i e^{-jk_{i+1}\left(x\sin\theta_{i+1} + z\cos\theta_{i+1}\right)} + E_{i+1}^r e^{-jk_{i+1}\left(x\sin\theta_{i+1} - z\cos\theta_{i+1}\right)} \\ H_{(i+1)x} = \dfrac{\cos\theta_{i+1}}{\eta_{i+1}}\left(-E_{i+1}^i e^{-jk_{i+1} z\cos\theta_{i+1}} + E_{i+1}^r e^{-jk_{i+1} z\cos\theta_{i+1}}\right) e^{-jk_{i+1} x\sin\theta_{i+1}} \end{cases}. \quad (9)$$

Suppose that the reflectivity of the interface between the ith and $(i+1)$th layers is defined as:

$$R_i = E_i^r / E_i^i. \quad (10)$$

According to (6)-(10), the reflectivity of the interface between the ith and $(i+1)$th layers of the conformal PML for the vertical polarization plane wave can be written as:

$$R_i^{\perp} = \frac{R_a + R_b R_{i+1}^{\perp} e^{-2jk_{i+1}d_{i+1}\cos\theta_{i+1}}}{R_b + R_a R_{i+1}^{\perp} e^{-2jk_{i+1}d_{i+1}\cos\theta_{i+1}}}, \quad (11)$$

where R_a and R_b are:

$$\begin{cases} R_a = \left(\eta_{i+1}\cos\theta_i - \eta_i\cos\theta_{i+1}\right) \\ R_b = \left(\eta_{i+1}\cos\theta_i + \eta_i\cos\theta_{i+1}\right) \end{cases}. \quad (12)$$

A similar derivation can be applied under horizontal polarization as illustrated in Fig. 4. The reflectivity of the interface between the ith and $(i+1)$th layer of the conformal PML is inferred as:

$$R_i^{\parallel} = \frac{R_c + R_d R_{i+1}^{\parallel} e^{-2jk_{i+1}d_{i+1}\cos\theta_{i+1}}}{R_d + R_c R_{i+1}^{\parallel} e^{-2jk_{i+1}d_{i+1}\cos\theta_{i+1}}}, \quad (13)$$

where R_c and R_d are expressed as follows:

$$\begin{cases} R_c = \left(\eta_{i+1}\cos\theta_{i+1} - \eta_i\cos\theta_i\right) \\ R_d = \left(\eta_{i+1}\cos\theta_{i+1} + \eta_i\cos\theta_i\right) \end{cases}. \quad (14)$$

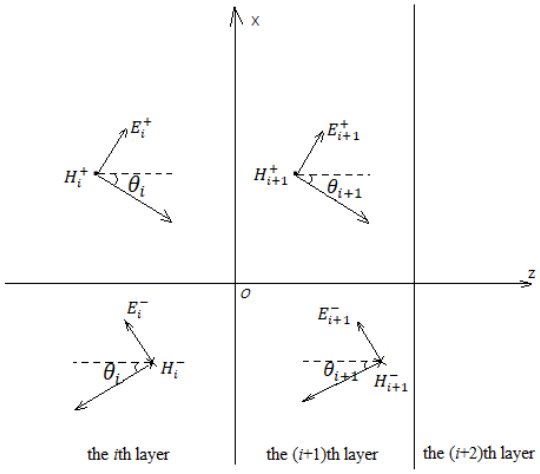

Fig. 4. Propagation of obliquely incident horizontal polarization wave in multilayer conformal PML.

If the extension order of complex extension variable is set to *m*, the complex extension variable [11] is defined as:

$$s(\xi_3) = 1 - j\delta\left(\frac{\xi_3}{t}\right)^m \tag{15}$$

where ξ_3 denotes the normal distance of the isometric surface along the *z*-axis; *t* represents the total thickness of the conformal PML; δ indicates the loss factor of the conformal PML.

For the case of two-dimensional, we can deduce that $s_1 = s_2$. Given Eq. (5), the impedance of the conformal PML is identical to that of the original scattering space; thus, the wavenumber of the conformal PML is rewritten as:

$$k_i = \left(\frac{s_2 s_3}{s_1}\right)k_0 = s_3 k_0 = \left\{1 - j\delta\left(\frac{\xi_3}{t}\right)^m\right\}k_0 . \tag{16}$$

Thus, (12) and (14) are simplified as:

$$\begin{cases} R_a = \cos\theta_i - \cos\theta_{i+1} \\ R_b = \cos\theta_i + \cos\theta_{i+1} \\ R_c = \cos\theta_{i+1} - \cos\theta_i \\ R_d = \cos\theta_{i+1} + \cos\theta_i \end{cases} . \tag{17}$$

Introducing (11) and (13) into (3), the reflectivity of the *i*th layer of the conformal PML under arbitrary polarization can be written as:

$$R_i = \sqrt{\left(R_i^{\perp}\cos\alpha\right)^2 + \left(R_i^{\parallel}\sin\alpha\right)^2} . \tag{18}$$

If the back surface of the *n*th layer of the conformal PML is total reflective, i.e., R_n=-1, the recurrence formula of reflectivity for the multilayer conformal PML can be written as:

$$\begin{cases} R_i^{\perp} = \dfrac{\left(\cos\theta_i - \cos\theta_{i+1}\right) + \left(\cos\theta_i + \cos\theta_{i+1}\right)R_{i+1}^{\perp}e^{-2jk_{i+1}d_{i+1}\cos\theta_{i+1}}}{\left(\cos\theta_i + \cos\theta_{i+1}\right) + \left(\cos\theta_i - \cos\theta_{i+1}\right)R_{i+1}^{\perp}e^{-2jk_{i+1}d_{i+1}\cos\theta_{i+1}}} \\ R_i^{\parallel} = \dfrac{\left(\cos\theta_{i+1} - \cos\theta_i\right) + \left(\cos\theta_{i+1} + \cos\theta\right)R_{i+1}^{\parallel}e^{-2jk_{i+1}d_{i+1}\cos\theta_{i+1}}}{\left(\cos\theta_{i+1} + \cos\theta\right) + \left(\cos\theta_{i+1} - \cos\theta_i\right)R_{i+1}^{\parallel}e^{-2jk_{i+1}d_{i+1}\cos\theta_{i+1}}} \\ R_i = \sqrt{\left(R_i^{\perp}\cos\alpha\right)^2 + \left(R_i^{\parallel}\sin\alpha\right)^2} \\ R_n = -1 \end{cases} . \tag{19}$$

While under vertical polarization, the recurrence formula of reflectivity for the multilayer conformal PML is simplified as:

$$\begin{cases} R_i = \dfrac{\left(\cos\theta_i - \cos\theta_{i+1}\right) + \left(\cos\theta_i + \cos\theta_{i+1}\right)R_{i+1}e^{-2jk_{i+1}d_{i+1}\cos\theta_{i+1}}}{\left(\cos\theta_i + \cos\theta_{i+1}\right) + \left(\cos\theta_i - \cos\theta_{i+1}\right)R_{i+1}e^{-2jk_{i+1}d_{i+1}\cos\theta_{i+1}}} \\ R_n = -1 \end{cases} . \tag{20}$$

Overall, the reflectivity of the conformal PML is expressed in logarithmic coordinate system, e.g., (21):

$$\begin{cases} \sigma = 20\lg|R| = 20\lg|R_0| \\ \sigma \sim \left(\delta, m, d_i, n, \theta_i, \lambda\right) \end{cases} . \tag{21}$$

Accordingly, the obliquely incident reflectivity of conformal PML depends only on the loss factor δ, extension order m, layer thickness di, overall layer number n, incident angle θ_i, and wavelength λ. Except for θ_i and λ, the other parameters, pertaining to the basic design parameters of the conformal PML, are to be discussed and optimized in the following sections.

IV. OPTIMIZATION ANALYSIS OF OBLIQUELY INCIDENT REFLECTIVITY

According to (21), the constitutive parameters affecting the obliquely incident reflectivity of the conformal PML include the layer thickness, loss factor, extension order and overall layer number. To delve into the impact of the mentioned constitutive parameters on the reflectivity, the central difference method undergoes a sensitivity analysis. The basic formula is expressed as:

$$\begin{aligned} f'(x_i) &= \frac{f(x_i + h) - f(x_i - h)}{2h} + O(h^2) \\ &\approx \frac{f(x_i + h) - f(x_i - h)}{2h}, \end{aligned} \tag{22}$$

where the step size h is set to 1% of the corresponding parameter. The sensitivity function $f(x_i)$ can be considered the obliquely incident reflectivity σ in (21), while the variables x_i can be considered one of the layer thickness, loss factor, extension order, and overall layer number in (21).

It is assumed that the frequency and wavelength of incident electromagnetic wave are set to f=30GHz and λ=0.01m, the initial parameters of conformal PML are set to δ=10, m=2, $d_i = 0.05\lambda$, n=5, and the disturbance step size is set to h=1% for the initial parameters of conformal PML, the sensitivity function $f(x_i)$ can be computed at the different incident angles θ_i (Table 1). Obviously, for the reflectivity impact of the conformal PML, the first refers to the layer thickness, the second is the extension order, while the overall layer number and loss factor are relatively small. Accordingly, the layer thickness and extension order should be adopted as the major design variables for reflectivity optimization.

Table 1: Sensitivity analysis results of constitutive parameters for conformal PML

Incident Angle/(°)	Layer Thickness	Loss Factor	Extension Order	Overall Layer Number
5	-52.8360	0.6605	-10.6282	-1.3027
10	-52.3634	0.6546	-10.5332	-1.2940
15	-51.5483	0.6444	-10.3692	-1.2788
20	-50.3495	0.6294	-10.1281	-1.2562
25	-48.7120	0.6089	-9.7987	-1.2247
30	-46.5717	0.5822	-9.3683	-1.1824
35	-43.8678	0.5484	-8.8245	-1.1273
40	-40.5626	0.5071	-8.1598	-1.0571
50	-36.6704	0.4584	-7.3770	-0.9704
55	-32.2839	0.4036	-6.4948	-0.8674
60	-27.5813	0.3448	-5.5489	-0.7510
65	-22.7980	0.2850	-4.5867	-0.6268
70	-18.1664	0.2271	-3.6549	-0.5021
75	-13.8553	0.1732	-2.7876	-0.3834
80	-9.9363	0.1242	-1.9991	-0.2745
85	-6.3879	0.0799	-1.2852	-0.1760

Given the requirements of actual electromagnetic scattering computation, this study adopts a five-layer conformal PML for reflectivity optimization. The cases of the identical value of layer thickness and different values of layer thickness are presented in the following. To optimize the obliquely incident reflectivity of conformal PML, the genetic algorithm (GA) [21], simulated annealing algorithm (SA) [22] and particle swarm optimization (PSO) [23] are employed.

(1) Case of the identical value of layer thickness

If the thickness of each layer is the same d, the layer thickness of the conformal PML in (21) can be rewritten as:

$$d_i = d = l * \lambda , \tag{23}$$

where the layer thickness can be expressed as l times the wavelength for the convenient calculation.

Given the precision of electromagnetic scattering computation and the computational cost of optimization iteration, the ranges of the layer thickness and extension order should be limited. Furthermore, to expand the search range of optimization algorithm, the value range of extension order is expanded from the integer to the real number. Thus, the optimization model under the identical value of layer thickness is defined as:

$$\begin{cases} \min & R = f\left(d, m\right) \\ s.t. & \dfrac{\lambda}{20} \le d \le \dfrac{\lambda}{2} \\ & 1 \le m \le 10 \end{cases} . \tag{24}$$

The optimization programs utilizing algorithms of GA, SA and PSO are developed and conducted in MATLAB. The optimization of obliquely incident reflectivity for the conformal PML is shown in Fig. 5. The optimization results are listed in Tables 2 and 3. It is suggested that the decrease in the reflectivity is obvious

after optimization. Compared with the three algorithms, PSO has the shortest running time and the maximal number of generations. GA exhibits the minimum number of generations, the longest running time and the maximal decrease. The number of generations and running time of SA are between GA and PSO.

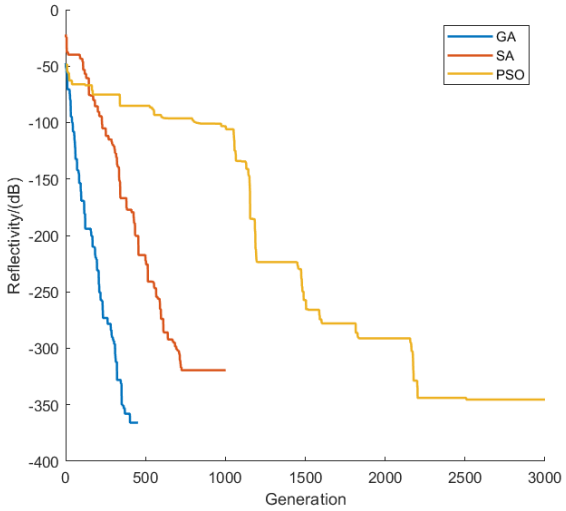

Fig. 5. Optimization of the obliquely incident reflectivity for conformal PML under the identical value of layer thickness.

Table 2: Parameter optimization results of conformal PML under the identical value of layer thickness

Opti.	Layer Thickness/(*λ)	Extension Order
Initial	0.05	2
GA	0.2818	4.0228
SA	0.3992	4.4515
PSO	0.3931	2.5613

Table 3: Reflectivity optimization results of conformal PML under the identical value of layer thickness

Opti.	Reflectivity (dB)	Decrease in Reflectivity (%)	Running Time (s)
Initial value	-120.1470	—	—
GA	-346.9674	188.7857	27.9730
SA	-336.1821	179.8090	16.2063
PSO	-335.8055	179.4955	10.1944

(2) Case of the different values of layer thickness

If the thickness of each layer d_i is different, the layer thickness of the conformal PML in (21) is rewritten as:

$$d_i = l_i * \lambda \,, \tag{25}$$

where the layer thickness is expressed as l_i times the wavelength for the convenient calculation.

Likewise, the optimization model under the different values of layer thickness is expressed as:

$$\begin{cases} \min \quad R = f\left(d_1, d_2, \cdots, d_n, m\right) \\ s.t. \quad \dfrac{\lambda}{20} \le d_i \le \dfrac{\lambda}{2} \\ \quad\quad 1 \le m \le 10 \end{cases} . \tag{26}$$

The optimization of obliquely incident reflectivity for the conformal PML is shown in Fig. 6. The optimization results are listed in Tables 4 and 5. It is suggested that the decrease in the reflectivity is obvious after optimization. Compared with the three algorithms, PSO exhibits the minimum number of generations and the least running time. SA has the largest number of generations. GA has the longest running time and the largest decrease. Compared with the case of the identical value of layer thickness, the reflectivity after optimization under different values of layer thickness is reduced for GA and PSO, while the running time of optimization is extended for SA and PSO.

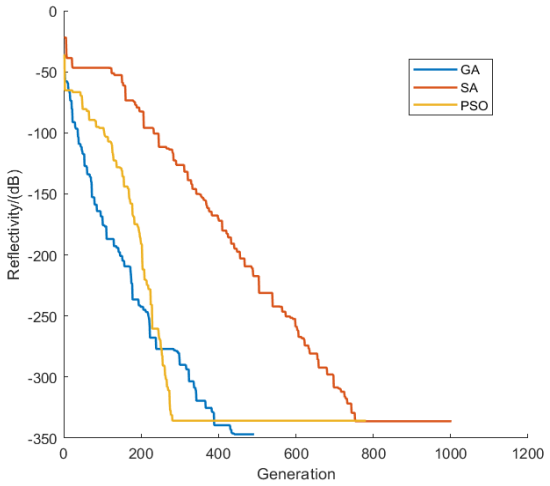

Fig. 6. Optimization of obliquely incident reflectivity for conformal PML under the different values of layer thickness.

Table 4: Parameter optimization results of conformal PML under the different values of layer thickness

Opti.	Layer Thickness/(*λ)					Extension Order
	The 1st Layer	The 2st Layer	The 3st Layer	The 4st Layer	The 5st Layer	
Initial	0.05	0.05	0.05	0.05	0.05	2
GA	0.4249	0.3588	0.2395	0.4576	0.3231	3.2311
SA	0.4159	0.4894	0.1113	0.4008	0.2789	2.9122
PSO	0.3898	0.3190	0.1401	0.3785	0.4022	2.8880

Table 5: Reflectivity optimization results of conformal PML under the different values of layer thickness

Opti.	Reflectivity (dB)	Decrease in Reflectivity (%)	Running Time (s)
Initial value	-120.1470	—	—
GA	-365.8395	204.4932	26.7663
SA	-319.3636	165.8107	19.3103
PSO	-361.1313	200.5745	11.1017

V. CONCLUSION

In the present study, the recurrence formula of oblique incidence reflectivity for the conformal PML is derived. The sensitivity analysis of reflectivity is conducted, covering the constitutive parameters for the conformal PML, i.e., the layer thickness, loss factor, extension order and overall layer number. The layer thickness and extension order are taken as the major optimization design parameters. Next, with the oblique incidence reflectivity as the optimization target, the optimization iteration and analysis on the conformal PML are conducted by the GA, SA and PSO algorithms. As revealed from the results, all the three optimization algorithms can determine the optimal reflectivity efficiently, which can distinctly enhance the absorbing effect of the conformal PML. Thus, the constitutive parameter optimization method in the present study can act as the basic parameter design method for conformal PML, as well as potential technical approach to determine electromagnetic scattering.

ACKNOWLEDGEMENT

This study was supported by National Science Foundation for Distinguished Young Scholars of China (11201375), Specialized Research Fund for the Doctoral Program of Higher Education of China (20106102120001) and Postdoctoral Science Foundation of China (201003680).

REFERENCES

[1] J. P. Berenger, "A perfectly matched layer for the absorption of electromagnetic waves," *Journal of Computational Physics*, vol. 114, no. 2, pp. 185-200, Oct. 1994.

[2] C. Wu, E. A. Navarro, P. Y. Chung, and J. Litva, "Modeling of waveguide structures using the non-orthogonal FDTD method with a PML absorbing boundary," *Microwave and Optical Technology Letters*, vol. 8, no. 4, pp. 226-228, Mar. 1995.

[3] J. P. Berenger, "Three-dimensional perfectly matched layer for the absorption of electromagnetic waves," *Journal of Computational Physics*, vol. 127, no. 2, pp. 363-379, Sep. 1996.

[4] W. C. Chew and J. M. Jin, "Perfectly matched layer in the discretized space: An analysis and optimization," *Electromagnetics*, vol. 16, no. 4, pp. 325-340, Jul-Aug. 1996.

[5] S. D. Gedney, "An anisotropic perfectly matched layer-absorbing medium for the truncation of FDTD lattices," *IEEE Transactions on Antennas and Propagation*, vol. 44, no. 12, pp. 1630-1639, Dec. 1996.

[6] J. P. Berenger, *Perfectly Matched Layer (PML) for Computational Electromagnetics*. Morgan & Claypool, 2014.

[7] Z. S. Sacks, D. M. Kingsland, R. Lee, and J. F. Lee, "A perfectly matched anisotropic absorber for use as an absorbing boundary condition," *IEEE Transactions on Antennas and Propagation*, vol. 43, no. 12, pp. 1460-1463, Dec. 1995.

[8] M. Kuzuoglu and R. Mittra, "Investigation of nonplanar perfectly matched absorbers for finite element mesh truncation," *IEEE Transactions on Antennas and Propagation*, vol. 45, no. 3, pp. 474-486, Mar. 1997.

[9] B. Donderici and F. L. Teixeira, "Conformal perfectly matched layer for the mixed finite element time-domain method," *IEEE Transactions on Antennas and Propagation*, vol. 56, no. 4, pp. 1017-1026, Apr. 2008.

[10] M. Kuzuoglu, B. B. Dundar, and R. Miitra, "Conformal perfectly matched absorbers in finite element mesh truncation," *IEEE Antennas and Propagation Society International Symposium Digest*, vol. 2, pp. 1176-1179, 2000.

[11] P. Liu, J. D. Xu, and W. Wan, "A finite-element realization of a 3-D conformal PML," *Microwave and Optical Technology Letters*, vol. 30, no. 3, pp. 170-173, Aug. 2001.

[12] T. Rylander and J. M. Jin, "Conformal perfectly

matched layers for the time domain finite element method," *IEEE Antennas and Propagation Society International Symposium Digest*, vol. 1, pp. 698-701, 2003.

[13] F. L. Teixeira, K. P. Hwang, W. C. Chew, and J.-M. Jin, "Conformal PML-FDTD schemes for electromagnetic field simulations: A dynamic stability study," *IEEE Transactions on Antennas and Propagation*, vol. 49, no. 6, pp. 902-907, Jun. 2001.

[14] O. Ozgun and M. Kuzuoglu, "Recent advances in perfectly matched layers in finite element applications," *Turkish Journal of Electrical Engineering and Computer Sciences*, vol. 16, no. 1, pp. 57-66, 2008.

[15] Z. Lou, D. Correia, and J.-M. Jin, "Second-order perfectly matched layers for the time-domain finite-element method," *IEEE Transactions on Antennas and Propagation*, vol. 55, no. 3, pp. 1000-1004, Mar. 2007.

[16] O. Ozgun and M. Kuzuoglu, "Iterative leap-field domain decomposition method: A domain decomposition finite element algorithm for 3D electromagnetic boundary value problems," *IET Microwaves Antennas & Propagation*, vol. 4, no. 4, pp. 543-552, Apr. 2010.

[17] Y. Xiao and Y. Lu, "Combination of PML and ABC for scattering problem," *IEEE Transactions on Magnetics*, vol. 37, no. 5, pp. 3510-3513, Sep. 2001.

[18] M. Movahhedi, A. Abdipour, H. Ceric, A. Sheikholeslami, and S. Selberherr, "Optimization of the perfectly matched layer for the finite-element time-domain method," *IEEE Microwave and Wireless Components Letters*, vol. 17, no. 1, pp. 10-12, Jan. 2007.

[19] Y. J. Zhang and X. H. Zhang, "Normal directional NURBS arithmetic of conformal PML," *Applied Computational Electromagnetics Society Journal*, vol. 29, no. 11, pp. 904-910, Nov. 2014.

[20] J. M. Jin. *The Finite Element Method in Electromagnetics*. Third Edition, Hoboken, NJ: Wiley, 2014.

[21] D. E. Goldberg, *Genetic Algorithms in Search, Optimization, and Machine Learning*. Addison-Wesley, Boston, 1989.

[22] J. Awange, B. Paláncz, R. Lewis, and L. Völgyesi, *Mathematical Geosciences: Hybrid Symbolic-Numeric Methods*. AG: Springer, 2018.

[23] S. Kiranyaz, T. Ince, and M. Gabbouj, *Multi-dimensional Particle Swarm Optimization for Machine Learning and Pattern Recognition*. AG: Springer, 2014.

Optimization Design of Electromagnetic Devices Using an Enhanced Salp Swarm Algorithm

Houssem R.E.H. Bouchekara [1], Mostafa K. Smail [2], Mohamed S. Javaid [1], and Sami Ibn Shamsah [1]

[1] Department of Electrical Engineering, University of Hafr Al Batin, Hafr Al Batin 31991, Saudi Arabia
bouchekara.houssem@gmail.com, javaid@uhb.edu.sa, sibnshamsah@uhb.edu.sa

[2] Institut Polytechnique des Sciences Avancées, 63 Boulevard de Brandebourg, 94200 Ivry-sur-Seine, France
mostafa-kamel.smail@ipsa.fr

Abstract ─ An Enhanced version of the Salp Swarm Algorithm (SSA) referred to as (ESSA) is proposed in this paper for the optimization design of electromagnetic devices. The ESSA has the same structure as of the SSA with some modifications in order to enhance its performance for the optimization design of EMDs. In the ESSA, the leader salp does not move around the best position with a fraction of the distance between the lower and upper bounds as in the SAA; rather, a modified mechanism is used. The performance of the proposed algorithm is tested on the widely used Loney's solenoid and TEAM Workshop Problem 22 design problems. The obtained results show that the proposed algorithm is much better than the initial one. Furthermore, a comparison with other well-known algorithms revealed that the proposed algorithm is very competitive for the optimization design of electromagnetic devices.

Index Terms ─ Design optimization, electromagnetic devices, salp swarm algorithm.

I. INTRODUCTION

Optimization of devices is an important task in different fields of engineering. It consists of determining some design variables or parameters in order to get the best performance of a device. Usually, this process is highly constrained that limit the final solution.

The process of optimization design is generally performed in the following three main steps:

1. Create an optimization design model or problem formulation.
2. Solve the optimization problem.
3. Analyze and interpret the obtained results.

In the first step, a mathematical model is created, or in other words, the problem is mathematically formulated. Here the framework of optimization is determined by defining the objective function to be minimized (or maximized), identifying the design variables to be optimized, and the constraints to be respected. Since the usefulness of the outcome primarily depends on this step, it is of utmost significance in the optimization design process.

The second step consists of solving the mathematical problem defined in the first step. Here three approaches can be usually used, including analytical approaches, graphical approaches, and numerical approaches.

The third and last step of the optimization design process is the posterior analysis. In this step, designers perform some analyses on the obtained design to verify its performance superiority by asking simple questions – is it optimal or can it be further improved or is it feasible and/or realizable.

The optimal design of Electromagnetic Devices (EMDs) follows the same steps described in this section. Furthermore, with the increase in the complexity of EMDs, more and more designers are using modern metaheuristic methods as optimization methods in the second step of the optimization design process.

In the literature, many metaheuristics have been implemented and applied to EMD optimization. Some examples of algorithms among others are: Genetic Algorithms (GA) [1], [2], Tabu Search (TS) [3], Simulated Annealing (SA) [4], evolution strategies (ES) [5], Electromagnetic-like Mechanism (EM) [6], Black Hole (BH) [7], Gravitational Search Algorithm (GSA) [8], Teaching Learning Based Optimization (TLBO) [9], Artificial Bee Colony (ABC) [10], Firefly Algorithm (FA) [11], League Championship Algorithm (LCA) [12], Social spider optimization (SSO) [13].

However, most of the modern metaheuristics are developed and tested on some well-known mathematical set of benchmarks, and then compared with each other to assess their performance. Therefore, using a metaheuristic, as it is developed and tested on mathematical benchmarks, without any modification or

Submitted On: April 28, 2020
Accepted On: October 13, 2020

https://doi.org/10.47037/2020.ACES.J.351203

1054-4887 © ACES

adaptation to design EMDs can lead to non-optimal solutions. Consequently, the objective of this paper is to develop an enhanced version of a new metaheuristic method developed in [14] which is called the Salp Swarm Algorithm (SSA) for the optimization design of EMDs.

The remainder of this paper is organized as follows. In section II, the SSA algorithm is presented. In section III, the developed ESSA is detailed. Section IV contains the discussion of the obtained result. Lastly, conclusions have been drawn in the final section of this paper.

II. SALP SWARM ALGORITHM

The SSA is inspired by the behavior of salps while navigating and foraging in oceans [14]. Salps leave in an environment hard to access, which makes research on these creatures not abundant. In the ocean usually, salps form a swarm called salp chain. In [14], a mathematical model is proposed to model the salp chain behavior. The pseudocode of the SSA is given in

Fig. 1 [14]. Like other population-based metaheuristics, the SSA initializes with a population of salps generated at random positions inside the searching space. Next, the population is categorized into two main groups called leaders (the salps in the front of the chain) and followers (the remaining salps of the chain). Then, the fitness of each salp is evaluated, and the best salp (that has the minimum fitness) is considered as the source of food to be chased by the salp chain.

The positions of the best and the follower salps are updated using the following equation [14]:

$$x_j^1 = \begin{cases} F_j + c_1\left(\left(ub_j - lb_j\right)c_2 + lb_j\right) & c_3 \geq 0 \\ F_j - c_1\left(\left(ub_j - lb_j\right)c_2 + lb_j\right) & c3 < 0 \end{cases}, \quad (1)$$

where j indicates the j[th] dimension, x_j^1 is the position of the first salp (leader), F_j is the position of the food source, ub_j and lb_j indicates the upper and lower bounds, respectively, $c_1 = 2e^{-\left(\frac{4\,\text{Current Iteration}}{\text{Maximum Number of Iterations}}\right)^2}$ is a balancing factor between exploration and exploitation, c_2 and c_3 are random numbers.

In the other side, the position of followers is updated using the following expression:

$$x_j^i = \frac{1}{2}\left(x_j^i + x_j^{i-1}\right). \quad (2)$$

Then if a salp crosses the border of the search space, it is brought back inside the search space. The process described here iterates until a predefined termination criterion is satisfied:

1	**Inputs**	The objective function, problem dimension, population size, Maximum number of iterations
2	**Output**	Best Salp
3	Initialization: initialize the salp population	
4	**while** the termination condition is not satisfied	
5	Calculate the fitness of each salp	
6	The best salp is set as F	
7	Update c_1	
8	**for** each salp (x_i)	
9	**if** i == 1	
10	Update the leading salp position	
11	**Else**	
12	Update the follower salp position	
13	**end if**	
14	Check if there are salps outside the search space	
15	**end for**	
19	**end while**	

Fig. 1. Pseudo code of the SSA algorithm.

III. ENHANCED SALP SWARM ALGORITHM

In this paper, an enhanced version of the SSA noted as ESSA is developed. The ESSA has the same general structure as the SSA with some modifications in order to enhance its performance for the optimization design of EMDs. For the ESSA, instead of moving the leader salp around the best position with a fraction of the distance between the lower and upper bounds as in eq. (1), another mechanism is used. In this mechanism, three different salps are randomly selected from the leader salps (x^1, x^2 and x^3). Then a random number (c_2) is generated. Based on this number, the position of the salp is updated as follows:

$$x_j^i = \begin{cases} x_j^1 + c_1\left(x_j^2 - x_j^3\right) & c_2 < \frac{1}{3} \\ x_j^2 + c_1\left(x_j^3 - x_j^1\right) & \frac{1}{3} < c_2 \leq \frac{2}{3} \\ x_j^3 + c_1\left(x_j^1 - x_j^2\right) & \frac{2}{3} < c_2 \leq 1 \end{cases}. \quad (3)$$

It is worth to mention that, In the SSA, the factor c_1 is a balancing factor between exploration and exploitation that varies in each iteration. However, in the ESSA, a random number generated using a normal distribution with mean parameter μ and standard deviation parameter σ. After several tests, μ and σ are selected as 0.4 and 0.1, respectively. These two

parameters can be modified or tuned in order to solve or optimize more devices.

Another modification incorporated on the ESSA compared with the SSA is that the positions of salps before their update is saved and compared to the positions after the update step. A salp moves to a new position only if this one is better than its old position.

IV. APPLICATION

Both SSA and ESSA are applied to the widely used Loney's solenoid and TEAM Workshop Problem 22 design problems. The following two subsections present the tested design problems and analyze the obtained results.

A. Loney's solenoid problem

One of the well renowned benchmarks in the optimal design of EMDs is Loney's solenoid. It is characterized by its geometry [15], having a relatively small number of degrees of freedom. Figure 2 shows the solenoid's axial cross section which consists of three coils; one acts as the main coil and the remaining two coils act as the correcting coils. The inner and outer radii of the main coil are represented by r_1 and r_2, having a length of h. Both correcting coils are of same dimensions, whereby r_3 and r_4 represent the inner and outer radii, each having the length L. Both correcting coils are separated by a distance S, symmetric about the z-axis.

The length L and the position S of the two correcting coils must be determined to generate a uniform magnetic flux density **B** in a certain interval along the main solenoid axis [16]. The determination of [16] (Coelho and Alotto, 2009) (Coelho and Alotto, 2009) both length and position can be treated as a design problem.

Mathematically, the problem can be stated as follows:

$$\min OF(S, L), \tag{4}$$

where the objective function F is given by:

$$OF = \frac{(B_{max} - B_{min})}{B_0}, \tag{5}$$

where: B_{min} and B_{max} denote the minimum and maximum inductions, respectively, inside the interval $(-z_0, z_0)$. At $z = 0$, the flux density is represented by B_0.

The developed ESSA is applied to Loney's benchmark and the outcome is compared to the initial version of SSA and other well-known optimization algorithms like: Particle Swarm Optimization (PSO), Genetic Algorithm (GA), Artificial Bee Colony (ABC), Differential Evolution (DE), and Biogeography-Based Optimization (BBO). Since all the tested algorithms are stochastic by nature due to the use of random numbers, all algorithms have been tested 30 times (to allow a fair statistical analysis) while evaluating objective function up to 2000 times in every run. The population size for all algorithms is 50.

Table 1 tabulates all the obtained results using different algorithms. In this table the statistical values of the objective function are displayed that include best, worst, mean and standard deviation (SD).

It can be noticed from this table that, while the SSA obtained the worst results in all statistical parameters across 30 runs, the ESSA obtained the best results in every sense demonstrating the tremendous enhancement incorporated on the initial version of the SSA.

It can also be noticed that both PSO and DE have achieved correct results since they are ranked second and third, respectively, when comparing the best values while ABC is second best when comparing mean values.

The best design obtained by the ESSA is specified by S = 12.6935 cm and L = 2.4328 cm with $OF(S, L) = 2.4536 \times 10^{-8}$.

Figure 3 shows the plot of objective function versus iterations for this case.

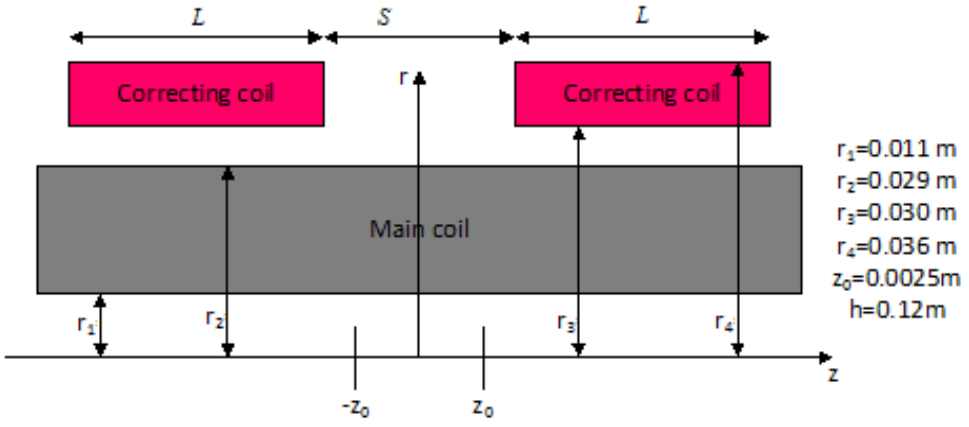

Fig. 2. Cross-section of Loney's solenoid.

Table 1: Simulation results of $OF \times 10^8$ for evaluating up to 2000 objective function evaluations in 30 runs

Algorithm	Best	Worst	Mean	SD
ESSA	2.4536	3.9663	3.7456	0.2651
PSO	2.6897	32.6602	4.7527	5.2770
DE	2.9335	26.3693	5.3043	5.7152
ABC	3.3661	5.3839	3.9539	0.4257
GA	3.4698	10.8799	4.5536	1.3575
BBO	3.8280	87.6055	9.6934	14.9701
SSA	5.3586	239.21	44.551	57.885

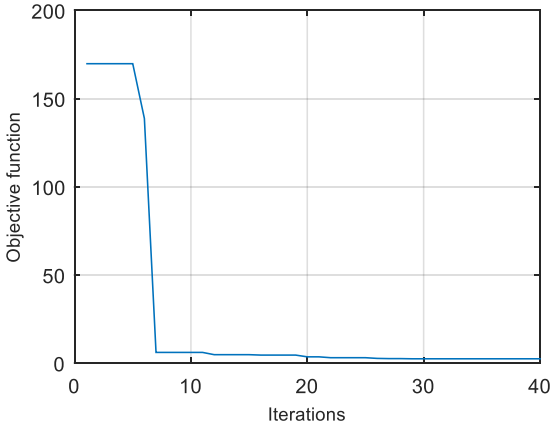

Fig. 3. Objective function $OF \times 10^8$ vs iterations for 2000 maximum objective function evaluations in the best run.

B. TEAM22 Benchmark

The TEAM Workshop Problem 22 or TEAM22 concerns the optimal design of a superconducting magnetic energy storage (SMES) device (Fig. 4). This problem consists of determining the optimal configuration of the SMES device that can store a certain amount of energy. At the same time the value of the stray field, is reduced as maximum with respect to a reference value [9]. This problem has eight design variables and its objective function is given by:

$$\mathrm{OF} = \frac{\mathrm{B}_{stray}^2}{\mathrm{B}_{norm}^2} + 100\,\frac{|E - E_{ref}|}{E_{ref}}, \tag{6}$$

where: E_{ref} =180MJ is the reference value of the desired energy, B_{norm} is the reference value of the stray field and it is equal to 200μT, B_{max} represent the maximum values of the magnetic induction, whereas the stray field B_{stray} (evaluated along a line a and line b on 22 equidistant points b sketched in
Fig. 4) is defined as:

$$\mathrm{B}_{stray}^2 = \frac{\sum_{i=1}^{22} |B_{stray,i}|^2}{22}. \tag{7}$$

The constraints imposed on the problem are:

$$R_1 + \frac{d_1}{2} < R_2 - \frac{d_2}{2}, \tag{8}$$

$$|\mathbf{J}| = (-6.4|\mathrm{B}_{\max}| + 54)\ A/\mathrm{mm}^2, \tag{9}$$

where: **J** is the current density.

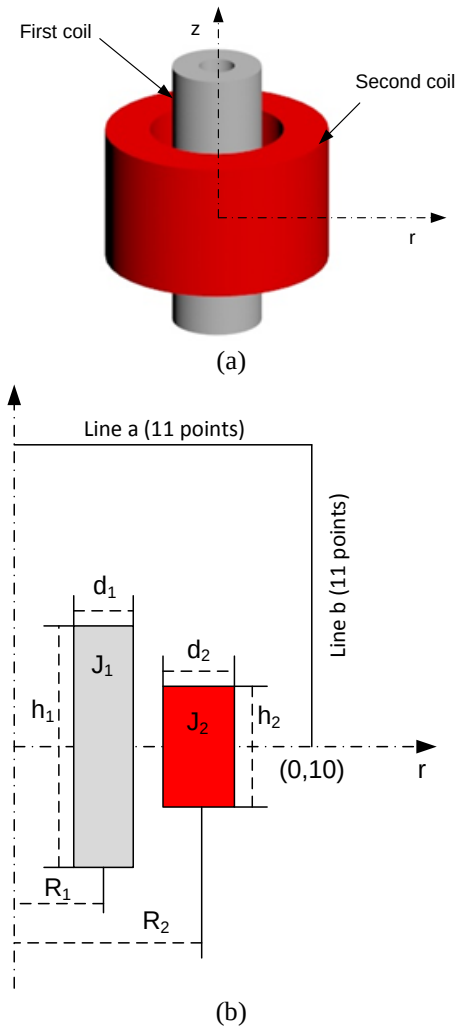

Fig. 4. TEAM22 configuration: (a) 3D representation of the SMES device, and (b) representation of the right-half transverse cut over the SMES device.

The developed ESSA has been applied to TEAM Workshop Problem 22 and the results are compared with the initial version SSA and other well-known optimization algorithms over 10 runs with 5000 maximum objective function evaluations in each run. The population size for all algorithms is kept 50.

The results obtained using the tested algorithms for the second benchmark are tabulated in Table 2. It must be noted from this table that the proposed ESSA is ranked at the top while the initial version of SSA is

ranked fourth when the comparison criterion is the best value obtained. Using the same criterion BBO and DE stand second and third, respectively. If the mean value is the ranking criterion, ESSA is ranked first while SSA is ranked 6 out of 7 algorithms or the penultimate one. Using the same criterion GA and BBO are ranked second and third, respectively. These results show one more time the improvement of the proposed ESSA compared to the initial SSA. They also show the superiority of the proposed algorithm compared with many other optimization algorithms.

The best design obtained by the ESSA is specified by R1 = 1.4809 m, R_2 = 2.4793 m, h_{12} = 1.2726 m, h_{22} = 1.2839 m, d_1 = 0.4845 m, d_2 = 0.1000 m, J_1 = 17.195 MA/m^2 and J_2 = -16.824 MA/m^2 with OF=0.5413.

Furthermore, the evolution of the objective function versus iterations for the second case is depicted in Fig. 5.

Table 2: Simulation results of OF for evaluating up to 5000 objective function evaluations in 10 runs

Algorithm	Best	Worst	Mean	SD
ESSA	0.5413	0.9057	0.7790	0.0971
BBO	0.6028	0.9656	0.8316	0.1303
DE	0.6396	0.9964	0.8593	0.1162
SSA	0.7146	1.0209	0.9489	0.1021
PSO	0.7197	1.0379	0.8994	0.1093
ABC	0.7279	1.4869	1.0388	0.2522
GA	0.7425	0.9037	0.8244	0.0498

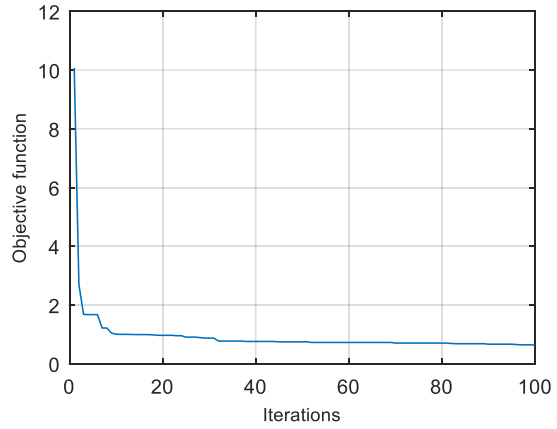

Fig. 5. Objective function OF vs iterations for 5000 maximum objective function evaluations in the best run.

V. CONCLUSIONS

In this paper, an enhanced version of the Salp Swarm Algorithm is developed and implemented for the design optimization of electromagnetic devices. The developed algorithm has better performance than the initial version. Furthermore, the ESSA has outperformed many other well-known optimization algorithms on the selected benchmark problem as it has been modified and adapted to the design of EMDs.

Future work can focus on developing a multi-objective salp swarm algorithm to be applied to more EMDs.

REFERENCES

[1] G. F. Uler, O. A. Mohammed, and C. S. Koh, "Utilizing genetic algorithms for the optimal-design of electromagnetic devices," *IEEE Trans. Magn.*, vol. 30, no. 6, pp. 4296-4298, 1994.

[2] S. R. H. Hoole, S. Sivasuthan, V. U. Karthik, A. Rahunanthan, R. S. Thyagarajan, and P. Jayakumar, "Electromagnetic device optimization: The forking of already parallelized threads on graphics processing units," *Applied Computational Electromagnetics Society Journal*, vol. 29, no. 9, pp. 677-684, 2014.

[3] E. Cogotti, A. Fanni, and F. Pilo, "A Comparison of optimization techniques for Loney's solenoids design : An alternative tabu search algorithm," *Electromagnetics*, vol. 36, no. 4, pp. 1153-1157, 2000.

[4] S. Alfonzetti, E. Dilettoso, and N. Salerno, "Simulated annealing with restarts for the optimization of electromagnetic devices," *IEEE Trans. Magn.*, vol. 42, no. 4, pp. 1115-1118, 2006.

[5] L. dos Santos Coelho and P. Alotto, "Electromagnetic device optimization by hybrid evolution strategy approaches," *Compel.*, vol. 26, no. 2, p. 269, 2007.

[6] H. R. E. H. Bouchekara, "Electromagnetic device optimization based on electromagnetism-like mechanism," *Applied Computational Electromagnetics Society Journal*, vol. 28, no. 3, 2013.

[7] H. R. E. H. Bouchekara, "Optimal design of electromagnetic devices using a black-hole-based optimization technique," *IEEE Trans. Magn.*, vol. 49, no. 12, pp. 5709-5714, 2013.

[8] L. D. S. Coelho, V. C. Mariani, N. Tutkun, and P. Alotto, "Magnetizer design based on a quasi-oppositional gravitational search algorithm," *IEEE Trans. Magn.*, vol. 50, no. 2, 2014.

[9] H. R. E. H. Bouchekara and M. Nahas, "Optimization of electromagnetics problems using an improved teaching-learning-based-optimization technique," *Applied Computational Electromagnetics Society Journal*, vol. 30, no. 12, 2015.

[10] X. Zhang, X. Zhang, S. Y. Yuen, S. L. Ho, and W. N. Fu, "An improved artificial bee colony algorithm for optimal design of electromagnetic devices," *IEEE Trans. Magn.*, vol. 49, no. 8, pp. 4811-4816, 2013.

[11] M. Alb, P. Alotto, C. Magele, W. Renhart, K. Preis, and B. Trapp, "Firefly algorithm for finding optimal shapes of electromagnetic devices," *IEEE*

Trans. Magn., vol. 52, no. 3, pp. 1-5, 2016.
[12] H. R. E. H. Bouchekara, M. Nahas, and H. M. Kaouach, "Optimal design of electromagnetic devices using the league championship algorithm," *Applied Computational Electromagnetics Society Journal*, vol. 32, no. 6, 2017.
[13] C. E. Klein, E. H. V Segundo, V. C. Mariani, and L. S. Coelho, "Modified social-spider optimization algorithm applied to electromagnetic optimization," vol. 9464, no. c, pp. 1-4, 2015.
[14] S. Mirjalili, A. H. Gandomi, S. Zahra, and S. Saremi, "Salp swarm algorithm : A bio-inspired optimizer for engineering design problems," vol. 114, pp. 163-191, 2017.
[15] P. Di Barba, A. Gottvald, and A. Savini, "Global optimization of Loney's solenoid a benchmark problem," *Int. J. Electromagn. Mech.*, vol. 6, pp. 273–276, 1995.
[16] L. D. S. Coelho and P. Alotto, "Particle swarm optimization combined with normative knowledge applied to Loney's solenoid design," *COMPEL Int. J. Comput. Math. Electr. Electron. Eng.*, vol. 28, no. 5, pp. 1155-1161, 2009.

Houssem R.E.H. Bouchekara is an Associate Professor at the Electrical Engineering Department of University of Hafr Al Batin. He has received his B.S. in Electrical Engineering from University Mentouri Constantine, Algeria, in 2004. He has received his Master in Electronic Systems and Electrical Engineering from Polytechnic School of the University of Nantes, France, 2005. He received his Ph.D. in Electrical Engineering from Grenoble Institute of Technology, France, in 2008. His research interest includes: Optimization techniques, Magnetic refrigeration, Electromagnetics, Electric machines and Power systems.

Mostafa Kamel Smail is an Associate Professor in the Aerospace Systems Department of Polytechnic Institute of Advanced Science – Paris – France. He received the master degree in Components and Antennas for Telecommunications in 2007 and the Ph.D. degree from University of Paris-Sud XI, France in 2010. His current research interests are wave propagation modeling, reliability of wiring, electromagnetic compatibility and Inverse modeling.

Muhammad Sharjeel Javaid received his B.S. in Electronic Engineering from GIK Institute, Pakistan in 2013. Later he completed his M.S. in Electrical Engineering from King Fahd University of Petroleum and Minerals, Saudi Arabia, in 2017. He has worked as active member of IET GIKI Chapter, and as General Secretary in IEEE KFUPM Chapter. Currently, he is serving as Lecturer in University of Hafr al Batin. He has the keen interest to work on Energy Markets, Distributed Generation Optimization,

Sami Ibn Shamsah is currently a Faculty Member in the College of Engineering at the University of Hafr Al Batin. He was graduated from King Fahd University of Petroleum and Minerals (KFUPM) with a B.Sc. degree in Mechanical Engineering and went to the University of Manchester to graduate with M.Sc. in Mechanical Engineering design and a Ph.D. in Mechanical Engineering. His research interests focus on the area of rotor dynamics and signal processing.

Approach for CM/DM Current Extraction and Crosstalk Analysis of Twisted-Wire Pairs with Random Non-uniform Twisting

Chao Huang [1], Yan Zhao [1*], Wei Yan [1,2], Yanxing Ji [1], Qiangqiang Liu [1], Shijin Li [1], and Yi Cao [1]

[1] School of Electrical & Automation Engineering
Nanjing Normal University, Nanjing 210046, China
1547796467@qq.com, *zhaoyang2@njnu.edu.cn, 61197@njnu.edu.cn, 397832514@qq.com, 1376684687@qq.com, lishijin@njnu.edu.cn, caoyi@njnu.edu.cn.

[2] Zhenjiang Institute for Innovation and Development
Nanjing Normal University, Zhenjiang 212004, China

Abstract ─ In this paper, a twisted-wire pairs (TWP) with random non-uniform twisting is established. It is divided into a complete pitch segment and a non-complete pitch segment by the ratio between the pitch and the length. The randomness of the actual TWP cable is accurately simulated by the following methods: 1) random combination of complete pitch segments; 2) random combination of non-complete pitch segments; 3) random combination between 1) and 2). Based on the TWP model, an equivalent multi-conductor transmission lines (MTLs) model can be obtained. The neural network algorithm is introduced to describe the complex relationship between the arbitrary position of the TWP and the per-unit-length (p.u.l) parameter matrix. In addition, the crosstalk and the common-mode (CM) and differential-mode (DM) noise under field-to-wire coupling are predicted. The numerical results show that crosstalk and CM/DM noise in TWP cable are susceptible to the twisted pitch at high frequencies. Compared with full-wave simulation, the accuracy of the proposed method is proved.

Index Terms ─ Crosstalk, common-mode (CM) and differential-mode (DM), field-to-wire coupling, neural network algorithm, random non-uniform twisting, twisted-wire pairs (TWP).

I. INTRODUCTION

Twisted-wire pairs (TWP) cable often used in the automotive and aerospace industries have good resistance to electromagnetic interference [1-3]. With the rise of current operating frequencies, predictions involving crosstalk and field-to-wire coupling noise are still a challenging issue. Therefore, the establishment of the TWP model (especially considering the non-uniformities that occur randomly in the TWP in actual wiring) is of primary importance in the follow-up research.

Taylor and Spadacini have studied the field-to-wire coupling model of TWP in reference planes [4-6] and free space [7, 8]. In [5], a worst case model was proposed to solve the CM/DM noise problem under field-to-wire coupling. In [9], the *Monte Carlo* (MC) algorithm was introduced to statistically represent the randomness of manually assembled cables. As well as the *Random Midpoint Displacement* (RMD) algorithm in [10, 11] and the *Random Displacement Spline Interpolation* (RDSI) method in [12], they are used to model the randomness of the cable. Due to the discontinuities between adjacent sections of wires generated by these methods, TWP cable cannot be accurately simulated.

In recent research, the *Cubic Hermite Interpolation Polynomial* was used to ensure the continuity of the traverse [13, 14]. The inhomogeneity of the per-unit-length (p.u.l) parameter matrix and the role of reflection from the ground plane in the radiation sensitivity (RS) are also studied. The complex relationship between the TWP position and the p.u.l parameter matrix has been proved in [15] to be described by a neural network. In our previous research [15-17] and [18], the crosstalk results of the cables were obtained using the BAS-BP (back propagation algorithm optimized by the beetle antennae search method) neural network. For the modeling of TWP non-uniformity, the complete pitch segments are considered in [6], but the non-uniformity largely comes from the combination of non-complete pitch segments. In this paper, the geometric model of TWP in the real world is accurately simulated by considering the combination between complete and incomplete pitch segments. Use the neural network algorithm to obtain the p.u.l parameter matrix at any position, and calculate the crosstalk and CM/DM noise

Submitted On: May 17, 2020
Accepted On: July 9, 2020

https://doi.org/10.47037/2020.ACES.J.351204

1054-4887 © ACES

in the TWP cable by FDTD method [19, 20].

This paper is organized as follows. In Section II, a TWP geometric model with random non-uniform twisting and a circuit model of wire-to-wire coupling and field-to-wire coupling are established. In Section III, the p.u.l parameter matrix is obtained by a neural network algorithm, and the crosstalk and CM/DM noise are predicted using FDTD technology. The comparison verification of the full-wave simulation based on the moment of method (MoM) is given in Section IV, and the results of crosstalk (CM/DM noise) are analyzed. Conclusions are eventually drawn in Section V.

II. GENERATION OF MODEL

A. Geometric model of TWP with random non-uniform twisting

TWP with random non-uniform twisting is a non-uniform transmission line. The model of TWP used in this paper is shown in Fig. 1. Traditional uniform TWP cables have the same twisting pitch, but due to manufacturing errors, random non-uniform twisting as shown in Fig. 1 may occur. Figure 1 (a) shows the model under the combination of different complete pitch segments (a certain cable length s_i is an integer multiple of the corresponding pitch p_i there); the model under different combinations of non-complete pitch segments (a certain cable length s_i is a non-integer multiple of the corresponding pitch p_i there) is shown in Fig. 1 (b); Fig. 1 (c) shows the model under the combination of complete pitch segments and non-complete pitch segments. The actual TWP is highly likely to be the model in Fig. 1 (c).

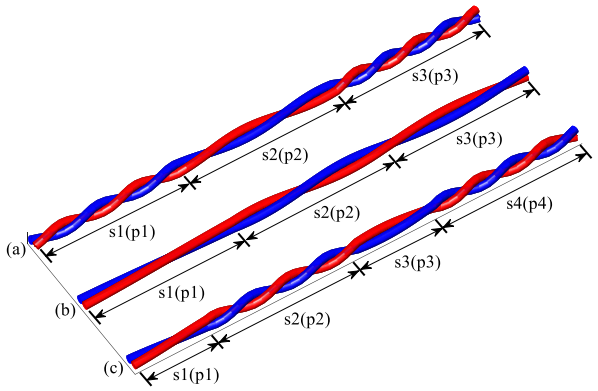

Fig. 1. TWP model with random non-uniform twisting. (a) TWP consisting of complete pitch segments. (b) TWP consisting of non-complete pitch segments. (c) TWP consisting of complete and non-complete pitch segments.

The wire is a cylindrical wire with an insulation layer, the wire radius is r, the center of the wire is d, the height of the twisted center from the ground is h, and the length of the TWP is L. The wire is twisted along the z-axis, and its parameters and reference ground are shown in Fig. 2 (b). The positions of the center points of the two wires are $\vec{l}_1$ and $\vec{l}_2$, which are expressed as follows:

$$\begin{cases} \vec{l}_1(x_1, y_1, z) = \frac{d}{2}\cos\theta\vec{a}_x + (h + \frac{d}{2}\sin\theta)\vec{a}_y + z\vec{a}_z \\ \vec{l}_2(x_2, y_2, z) = \frac{d}{2}\cos(\theta + \frac{\pi}{2})\vec{a}_x + (h + \frac{d}{2}\sin(\theta + \frac{\pi}{2}))\vec{a}_y + z\vec{a}_z \end{cases}, \quad (1)$$

where $\vec{a}_x$, $\vec{a}_y$, and $\vec{a}_z$ represent unit vectors of the x, y, and z axes, respectively. θ is the cross-section rotation angle at each position z, which is related to different pitch lengths:

$$\theta = f(z). \quad (2)$$

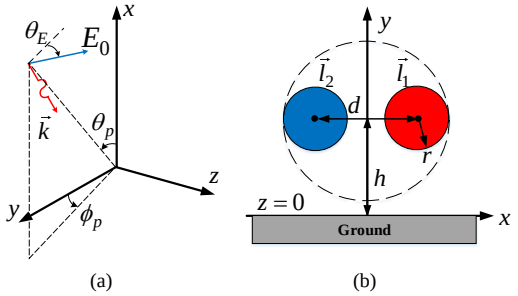

Fig. 2. External excitation field and cable parameters. (a) Plane wave electromagnetic field with electric field intensity E. (b) Cross section of initial position.

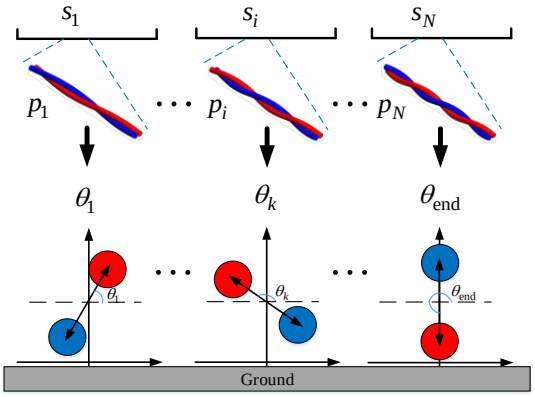

Fig. 3. Cross-section and rotation angle corresponding to different z values.

Figure 3 is a cross-section and a rotation angle at each z value obtained during the combination process based on Fig. 1 (c). S_i is the set of z values in a segment position in TWP, s_i is the length of the corresponding segment in the axial direction, and p_i is the type of the corresponding pitch length. The cross-section rotation angle in each section of S_i is:

$$\theta=\begin{cases}\dfrac{2\pi z}{p_1} & i=1, z\in S_1\\ \displaystyle\sum_{j=1}^{i-1}\frac{2\pi s_j}{p_j}+\frac{2\pi(z-\sum_{j=1}^{i-1}s_j)}{p_i} & i\geq 2, z\in S_i\end{cases}. \tag{3}$$

The case of i=1 corresponds to uniform TWP, and the number of pitch types of general non-uniform TWP is all equal to or greater than two.

B. Circuit model with termination conditions

Large electromagnetic interference noise to TWP is mainly expressed by crosstalk in wire-to-wire coupling and CM/DM in field-to-wire coupling. Figures 4 (a) and (b) show the termination conditions in different situations. The equivalent circuit models of its unit length are shown in Figs. 4 (c) and (b). r_{ij}, l_{ij}, c_{ij}, and g_{ij} represent the elements in the parameter matrix of resistance **R**, inductance **L**, capacitance **C**, and conductance **G**, respectively, where i,j=1,2.

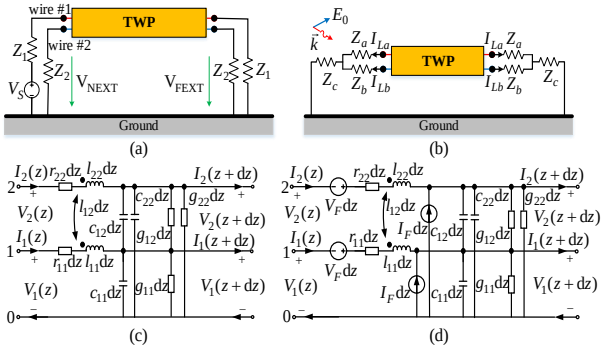

Fig. 4. Termination conditions and equivalent circuit. (a) Termination conditions for wire-to-wire coupling. (b) Termination conditions for field-to-wire coupling. (c) Unit equivalent circuit for wire-to-wire coupling. (d) Unit equivalent circuit for field-to-wire coupling.

The satisfied MTL equation [2] is:

$$\begin{cases}\dfrac{\partial\mathbf{V}(z,t)}{\partial z}+\mathbf{R}(z)\mathbf{I}(z,t)+\mathbf{L}(z)\dfrac{\partial\mathbf{I}(z,t)}{\partial t}=\mathbf{V}_F(z,t)\\ \dfrac{\partial\mathbf{I}(z,t)}{\partial z}+\mathbf{G}(z)\mathbf{V}(z,t)+\mathbf{C}(z)\dfrac{\partial\mathbf{V}(z,t)}{\partial t}=\mathbf{I}_F(z,t)\end{cases}, \tag{4}$$

where $\mathbf{V}(z,t)$, $\mathbf{I}(z,t)$ represent the voltage and current vectors of the cable at different positions z and at time t. $\mathbf{R}(z)$, $\mathbf{L}(z)$, $\mathbf{C}(z)$, and $\mathbf{G}(z)$ respectively represent the resistance, inductance, capacitance, and conductance matrix of the corresponding cross-sections at different positions z, that is, the per-unit-length (p.u.l) parameter matrix. $\mathbf{V}_F(z,t)$, $\mathbf{I}_F(z,t)$ represents the equivalent voltage and current sources of the external excitation field, which can be written as follows:

$$\begin{cases}\mathbf{V}_F(z,t)=\dfrac{\partial}{\partial z}\mathbf{E}_T(z,t)+\mathbf{E}_L(z,t)\\ \mathbf{I}_F(z,t)=\mathbf{C}(z)\dfrac{\partial}{\partial t}\mathbf{E}_T(z,t)\end{cases}, \tag{5}$$

where $\mathbf{E}_T(z,t)$ and $\mathbf{E}_L(z,t)$ represent the horizontal and vertical components of the incident electric field, respectively. Considering the non-uniformity of the TWP, z in each section of $\mathbf{E}_T$ and $\mathbf{E}_L$ can be approximately replaced by the z position at the left end.

The incident electric field is a uniform plane wave. The general expression is:

$$\vec{E}^{inc}(x,y,z,t)=(e_x\vec{a}_x+e_y\vec{a}_y+e_z\vec{a}_z)E_0(t-\frac{x}{v_x}-\frac{y}{v_y}-\frac{z}{v_z}). \tag{6}$$

The components of the incident electric field along the coordinate system are:

$$\begin{cases}e_x=\sin\theta_E\sin\theta_p\\ e_y=-\sin\theta_E\cos\theta_p\cos\phi_p-\cos\theta_E\sin\phi_p\\ e_z=-\sin\theta_E\cos\theta_p\sin\phi_p+\cos\theta_E\cos\phi_p\end{cases}, \tag{7}$$

where v_x, v_y, and v_z represent the components of the propagation velocity in each axis direction of the coordinate system:

$$\mathbf{E}_T(z,t)=\begin{bmatrix}\int_{x_0}^{x_1}E_x^{inc}(x_1,y_1,z,t)dx\\ \int_{x_0}^{x_2}E_x^{inc}(x_2,y_2,z,t)dx\end{bmatrix}, \tag{8}$$

$$\mathbf{E}_L(z,t)=\begin{bmatrix}E_z^{inc}(x_1,y_1,z,t)-E_z^{inc}(x_0,y_0,z,t)\\ E_z^{inc}(x_2,y_2,z,t)-E_z^{inc}(x_0,y_0,z,t)\end{bmatrix}, \tag{9}$$

where E_x^{inc} and E_z^{inc} are the horizontal and vertical components of the uniform plane wave. $E_z^{inc}(x_0,y_0,z,t)$ represents the magnitude of the longitudinal component at the reference ground (x_0=x, y_0=0).

As shown in Fig. 4 (a), the voltage and current on the transmission line also satisfy the formula (4) without applying an external excitation field. However, the equivalent voltage and current sources are set to zero, that is, $\mathbf{V_F}(z,t)$=$\mathbf{I_F}(z,t)$=**0**.

III. THE EXTRACTION AND APPLICATION OF P.U.L PARAMETER MATRIX

A. P.u.l parameter matrix

Equivalent voltage and current sources can be calculated using uniform plane waves. However, there are different p.u.l parameter matrices at different positions z. It is difficult to obtain a parameter matrix of any angle in the traditional way [14]. Any determined rotation angle of the cross-section has its own corresponding parameter matrix, and there is a non-

linear mapping relationship between the rotation angle and the parameter matrix. The transformations of the four p.u.l parameter matrices are the same. For simplicity, they can be expressed as follows:

$$\mathbf{M}(z)=\begin{bmatrix} m_{11} & m_{12} \\ m_{21} & m_{22} \end{bmatrix}, \tag{10}$$

where $\mathbf{M}(z)$ represents the cross-section $\mathbf{R}(z)$, $\mathbf{L}(z)$, $\mathbf{C}(z)$, $\mathbf{G}(z)$ p.u.l parameter matrix, and m_{ij} represents the specific resistance r_{ij}, inductance l_{ij}, capacitance c_{ij} and conductance g_{ij}. There is a complicated mathematical relationship between $\mathbf{M}(z)$ and the rotation angle:

$$\mathbf{M}(z) = g_{\mathbf{M}}(\theta). \tag{11}$$

In [17], the p.u.l parameter matrix corresponding to the different rotation angles of the cross-section can be obtained by prediction through the BAS-BP neural network. The network topology is shown in Fig. 5, but the hidden layer n_h and the output layer n_o are different from the previous [17].

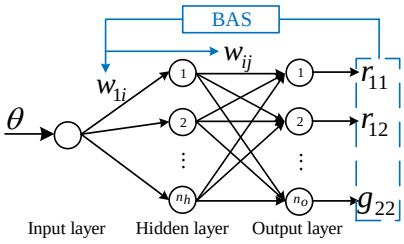

Fig. 5. Topological structure of BAS-BP neural network.

The input of the network is the cross-section rotation angle θ, and the output is a column vector consisting of the elements of the parameter matrix:

$$O=[r_{11}, r_{12}, r_{22}, l_{11}, l_{12}, l_{22}, c_{11}, c_{12}, c_{22}, g_{11}, g_{12}, g_{22}]^T. \tag{12}$$

After training the network with a small amount of data extracted in advance, the p.u.l parameter matrix of any rotation angle can be obtained. Considering the symmetry of the cross-section and the periodicity of the rotation angle, the input angle of the training network only needs 0°~180°. The result $\mathbf{M}(z')$ at 180°~360° only needs to perform row and column transformation on the corresponding prediction result $\mathbf{M}(z)$, as shown below. The result above 360° is the same as the corresponding result within 360°:

$$\mathbf{M}(z')=\begin{bmatrix} 0 & 1 \\ 1 & 0 \end{bmatrix}\mathbf{M}(z)\begin{bmatrix} 0 & 1 \\ 1 & 0 \end{bmatrix}. \tag{13}$$

B. Application in crosstalk

Considering the situation of Fig. 4 (c), the voltage and current are divided on the cable in space-time as shown in Fig. 6.

$\mathbf{V}_j^n$ and $\mathbf{I}_j^n$ in Fig. 6 can be expressed as:

$$\mathbf{V}_j^n = \mathbf{V}(j\Delta z, n\Delta t), \mathbf{I}_j^n = \mathbf{I}(j\Delta z, n\Delta t). \tag{14}$$

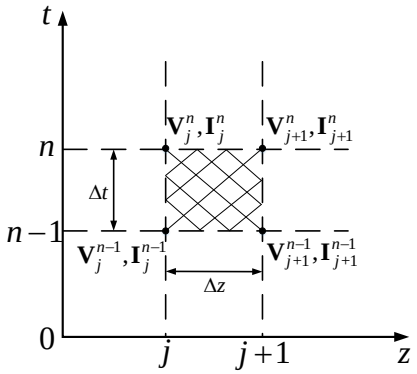

Fig. 6. Spatial-temporal dispersion of voltage and current.

Equation (4) can be discretized according to the Implicit-Wendroff format, as shown below:

$$\frac{\mathbf{V}_{j+1}^n - \mathbf{V}_j^n + \mathbf{V}_{j+1}^{n-1} - \mathbf{V}_j^{n-1}}{2\Delta z} + \frac{\mathbf{R}(j\Delta z)(\mathbf{I}_{j+1}^n + \mathbf{I}_j^n + \mathbf{I}_{j+1}^{n-1} + \mathbf{I}_j^{n-1})}{4} + \frac{\mathbf{L}(j\Delta z)(\mathbf{I}_j^n - \mathbf{I}_j^{n-1} + \mathbf{I}_{j+1}^n - \mathbf{I}_{j+1}^{n-1})}{2\Delta t} = 0, \tag{15}$$

$$\frac{\mathbf{I}_{j+1}^n - \mathbf{I}_j^n + \mathbf{I}_{j+1}^{n-1} - \mathbf{I}_j^{n-1}}{2\Delta z} + \frac{\mathbf{G}(j\Delta z)(\mathbf{V}_{j+1}^n + \mathbf{V}_j^n + \mathbf{V}_{j+1}^{n-1} + \mathbf{V}_j^{n-1})}{4} + \frac{\mathbf{C}(j\Delta z)(\mathbf{V}_j^n - \mathbf{V}_j^{n-1} + \mathbf{V}_{j+1}^n - \mathbf{V}_{j+1}^{n-1})}{2\Delta t} = 0. \tag{16}$$

Further simplified to:

$$\begin{cases} \mathbf{V}_j^n - \mathbf{V}_{j+1}^n + \mathbf{A}_{Vj}(\mathbf{I}_j^n + \mathbf{I}_{j+1}^n) = -\mathbf{V}_j^{n-1} + \mathbf{V}_{j+1}^{n-1} + \mathbf{B}_{Vj}(\mathbf{I}_j^{n-1} + \mathbf{I}_{j+1}^{n-1}) \\ \mathbf{A}_{Ij}(\mathbf{V}_j^n + \mathbf{V}_{j+1}^n) + \mathbf{I}_j^n - \mathbf{I}_{j+1}^n = \mathbf{B}_{Ij}(\mathbf{V}_j^{n-1} + \mathbf{V}_{j+1}^{n-1}) - \mathbf{I}_j^{n-1} + \mathbf{I}_{j+1}^{n-1} \end{cases}, \tag{17}$$

where the coefficient matrix is:

$$\begin{aligned} \mathbf{A}_{Vj} &= -(\mathbf{R}(j\Delta z)/2 + \mathbf{L}(j\Delta z)/\Delta t)\Delta z, \\ \mathbf{B}_{Vj} &= (\mathbf{R}(j\Delta z)/2 - \mathbf{L}(j\Delta z)/\Delta t)\Delta z, \end{aligned} \tag{18a}$$

$$\begin{aligned} \mathbf{A}_{Ij} &= -(\mathbf{G}(j\Delta z)/2 + \mathbf{C}(j\Delta z)/\Delta t)\Delta z, \\ \mathbf{B}_{Ij} &= (\mathbf{G}(j\Delta z)/2 - \mathbf{C}(j\Delta z)/\Delta t)\Delta z. \end{aligned} \tag{18b}$$

The termination load at both ends is Z_1=Z_2, and the excitation source Vs is added to one of the lines as the termination condition. Combining formulas (17), the near-end voltage $\mathbf{V}(0, t)$ and the far-end voltage $\mathbf{V}(L,t)$, and the voltage and current at any position and time can be obtained. Since the format (17) is unconditionally stable, the discrete solution of equation (17) converges to the analytical solution of equation (4). As for the near-end crosstalk (NEXT) and the far-end crosstalk (FEXT), the voltage can be transformed from the time domain to the frequency domain and is obtained by equation (19).

$$\mathrm{NEXT} = 20\log_{10}(V_2(0, f)/V_s), \tag{19a}$$

$$\mathrm{FEXT} = 20\log_{10}(V_2(L, f)/V_s). \tag{19b}$$

C. Application in CM/DM current under feld-to-wire coupling

Considering the situation of Fig. 4 (d) and the effect of a uniform plane wave, the same time-space division is shown in Fig. 6. The voltage and current satisfy equation (4), the difference is that it has the effect of uniform plane wave. The discretized equation is:

$$\mathbf{V}_j^n - \mathbf{V}_{j+1}^n + \mathbf{A}_{Vj}(\mathbf{I}_j^n + \mathbf{I}_{j+1}^n) = -\mathbf{V}_j^{n-1} + \mathbf{V}_{j+1}^{n-1} + \mathbf{E}_{Vj} + \mathbf{B}_{vj}(\mathbf{I}_j^{n-1} + \mathbf{I}_{j+1}^{n-1}), \tag{20}$$

$$\mathbf{A}_{Ij}(\mathbf{V}_j^n + \mathbf{V}_{j+1}^n) + \mathbf{I}_j^n - \mathbf{I}_{j+1}^n = -\mathbf{I}_j^{n-1} + \mathbf{I}_{j+1}^{n-1} + \mathbf{E}_{Ij} + \mathbf{B}_{Ij}(\mathbf{V}_j^{n-1} + \mathbf{V}_{j+1}^{n-1}), \tag{21}$$

where the other two parameter matrices are:

$$\begin{cases} \mathbf{E}_{Vj} = (\mathbf{A}_L - \frac{1}{v_z}\mathbf{A}_T)\frac{2\Delta z}{\Delta t}(E_0(n\Delta t - \frac{j\Delta z}{v_z}) - E_0((n-1)\Delta t - \frac{j\Delta z}{v_z})) \\ \mathbf{E}_{Ij} = \mathbf{C}(j\Delta z)\mathbf{A}_T\frac{2\Delta z}{\Delta t}(E_0(n\Delta t - \frac{j\Delta z}{v_z}) - E_0((n-1)\Delta t - \frac{j\Delta z}{v_z})) \end{cases}, \tag{22}$$

where

$$\mathbf{A}_T = \begin{bmatrix} e_x x_1 + e_y y_1 \\ e_x x_2 + e_y y_2 \end{bmatrix}, \mathbf{A}_L = \begin{bmatrix} \frac{x_1}{v_x} + \frac{y_1}{v_y} \\ \frac{x_2}{v_x} + \frac{y_2}{v_y} \end{bmatrix} e_x. \tag{23}$$

The symmetrical load at both ends is Z_a=Z_b and Z_c, which constitutes the terminal condition. Combined with formula (21), the voltage and current at any position and time can be obtained. The CM/DM current at the left end of the circuit can be expressed as equation (24):

$$I_{L-CM} = (I_1(0, f) + I_2(0, f))/2, \tag{24a}$$

$$I_{L-DM} = (I_1(0, f) - I_2(0, f))/2. \tag{24b}$$

IV. NUMERICAL EXPERIMENT VERIFICATION AND ANALYSIS

A. Validation of the proposed method

The wire used in this paper is a copper core wire, and the outer insulation material is polyvinyl chloride (PVC). Where r=1.2mm, d=2r=2.4mm, h=8mm, L= 1m. The p.u.l parameter matrix set for network training is obtained by the finite element method (FEM) [16]. A set of data is extracted every 5° within 0°~180°, and a total of 36 sets of data are extracted for training network. The results are predicted using different random rotation angles and compared with the results obtained by FEM calculations. The relative errors of the pul parameter matrices **R**(z), **L**(z), **C**(z) and **G**(z) in the unit scales of Ω/m, nH/m, pF/m, and mS/m are shown in Fig. 7, which are all less than 5×10^{-3}.

In order to illustrate the accuracy of the proposed method in crosstalk prediction and CM/DM current prediction for TWP cable with random non-uniform twisting, a TWP model was randomly selected. The terminal port accesses the load, as shown in Fig. 4 (a) and Fig. 4 (b), respectively. Where Z_1=Z_2=50Ω, Z_a=Z_b=50Ω, Z_c=100Ω. As shown in Fig. 8, the prediction result under the wire-to-wire coupling and field-to-wire coupling (solid red line) are compared with the MoM (black dotted line) method. It can be seen from Table 1 that the maximum and minimum values of the average error are 3.524% and 0.158%, respectively.

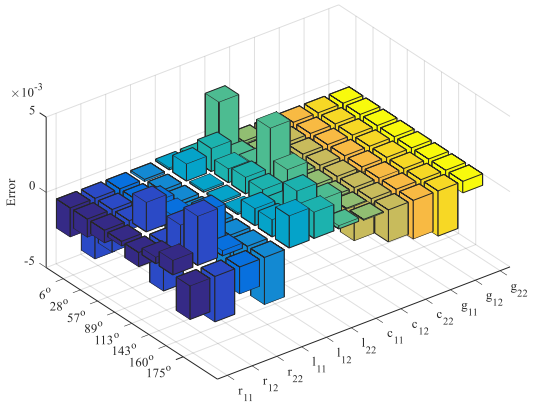

Fig. 7. Error histogram of p.u.l parameter matrix at different rotation angles.

The TWP cable is divided into 1000 sections. The externally applied excitation field is an uniform plane wave electric field incident at the port, where E_0=1V/m, θ_p=90°, ϕ_p=-90° and θ_E=90°. Considering the frequency of the signal source, the frequency range of the crosstalk result is 0.1MHz~1GHz, and the frequency range of the CM/DM current result is 1MHz~1GHz. The results further prove that the method in this paper has a more accurate prediction ability for the electromagnetic anti-interference performance of TWP cable with random non-uniform twisting.

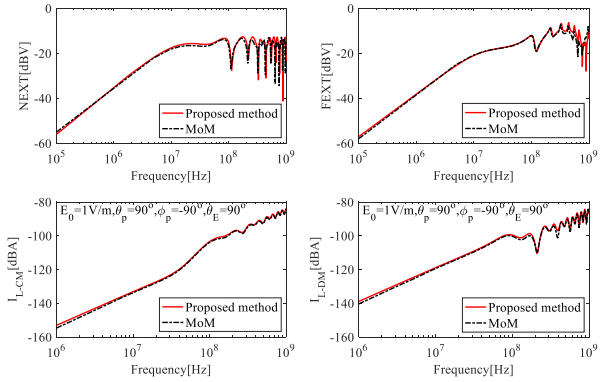

Fig. 8. Results verification of crosstalk and CM / DM current.

Table 1: Average error (%) of crosstalk and CM/DM current

Frequency (MHz)	0.1~100	100~500	500~1000
NEXT	2.140	1.864	1.131
FEXT	1.945	0.332	2.250
$I_{L\text{-}CM}$	3.524	0.158	0.948
$I_{L\text{-}DM}$	2.523	1.920	0.551

B. Prediction of crosstalk

The crosstalk results are shown in Fig. 9. Figures 9 (a) and 9 (b) are near-end crosstalk (NEXT) and far-end crosstalk (FEXT), respectively. A total of 500 sets of TWP models with random non-uniform twisting are calculated, and the CPU time of each set is 52.11s. NEXT and FEXT reach a minimum of -56.2dB and -57.3dB at 0.1MHz, respectively, and a maximum of -12.5dB and -6.23dB at 613MHz and 445MHz, respectively.

The ranges of the upper and lower envelope widths of the NEXT and NEXT curves are 0.024~25.197 dB and 0.045~17.483 dB, respectively. The envelope width fluctuates less in the low frequency range, indicating that different TWP models are less affected. The envelope width changes greatly in the high-frequency range, indicating that the TWP models is susceptible to high-frequency signals, and its crosstalk increases correspondingly.

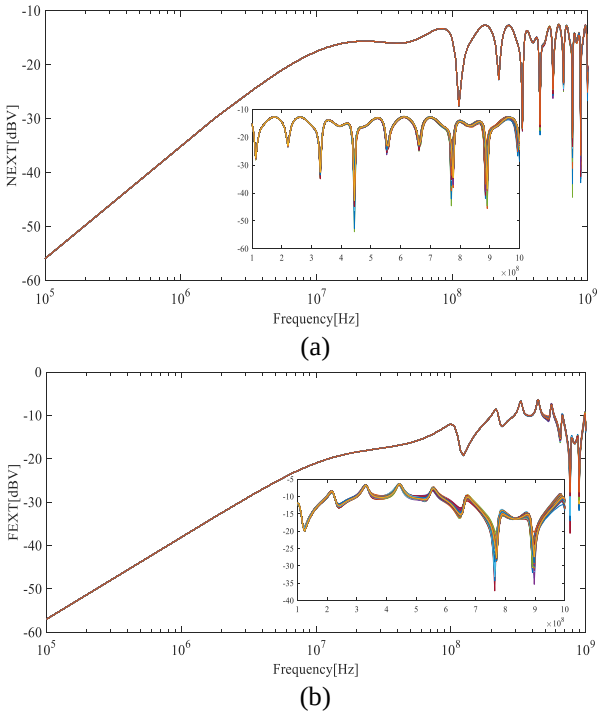

Fig. 9. Wire-to-wire coupling model: crosstalk prediction. (a) Near-end crosstalk (NEXT). (b) Far-end crosstalk (FEXT).

C. Prediction of CM/DM currents

The results of the CM and DM currents irradiated by the plane electric field wave incident at the port are shown in Fig. 10. Figures 10 (a) and 10 (b) show the CM current and DM current, respectively. As with crosstalk, 500 groups of the TWP models are calculated, and the CPU time of each group is 68.74s. The maximum and minimum of CM and DM currents are much reduced compared to crosstalk. This indicates that the effect of field-to-wire coupling is less than the effect of wire-to-wire coupling. The overall trend of CM and DM currents is a straight rise along a slope of 20dB/decade, and the amplitude fluctuation in the high frequency region is small.

The envelope widths of CM and DM currents are 0.399~2.369dB and 0.208~11.695dB, respectively. The envelope width of the CM current is more evenly distributed over the entire frequency range. The envelope width of the DM current is smaller in the low frequency range, but is larger in the high frequency range. This shows that the DM current of the TWP model is more susceptible to high frequency signals.

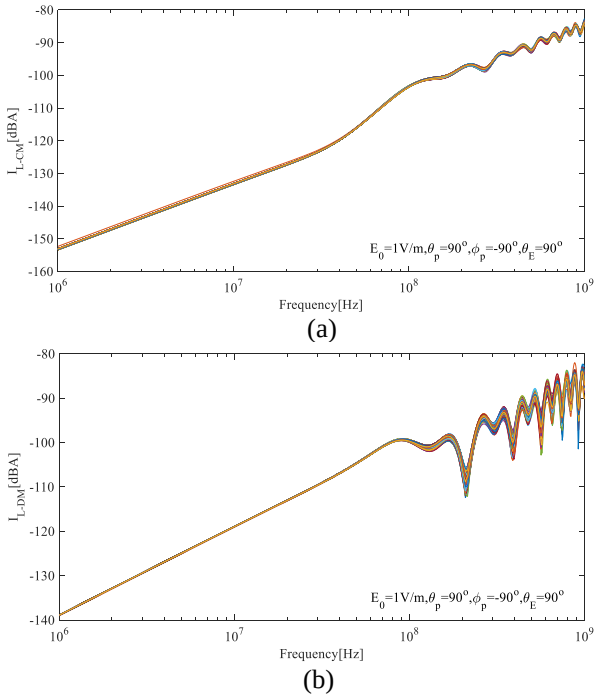

Fig. 10. Field-to-wire coupling model: CM and DM current prediction. (a) CM current and (b) DM current.

Figure 10 is a CM and DM current curve under the irradiation of a plane wave incident at a port. The general actual situation is that the position and the incident angle of the plane wave are both random irradiation with uncertainty. The field-to-wire coupling model under the random position uniform plane wave irradiation is shown in Fig. 11. Figures 11 (a) and 11 (b) show the CM

current and DM current, respectively. A total of 1,000 TWP models under uniform plane wave irradiation with random positions were calculated, and the CPU time spent by each group was 71.83s.

The envelope widths of CM and DM currents are 29.873~56.783dB and 29.755~56.823dB, respectively. Its width is larger than that of a single plane wave. Compared with Fig. 10, CM and DM are greatly affected by the externally applied excitation field. The reason is that the amplitudes of the CM and DM currents are mainly determined by the externally applied excitation field.

It can be seen that all the curves are under the black dotted line in Fig. 11, which represent the worst case of the CM and DM currents. Its initial values start from -143.31dB and -78.46dB, respectively. It can be noticed that the curve of Fig. 10 will show different changing trends in some frequency ranges. This is because different wave angles may cause the observed CM and DM currents to increase or decrease.

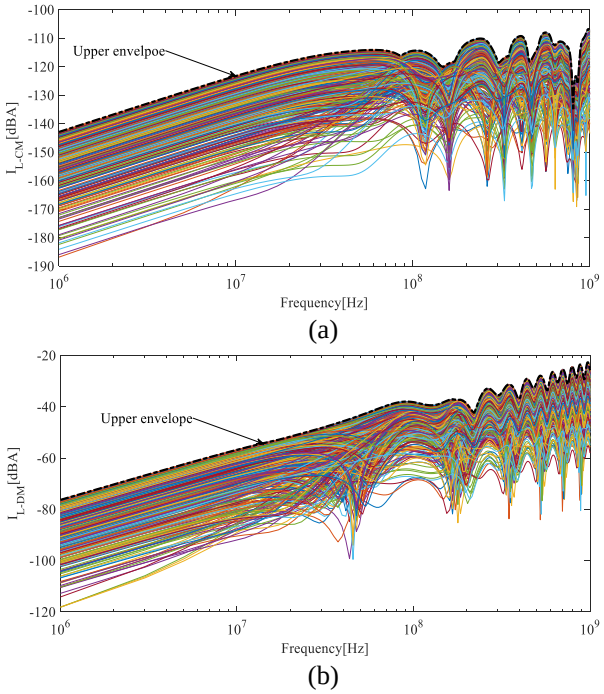

Fig. 11. Field-to-wire coupling model under uniform plane wave irradiation at random position. (a) CM current and (b) DM current.

V. CONCLUSION

In this paper, a new TWP model is proposed. The model considers the randomness of the twisting pitch and the combination of different pitch types. A TWP model is established for the combination of complete pitch segments and non-complete pitch segments, which overcomes the randomness problem in the references.

The p.u.l parameter matrix at any position was obtained by a neural network algorithm, and the FDTD method was used to solve the crosstalk under the wire-to-wire coupling model and the CM/DM current under the field-to-wire coupling model. The full-wave electromagnetic simulation (based on the MoM method) is used for comparison and verification, which proves that the proposed method has high accuracy.

In crosstalk results, TWP with random non-uniform twisting are susceptible to high-frequency signals, and the low-frequency range is less affected. In the CM and DM noise results, the DM current is more susceptible to high-frequency signals than the CM current. However, for CM and DM currents, the impact of uniform plane wave irradiation position and wave angle is greater than the effect of random non-uniform twist pitch. These influencing factors will have important reference significance in subsequent research and engineering applications.

ACKNOWLEDGMENT

The paper is supported by National Natural Science Foundation of China (51475246), National Natural Science Foundation of Jiangsu Province (BK20161019), Aviation Science Foundation (20172552017), and Nanjing International Industrial Technology R&D Cooperation Project under Grant 201911021.

REFERENCES

[1] F. Grassi, "Immunity to conducted noise of data transmission along DC power lines involving twisted-wire pairs above ground," *IEEE Trans. Electromagn. Compat.*, vol. 55, no. 1, pp. 195-207, Feb. 2013.

[2] C. R. Paul, *Analysis of Multiconductor Transmission Lines*. 2nd ed., New York, USA: Wiley, 1994.

[3] C. D. Taylor and J. P. Castillo, "On the response of a terminated twisted-wire cable excited by a plane-wave electromagnetic field," *IEEE Trans. Electromagn. Compat.*, vol. 22, no. 1, pp. 16-19, Feb. 1980.

[4] R. Stolle, "Electromagnetic coupling of twisted pair cables," *IEEE J. Sel. Areas Comm.*, vol. 20, no. 5, pp. 883-892, June 2002.

[5] G. Spadacini, F. Grassi, F. Marliani, and S. A. Pignari, "Transmission-line model for field-to-wire coupling in bundles of twisted-wire pairs above ground," *IEEE Trans. Electromagn. Compat.*, vol. 56, no. 6, pp. 1682-1690, Dec. 2014.

[6] G. Spadacini and S. A. Pignari, "Numerical assessment of radiated susceptibility of twisted-wire pairs with random non-uniform twisting," *IEEE Trans. Electromagn. Compat.*, vol. 55, no. 5, pp. 956-964, Jan. 2013.

[7] G. Spadacini and S. A. Pignari, "Radiated susceptibility of a twisted-wire pair illuminated by a random plane-wave spectrum," *IEICE Trans.*

Commun., vol. E93-B, no. 7, pp. 1781-1787, July 2010.

[8] S. A. Pignari and G. Spadacini, "Plane-wave coupling to a twisted-wire pair above ground," *IEEE Trans. Electromagn. Compat*., vol. 53, no. 2, pp. 508-523, May 2011.

[9] S. Shiran, B. Reiser, and H. Cory, "A probabilistic model for the evaluation of coupling between transmission lines," *IEEE Trans. Electromagn. Compat.*, vol. 35, no. 3, pp. 387-393, Aug. 1993.

[10] D. Weiner and G. Capraro, "A statistical approach to EMI theory and experiment - Part 2," *presented at the 1987 Zurich Symp. Electromagn. Compat*., Zurich, Switzerland, 1987.

[11] S. Salio, F. Canavero, D. Lecointe, and W. Tabbara, "Crosstalk prediction on wire bundles by Kriging approach," *in Proc. IEEE Int. Symp. Electromagn. Compat*., vol. 1, pp. 197-202, 2000.

[12] S. Sun, G. Liu, J. L. Drewniak, and D. J. Pommerenke, "Hand-assembled cable bundle modeling for crosstalk and common-mode radiation prediction," *IEEE Trans. Electromagn. Compat*., vol. 49, no. 3, pp. 708-718, Aug. 2007.

[13] A. Shoory, M. Rubinstein, A. Rubinstein, C. Romero, N. Mora, and F. Rachidi, "Application of the cascaded transmission line theory of Paul and McKnight to the evaluation of NEXT and FEXT in twisted wire pair bundles," *IEEE Trans. Electromagn. Compat*., vol. 55, no. 4, pp. 648-656, Aug. 2013.

[14] X. K. Liu, F. Grassi, G. Spadacini, and S. A. Pignari, "Physically based modeling of hand-assembled wire bundles for accurate EMC prediction," *IEEE Trans. Electromagn. Compat*., pp. 1-9, June 2019.

[15] C. P. Yang, W. Yan, Y. Zhao, Y. Chen, C. M. Zhu, and Z. B. Zhu, "Analysis on RLCG parameter matrix extraction for multi-core twisted cable based on back propagation neural network algorithm," *IEEE Access*., vol. 7, pp. 126315-126322, Aug. 2019.

[16] Y. Zhao and Y. Y. Wang, "A new finite-element solution for parameter extraction of multilayer and multiconductor interconnects," *IEEE Microwave and Guided Wave Letters.*, vol. 7, no. 6, pp. 156-158, June 1997.

[17] C. Huang, W. Yan, Y. Zhao, Q. Q. Liu, and J. M. Zhou, "A new method for predicting crosstalk of random cable bundle based on BAS-BP neural network algorithm," *IEEE Access*, vol. 8, pp. 20224-20232, Jan. 2020.

[18] F. Dai, G. H. Bao, and D. L. Su, "Crosstalk prediction in non-uniform cable bundles based on neural network," *Proceedings of the 9th International Symposium on Antennas, Propagation and EM Theory*, Guangzhou, pp. 1043-1046, 2010.

[19] A. T. Matsu, F. Rachidi, and M. Rubinstein, "A technique for calculating voltages induced on twisted-wire pairs using the FDTD method," *IEEE Trans. Electromagn. Compat*., vol. 59, no. 1, pp. 301-304, Oct. 2016.

[20] P. F. Zhang, X. L. Du, J. Zou, J. S. Yuan, and S. L. Huang, "Iterative solution of MTL based on the spatial decomposition and the second-order FDTD," *IEEE Trans. Magnetics*., vol. 54, no. 3, pp. 1185-1193, Mar. 2018.

Chao Huang was born in Anhui Province, China. He received the B.S degree in School of Electrical Engineering and Automation from Anhui University of Technology, Maanshan, China, in 2018. He is currently working toward the Master's degree in Electrical Engineering at Nanjing Normal University, Nanjing, China. His main research interests include multi-conductor transmission lines and EMC.

Yang Zhao received his B.E., M.E., and Ph.D. degree all in Power Electronic Technology from Nanjing University of Aeronautics and Astronautics, Nanjing, China, in 1989 and 1992, and 1995, respectively. He is currently the Professor with Nanjing Normal University. His research interests are in the areas of Electromagnetic Compatibility, Power Electronics and Automotive Electronics.

Wei Yan Doctor & Assoc. Professor from Nanjing Normal University. He obtained the Physics and Electronics Ph.D. and Electrical Engineering M.S. from Nanjing Normal University in 2014 and 2011. He is the Senior Member of China Electrical Technology Association and the evaluation expert of the Electromagnetic Compatibility Calibration Specification of China.

Antenna Resonant Frequency Modeling based on AdaBoost Gaussian Process Ensemble

Tianliang Zhang [1], Yubo Tian [2], Xuezhi Chen [3], and Jing Gao [4]

[1] School of Electronics and Information
Jiangsu University of Science and Technology, Zhenjiang 212003, China
757938546@qq.com

[2] School of Electronics and Information
Jiangsu University of Science and Technology, Zhenjiang 212003, China
tianyubo@just.edu.cn

[3] School of Electronics and Information
Jiangsu University of Science and Technology, Zhenjiang 212003, China
1152871387@qq.com

[4] School of Electronics and Information
Jiangsu University of Science and Technology, Zhenjiang 212003, China
1275369073@qq.com

Abstract — The design of electromagnetic components generally relies on simulation of full-wave electromagnetic field software exploiting global optimization methods. The main problem of the method is time consuming. Aiming at solving the problem, this study proposes a regression surrogate model based on AdaBoost Gaussian process (GP) ensemble (AGPE). In this method, the GP is used as the weak model, and the AdaBoost algorithm is introduced as the ensemble framework to integrate the weak models, and the strong learner will eventually be used as a surrogate model. Numerical simulation experiment is used to verify the effectiveness of the model, the mean relative error (MRE) of the three classical benchmark functions decreases, respectively, from 0.0585, 0.0528, 0.0241 to 0.0143, 0.0265, 0.0116, and then the method is used to model the resonance frequency of rectangular microstrip antenna (MSA) and coplanar waveguide butterfly MSA. The MRE of test samples based on the APGE are 0.0069, 0.0008 respectively, and the MRE of a single GP are 0.0191, 0.0023 respectively. The results show that, compared with a single GP regression model, the proposed AGPE method works better. In addition, in the modeling experiment of resonant frequency of rectangular MSA, the results obtained by AGPE are compared with those obtained by using neural network (NN). The results show that the proposed method is more effective.

Index Terms — AdaBoost algorithm, Gaussian process ensemble, microstrip antenna, resonant frequency.

I. INTRODUCTION

When studying electromagnetic optimization problems, the electromagnetic simulation software, such as HFSS, is generally used to build the model, and some accurate sample data is obtained by calling the HFSS software for optimization. The general method to optimize microwave structure is using HFSS exploiting global optimization method. However, it will be very time-consuming because HFSS is called for thousands of times for the evaluation of fitness function of the global optimization method. The time may be several days or even several months, and it is insufferable [1]. Based on this problem, many scholars have proposed methods of using surrogate models, such as neural networks (NN) [2,3], support vector machines (SVM) [4,5], linear regression [6,7] and Gaussian process (GP) [8,9], and some have achieved results that meet the standards. However, when using surrogate models, it is still necessary to use the HFSS software to simulate some data. Because it is not easy to obtain a large number of sample data, the accuracy of the established model sometimes cannot meet the requirements. This study proposes an AdaBoost GP ensemble (AGPE) method, using the GP as the weak learning model and the AdaBoost algorithm [10,11] as the ensemble framework.

Submitted On: June 29, 2020
Accepted On: October 20, 2020

https://doi.org/10.47037/2020.ACES.J.351205

1054-4887 © ACES

Some weak GPs are weighted and integrated to obtain a strong learner. Compared with the single GP, the method proposed in this study can obtain higher accuracy under the premise of the same training samples, while the single GP requires more training samples to achieve the modeling accuracy of the method proposed. Therefore, the proposed method saves the time of using HFSS software to simulate samples.

As a machine learning (ML) algorithm, GP has attracted a lot of attention in recent years [12]. Compared to other ML algorithms such as NN, the GP has two major advantages: 1) The GP requires few parameters to be learned during the training process and is easy to implement; 2) It has a good effect on solving the complex problems of insufficient samples and non-linearity [13]. At present, in the field of electromagnetism, GP has been used as a surrogate model, and some results have been obtained.

With the great leap of modern industrial level, the problems faced are more and more complex. At this time, the concept of ensemble learning [14,15] came into being, and gradually attracted a large number of scholars. In 1990, Schapire used the constructive method to prove the theory that integrating multiple weak learners can get stronger learners, and proved the excellence of integrated learning [16]. In 1996, the Bagging algorithm came out [17]. The algorithm processes training samples through Bootstrap method, and obtains a number of training subsets with the same number but certain similarity. Then, it uses these subsets to train several weak models, and finally integrates several weak models. AdaBoost algorithm was proposed by Freund et al. in 1996 [18], and realized the great leap from theoretical research to practical application of integrated learning. In 2016, Chen et al. proposed an improved Boosting model using residual learning, namely XGBoost [19]. This model and its improved model are very popular in various fields. When dealing with many problems, its learning performance can be compared with that of deep neural network (DNN).

AdaBoost algorithm is proposed on the basis of Boosting, which is one of the three ensemble algorithms. It has been widely concerned in the field of ML [20]. It is applicable to classification and regression problems [21,22], but most of them are currently used to deal with classification problems. In reference [23], the AdaBoost algorithm and decision tree are combined to classify electromagnetic radiation and other related characteristics. In reference [24], the AdaBoost algorithm and NN are combined to classify high-resolution radar. In this study, the AdaBoost algorithm is used to deal with the regression problem, and an algorithm based on the AGPE is proposed. The advantage of the proposed method is illustrated by benchmark functions and resonance frequency of microstrip antennas (MSAs).

II. GAUSSIAN PROCESS

From the mathematical point of view, GP is a kind of functional distribution, which represents a set of random variables subject to joint Gaussian distribution. The GP is uniquely determined by mean function and covariance function [25].

Suppose there is a training sample set, $D=\{(\mathbf{x}_i,\mathbf{y}_i)\}, i=1,\cdots,n,\ \mathbf{x}_i\in R^d, \mathbf{y}_i\in R$. n is the number of samples and d is the dimension of training samples. Then the mean function and covariance function are as follows:

$$m(\mathbf{x})=E[f(\mathbf{x})], \tag{1}$$

$$k(\mathbf{x},\mathbf{x}')=E\left[\left(f(\mathbf{x})-m(\mathbf{x})\right)\left(f(\mathbf{x}')-m(\mathbf{x}')\right)\right], \tag{2}$$

where $\mathbf{x},\mathbf{x}'\in R^d$ is a random variable, so GP can also be expressed by the following formula:

$$f(\boldsymbol{x})\sim GP(m(\boldsymbol{x}),k(\boldsymbol{x},\boldsymbol{x}')). \tag{3}$$

Assuming that the test sample is $\mathbf{x}^*$, the prediction distribution of the GP model is the joint Gaussian distribution formed by the training sample and the test sample:

$$\begin{bmatrix}\boldsymbol{y}\\ f^*\end{bmatrix}\sim N\left\{0,\begin{bmatrix}K(\boldsymbol{x},\boldsymbol{x})+\sigma_n^2\boldsymbol{I} & K(\boldsymbol{x},\boldsymbol{x}^*)\\ K(\boldsymbol{x}^*,\boldsymbol{x}) & K(\boldsymbol{x}^*,\boldsymbol{x}^*)\end{bmatrix}\right\}, \tag{4}$$

where $\mathbf{x},\mathbf{x}^*$ is the input of training sample and test sample, $\mathbf{y}, f^*$ is the label of training sample and test sample, and $K(\boldsymbol{x},\boldsymbol{x}), K(\boldsymbol{x}^*,\boldsymbol{x})$ is the covariance matrix respectively.

The most important part of GP is the setting of kernel function. Through the mapping of kernel function, the relationship between input and output is established. In general, the setting of kernel function needs to meet Mercer condition [26]. There are many common kernel functions, such as radial basis kernel function, Matern series and so on.

In the training process of GP, only a group of super parameters need to be learned, which is also the only parameter to be determined. The properties of GP are determined by the super parameters that are generally obtained by the maximum likelihood method. The conditional probability of training samples is calculated, and then the logarithmic likelihood function $L(\theta)$ is calculated. The final optimization algorithm is conjugate gradient algorithm [27]. $L(\theta)$ and its partial derivatives are as follows:

$$L(\theta)=-\frac{1}{2}\boldsymbol{y}^T\boldsymbol{C}^{-1}\boldsymbol{y}-\frac{1}{2}\log|\boldsymbol{C}|-\frac{n}{2}\log 2\pi, \tag{5}$$

$$\frac{\partial L(\theta)}{\partial\theta_i}=\frac{1}{2}tr((\boldsymbol{\alpha}\boldsymbol{\alpha}^T-\boldsymbol{C}^{-1})\frac{\partial C}{\partial\theta_i}). \tag{6}$$

After the optimal super parameter is obtained, the test sample can be estimated according to Equations (1) and (2).

III. THE PROPOSED ADABOOST GAUSSIAN PROCESSES ENSEMBLE (AGPE)

AdaBoost is also called adaptive boosting. Its core idea is to generate strong learners by weighted combination of iterative basic learners. This algorithm can effectively avoid over fitting problem [28]. In this study, the algorithm is combined with GP to solve the regression problem. AdaBoost algorithm can be described as follows. First, Bootstrap is used to generate a set of equal number of sub training sets from the original training samples, and each sample is given equal initial weight to train a GP regression model; then the error rate of the model is calculated and the training sample weight is updated according to the error rate; finally, the weight of the model is calculated. By repeating the above process, several models can be obtained, and the output results can be obtained according to the weight ensemble.

Suppose the original sample set is $D=\left\{\left(x_1,y_1\right),\left(x_2,y_2\right),\cdots,\left(x_N,y_N\right)\right\}$, where N is the number of samples. Table 1 is the pseudo code of the proposed AGPE algorithm. The specific steps are as follows:

1) Bootstrap is used to generate a set of sub training sets with the number of N from the original samples D, and each sample is given equal initial weight $W_1=\left(\omega_1,\cdots,\omega_i\right), i=1,\cdots,N$, $\omega_i=1/N$.

2) According to the training subset generated above, the GP is trained and the maximum error on the training set is calculated:

$$E_m=\max\left|y_i-GP_m(x_i)\right|, \tag{7}$$

Calculate the relative error of each sample:

$$e_{mi}=\frac{\left|y_i-GP_m(x_i)\right|}{E}, \tag{8}$$

The error rate of the training set of the model can be obtained:

$$e_m=\sum_{i=1}^{N}\omega_{mi}e_{mi}. \tag{9}$$

3) According to the error rate, the weight coefficient of the model is calculated:

$$\alpha_m=\frac{e_m}{1-e_m}. \tag{10}$$

4) Update sample weight:

$$W_{m+1}=\frac{\omega_{mi}}{Z_m}\alpha_m^{1-e_{mi}}, \tag{11}$$

where Z is a normalization factor:

$$Z_m=\sum_{i=1}^{N}\omega_{mi}\alpha_m^{1-e_{mi}}. \tag{12}$$

5) Repeat the above process K times to get K GP models, and integrate them to get the final model as follows:

$$f(x)=\sum_{m=1}^{K}\left(\ln\frac{1}{\alpha_m}\right)GP_m(x). \tag{13}$$

Table 1: Pseudo code of the proposed AGPE algorithm

Input: Training set $D=\left\{\left(x_1,y_1\right),\left(x_2,y_2\right),\cdots,\left(x_N,y_N\right)\right\}$; Iteration times T.

Initialize: $W_1(i)=1/N$, where $i=1,2,\cdots,N$.

Do for: $t=1,2,\cdots,T$

1. Use Bootstrap to generate a subset of the training sample D_t from D.
2. Use the training subset D_t to train the weak learner GP_t.
3. Calculate the error rate of the basic learner on the training set e_t:

$$e_t=\sum_{i=1}^{N}W_t(i)\varepsilon_t,$$

$$\varepsilon_t=\frac{\left|y_i-GP_t(x_i)\right|}{\max\left|y_i-GP_t(x_i)\right|},$$

If $e_t>0.5$, then go to step 1 to continue the cycle;
End if

4. Let $\alpha_t=\ln\frac{e_t}{1-e_t}$;
5. Update the weight of training samples W_t;

$$W_{t+1}(i)=\frac{W_t(i)}{Z_t}\alpha_t^{1-\varepsilon_t},$$

Where Z_t is the normalization factor;

End for

Output: Final regression:

$$f(x)=\sum_{t=1}^{N}\left(\ln\frac{1}{\alpha_t}\right)GP_t(x).$$

IV. CASES STUDY

A. Benchmark functions

In this part, three classical benchmark functions are selected to verify the superiority of the proposed AGPE algorithm. The specific information of the test functions is shown in Table 2. At the same time, in order to show the superiority of the proposed method, it is compared with a single GP regression model, and mean relative error (MRE) is selected as the evaluation index, which is defined by:

$$MRE=\frac{1}{n}\sum_{i=1}^{n}\frac{\left|f(x_i)-y(x_i)\right|}{y(x_i)}. \tag{14}$$

Table 2: Benchmark functions

Function	Function Expression	Dim.	Search Space
Schaffer	$f(x)=0.5+\frac{\left(\sin\sqrt{x_1^2+x_2^2}-0.5\right)}{\left(1+0.001\left(x_1^2+x_2^2\right)\right)^2}$	2	-100～100
Rastrigin	$f(x)=\sum_{i=1}^{n}\left(x_i^2-10\cos\left(2\pi x_i^2\right)+10\right)$	3	-20～20
Schwefel	$f(x)=418.9829n+\sum_{i=1}^{n}\left(x_i\sin(\sqrt{\lvert x_i\rvert})\right)$	3	-500～500

In this case, the number of samples $NP=35$, in which 5 groups are randomly selected as test samples and the rest as training samples. Table 3 shows the MRE comparison between the proposed model and a single model on the test set, and Fig. 1 shows the comparison of the prediction results of test samples between the proposed method and a single model. The abscissa in the figure represents the number of test samples, and the ordinate represents the value corresponding to the test samples. According to the results in Table 3 and Fig. 1, the MRE of the three benchmark functions is 0.0585, 0.0528 and 0.0241 respectively by single GP, whereas the MRE is 0.0143, 0.0265 and 0.0116 respectively by the proposed method in this paper. Therefore, the modeling effect of the method proposed in this paper is better than that of the single GP model.

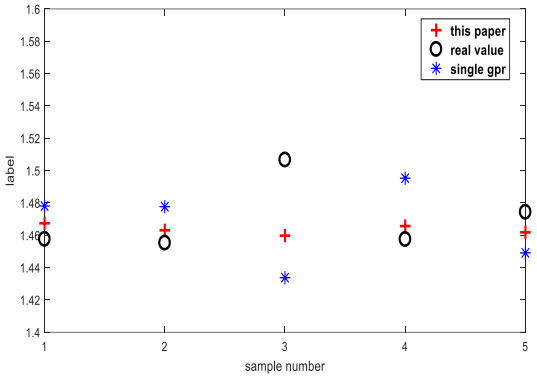

(a)

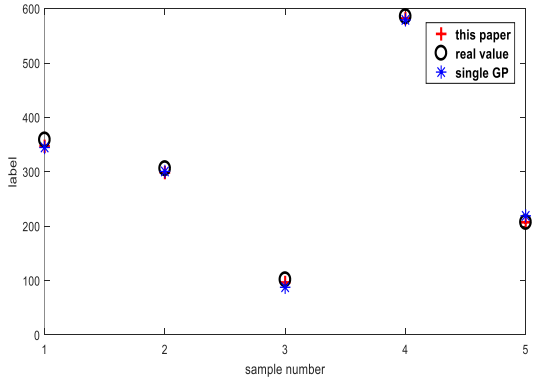

(b)

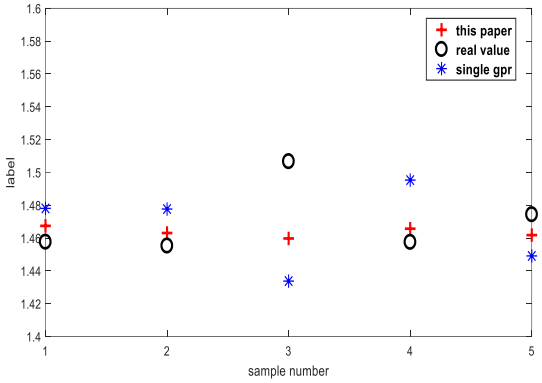

(c)

Fig. 1. Prediction results comparison of test samples: (a) for Schaffer function, (b) for Rastrigin function, and (c) for Schwefel function.

Table 3: MRE comparison of the benchmark functions

Methods	Schaffer	Rastrigin	Schwefel
Single GP	0.0585	0.0528	0.0241
This paper	0.0143	0.0265	0.0116

B. Resonant frequency modeling of rectangular MSA

Antenna plays an irreplaceable role in the communication system. MSA has the advantages of small size, light weight and easy fabrication, and has been widely used in aerospace, medical, mechanical and other fields [29]. The MSA can be set to different shapes as required. In this paper, the resonant frequency of rectangular MSA is used for modeling, and its structure is shown in Fig. 2.

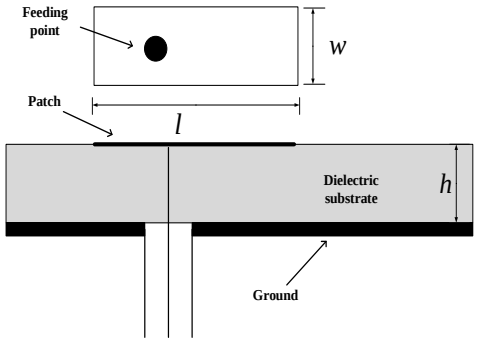

Fig. 2. The rectangular MSA.

In this modeling, the width *w*, length *l*, height *h* and dielectric constant ε_r of the MSA are as input, and the resonance frequency f_{11} (MHz) is as output. We select 33 groups of data from Reference [30] and list them in Table 4 to model according to the proposed AGPE method, in which those with tag* are test sample. The prediction results of this paper are compared with other literature and single GP.

Table 4: Resonant frequency of the rectangular MSA in TM_{10} mode

w (cm)	l (cm)	h (cm)	ε_r	f_{ME}	f_{EDBD}	f_{DBD}	f_{BP}	f_{AGPE}	f_{GP}
0.850	1.290	0.017	2.22	7740*	7935.5	7890.1	7858.6	7965	8032.8
0.790	1.185	0.017	2.22	8450	8328.2	8226.0	8233.1	8450	8450
2.000	2.500	0.079	2.22	3970	4046.4	4023.0	4075.4	3970	3970
1.063	1.183	0.079	2.25	7730	7590.1	7567.3	7616.8	7730	7730
0.910	1.000	0.127	10.2	4600	4604.8	4573.9	4592.4	4600	4600
1.720	1.860	0.157	2.33	5060*	4934.2	4914.0	4930.3	5041	5156.3
1.810	1.960	0.157	2.33	4805	4699.2	4684.8	4703.3	4805	4805
1.270	1.350	0.163	2.55	6560	6528.6	6502.8	6516.5	6560	6560
1.500	1.621	0.163	2.55	5600*	5503.2	5473.3	5449.0	5601	5535.3
1.337	1.412	0.200	2.55	6200	6176.6	6142.6	6147.2	6200	6200
1.120	1.200	0.242	2.55	7050	7099.6	7064.3	7132.9	7050	7050
1.403	1.485	0.252	2.55	5800	5805.6	5768.8	5765.7	5800	5800
1.530	1.630	0.300	2.50	5270	5287.7	5260.3	5254.0	5270	5270
0.905	1.018	0.300	2.50	7990	7975.5	7881.8	8002.2	7990	7990
1.170	1.280	0.300	2.50	6570*	6674.8	6632.8	6682.7	6558	6600.5
1.375	1.580	0.476	2.55	5100	5311.8	5293.2	5291.4	5100	5100
0.776	1.080	0.330	2.55	8000	7911.1	7841.6	7942.5	8000	8000
0.790	1.255	0.400	2.55	7134	7183.2	7162.1	7215.9	7134	7134
0.987	1.450	0.450	2.55	6070*	6173.0	6155.1	6170.2	6074	6040.7
1.000	1.520	0.476	2.55	5820	5931.0	5918.0	5924.5	5820	5820
0.814	1.440	0.476	2.55	6380	6424.0	6417.5	6430.7	6380	6380
0.790	1.620	0.550	2.55	5990	5866.1	5873.9	5870.5	5990	5990
1.200	1.970	0.626	2.55	4660	4699.0	4728.0	4718.9	4660	4660
0.783	2.300	0.854	2.55	4600*	4459.1	4517.1	4519.2	4644	4847.4
1.256	2.756	0.952	2.55	3580	3659.8	3655.7	3644.6	3580	3580
0.974	2.620	0.952	2.55	3980	3952.9	3982.6	3975.9	3980	3980
1.020	2.640	0.952	2.55	3900	3905.4	3930.0	3922.2	3900	3900
0.883	2.676	1.000	2.55	3980	3938.8	3970.7	3965.3	3980	3980
0.777	2.835	1.100	2.55	3900	3825.5	3851.1	3845.9	3900	3900
0.920	3.130	1.200	2.55	3470*	3481.4	3466.2	3458.4	3465	3478.1
1.030	3.380	1.281	2.55	3200	3230.3	3184.7	3178.0	3200	3200
1.265	3.500	1.281	2.55	2980	3036.1	2965.6	2961.2	2980	2980
1.080	3.400	1.281	2.55	3150	3191.2	3140.4	3134.0	3150	3150
Absolute error sum of all data					2329	2427	2372	**310**	770
MRE of test samples					0.0192	0.0162	0.0174	**0.0069**	0.0191

In Table 4, the training data of rectangular MSA are given in columns 1~4, the measured value in column 5, and the NN results given by Guney et al. [30] are listed in columns 6~8, and f_{EDBD}, f_{DBD}, f_{BP}, respectively, represent the predicted resonance frequency of the NN model using the EDBD (extended delta bar delta), DBD (delta bar delta) and BP (back propagation) algorithm. Columns 9 and 10 respectively show the results obtained by using the proposed method in this paper and the single GP model. At the same time, the absolute error sum of each method is given in the penultimate row of Table 4, and the MRE of test samples according to the proposed method and other models is given in the penultimate row. It can be seen from Table 4 that the total absolute error calculated by the proposed method in this paper is 310MHz, which is superior to the calculation results of other documents and single GP, and the MRE of test sample is smaller than that of other models, which shows the excellence and effectiveness of the proposed algorithm in this paper.

C. Resonant frequency modeling of coplanar waveguide (CPW) butterfly MSA.

In order to verify the effectiveness of the proposed method further, the resonance frequency of coplanar waveguide (CPW) butterfly MSA (shown in Fig. 3) is modeled. Through HFSS simulation software, training data are obtained. Selecting h, W, L are as input data, and resonance frequency f_{11} (MHz) is as output, where h represents the thickness of the dielectric substrate, L, W respectively represents the length of the butterfly antenna and the length corresponding to the opening Angle. 30 groups of data are selected for modeling, in which 25 groups are as training data and the other 5 groups are as testing data. Finally, the result computed by the proposed AGPE algorithm is compared with that

of single GP, shown in Fig. 4 and Table 5. We can see from Fig. 4 and Table 5 that the MRE of the AGPE model and single GP model are 0.0008 and 0.0023 respectively, and the prediction value of the AGPE model is closer to the real value than that of single GP, which means the accuracy and generalization performance of the AGPE model is better than that of single GP.

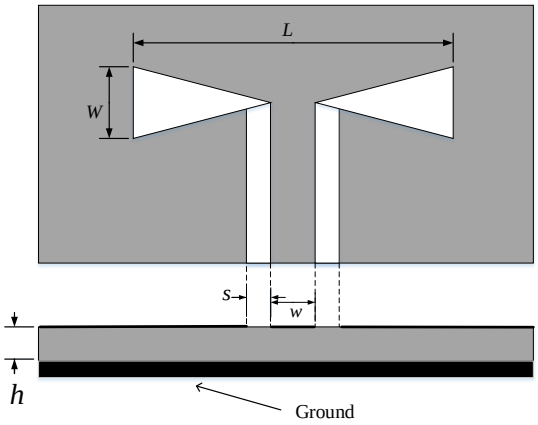

Fig. 3. The CPW butterfly MSA.

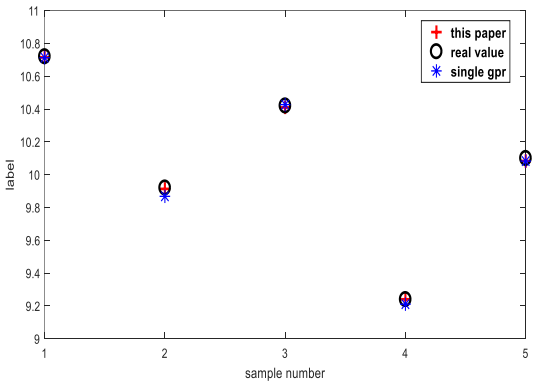

Fig. 4. Prediction results comparison of test samples for the CPW butterfly MSA

Table 5: Simulation results of the CPW butterfly MSA

Methods	MRE
Single GP	0.0023
This paper	0.0008

V. CONCLUSION

This study proposes an algorithm named AdaBoost Gaussian process ensemble (AGPE). The core of this algorithm is to use Gaussian process as weak learner and the AdaBoost algorithm as ensemble framework. Firstly, we obtain a group of weighted weak learners, and then integrate them to get the final strong learner. Through modeling of the benchmark functions and the resonant frequencies of rectangular microstrip antenna and coplanar waveguide butterfly microstrip antenna, it can be seen that the proposed AGPE method has higher accuracy than that of single GP. At the same time, compared with the neural network method in other literature, the proposed AGPE method also shows some advantages. The proposed method in the study is also easily be used in other microwave components modeling in the field of electromagnetics.

ACKNOWLEDGMENT

This work is supported by the National Natural Science Foundation of China (NSFC) under No. 61771225 and Jiangsu Province Qinglan project.

REFERENCE

[1] X. X. Liu, X. H. Yin, and Q. J. Yang, "Research and analysis of human brain and electromagnetic radiation SAR based on HFSS," *International Conference on Intelligent Transportation, IEEE Computer Society*, Xia-Men, China, pp. 778-781. Apr. 2018.

[2] I. Khan, Y. B. Tian, and S. U. Rahman, "Design annular ring microstrip antenna based on artificial neural network," *IEEE Advanced Information Management, Communicates, Electronic and Automation Control Conference (IMCEC)*, Xi'an, China, pp. 2033-2037, Aug. 8-11, 2018.

[3] F. Chen and Y. B. Tian, "Modeling resonant frequency of rectangular microstrip antenna using CUDA-based artificial neural network trained by particle swarm optimization algorithm," *The Applied Computational Electromagnetics Society Journal*, vol. 2, no. 12, pp. 1025-1034, 2014.

[4] F. Y. Sun, Y. B. Tian, and Z. L. Ren, "Modeling the resonant frequency of compact microstrip antenna by the PSO-based SVM with the hybrid kernel function," *International Journal of Numerical Modelling: Electronic Networks, Devices and Fields*, vol. 29, no. 6, pp. 1129-1139, 2016.

[5] X. M. Han, J. J. Wang, and Z. K. Wu, "Learning solutions to two dimensional electromagnetic equations using LS-SVM," *Neuro Computing*, vol. 317, no. 23, pp. 15-27, 2018.

[6] S. L. Zhuang and A. Y. Wang, "Optimization design of permanent magnet synchronous generator in wind turbines based on improved particle swarm algorithm," *Journal of Electric Power*, vol. 34, no. 1, pp. 64-67, 2019.

[7] Y. M. Zhang, N. H. Kim, and C. Park, "Multifidelity surrogate based on single linear regression," *AIAA Journal*, vol. 56, no. 12, pp. 1-9, 2018.

[8] J. P. De Villiers and J. P. Jacobs, "Gaussian process modeling of CPW-fed slot antennas," *Progress in Electromagnetics Research*, vol. 98, no. 1, pp. 233-249, 2009.

[9] P. Gardner, T. J. Rogers, and C. Lord, "Sparse Gaussian process emulators for surrogate design modelling," *Applied Mechanics and Materials*, vol. 855, pp. 18-31, 2018.
[10] Z. H. Zhou, "Learn ware: On the future of machine learning," *Frontiers of Computer Science in China*, vol. 10, no. 4, pp. 170-185, 2016.
[11] S. Yadahalli and M. K. Nighot, "AdaBoost based parameterized methods for wireless sensor networks," *2017 International Conference on Smart Technologies for Smart Nation (Smart Tech. Con.)*, Bangalore, pp. 1370-1374, 2017.
[12] X. Z. Chen, Y. B. Tian, T. L. Zhang, and J. Gao, "Differential evolution based manifold Gaussian process machine learning for microwave filter's parameter extraction," *IEEE Access*, vol. 8, pp. 146450-146462, 2020.
[13] J. P. Jacobs and S. Koziel, "Single-model versus ensemble-model strategies for efficient gaussian process surrogate modeling of antenna input characteristics," *Electromagnetics in Advanced Applications (ICEAA). IEEE*, Torino, Italy, pp. 510-513, Sep. 9-13, 2013.
[14] Y. M. Tian and X. T. Wang, "SVM ensemble method based on improved iteration process of AdaBoost algorithm," *Chinese Control and Decision Conference (CCDC)*, Chongqing, China, pp. 4026-4032, May 28-30, 2017.
[15] X. Chen, Z. H. Zhou, and Y. Zhao, "ELLPMDA: Ensemble learning and link prediction for Mirna-disease association prediction," *RNA Biology*, vol. 15, no. 6, pp. 01-50, 2018.
[16] R. E. Schapire, "The strength of weak learnability," *Machine Learning*, vol. 5, no. 2, pp. 197-227, 1990.
[17] B. Leo, "Bagging predictors," *Machine Learning*, vol. 24, no. 2, pp. 123-140, 1996.
[18] R. E. Schapire, "The strength of weak learnability (extended abstract)," *30th Annual Symposium on Foundations of Computer Science, Research Triangle Park*, North Carolina, USA, pp. 197-227, Oct. 30-Nov. 1, 1989.
[19] T. Q. Chen and C. Guestrin, "XGBoost: A scalable tree boosting system," *Proceedings of the 22nd ACM SIGKDD International Conference on Knowledge Discovery and Data Mining*. New York, USA, pp. 785-794, Aug. 13-17, 2016.
[20] K. W. Walker, Z. Jiang, "Application of adaptive boosting (AdaBoost) in demand-driven acquisition (DDA) prediction: A machine-learning approach," *The Journal of Academic Librarianship*, vol. 45, no. 3, pp. 203-212, 2019.
[21] X. L. Guo and K. Uehara, "Graph-Based semi-supervised regression and its extensions," *International Journal Advanced Computing Science Application*, vol. 6, no. 6, pp. 260-269, 2015.
[22] Q. S. Wu and H. Nagahashi, "Analysis of generalization ability for different AdaBoost variants based on classification and regression trees," *Journal of Electrical and Computer Engineering*, vol. 2015, pp. 1-17, 2015.
[23] J. Nie, S. C. Yang, and Q. Ren, "A novel classification method based on AdaBoost for electromagnetic emission," *The Applied Computational Electromagnetics Society Journal*, vol. 34, no. 6, pp. 962-969, 2019.
[24] B. Li, X. G. Zhang, and H. Fang, "An improved bp-AdaBoost algorithm and its application in radar multi-target classification," *Journal of Nanjing University (Natural Science Edition)*, vol. 53, no. 5, pp. 984-989, 2017.
[25] J. Gao, Y. B. Tian, and X. Zheng, "Resonant frequency modeling of microwave antennas using Gaussian process based on semi-supervised learning," *Complexity*, vol. 2020, 2020.
[26] P. S. Pramudita, L. R. Zuhal, and K. Shimoyama, "Gaussian process surrogate model with composite kernel learning for engineering design," *AIAA Journal*, vol. 58, no. 6, pp. 1864-1880, 2020.
[27] Z. Qiang, Y. Chen, and Y. B. Tian, "Study on optimal design of GPS microwave devices by Gaussian process modeling based on particle swarm optimization," *Journal of Radio Science*, vol. 31, no. 5, pp. 927-932, 2016.
[28] X. Yu, J. Y. Lin, and F. Jiang, "A cross-domain collaborative filtering algorithm based on feature construction and locally weighted linear regression," *Computational Intelligence and Neuroscience*, vol. 2018, pp. 1-12, 2018.
[29] X. H. Fan, Y. B. Tian, and Y. Zhao, "Optimal design of microwave devices by fitness-estimation-based particle swarm optimization algorithm," *The Applied Computational Electromagnetics Society Journal*, vol. 33, no. 11, pp. 1259-1267, 2018.
[30] K. Guney, S. Sagiroglu, and M. Erler, "Generalized neural method to determine resonant frequencies of various microstrip antennas," *International Journal of RF and Microwave Computer-Aided Engineering*, vol. 12, no. 1, pp. 131-139, 2002.

Tianliang Zhang was born in Maanshan, China, 1994. In 2018, he received his bachelor's degree in Electrical and Electronics Engineering from West Anhui University, China. Now, he is a master candidate in Jiangsu University of Science and Technology. His current research interests include the design of microstrip antenna and optimization, machine learning and optimization algorithm.

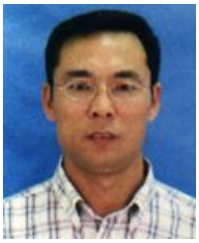

Yubo Tian was born in Changtu, China, in 1971. He received the Ph.D. degree at Nanjing University in 2004. He is a Full Professor with the School of Electronics and Information, Jiangsu University of Science and Technology now. His research interest is applications of computational intelligence to the electromagnetics field.

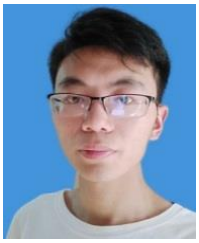

Xuezhi Chen was born in Nantong, China, in 1995. He received the Tech. bachelor degree in Nanjing Institute of Technology. Now, he is studying for master's degree in Jiangsu University of Science and Technology. His research interest is rapid optimization design of microwave devices.

Jing Gao was born in Huaian, Jiangsu Province, China, in 1995. She is a master student at Jiangsu University of Science and Technology now. Her research interests include signal processing theory and technology.

Circularly Polarized Jute Textile Antenna for Wi-MAX, WLAN and ISM Band Sensing Applications

Ram Sandeep D. [1], Prabakaran N. [1], Madhav Boddapati T. P. [1], and Narayana K. L. [2]

[1] Department of ECE, KLEF, Guntur, 522502, India
askram91@gmail.com, prabakaran@kluniversity.in, btpmadhav@kluniversity.in

[2] Department of Mechanical Engineering, Guntur,522502, India
drkln@kluniversity.in

Abstract ─ This study exhibits a circularly polarized (CP) conformal antenna actualized by using a jute textile as a substrate. Its sensing 3.5, 4.9, and 5.8 GHz in the Wi-MAX, WLAN, and ISM radio bands. The topology of the proposed antenna has relied on a curvature structure as the prime radiating element, and ground structure whirled in contradictive arrangement to the patch. Conductivity was materialized by applying copper paint through the traditional painting approach, i.e., brush painting. This fabrication method allows attaining the conformability with minimized size, lightweight, and low sensitivity to the environment without weakening the radiating performance. These attributes allowed the jute textile antenna appropriately for the incorporation in wearable devices for body-driven applications. The electromagnetic properties of the projected jute textile antenna accomplished in simulations were confirmed through the measurement of the antenna in an anechoic chamber. The CP jute textile antenna shows a peak gain of 4.93, 8.86, and 10.07dBi at 3.5, 4.9, and 5.8 GHz (WiMAX, WLAN, and ISM).

Index Terms ─ Circular polarization, copper paint, ISM band, WiMAX, WLAN.

I. INTRODUCTION

Over the most recent couple of years, the implementation of wearable antennas for body-driven communication has drawn attention from engineers and researchers because of its increasing demand in the field of military and civil applications [1]. Traditional available rigid antennas are found difficult in mounting on the human body and causes discomfort owing to its inability to bend and move in different directions. The utilization of fabric materials as the substrate for micro-wave elements and structures seems to remain a desirable feature that ensures immense lead in the actualization of the wearable antennas for wireless communications. This developing attention has promoted the realization of numerous antenna topologies, together with printed dipoles [2], and patch antennas [3] with the underlying principle of decreasing its size and increasing its efficiency. Also, textile antennas (textenna) utilizing the snap-on push button were lately proposed [4].

Because of the recurrent movement of the human body, it gets hard to stabilize polarization align of the transceiver nodes for better power reception. Therefore, the circular polarization (CPn) feature aptly substitutes the need for continual aligning of the two nodes for maximum power reception. It also has many added advantages like exhibits resistance to signal degradation reported out of climatic changes, provides a highly reliable communication link, and overcome multipath effects [5-7]. In [8], the authors proposed a CP Jia-shaped antenna; the CPn is achieved by optimizing the feed position. A dual-band annually slot antenna for dual sense CPn was presented [9]. In [10], a 3-d CP helix antenna was reported on the FR-4 substrate with wide 3db beamwidth. A reconfigurable polarization antenna was proposed for WLAN applications; two-pin diodes are used to achieve polarization diversity [11]. In [12], the authors presented both frequency and polarization reconfigurable antenna duly operating in five different states by using five-pin diodes. Most of these works are developed on rigid substrates, which are found not fit for on-body communication applications.

This study exhibits a novel CP semicircular shaped antenna inspired by a very famous Tai-Chi symbol accomplished with textile materials. Many parameters are needed to consider while designing a textenna since wearable antennas work in proximity to the human body, in addition to antenna properties such as form factor, polarization, bandwidth, and weight should also be deliberately considered. It is imperative to take note that there are very few textennas structures that can fulfill these prerequisites all the while.

The objectives of the present work were to:

(i) Use textile materials as substrates which are either effectively utilized in the textile manufacturing plant, or readily available in the native market.

Submitted On: January 21, 2020
Accepted On: October 20, 2020

https://doi.org/10.47037/2020.ACES.J.351206

1054-4887 © ACES

(ii) Carry out a fabrication procedure that is basic and appropriate enough to be helpful for industry line production.
(iii) Designing it as compact and low-profile to fit on the clothing of the wearer, hence its presence outwardly unnoticeable and doesn't cause discomfort to the wearer.
(iv) Make it practical for on-body communication with CP.

II. MATERIAL AND ANTENNA DESIGN

In respect of the substrates incorporated for actualization of the textenna, in this present writeup, various textiles have been utilized. A few such fabric materials are considered to be as cotton and silk. Based on the magnetic, electrical properties of the material and the access feasibility, textile selection has been considered. While making use of the textile substrates, it should primarily be adaptable and non-mutilative; besides, it must exhibit proper mechanical features (for example, homogeneity in thickness). Also, its humidity recapture ought to remain <7%, with the end goal that the textenna attributes stay steady under diverse relative moisture circumstances.

In the present work, treated jute fibers with a thickness of 1.5 mm were chosen, due to its flexibility, low moisture retention, and lightness. Moreover, the conductive copper paint sits well on its surface, and it is shock-absorbent too. Comparative analysis of various antenna models on different substrates are presented in Table 1.

Table 1: Comparative study of the proposed textile antenna with the recent works

Reference and Substrate	**Dimensions (mm^3)**	**Frequency (GHz) & Applications**	**Gain (dBi) & Circular Polarization (Yes or No)**
[13] Textile	57×32.1×3.6	2.45 (ISM)	3.39 (no)
[14] FR4	50×50 ×1.6	2.3 (WI-MAX)	2.7 (no)
[15] FR4	100×90×3.3	2.42 (WLAN)	5 (no)
[16] Textile	140×80×5	2.45 (ISM)	6.8 (no)
This work (Jute textenna)	20×16 ×1.5	3.5 (WI-MAX), 4.9 (WLAN), 5.8(ISM)	4.93, 8.86, 10.07 (yes)

The proposed antenna geometry is shown in Fig. 1, and detailed dimensions are provided in Table 2. The design and simulations of proposed textenna are carried out by Ansys HFSS 19.0 software. Conductive copper paint is brush painted on cotton, silk, and jute with a thickness of 0.6, 0.4, and 1.5 mm, respectively.

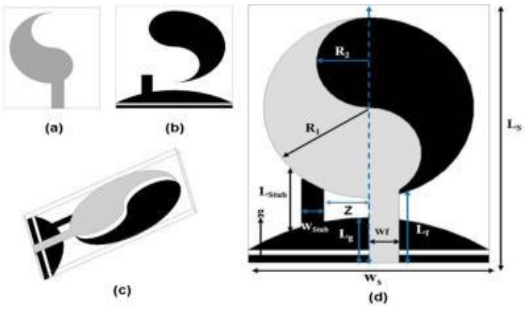

Fig. 1. Proposed antenna: (a) front plane, (b) ground plane, (c) adjacent view, and (d) geometry of CP jute textenna.

Table 2: The proposed antenna geometry in detail (mm)

L_s	W_s	W_f	L_f
20	16	2	5
h	g	L_{stub}	W_{stub}
1.5	0.5	2.5	1.5
R1	R2	L_g	Z
7	3.5	2.5	2.5

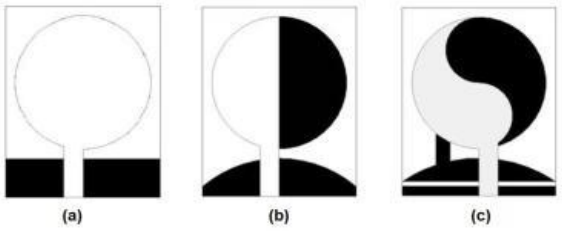

Fig. 2. Iteration wise evolution of the proposed textenna: (a) first iteration, (b) second iteration, and (c) third iteration.

The proposed antenna is developed from a circular structure, and its evolution steps are illustrated in Fig. 2. As shown in Fig. 2 (a) in first iteration, a simple circular patch with a 7mm radius (R_1) was taken in the radiating side, and a similar circular like entity on a rectangle was placed in the ground plane. Figure 4 illustrates the resonating frequencies concerning iteration steps, for the first iteration, it is resonated at dual-band with a span of 3.65 to 5.4 GHz and 6.4 to 9.4 GHz. The radius of the circle (R_1) plays a crucial role in determining the resonating frequency. The radius value R_1 is parametrized from 6-8 mm along with the ground structure that contains a similar circle. Figure 3 illustrates the frequency response concerning the change of radius from 6-8 mm. The radius of the circular patch structure [17] is given by equation (1):

$$a = \frac{F}{\left\{1+\frac{2h}{\pi \epsilon_r F}\left[\ln\left(\frac{\pi F}{2h}\right)+1.7726\right]\right\}^{\frac{1}{2}}}, \quad (1)$$

$$F = \frac{8.791\times10^{9}}{f_r\sqrt{\epsilon_r}}. \quad (2)$$

By considering the fringing effects. The effective radius of the patch is given by:

$$a_e = a\left\{1+\frac{2h}{\pi \epsilon_r a}\left[\ln\left(\frac{\pi a}{2h}\right)+1.7726\right]\right\}^{\frac{1}{2}}. \quad (3)$$

Where h is the height of the substrate, ε_r is the dielectric constant, f_r is the resonant frequency.

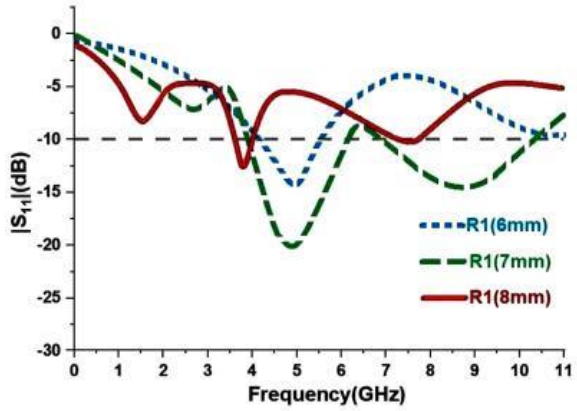

Fig. 3. Frequency response to the parametric analysis of radius R_1 (6-8 mm).

For a radius of 6 mm, the antenna resonated at 4.9 GHz with a return loss of -14 dB. For a radius of 8 mm, it resonated at 3.5 with a return loss of -13 dB. From the above parametric analysis, the circular patch with a 7 mm radius resonated better with dual-band than 6 and 8mm. So, a radius of 7 mm was considered in the patch and ground structures. The first iteration model did not operate with a CPn in any of the operating bands.

In the second iteration, as shown in Fig. 2 (b), the circular patch and ground structures are divided into two equal halves that are arranged in an inverse direction in patch and ground, respectively. The ground plane rectangular structure is changed as a semi-elliptical structure. The wide bands in the first iteration are now converted as a narrow band and resonating at 3.15, 4.95, and 6.40 GHz consecutively. As illustrated in Fig. 5, the values of the axial ratios (ARs) of this model are not under the 3db range, so it does not operate with a CPn. In the third iteration, as shown in Fig. 2 (c), the antenna patch comprises a half with radius R_1 (7 mm) in which two crescents with radius R_2 (R_2=R_1/2) are evacuated and integrated on top and bottom of the half-circle (R_1), separately. A stereotype of alterations are adapted in the ground plane, contrarily.

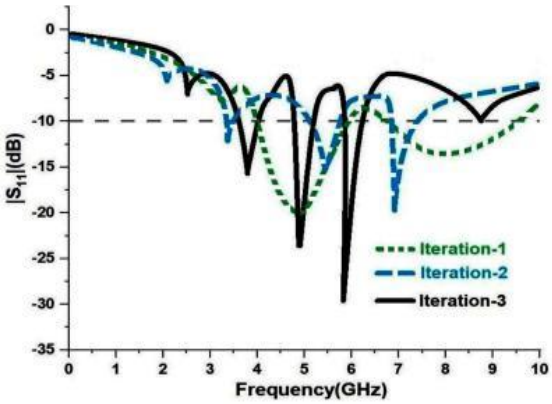

Fig. 4. Iteration wise results of the reflection coefficient.

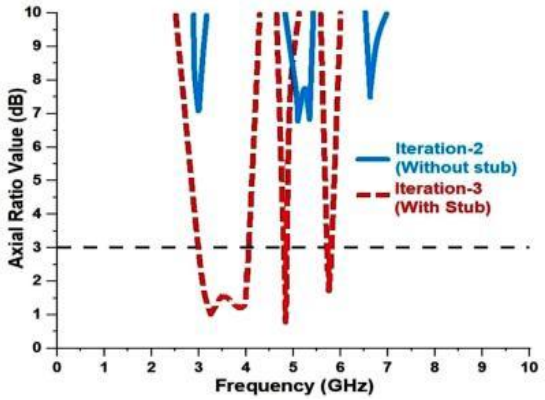

Fig. 5. Iteration wise results of the axial ratios (ARs).

The antenna ground was built on a rectangular structure over which a semi-elliptical structure with a stub was placed. The essential parameters for attaining CPn and impedance matching at the resonating frequencies are the L_{stub} (stub length) and the Z (the distance from the symmetric axis to the stub). The effect of the stub on CPn is illustrated in Fig. 5. For achieving a decent impedance matching between the patch of the antenna and 50 Ω port, the asymmetric microstrip line is used, where L_f is the length, and W_f is the width of the feed line. As illustrated in Fig. 4, this final model resonated at 3.5, 4.9, and 5.8 GHz successively with a CPn feature.

In this study, to realize the conductive parts of the antenna, the copper paint was utilized, which can be brush-painted. Using this unique approach, the proposed antenna design was brush painted on cotton, silk, and jute substrate. Figure 6 shows the 10x optical zoom images of cotton, silk, and jute textiles, taken by a digital single-lens reflector camera to show the surface structural differences and fiber intervention. Photographs of the

cotton, silk, and jute textile antenna prototypes are shown in Fig. 7.

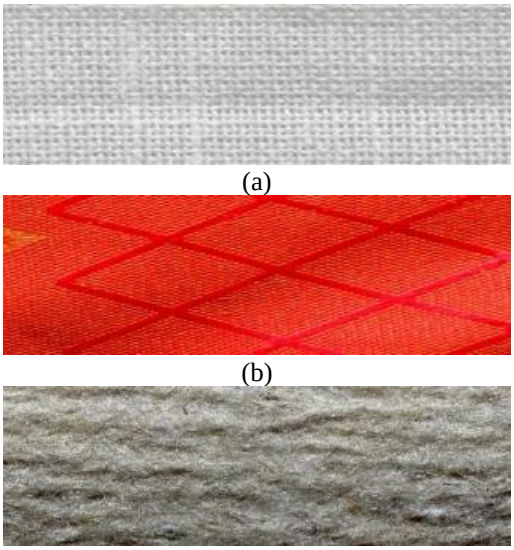

Fig. 6. Photographs of textiles in 10x optical zoom: (a) cotton, (b) silk, and (c) jute.

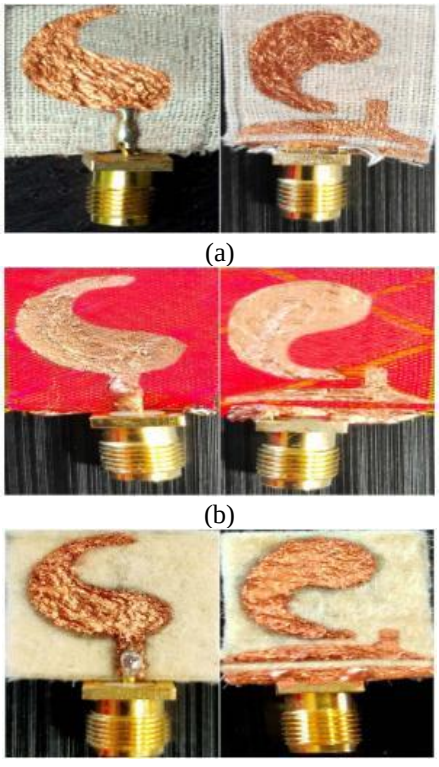

Fig. 7. Photos of :(a) cotton fabricated model front plane, and ground plane, (b) silk fabricated model front plane and ground plane, and (c) CP jute textile fabricated model front plane, and the ground plane.

III. RESULT ANALYSIS

Performance of the antennas were studied in free space, and all the simulated models are experimentally verified to evaluate the performance. Figure 8 (a) shows the simulated and measured reflection coefficient of the CP jute fabricated model, which resonates at 3.5, 4.9, and 5.8 GHz. The specifications of WiMAX, WLAN, and ISM are satisfied (return loss >10dB). The same design was fabricated on cotton and silk textiles to examine the responses concerning the change of textiles. They resonated at 4.6 GHz (Fig. 8 (b)) and 5.15, 9.35 GHz (Fig. 8 (c)).

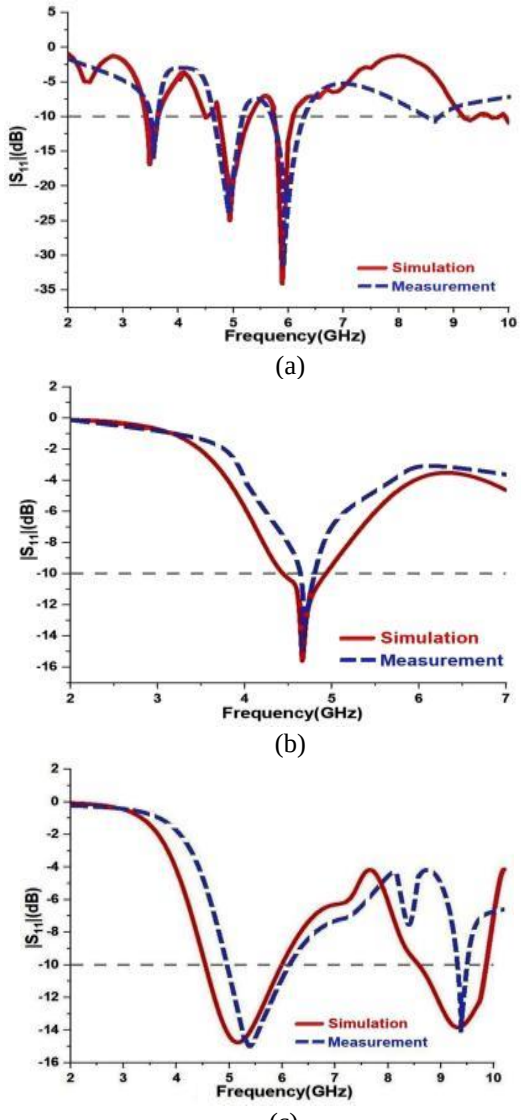

Fig. 8. Simulated and measured reflection coefficient of: (a) CP jute antenna, (b) cotton textile fabricated model, and (c) silk textile fabricated model.

The ARs of the jute textenna in the boresight

direction were gauged. As shown in Fig. 9. A decent agreement between measured and simulated results are observed. The resonating frequency band where the AR is <3 dB ranges from 3.090-3.994, 4.85-4.95, and 5.70-5.85 respectively; hence, the jute textenna is CP, and it covers the WiMAX, WLAN, and ISM bands.

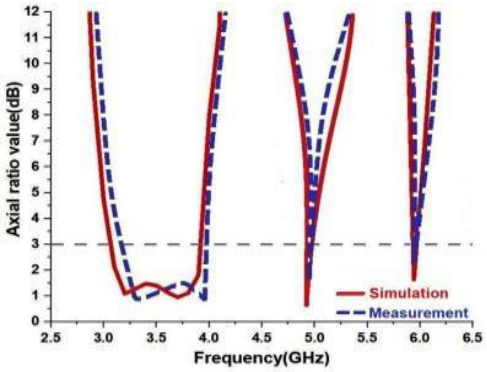

Fig. 9. Measured and simulated ARs of the CP jute textenna.

To demonstrate guaranteeing the CPn characteristic of the antenna. Figure 10 illustrates the +z surface current flow of the jute texteena at three operating frequencies, 3.5, 4.9, and 5.8 GHz. Likewise, in Fig. 10, relating to the changes of phase of the antenna, surface currents rotates in a round way in dextrorotatory direction. The explanation behind revolution can be named for two significant causes: (1) By utilizing asymmetric feed, it allows for flowing the currents in aside. Consequently, currents will move to the opposite side through the crescent path of the patch, and hence a CPn state occurs. (2) thus, that electrical charges consistently aggregate at keen points. In this way, the electrical charges on patch move to sharp end from the wide side end, for the most part, in keen end attached toward parasitic structure, and continually this procedure happens on the rear side of the substrate.

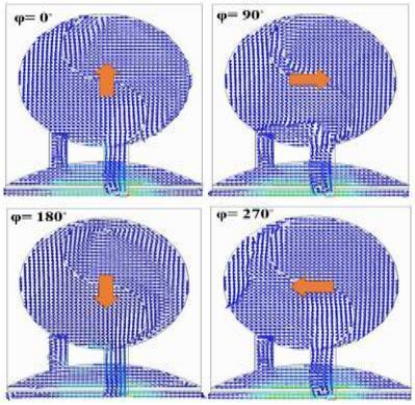

(a)

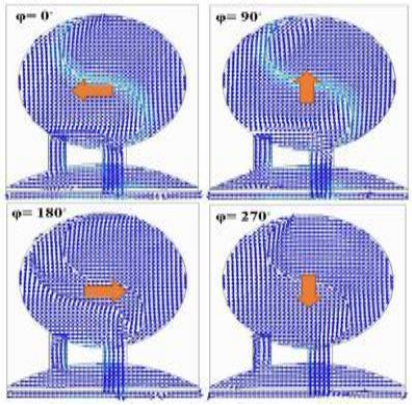

(b)

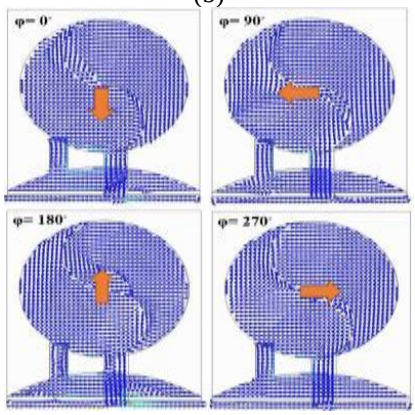

(c)

Fig. 10. Surface currents distribution of the jute textenna at +z for: (a) 3.5, (b) 4.9, and (c) 5.8 GHz.

The gain and efficiency characteristics of the proposed textenna are illustrated in Fig. 11, the gain values are 4.93, 8.86, 10.07 dBi at 3.5, 4.9, and 5.8 GHz (WiMAX, WLAN, ISM). Correspondingly the efficiency of the antenna in the resonating frequencies ranges from 83 to 89%.

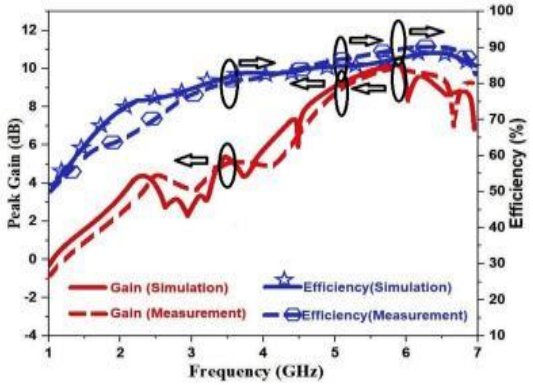

Fig. 11. Simulation and measured gain and efficiency of the proposed textenna.

IV. MEASUREMENT AND ANALYSIS

In addition to, the radiation characteristic of the CP jute textenna was validated in an anechoic chamber. The radiation patterns of LHCP and RHCP on the two principal planes (E-plane and H-plane) for 3.5, 4.9, and 5.8 GHz are as seen in Fig. 12.

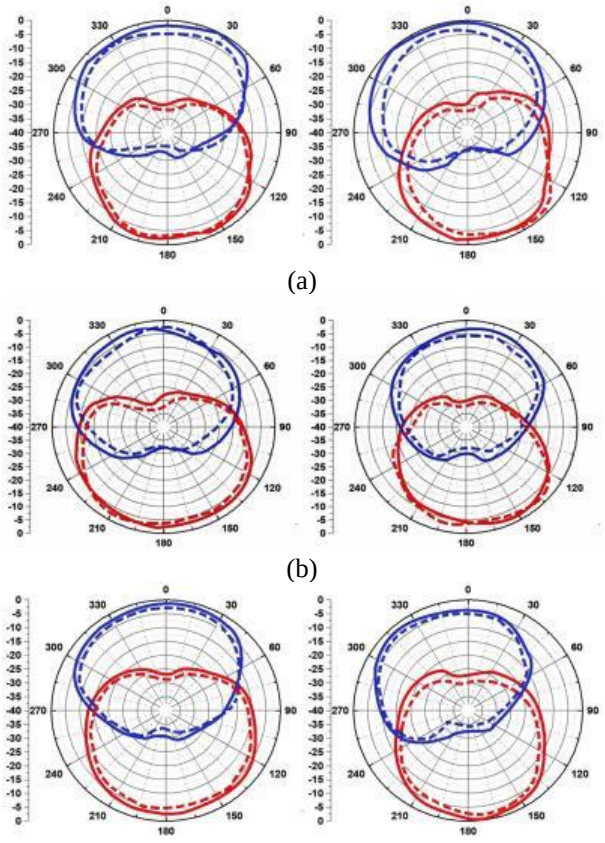

Fig. 12. Measured and simulated radiation patterns at: (a) 3.5, (b) 4.9, and (c) 5.8 GHz. (Continuous blue line: RHCP simulated, dashed blue line: RHCP measured, continuous red line: LHCP simulated, dashed red line: LHCP measured).

Figure 13 shows the spectrum analyzer sensing results for different operating bands and the evidence of measurement.

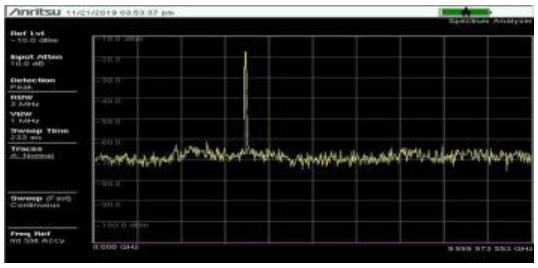

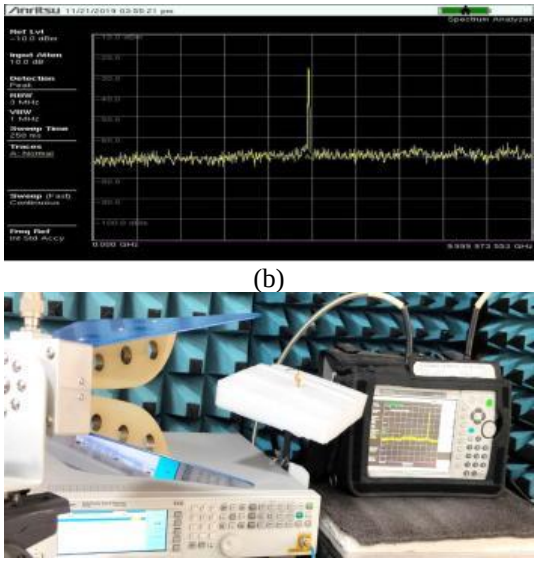

Fig. 13. Signal sensing and measurement setup: (a) 3.5, (b) 4.9 GHz, and (c) 5.8 GHz.

V. CONCLUSION

A circularly polarized jute textile substrate with a semicircular shaped antenna was proposed and actualized. The perfect demonstration of the antenna as far as radiation patterns, input matching, and axial ratios shows the high proficiency that can be acquired by espousing the jute material as the substrate. The textile antenna is distinguished by ease of fabrication, mechanical firmness, wide beamwidth, and a simple, semicircular based design. It creates the anticipated circular polarization for a strong radio frequency sensing link. Thus, the circularly polarized antenna paves the way for utilizing the components for exclusive exercises such as tracking and localization of rescue operations.

ACKNOWLEDGMENT

Authors want to thank the Department of Science and Technology, India, for supporting this work through the FIST Grant of SR/FST/ET-II/2019/450, and SEED/TIDE/2018/33/G.

REFERENCES

[1] A. G. Al-Sehemi, A. A. Al-Ghamdi, N. T. Dishovsky, N. T. Atanasov, and G. L. Atanasova, "Wearable antennas for body-centric communications: Design and characterization aspects," *Applied Computational Electromagnetics Society Journal*, vol. 34, no. 8, pp. 1172-1181, 2019.

[2] Y. Jiang, L. Xu, K. Pan, T. Leng, Y. Li, L. Danoon, and Z. Hu, "e-Textile embroidered wearable near-field communication RFID antennas," *IET Microwaves, Antennas & Propagation*, vol. 13, no. 1, pp. 99-104, 2018.

[3] W. Huang and A. A. Kishk, "Compact antenna designs for wearable and portable medical system," *Applied Computational Electromagnetics Society Journal*, vol. 26, no. 4, pp. 295-302, 2011.
[4] X. Hu, S. Yan, and G. A. Vandenbosch, "Compact circularly polarized wearable button antenna with broadside pattern for U-NII worldwide band applications," *IEEE Transactions on Antennas and Propagation*, vol. 67, no. 2, pp. 1341-1345, 2018.
[5] Y. F. Lin, Y. C. Kao, S. C. Pan, and H. M. Chen, "Bidirectional radiated circularly polarized annular-ring slot antenna for portable RFID reader," *Applied Computational Electromagnetics Society Journal*, vol. 25, no. 3, pp. 182-189, 2010.
[6] M. L. Sabran, S. K. A. Rahim, P. J. Soh, C. Y. Leow, and G. Vandenbosch, "A simple electromagnetically fed circularly-polarized circular microstrip antenna," *Applied Computational Electromagnetics Society Journal*, vol. 30, no. 11, pp. 1180-1187, 2015.
[7] M. Tecpoyotl-Torres and J. G. Vera-Dimas, "Simulation, fabrication, and performance comparison of a GPS antenna with radome on the roof of an automobile," *Applied Computational Electromagnetics Society Journal*, vol. 28, no. 7, pp. 581-590, 2013.
[8] K. L. Chung, X. Yan, Y. Li, and Y. Li, "A Jia-shaped artistic patch antenna for dual-band circular polarization," *AEU- International Journal of Electronics and Communications*, vol. 120, 2020. doi.org/10.1016/j.aeue.2020.153207.
[9] J. Li, J. Shi, L. Li, T. A. Khan, J. Chen, Y. Li, and A. Zhang, "Dual-band annular slot antenna loaded by reactive components for dual-sense circular polarization with flexible frequency ratio," *IEEE Access*, vol 6, pp. 64063-64070, 2018.
[10] Y. Li and R. Mittra, "A three-dimensional circularly polarized antenna with a low profile and a wide 3-dB beamwidth," *Journal of Electromagnetic Waves and Applications*, vol. 30, no. 1, pp. 89-97, 2016.
[11] V. Zarei, H. Boudaghi, M. Nouri, and S. A. Aghdam, "Reconfigurable circular polarization antenna with utilizing active devices for communication systems," *Applied Computational Electromagnetics Society Journal*, vol. 30, no. 9, pp. 990-995, 2015.
[12] A. Sedghara and Z. Atlasbaf, "A new dual-band, dual-polarized, and single feed reconfigurable antenna," *Applied Computational Electromagnetic Society Journal*, vol. 31, no. 1, pp. 26-31, 2016.
[13] A. Alemaryeen and S. Noghanian, "AMC integrated textile monopole antenna for wearable applications," *Applied Computational Electromagnetic Society Journal*, vol. 31, no. 6, pp. 612-618, 2016.
[14] P. M. Paul, K. Kandasamy, and M. S. Sharawia, "Tri-band circularly polarized strip and SRR loaded slot antenna," *IEEE Transactions on Antennas and Propagation*, vol. 66, no. 10, pp. 5569-5573, 2018.
[15] Y. Hong, J. Tak, and J. Choi, "An all textile SIW cavity-backed circular ring slot antenna for WBAN applications," *IEEE Antennas and Wireless Propagation Letters*, vol. 15, pp. 1995-1999, 2016.
[16] S. Yan, V. Volskiy, and G. A. Vandenbosch, "Compact dual-band textile PIFA for 433-MHz/ 2.4-GHz ISM bands," *IEEE Antennas and Wireless Propagation Letters*, vol. 16, pp. 2436-2439, 2017.
[17] C. A. Balanis, *Antenna Theory: Analysis and Design*. John Wiley & Sons, New York, 2016.

Ram Sandeep Duvvada received his Bachelor and Master of Technology degrees from JNTUK in 2014 and 2017, respectively. Currently, he is pursuing Ph.D. in KLEF, Guntur, India. His research interests include flexible textile antennas and medical antennas.

N. Prabakaran received his Ph.D. degree from Satyabama University, India. Currently, he is working as an Associate Professor in the Department of ECE, KLEF. His research interests are wireless communications and wireless networks.

B. T. P. Madhav is working as Professor in ECE and Associate Dean at KLEF. He has published more than 292 papers in Scopus and SCI journals. He is a reviewer for several international journals including IEEE, Elsevier, Springer, Wiley, and Taylor and Francis.

K. L. Narayana is working as Professor & Dean (R&D) in the Department of ME at KLEF. He has around 40 + publications, out of which 29 are SCOPUS & WoS Journals. He is a life member of IME, CMSI, and ISTE. His research interests include materials, design and additive manufacturing of metals.

Wideband Octagonal Dual Circularly Polarized Sub-array Antenna for Ku-Satellite Systems

Khalid. M. Ibrahim [1], Walaa. M. Hassan [1], Esmat A. Abdallah [2], and Ahmed M. Attiya [1]

[1] Microwave Engineering Department
Electronics Research Institute, Cairo, Egypt
khaledmus@gmail.com, walaa81hassan@yahoo.com, attiya@eri.sci.eg

[2] Microstrip Department
Electronics Research Institute, Cairo, Egypt
esmataa2@hotmail.com

Abstract ─ In this paper the analysis and design of a dual circularly polarized 4×4 antenna array operating in Ku-band are discussed with emphasis on its sequential feeding network. The dual circular polarization is achieved by feeding a stacked octagonal patches with a wideband branch line coupler. The proposed 4×4 antenna array is based on two separate sequential feeding networks for LH and RH circular polarizations. The advantage of the proposed feeding network is that it is implemented on a single layer. Simulation results by using both HFSS and CST are presented for comparison. In addition, experimental verifications are presented**.**

Index Terms ─ Antenna array, circular polarization, feeding network, satellite antenna, wideband antenna.

I. INTRODUCTION

On-move satellite communication systems at Ku band have a significant importance in different applications where it may not be available other communication systems with similar bandwidth and service stability [1]. These on-move satellite communication systems are quite suitable for vehicles in rural areas, airplanes and ships in rivers and seas. These applications require low profile, low weight, dual polarization and wideband antenna systems. In addition, these antennas should satisfy the ITU requirements to avoid interference with other satellites [2]. The proposed operating frequency range is from 10.5 GHz to 14.5 GHz with dual circular polarizations. Printed antenna arrays with properly tapered feeding network inside radoms are good candidates for these applications. Other configurations based on waveguide antenna array are also found in literature [3]-[5]. However, these configurations have larger weight and less conformity compared to printed antennas like microstrip antennas. Different configurations of printed antenna elements for this frequency band are presented in literature [6]-[8]. However, the main problem lies in developing appropriate feeding network to introduce an antenna array of these radiating elements which sustain wideband and dual polarization properties in addition to the required properties of the radiation pattern. To simplify the feeding network, the antenna array is divided into smaller sub-arrays composed of 4×4 radiating elements. Each sub-array is fed by a uniform distribution network while a master separated non-uniform distribution network is used to feed these sub-arrays [9]. On the other hand, for the case of a circularly polarized antenna array, the axial ratio would be enhanced by using a combination of circularly polarized elements with a sequential feeding network. Implementing this sequential feeding network for a single circular polarization is discussed by using different configurations in [4], [10]-[11]. However, these configurations of sequential feeding networks cannot be used for dual circular polarizations at the same layer. This increases the number of layers in the feeding network for the case of dual circular polarization which increases the cost, weight and manufacturing complexity. Another configuration based on substrate integrated waveguide for dual circular polarization is introduced in [12]. However, this configuration has a limited bandwidth in the range from 11.8 to 13 GHz only. Thus, for the proposed application, it is required to develop a dual sequential feeding network on the same layer for a 4×4 sub-array. A similar antenna configuration is presented in [13] based on multi-layered FSS integrated with AMC structure fed by a double sided dipole array. However, this structure is operating in the Ku-band in the frequency range from 14 to 15.5 GHz only and in the X-band from 7.5 to 8.5 GHz.

The target of the present paper is to design a single layer sequential feeding network for a Ku-band dual

Submitted On: July 27, 2020
Accepted On: November 29, 2020
https://doi.org/10.47037/2020.ACES.J.351207

1054-4887 © ACES

circularly polarized 4×4 antenna sub-array operating in the frequency range from 10.5 to 14.5 GHz. This sub-array is designed to be integrated in a complete antenna array for on-move satellite communication system. The size of this sub-array is limited to be less than 75×75 mm^2. This limited size increases the complexity of designing dual sequential feeding network on a single layer due to the coupling between the different parts of the feeding network. In addition, the required wide bandwidth, which is nearly 27.5%, represents another important challenge in the design of this feeding network.

The paper is organized as follows: Section II presents analysis and design of a dual circular polarized octagonal radiating element. Section III presents analysis and design of 4×4 sequential fed dual circular polarized antennas. The simulation process are developed by using HFSS ver.14 [14] and verified by using CST ver.2012 [15]. The experimental results are presented in Section IV. Finally, the conclusion is presented in Section V.

II. ANALYSIS AND DESIGN OF DUAL CIRCULAR POLARIZED OCTAGONAL RADIATING ELEMENT

To obtain a wideband operation, stacked microstrip patch antenna configuration is proposed to be the radiating element of this antenna array as shown in Fig. 1 (a). The bandwidth of this stacked configuration can be enhanced by introducing an electrically thick layer of a low dielectric material between the fed element and the parasitic element. Foam is a quite suitable material for this purpose where its dielectric constant is around 1.07. The key parameters in the design of this wideband radiating element are the substrate parameters of the fed element, the dimensions of the fed element, the dimensions of the parasitic element, the separation between the fed element and the parasitic element, and the parameters of the superstrate which holds the parasitic element. The proposed geometry of the fed and parasitic elements in the present antenna are octagonal shape as shown in Figs. 1 (b).

The substrate of the fed element is a grounded Rogers 5880 with a dielectric constant $\varepsilon_r = 2.2$, $\tan\delta = 0.0009$ and dielectric thickness $L_2 = 0.787$mm. The parasitic element is printed on RO3003 substrate of a thickness $L_1 = 0.25$ mm. The dielectric constant of this substrate is 3 and its loss tangent is 0.001. The two substrates are separated by a foam layer of thickness $L_F = 2$ mm.

The analysis of this antenna configuration starts with approximate circular patches to obtain approximate dimensions of the fed patch and the parasitic patch. Then these approximate dimensions are tuned by using numerical electromagnetic simulation tools like HFSS and CST to obtain the required operating bandwidth.

The resonant frequency of TM_{110} mode for a circular patch antenna on the lower substrate can be obtained by using cavity model as following [17]:

$$f_0 = \frac{1.841c}{2\pi a_e\sqrt{\varepsilon_r}}, \tag{1}$$

where a_e is the effective radius taking into account the fringing effect. This effective radius is given by:

$$a_e = a\sqrt{1+\frac{2h}{\pi a\varepsilon_r}\left[\ln\left(\frac{\pi a}{2h}\right)+1.7726\right]}. \tag{2}$$

For design purpose, the radius of a circular microstrip antenna which would be resonant at frequency f_0 can be obtained as follows:

$$a = \frac{F}{\sqrt{1+\frac{2h}{\pi\varepsilon_r F}\left[\ln\left(\frac{\pi F}{2h}\right)+1.7726\right]}} \text{ cm}, \tag{3}$$

where

$$F = \frac{8.791\times10^9}{f_0\sqrt{\varepsilon_r}}. \tag{4}$$

On the other hand, the resonance of the upper patch is obtained by using an equivalent relative permittivity given by:

$$\varepsilon_{ef} = \frac{4\varepsilon_{re}\varepsilon_{r,dyn}}{\left(\sqrt{\varepsilon_{re}}+\sqrt{\varepsilon_{r,dyn}}\right)^2}, \tag{5}$$

where

$$\varepsilon_{re} = \frac{\varepsilon_r\left(1+L_f/L_2\right)}{\left(1+\varepsilon_r L_f/L_2\right)}, \tag{6}$$

and

$$\varepsilon_{r,dyn} = \frac{C_{dyn}(\varepsilon=\varepsilon_0\varepsilon_{re})}{C_{dyn}(\varepsilon=\varepsilon_0)}, \tag{7}$$

where C_{dyn} is the dynamic capacitance. The details of calcualting $\varepsilon_{r,dyn}$ can be found in [18].

Based on th above analysis, the intial designs of the lower and the upper patches are obtained as circular patches with radii $R_1 = 4.1\,mm$ and $R_2 = 4.4\,mm$ respectively. These radii are corresponding to resonant frequencies 13 GHz and 12 GHz respectively to enable operation from 10.5 GHz to 14.5 GHz. These initial dimensions are then cut in octagonal shapes as shown in Fig. 1 (b) to tune the matching of this antenna structure to the required operating band. This adjustment is done numerically by using numerical simulation tools.

On the other hand, a dual circular polarized antenna can be obtained by developing a dual feeding network which introduces two simultaneous feeding points of equal amplitudes and phase shifts of $\pm90^o$. Quadrature branch-line coupler (BLC) is a quite appropriate candidate for this application. However, conventional BLC has a narrow bandwidth. A multi-section BLC configuration with loading stub elements as shown Fig. 1 (c), has different degrees of freedom to be optimized it for wideband operation [16]. The feeding BLC is printed on a substrate RO3003 with thickness $L_3 = 0.25$ mm. Table 1 shows the optimized dimensions of the designed BLC and the stacked antenna.

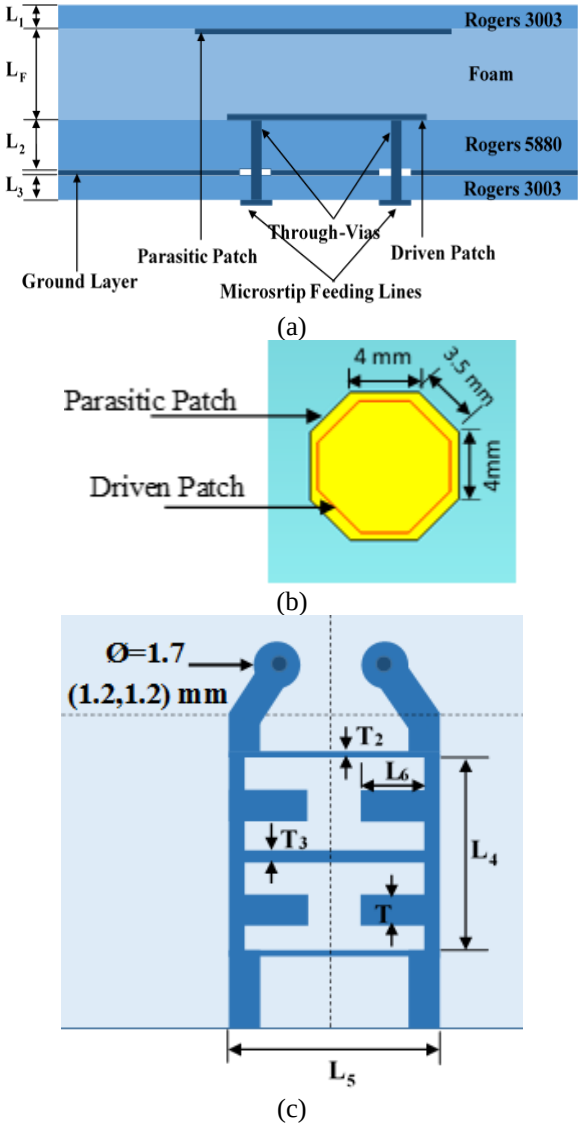

Fig. 1. Geometry of the wideband dual circular polarized antenna element: (a) the side view of the complete antenna element, (b) proposed octagonal patches, and (c) microstrip feeding branch line coupler.

Table 1: Dimensions of the branch line coupler

Parameters	Values (mm)
L4	4.95
L5	5.28
L6	1.2
T	0.9
T2	0.3
T3	0.6

Figure 2 shows the reflection coefficient of the designed octagonal radiating element. The optimized dimensions of the parasitic octagonal patches have vertical and horizontal edges of 4 mm and tilted edges of 3.5 mm. While, the fed octagonal patch have vertical and horizontal edges of 3 mm and tilted edges of 2.5 mm. Due to the symmetry of the designed antenna structure, the reflection coefficients of the two ports are identical. The obtained reflection coefficient of the single element is below -20 dB over all the required bandwidth. Figure 3 shows the axial ratio of the radiated fields in the broadside direction. The obtained axial ratio is below 2dB in the entire operating band.

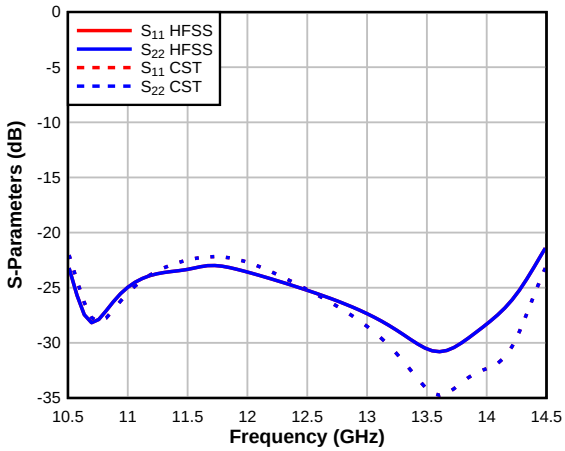

Fig. 2. Reflection coefficient of the single element.

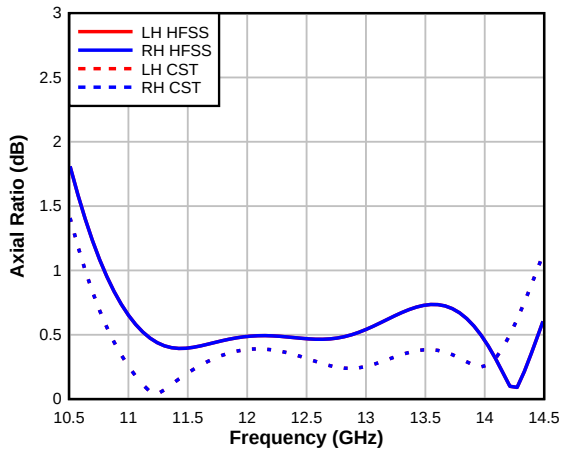

Fig. 3. Axial ratio of the single element.

III. ANALYSIS AND DESIGN OF 4×4 SEQUENTIAL FED DUAL CIRCULAR POLARIZED ANTENNA

The 4 × 4 sub-array is divided into four identical 2×2 sub-cells as shown in Fig. 4. The basic idea of a dual sequential feeding network is to rotate the radiating elements by steps of 90° in addition to changing the phase between the radiating elements by ±90° in a sequential form to obtain LH or RH circular polarization. This sequential feeding mechanism improves the

circular polarization characteristics of antenna array. The key point in the design of such sequential feeding network is to maintain the required phase shifts along the required operating bandwidth. The proposed sequential feeding network is composed of Wilkinson power dividers and appropriate delay lines to introduce the required phase shift. The spacing between the radiating elements is assumed to be 18 mm (0.75 λ_0 at the center frequency) as shown in Fig. 4.

This spacing would introduce a 4×4 array of size 72×72 mm^2 which satisfy the required dimensions of the sub-array for a complete antenna array for Ku-band satellite communication. However, the spacing between the elements is not sufficient to use straight lines for the required phase shifts. Thus, different bends are used to introduce the required lengths of delay lines. In addition, for practical implementation, it is required to add pads for the connectors which would be used to feed this sub-array as shown in Fig. 4. To obtain accurate simulation results, these pads should be included in the simulation.

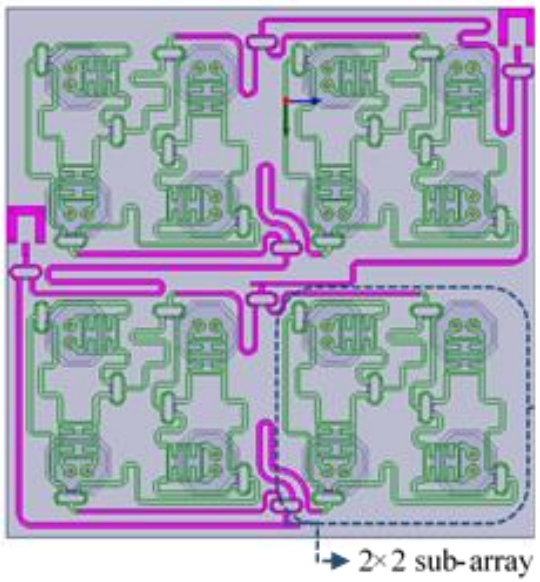

Fig. 4. Sequential feeding network for dual circularly polarized 4×4 radiating elements.

IV. EXPERIMENTAL RESULTS

In this section the experimental results of the designed 4×4 sequential fed antenna array are presented. Figure 5 shows the fabricated antenna structure. Figure 6 shows the used measurement setup inside an anechoic chamber Inc. Model (NSI) 7005-30. Figure 7 shows the measured reflection coefficients for the two excitation ports of both LH and RH circular polarizations together with the simulated results. It can be noted that the measured reflection coefficients satisfy the required specifications to be less than -10dB over the entire operating frequency band. Figure 8 shows the radiation patterns for both RH and LH excitations at 12.7 GHz. The obtained peak gain is around 17 dBi. It can be noted that the cross-polarized component is less than -20dB compared to the co-polarized in the broadside directions for both RH and LH cases. Figure 9 shows the measured and simulated axial ratios for the two circular polarizations as a function of frequency. It can be noted that the measured results satisfy the condition of axial ratio to be less than 3dB for both LH and RH circular polarizations on almost entire operating frequency band. According to the measured results, it can be concluded that the designed dual sequential feeding network introduces the required specifications of matching and radiation properties in the required operating frequency band.

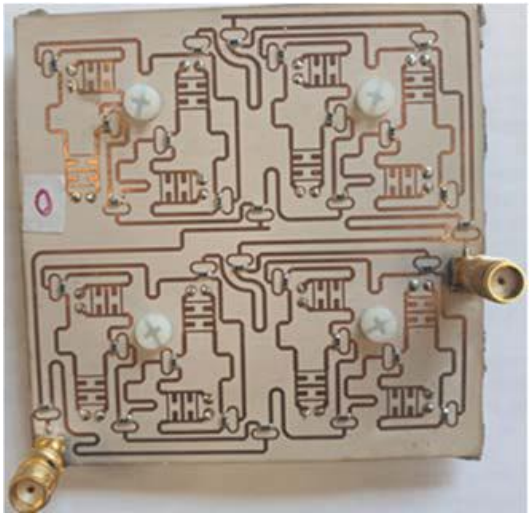

(a)

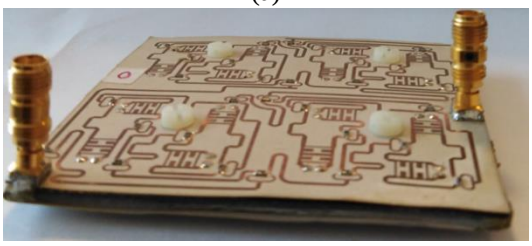

(b)

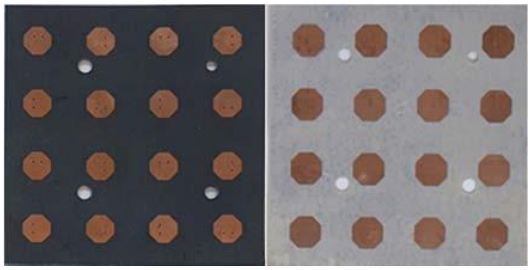

(c)

Fig. 5 Fabricated 4×4 sequential fed antenna: (a) bottom side, (b) side view, and (c) driven and parasitic octagonal patches.

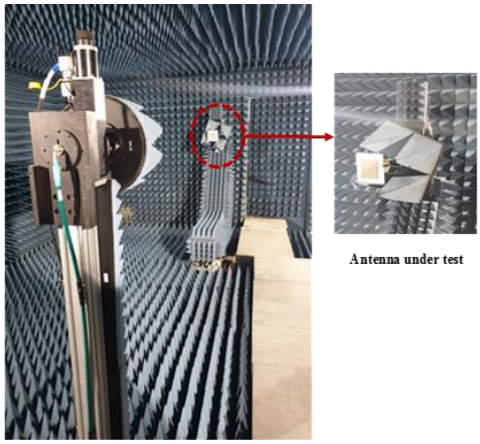

Fig. 6. Measurement setup of the fabricated antenna.

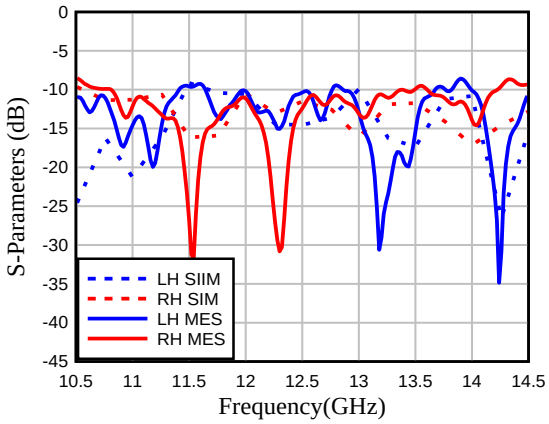

Fig. 7. Measured and simulated reflection coefficient of the 4×4 sequential fed antenna for LH and RH circular polarizations.

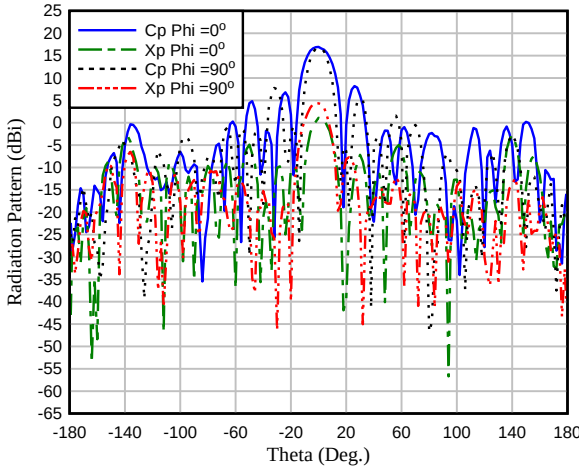

(a)

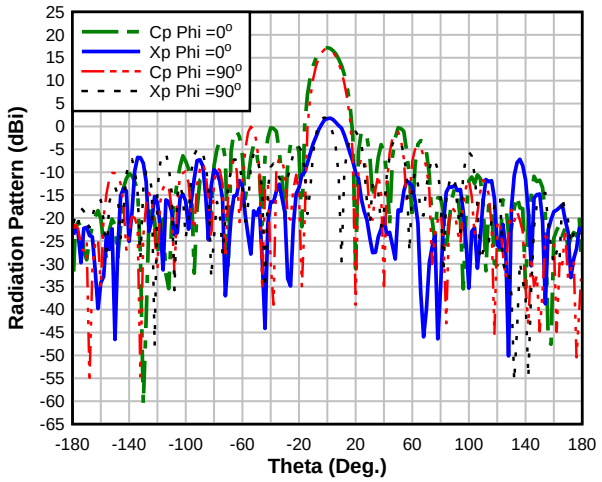

(b)

Fig. 8. Measured radiation patterns for: (a) RH and (b) LH circular polarizations at 12.7 GHz.

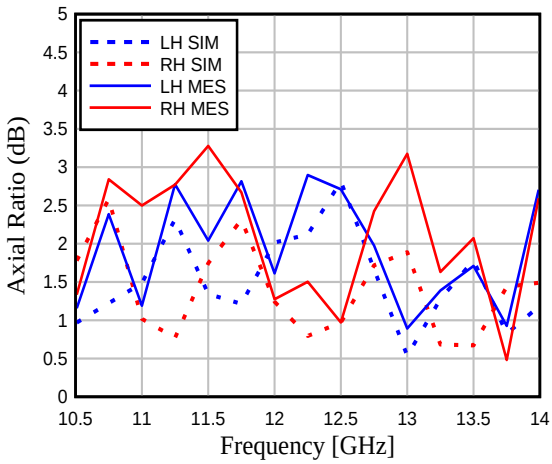

Fig. 9. Measured and simulated axial ratio of the 4×4 sequential fed antenna for LH and RH circular polarizations.

Table 2 shows a comparison between the proposed antenna and previously published configurations for circularly polarized antenna arrays. Based on this comparison, it can be noted that the main advantage of the proposed antenna is the wider bandwidth compared to other configurations. In addition, the antennas in [9-12] are single circularly polarized antennas while the proposed antenna is dual circularly polarized. On the other hand, the antenna in [13] has a quite narrow operating bandwidth compared to the proposed antenna.

Table 2: Comparison between the proposed antenna and previously published antennas

Ref.	No. of Layers	Feeding Technique	Operating Bandwidth (GHz)
[9]	Single layer	Circularly Polarized Microstrip antenna with simplified feed network	9.8 – 11.23
[10]	Single layer	Circularly Polarized 2×2 patch array using a sequential-phase feeding network	5.20 – 6.23
[11]	Single layer	Circularly Polarized Uniform Transmission Lines Using Sequential-Phase Feed	2.08 – 2.95
[12]	Single layer	Circularly Polarized Slotted Substrate Integrated Waveguide Antenna Arrays	11.95 – 12.95
[13]	Multi-layer	Dual Circularly Polarized double-sided dipole array	Dual Band 8.15 – 8.35 and 14.2 – 14.8
This work	Multi-layer	Dual Circularly Polarized 4×4 stacked circular patches antenna array using Sequential feed	Wide band 10.95 – 14.5

V. CONCLUSION

Design and analysis of a dual sequential feeding network for a dual circularly polarized 4×4 antenna array in Ku-band are presented. The radiating element is composed of a wideband stacked octagonal patches fed by a wideband branch line coupler to introduce the required dual circular polarizations. The radiating elements are arranged in sequential forms of 2×2 elements and connected together by two main feeding networks; one for LH circular polarization and the other for RH circular polarization. The effects of coupling between the different parts of the complete feeding network is compensated by adding appropriate stubs to improve the matching and the axial ratios along the design operating frequency band from 10.5 to 14.5 GHz.

REFERENCES

[1] H.-T. Zhang, W. Wang, M.-P. Jin, and X.-P. Lu., "A dual-polarized array antenna for on-the-move applications in Ku-band," *IEEE-APS Topical Conference on Antennas and Propagation in Wireless Communications (APWC)*, pp. 5-8; Cairns, Australia, 2016.

[2] Methods for the determination of the coordination area around an earth station in frequency bands between 100 MHz and 105 GHz, 2016 Edition of ITU Radio Regulations, vol. 2, Appendix 7, 2016.

[3] H.-T. Zhang, W. Wang, M.-P. Jin, Y.-Q. Zou, and X. Liang, "A novel dual-polarized waveguide array antenna for Ku band satellite communications," *IEEE International Symposium on Antennas and Propagation & USNC/URSI National Radio Science Meeting*, San Diego, California, USA, pp. 633-634, 2017.

[4] M. Akbari, A. Farahbakhsh, and A.-R. Sebak, "Ridge gap waveguide multilevel sequential feeding network for high-gain circularly polarized array antenna," *IEEE Trans. Antennas and Propagation*, vol. 67, no. 10, pp. 251-259, 2019.

[5] G. L. Huang, S. G. Zhou, and T. Yuan, "Design of a compact wideband feed cluster with dual-polarized sum-and difference-patterns implemented via 3-D metal printing," *IEEE Trans. Industrial Electronics*, vol. 65, no. 9, pp. 7353-7362, 2018.

[6] M. K. Verma, B. K. Kanaujia, J. P. JSaini, and P. Saini, "A novel circularly polarized gap-coupled wideband antenna with DGS for X/Ku-band applications," *Electromagnetics*, vol. 39, no. 3, pp. 186-197, 2019.

[7] S. Liu, K. Jiang, G. Xu, X. Ding, K. Zhang, J. Fu, and Q. Wu, "A dual-band shared aperture antenna array in Ku/Ka-Bands for beam scanning applications," *IEEE Access*, 7, pp. 78794-78802, 2019.

[8] A. Harrabi, T. Razban, Y. Mahe, L. Osman, and A. Gharsallah, "Theoretical approach for the design of a new wideband Ku-band printed antenna," *Applied Computational Electromagnetics Society Journal*, vol. 30, no. 11, pp. 1200-1208, 2015.

[9] T. Sallam and A. M. Attiya., "Different array synthesis techniques for planar antenna array," *Applied Computational Electromagnetics Society Journal*, vol. 34, no. 5, pp. 716-723, 2019.

[10] Y. Zou, H. Li, Y. Xue, and B. Sun, "A high-gain compact circularly polarized microstrip array antenna with simplified feed network," *Int. J. of RF Micro. Comput. Aided Eng.*, e21964, 2019.

[11] C. Deng, Y. Li, Z. Zhang, and Z. Feng, "A wideband sequential-phase fed circularly polarized

patch array," *IEEE Trans. Antennas and Propag.*, vol. 62, no. 7, pp. 3890-3893, 2014.

[12] S.-K. Lin and Y.-C. Lin, "A compact sequential-phase feed using uniform transmission lines for circularly polarized sequential-rotation arrays," *IEEE Trans. Antennas and Propag*., vol. 59, no. 7, pp. 2721-2724, 2011.

[13] R. Kazemi, S. Yang, S. H. Suleiman, and A. E. Fathy, "Design procedure for compact dual-circularly polarized slotted substrate integrated waveguide antenna arrays," *IEEE Trans. Antennas and Propag.*, vol. 67, no. 6, pp. 3839-3852, 2019.

[14] Ansoft High Frequency Structure Simulator (HFSS) ver. 14, Ansoft Corp., 2014.

[15] CST Microwave Studio, ver. 2012, Computer Simulation Technology, Framingham, MA, 2012.

[16] J. Zhu, Y. Yang, S. Li, S. Liao, and Q. Xue, "Dual-band dual circularly polarized antenna array using FSS-integrated AMC ground for vehicle satellite communications," *IEEE Trans. Vehic. Tech.*, vol. 68, no. 11, pp. 10742-10751, 2019.

[17] C. A. Balanis, *Antenna Theory: Analysis and Design*. John Wiley & Sons, 2016.

[18] M. Mahajan, S. K. Khah, and T. Chakravarty, "Extended cavity model analysis of stacked circular disc," *Progress in Electromagnetics Research*, vol. 65, pp. 287-308, 2006.

A Broadband Dual-polarized Antenna with CRR-EBG Structure for 5G Applications

Peng Chen, Lihua Wang, and Tongyu Ding

Information Engineering College
Jimei University, Xiamen, Fujian, 361021, China
chenpeng@jmu.edu.cn, liliya@jmu.edu.cn, tyding@jmu.edu.cn

Abstract ─ In this paper, a broadband dual-polarized antenna with concentric rectangular ring electromagnetic bandgap (CRR-EBG) structure is proposed for 5G applications. The antenna consists of a pair of ±45° cross dipoles, an EBG array, and two inverted L-shaped improved feeding structures. In particular the ring part of the feeding structures can reduce the coupling between two ports. The leaky wave area of the EBG structure can be used to increase bandwidths. According to the measured results, the bandwidths of port1 and port2 are 32% (3.04-4.21GHz) and 28.3% (3.13-4.16GHz), respectively. The port-to-port isolation can reach up to 23 dB, and the average gain is approximately 5 dBi. The antenna has the advantages of a wide band, good isolation and a stable radiation pattern, which can be better used in 5G communications.

Index Terms ─ 5G, dual-polarized, electromagnetic band-gap (EBG), wideband.

I. INTRODUCTION

With the fast development of wireless communication systems and a looming shortage of wireless spectrum, the wireless industry has recognized the significance of multi-band and wideband antennas for future wireless communication systems [1-7]. In this sense, dual-polarized antennas, especially ±45° polarized antennas [8-11] have been widely proposed to determine multipath fading, pulling in signals from all directions better. It is worth noting that we added the electromagnetic band-gap (EBG) structure to the designed dual-polarized antenna for band spread.

The EBG structure is divided to a high-impedance surface (HIS) [12] and uniplanar compact (UC) surface [13-14]. In [15], the designed CSRR-EBG structures reduce the starting frequency of the first band gaps by 28%, and are used for multi-band applications. It is well known that for most dual-polarized antennas, such as those reported in [16] and [17], the stable unidirectional radiation pattern characteristics are mainly determined by the shape and size of the metal reflector. Since the antenna and reflector are generally one-quarter-wavelength apart, it is non-trivial to realize a low-profile antenna in this framework. On the contrary, owing to the in-phase reflection characteristic of EBG structure, the distance between antenna and reflector can be less than one-quarter-wavelength, and therefore reducing the size of the antenna [18]. EBG structure can also make use of leaky wave region to achieve bandwidth expansion [19-20] and better isolation [21-22]. In [23], Meander-Perforated Plane (MPP-EBG) structure was reported to improve the slow-wave effect, reduce the size and broaden the bandwidth.

In this paper, a broadband dual-polarized base-station antenna with CRR-EBG structure for 5G applications is proposed. The designed antenna provides good coverage of the frequency bands from 3.13 GHz to 4.16 GHz, intended for potential 5G applications. The simulated and measured results are obtained using Ansys HFSS 15, an Agilent vector analyzer and OTA. Detailed discussions of the design are provided as follows.

II. ANTENNA DESIGN

The geometric structure of the broadband dual-polarized antenna with EBG structure is presented in Figs. 1 and 2. The antenna is mainly composed of three parts: a pair of ±45° cross dipoles, an EBG array and two improved feeding structures with an inverted L-shaped structure. The three components are printed on an FR4 substrate with a relative dielectric constant of 4.4 and a thickness of 1 mm. The EBG structure attached to the lower dielectric plate consists of 48 units. If we remove the overlap the EBG structure and balun structure, the electromagnetic interference will be reduced.

The patch structure is composed of a pair of irregular hexagons dipole in Fig. 1 (b). Two pairs of small rectangles are formed on the dipoles, which are used to avoid short-circuit between the feeding structure and the dipole. The dipoles can be connected to the ground plane primarily through two pairs of rectangular patches, which are placed vertically in the EBG structure and attached to one side of the feeding line. On the other side of the balun, the inverted L-shaped feeding line is also placed vertically in the EBG surface and is used

Submitted On: October 19, 2020
Accepted On: November 29, 2020

https://doi.org/10.47037/2020.ACES.J.351208

1054-4887 © ACES

to excite the antenna. The half ring shape of the two inverted L-shaped feeding lines is intended to reduce coupling between the ports, where the bottom ends of the feeding lines are connected to the SMA connectors in Fig. 2.

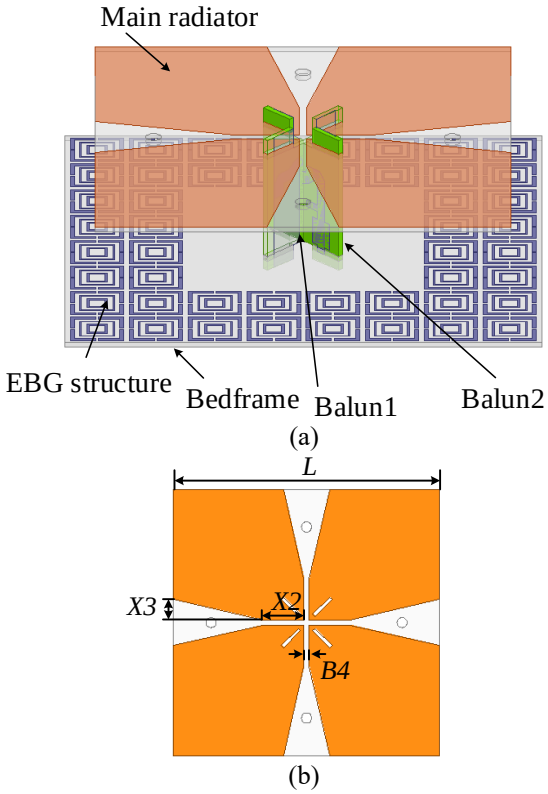

Fig. 1. (a) 3-D view of the proposed antenna, and (b) geometry of the patch.

In order to better understand the working principle of the feeding lines, the equivalent ac circuit diagram of the feeding structure is given in Fig. 3. In the feeding structure, the open branches, branch1 and branch2, can be equivalent to LC resonance circuit. Each open branch can be equivalent to LC resonant circuit, among which the resonance point of branch1 and branch2 are 3.8 GHz and 4.45 GHz, respectively. Series resonance circuits suppress harmonics when they resonate. Moreover, the slot coupling can be seen as inductance.

Figure 4 shows the geometric structure of the designed EBG array and a single EBG unit. The rectangular slots are made in a square patch, which form the EBG structure we designed. The CRR-EBG structure belongs to Uni-planar Compact EBG (UC-EBG). The CRR-EBG can be equivalent to a parallel LC model, the resonant frequency of which lends the high-impedance band-gap characteristics to the CRR-EBG structure, as shown in formulas (1) and (2):

$$w_0 = \frac{1}{\sqrt{LC}}, \tag{1}$$

$$z_s = \frac{j\omega L}{1-w^2 LC}. \tag{2}$$

A 26mm diameter cylinder is subtracted from the reflector to make it easier connected with SMA connector in actual measurement. The antenna is analyzed and optimized by HFSS 15, and the optimal values defined in Figs. 1 and 2 are listed as follows (unit: mm): *X2*=12, *X3*=6, *B4*=1.5, *L*=78, *M3*=14, *D4*=7, *W4*=4.6, *W5*=1.3, *D5*=2.8, *D7*=10, *W6*=2.4, *Rin*=1.7, *Rout*=4.1, *L5*=20, *BL*=6, *H1*=28, *W1*=2.25, *D1*=5, *D2*=9, *BW2*=5.8, *W7*=1.8735, *BW*=3, *GL*=164, *GH*=8, *T*=1, *N*=0.32, *We*=0.48, *M*=8.5, *A*=10, *L3*=89.4.

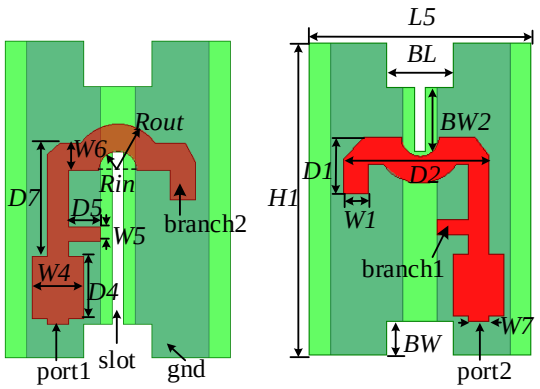

Fig. 2. Feeding structure for port1 and port2.

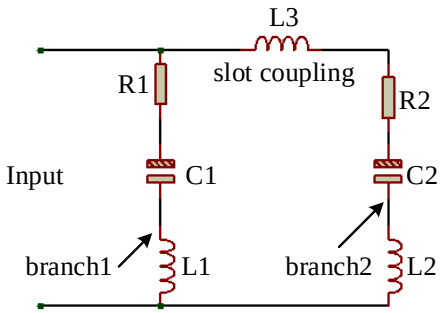

Fig. 3. Equivalent AC circuit diagram of the feeding structure.

Figure 5 shows a comparison of simulated S_{11} values for the dual-polarized dipole with and without an EBG structure for port1. It can be observed from Fig. 5 that the EBG structure has a great impact on impedance matching. When the EBG structure is not added, the impedance bandwidth is narrow with low frequency (3.02–3.15 GHz) and high frequency (4.1–4.74 GHz) for $S_{11} \leqslant -10$dB. By adding the EBG structure, a wide impedance bandwidth from 3.14 to 4.8 GHz is realized.

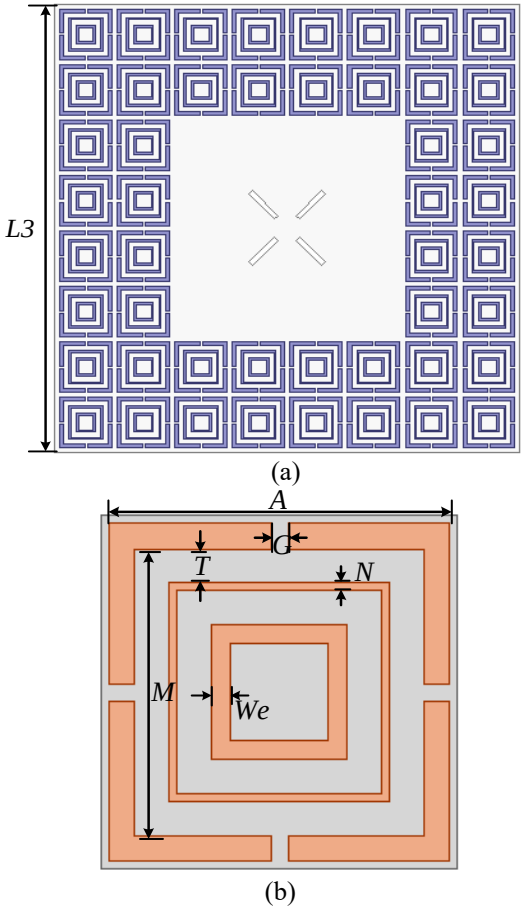

Fig. 4. (a) EBG array (b) geometry of the single EBG unit.

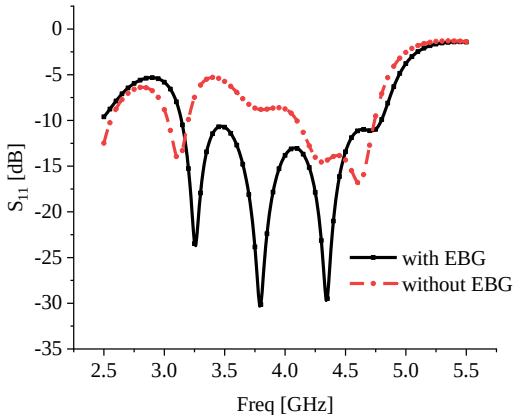

Fig. 5. Comparison of proposed antenna with and without EBG structure.

III. RESULTS AND DISCUSSION

S-parameters in this work were measured by a network analyzer. Gain and radiation patterns were measured in an OTA anechoic chamber. As shown in Fig. 6 (a), simulated and measured S-parameters of the antenna are given for port1 and port2. As can be seen from the S-parameter diagram, the simulated bandwidth is 37% (3.13-4.55GHz) and 34.1% (3.13-4.42GHz) for port1 and port2, respectively while the measured bandwidth is 28.3% (3.13-4.16GHz), the center frequency being 3.64 GHz. As can be seen from the simulated and measured results, the reflection coefficients are different at the two ports. The main reasons are as follows. First, the structure of the feeding lines at the two ports is not completely the same, especially for the ring part. Second, uneven welding resulted in a non-parallel state between the planes, having a strong impact on the reflection coefficients. The simulated and measured gains and isolation degree are presented in the Fig. 6 (b). The isolation performance in the operating band is better than 23 dB and the simulated gain is about 5 dBi. Furthermore, the bandwidth of the antenna with EBG is widened because of its leaky region. The experimental results are in good agreement with the simulation results.

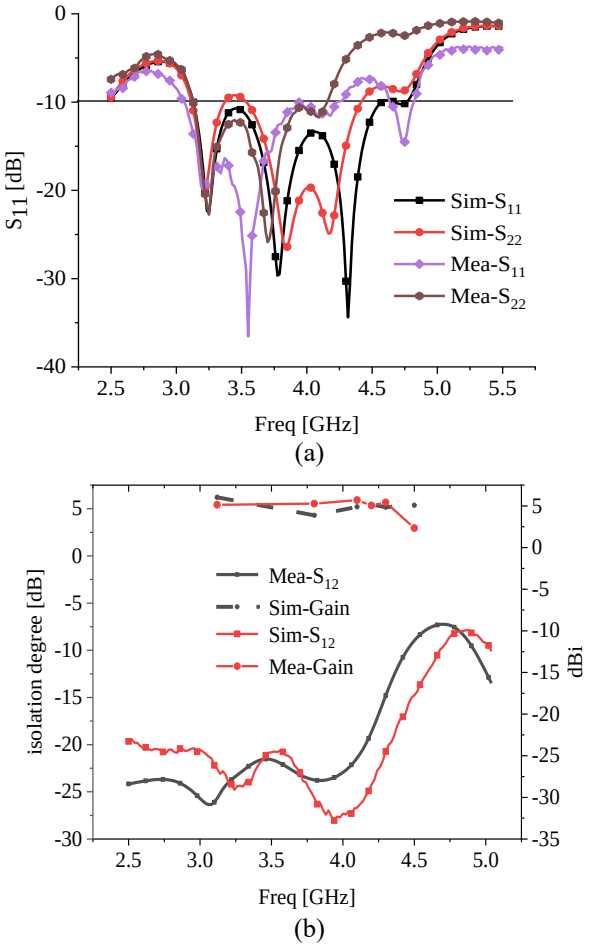

Fig. 6. Simulated and measured S-parameters of antenna.

Figure 7 shows the comparison of simulated and measured radiation patterns of the design at the frequencies of 3.12, 3.80 and 4.5 GHz, respectively. At 3.12 GHz, the radiation pattern consistency between simulation and measurement is relatively high. Among them, the radiation patterns are relatively stable at 3.8 GHz and 4.5 GHz. It can be seen from the direction diagram that the gain is about 4.8 dBi, and the directivity of the simulated and measured radiation patterns is consistent. Figure 8 presents the fabricated prototype of the antenna as well as the antenna test scenario. Compared with the antenna without EBG structure in [8], the proposed antenna broadens the frequency band, and improves the stability of the antenna radiation pattern.

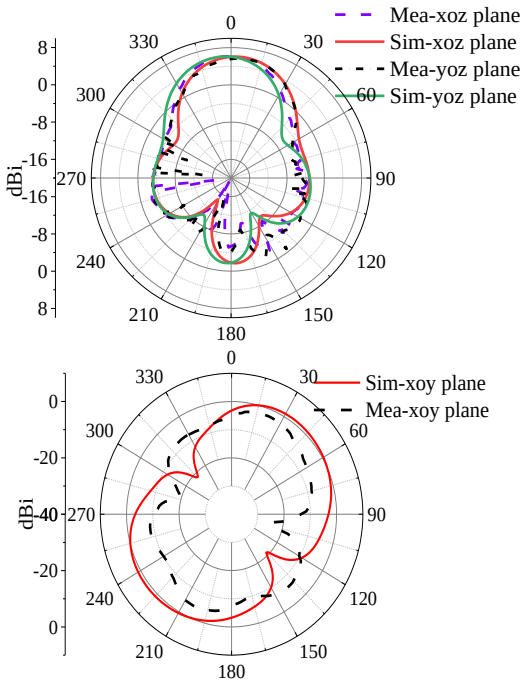

(a) 3.12GHz

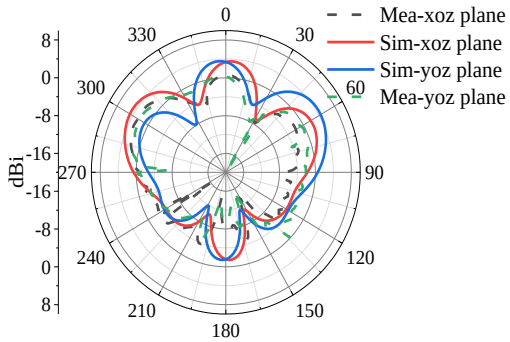

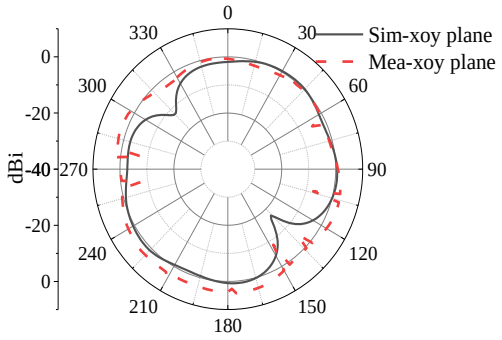

(b) 3.8GHz

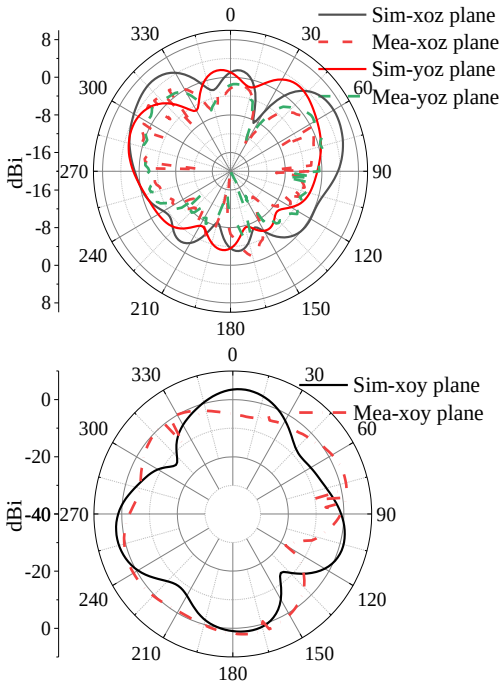

(c) 4.5GHz

Fig. 7. Simulated and measured radiation pattern of antenna: (a) 3.12 GHz, (b) 3.8 GHz, and (c) 4.5 GHz.

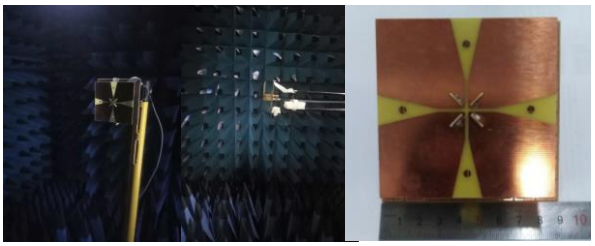

Fig. 8. Antenna in test and fabricated prototype of the antenna.

Table1: Comparison of the proposed antenna with references

Ref.	Bandwidth (GHz)	Gain (dBi)	Isolation	Type of EBG
[8]	3.12-3.68	5.84	＞23.5	/
[10]	3.16-3.48	/	＞30	TVS-EBG
[15]	3.31-4.33	/	＞20	CSRR-EBG
[19]	3.60-4.06	/	＞20	ELV-EBG
Pro.	3.13-4.42	5	＞23	CRR-EBG

λ_0 is the wavelength in free space at center operating frequency.

In Table 1, the performance of the proposed antenna is compared with previously published antennas. The antenna's bandwidth of our design operates 3.1 to 4.42 GHz, which is wider than that published references. The port-to-port isolation is slightly higher than [15] and [19]. But the gain is lower than that of Ref. [8]. To sum up, the performance of the antenna is better than other references in the table.

IV. CONCLUSION

A wideband dual-polarized base station antenna with EBG structure is presented herein, where the leaky wave region of EBG has been used to expand the frequency band and yield a stable radiation pattern of the antenna. The loop design of the feeding structures proves to be capable of reducing port coupling significantly. The antenna operates in the frequency band of 3.13-4.16 GHz. Simulated results prove that the design has the advantages of good bandwidth, stable radiation pattern and high isolation degree. Future work will be focused on further optimization of the radiation patterns and other antenna performance.

ACKNOWLEDGMENT

This work was supported by Natural Science Foundation of Fujian Province (Grant No. 2020J02042, 2019J01718 and 2018J05109).

REFERENCES

[1] C. Lei, L. L. Chen, J. Q. Zhang, and L. Dan, "A broadband dipole antenna with parasitic patch loading," *IEEE Antennas Wirel. Propag. Lett.*, vol. 17, pp. 1717-1721, Sept. 2018.

[2] G. Feng, L. Chen, X. Wang, X. Xue, and X. Shi, "Broadband circularly polarized crossed bowtie dipole antenna loaded with parasitic elements," *IEEE Antennas Wirel. Propag. Lett.*, pp. 114-117, Jan. 2018.

[3] J. Tao, Q. Feng, and L. Tao, "Dual-wideband magnetoelectric dipole antenna with director loaded," *IEEE Antennas Wirel. Propag. Lett.*, vol. 17, no. 10, pp. 1885-1889, Oct. 2018.

[4] X. Chao, J. Yin, L. Xiang, P. Feng, and Y. Jian, "An ultrawideband dipole with a director as a feed for reflector antennas," *IEEE Antennas Wirel. Propag. Lett.*, vol. 16, no. 99, pp. 1341-1344, Dec. 2017.

[5] C.-W. Hsiao and W.-S. Chen, "Broadband dual-polarized base station antenna for LTE/5G C-band applications," *The 2018 Cross Strait Quad-Regional Radio Science and Wireless Technology Conference (CSQRWC)*, Xuzhou, China, July 2018.

[6] Y. Li, W. Li, and W. Yu, "A multi-band/UWB MIMO/diversity antenna with an enhanced isolation using radial stub loaded resonator," *Appl. Comput. Electromagn. Soc. J.*, vol. 28, no. 1, pp. 8-20, Jan. 2013.

[7] K. L. Chung, X. Yan, and Y. Li, "A Jia-shaped artistic patch antenna for dual-band circular polarization," *AEU-International Journal of Electronics and Communications*, vol. 120, article ID 153207, June 2020.

[8] P. Chen and L. Wang, "A dual-polarized sakura-shaped base station antenna for the fifth generation (5G) communications," *Appl. Comput. Electromagn. Soc. J.*, vol. 35, no. 5, pp. 567-571, May 2020.

[9] D. Su, J. J. Qian, Y. Hua, and D. Fu, "A novel broadband polarization diversity antenna using a cross-pair of folded dipoles," *IEEE Antennas Wireless Propagation Letters*, vol. 4, pp. 433-435, Dec. 2005.

[10] P. P. Bhavarthe, S. S. Rathod, and K. T. V. Reddy, "A compact two via slot-type electromagnetic bandgap structure," *IEEE Microw. Wirel. Compon. Lett.*, vol. 27, no. 5, pp. 446-448, May 2017.

[11] L. Peng, C.-L. Ruan, and Z.-Q. Li, "A novel compact and polarization-dependent mushroom-type EBG using CSRR for dual/triple-band applications," *IEEE Microw. Wirel. Compon. Lett.*, vol. 20, no. 9, pp. 489-491, Sept. 2010.

[12] S. Y. Luo, Y. S. Li, Y. F. Xia, and L. Zhang, "A low mutual coupling antenna array with gain enhancement using metamaterial loading and neutralization line structure," *Appl. Comput. Electromagn. Soc. J.*, vol. 34, no. 3, pp. 411-418, 2019.

[13] M. J. Al-Hasan, T. A. Denidni, and A. R. Sebak, "Millimeter-wave EBG-based aperture-coupled dielectric resonator antenna," *IEEE Trans. Antennas Propag.*, vol. 61, no. 8, pp. 4354-4357, Aug. 2013.

[14] T. Jiang, T. Jiao, and Y. Li, "A low mutual coupling MIMO antenna using periodic multi-layered electromagnetic band gap structures," *Appl. Comput. Electromagn. Soc. J.*, vol. 33, no. 3, pp. 305-311, Mar. 2018.

[15] L. Peng, C.-L. Ruan, and Z.-Q. Qiang, "A novel compact and polarization-dependent mushroom-type EBG using CSRR for dual/triple-band applications," *IEEE Microw. Wirel. Compon. Lett.,* vol. 20, no. 9, pp. 489-491, Sept. 2010.

[16] C. Ding, H. Sun, Y. Guo, P. Qin, and Y. Yang, "Beamwidth control of base station antennas employing reflectors and directors" *2015 International Symposium on Antennas and Propagation (ISAP)*, Hobart, TAS, Australia, Nov. 2015.

[17] H. Huang, Y. Liu, and S. Gong, "A broadband dual-polarized base station antenna with anti-interference capability," *IEEE Antennas Wirel. Propag. Lett.*, vol. 16, pp. 613-616, July 2016.

[18] Z. Nie, H. Zhai, L. Liu, J. Li, D. Hu, and J. Shi, "A dual-polarized frequency-reconfigurable low-profile antenna with harmonic suppression for 5G application," *IEEE Antennas Wirel. Propag. Lett.*, vol. 18, no. 6, pp. 1228-1232, June 2019.

[19] E. Rajo-Iglesias, L. Inclan-Sanchez, J.-L. Vazquez-Roy, and E. Garcia-Muoz, "Size reduction of mushroom-type EBG surfaces by using edge-located vias," *IEEE Microw. Wirel. Compon. Lett.*, vol. 17, no. 9, pp. 670-672, Sept. 2007.

[20] Y. Li, W. Li, and Q. Ye, "A reconfigurable triple-notch-band antenna integrated with defected microstrip structure band-stop filter for ultra-wideband cognitive radio applications," *Int. J. Antennas Propag.*, vol. 2013, p. 13, article ID 472645, 2013.

[21] J. Jiang, Y. Xia, and Y. Li, "High isolated X-band MIMO array using novel wheel-like metamaterial decoupling structure," *Appl. Comput. Electromagn. Soc. J*, vol. 34, no. 12, pp. 1829-1836, Dec. 2019.

[22] K. L. Chung, X. Yan, A. Cui, and Y. Li, "Circularly-polarized linear antenna array of non-identical radiating patch elements for WiFi/WLAN applications," *AEU-International Journal of Electronics and Communications*, article ID 153526, Nov. 2020.

[23] M. Kim, "A compact EBG structure with wideband power/ground noise suppression using meander-perforated plane," *IEEE Trans. Electromagn. Compat*., vol. 57, no. 3, pp. 595-598, June 2015.

Design and Analysis of Reflectarray Compound Unit Cell for 5G Communication

Tahir Bashir [1], Han Xiong [1,2*], Abdul Aziz [3], Muhammad Ali Qureshi [3], Haroon Ahmed [1], Abdul Wahab [1], and Muhammad Umaid [4]

[1] School of Microelectronics and Communication Engineering, Chongqing University, Chongqing, 400044, China
{tahircqu, haroonahmed97, wahab.engr55}@gmail.com

[2] Collaborative Innovation Center of Light Manipulations and Applications
Shandong Normal University, Jinan, 250358, China
hxiong@cqu.edu.cn*

[3] Department of Telecommunication Engineering, The Islamia University Bahawalpur, 63100, Pakistan
{abdul.aziz, ali.qureshi}@iub.edu.pk

[4] School of Electrical Engineering, Chongqing University, Chongqing, 400044, China
umaidrao@gmail.com

Abstract ─ In this paper, a single-layer compound unit element is proposed for reflectarray antenna design operating in Ka-band (26.5-29.5GHz) at the center frequency of 28GHz. A systematic study on the performance of a compound unit element is examined first. The structure of the proposed unit element is a unique combination of two different shape simple patches i.e. cross dipole and square patches. The desired phase range is achieved due to the multi-resonance of both patch elements with a single layer without any air-gap. The compound unit element is simulated by computer models of CST Microwave studio based on the Floquet approach (infinite periodic approach) and it has achieved 348.589º reflection phase range. Furthermore, the analysis of the reflection phase range, S-curve gradient, reflection magnitude, fabrication tolerance, and surface current density is also simulated and demonstrated. Based on the remarkable performance, the proposed element can be considered as the best element of single-beam or multi-beam reflectarray antenna design for 5G applications.

Index Terms ─ Floquet approach, reflectarray, reflection phase range, single-layer, 5G.

I. INTRODUCTION

Reflectarrays are the innovative alternative of conventional parabolic reflectors and phased array antennas due to its novelty and advantages such as light weight, small size, electronic beam steering capability, ease in deployment, and low design complexity [1-3]. Reflectarrays are flat reflectors array antennas consisting of isolated variable-size unit elements on a grounded dielectric substrate with a certain tuning to produce the progressive phase distribution and generate the single-beam or multiple-beams when illuminated by a feed antenna [4-6]. The unit elements on the reflectarray aperture are pre-designed with a specific phase shift to retransmit the incident waves in the form of a beam. The required phase shift is acquired from the reflection phase range curve that is generated by varying one of the geometrical parameters of the unit element according to the design consideration [7,8]. Two main characteristics are important for the designing of unit elements: one is maximum reflection phase range with low fabrication tolerance and the second is minimum reflection loss [9,10]. The unit element is the basic component for the reflectarray antenna design that reflects the incident waves in a specific direction with progressive phase distribution by making a beam. Several designed methods have been proposed over the years to control the reflection phases such as the same size patches with variable stub length, variable size patches, and element rotation technique for circular polarized design [11,12].

Characterization of unit elements in the implementation and analysis of a reflectarray antenna is the most significant part regardless of the choice of the phasing mechanism. The reflection phases of the radiating unit elements are approximated by some degree due to some limitations of fullwave simulation for the reflectarray antenna. The mutual coupling effect between elements of a reflectarray is approximated by using an

Submitted On: July 1, 2020
Accepted On: November 30, 2020

https://doi.org/10.47037/2020.ACES.J.351209

1054-4887 © ACES

infinite periodic boundary. This technique is valid because several reflectarray antennas based on this technique have been demonstrated.

Different models are available to investigate the mutual coupling between the reflectarray unit elements using periodic approximation such as waveguide simulator approach, TEM waveguide approach, and infinite array approach [13-15]. In the infinite array approach, the unit element is simulated by using a periodic boundary condition [16]. This approach is more general than other approaches. Since the periodic environment of the unit element can be simulated more accurately in order to obtain the reflection characteristics for the oblique excitation angle. The infinite array approach is a conventional method to analyze the reflection characteristics of the reflectarray unit element. Due to easy analysis, the most preferred shapes for reflectarray are square and rectangular but a unique compound unit element is presented in this paper.

The purpose of this research work is to increase the phase range of a single thin layer unit cell without any air-gap between ground and the patch element to reduce fabrication complexity by using a combination of different simple multi-resonant elements. The new multi-resonant reflectarray unit cell has successfully achieved almost 360° phase range at 28 GHz and it can be used to design any single-beam or multi-beam reflectarray antenna for 5G applications. In order to investigate the performance of the proposed element, the reflection characteristics including reflection phase range, reflection magnitude, fabrication tolerance, and surface current density are also studied in this paper. The element design and simulation results are discussed in the following section.

II. DESIGN AND ANALYSIS OF THE PROPOSED COMPOUND UNIT ELEMENT

A. The design of compound unit element

We conducted the fullwave simulations using the CST microwave studio to investigate the scattering characteristics of the proposed unit element based on the Floquet approach (infinite periodic approach). This approach is useful to approximate the mutual coupling between elements because it has considered each element as taken from an infinite periodic array structure. The periodic boundary conditions are applied to the unit element when it is surrounded by a uniform infinite environment and the unit element excitation is achieved by a plane wave as shown in Fig. 1. The proposed unit element is a combination of two different patches, i.e., cross dipoles and square patches as shown in Fig. 2. Roger RT5880 is used as a separator between the ground plane and reflecting patch with standard substrate thickness, permittivity, and loss tangent 0.127*mm*, 2.2, and 0.0009 respectively that is available in the datasheet and the element periodicity is 0.5λ at operating frequency 28GHz. We used periodic boundary conditions along the *x*-axis and the *y*-axis while the *z*-axis is kept open. The configuration and parameters of the proposed element are mentioned in Fig. 2 and Table 1 respectively.

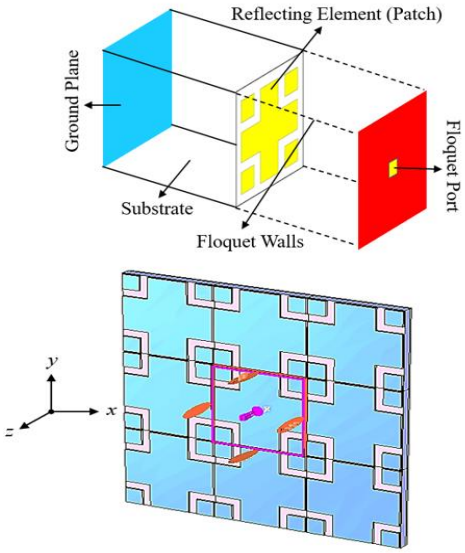

Fig. 1. Infinite periodic array structure with the unit element in CST.

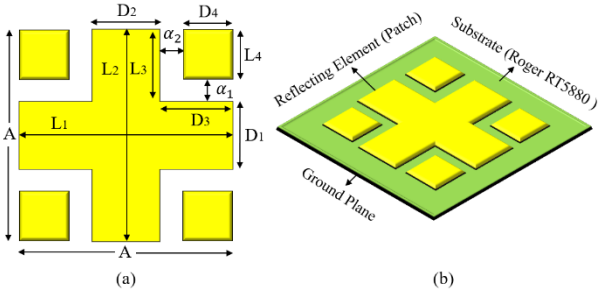

Fig. 2. The geometry of the compound unit element: (a) top view of the patch, and (b) 3D view of the unit element.

Table 1: Design parameters of the compound element

Parameters	Description	Values
$L_1 = L_2$	Length of *x* and *y* dipoles	5.25mm
$D_1 = D_2$	Width of *x* and *y* dipoles	2.272mm
$L_3 = D_3$	Arm length of cross dipoles	1.136mm
$L_4 = D_4$	Length and width of a square patch	1mm
$\alpha_1 = \alpha_2$	The gap between dipoles and square patch	0.5mm
A	Length and width of complete patch	5.25mm

III. SIMULATION RESULTS AND DISCUSSION

In order to control the reflection phase response, the variable-patch size method is used for the proposed unit element design. The proposed element has achieved a maximum reflection phase range of 348.589° by varying the patch size (including cross dipoles and square patches) from 2.5mm to 5.25mm as shown in Fig. 3. All the geometric parameter changes accordingly as the patch size varies. The reflection magnitude is the reduction in magnitude of the incident field after reflection, it depends on the dielectric properties of the substrate and the conductor used in the ground and it is close to 1 as shown in Fig. 4:

$$R_L = \alpha_d + \alpha_c\,, \tag{1}$$

where, R_L is the reflection loss and α_d and α_c are the attenuation due to the dielectric substrate and conductor loss respectively. Reflection phase variations are acquired by varying the geometrical parameter of the element, but in most cases, only one geometrical parameter is needed to adjust the reflection phase value. The substrate thickness, dielectric permittivity, incidence angle, and array periodicity are also important quantities for reflection phase performance instead of element shape and size. Table 2 shows the performance comparison between the proposed element and other single-layer unit elements in terms of the reflection phase range and proves that the proposed element is best for reflectarray antenna design. The maximum reflection phase range is a relevant figure of merit to characterize the performance of the reflectarray element [8]:

$$\Delta = \varphi_{max} - \varphi_{min}, \tag{2}$$

where, φ_{max} and φ_{min} are the maximum and minimum reflection phases respectively at the operating frequency 28GHz shown in Fig. 3. The reflection phase curve shows variation near the resonance patch size, it means a small variation in the patch size significantly changes the reflection phases. Therefore, fabrication tolerance is the second figure of merit for reflectarray unit element performance. The fabrication tolerance is defined as the partial derivative of the observing variation in the reflection phases to the patch size as shown in Fig. 5. The fabrication tolerance is assumed to be 0.01 mm. Therefore, continuous phase resolution can used to design reflectarray:

$$\sigma = max\ |\frac{\partial \vartheta}{\partial A}|. \tag{3}$$

Fabrication tolerance depends on the reflection phase gradient, smother reflection phase curve offers low fabrication tolerance or highly tolerant with the fabrication error and vice versa. It is important to note here that the partial derivative of reflection phases to dimension *A* of the element is an important parameter to define the sensitivity and the effect of all other remaining quantities is much lower than the effect of *A*. While the parameters σ and Δ are calculated at operating frequency f_o. It is interesting to realize how much the reflection phase changes when varying the frequency. If the frequency changes, there are two main effects: the desired reflection phase of elements changes due to the variation of the electrical path length and the reflection phase obtained for a given patch size is also different [17].

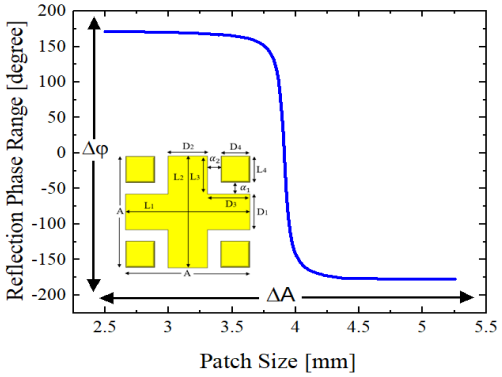

Fig. 3. The reflection phase response of the compound unit element.

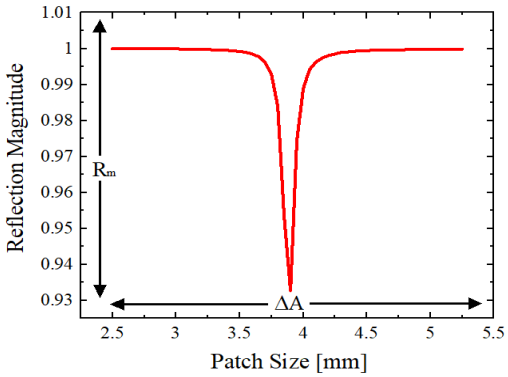

Fig. 4. The reflection magnitude curve of the compound unit element.

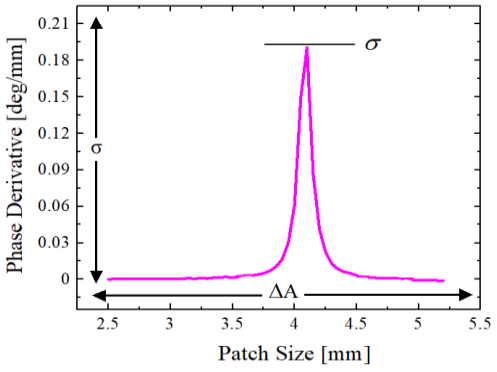

Fig. 5. The plot of the derivative of the reflection phase curve versus patch size at operating frequency of 28GHz.

Table 2: Performance comparison between the proposed element and other published single-layer unit elements

References	Types of Unit Element	Reflection Phase Range
[18]	Square loop with split ring and Circular loop with split ring	280°, 260°
[19]	Square, Triangular, Minkowski, Square loop	315°, 310° 315°, 340°
[20]	Hexagonal	340°
[21]	Radiating element	305°
[22]	Tunable unit cell	330.6°
[23]	Reconfigurable unit cell	330°
[24]	Rectangular slot, Circular slot	279°, 278°
[25]	Time modulated reflectarray unit cell	300°
[26]	Double cutted ring element	290°
[27]	Pair of fractal patches	320°
Proposed	**Compound unit element**	**348.589°**

The interaction of the incident electric field with reflecting element and substrate is demonstrated by surface current distribution as shown in Fig. 6. This is another important figure of merit to understand the electrical behavior of the unit element. The current density on the surface of the resonating unit element is generated by the concentration of the incident field. These fields have reached its maximum values at the resonance frequency f_o and reflectarray also has shown maximum reflectivity at the resonance frequency and it offered a higher loss. The surface current distribution of the reflecting element is 112*A/m* and the maximum current is on the center of the dipoles as depicted in Fig. 6. Surface current density is inversely proportional to the reflection area of the unit element [28]. If reflectarray aperture has an excess of small size elements it increases the reflection losses, surface current density and reduces the overall performance of the reflectarray antenna [29]. The maximum current density and current amount as specified by Maxwell's equation [30,31]:

$$I = \oint \vec{J}.ds. \quad (4)$$

Also, the current density ($\vec{J}$) is related to the incident electric field $\vec{E}$ represented as follow:

$$\vec{J} = \sigma \vec{E}\,, \quad (5)$$

where σ is the electrical conductivity of the material. Table 3 shows the performance summary of the compound unit element.

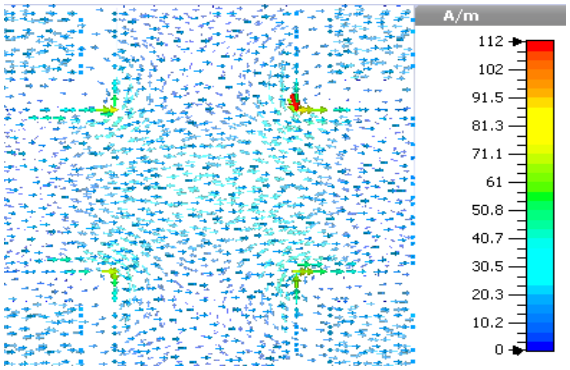

Fig. 6. Surface current density on the reflectarray unit element at the operating frequency of 28GHz.

Table 3: Performance analysis of the compound element

Performance Figures	Compound Unit Element
Frequency Band	26.5-29.5GHz
Operating Frequency	28GHz
Reflection Phase Range	348.589°
Linear Static Phase Range	145°
Reflection Magnitude	0.932
Fabrication Tolerance	0.2
Surface Current Density	112 *A/m*

IV. CONCLUSION

In this paper, we proposed a compound unit element using a single-layer topology for the reflectarray antenna design at an operating frequency of 28GHz. The proposed element is integrated by a variable-size phase shift technique using an infinite periodic array structure in a computer model CSTMv15. From the simulation results analysis, the compound element shows good performance in terms of maximum reflection phase range with minimum reduction in the magnitude of the incident field, fabrication tolerance, and surface current density. The proposed geometry may become a good reflector of single-beam or multi-beam reflectarray antenna for 5G applications.

ACKNOWLEDGMENT

This work is supported by the National Natural Science Foundation of China (No. 61501067); Fundamental Research Funds for the Central Universities (2019CDQYTX033).

REFERENCES

[1] J. Huang and J. A. Encinar, *Reflectarray Antennas*. John Wiley & Sons Publication, 2008.

[2] S. Costanzo, "Reflectarray antennas: Analysis and synthesis techniques," *International Journal of Antennas and Propagation*, vol. 2012, pp. 945682, 2012.

[3] R. R. Elsharkawy, M. Hindy, A. A. Saleeb, and El. Rabaie, "A reflectarray with octagonal unit cells for 5G applications," *Wireless Personal Communications*, vol. 97, pp. 2999-3016, 2017.

[4] W. Hong, Z. H. Jiang, C. Yu, J. Zhou, P. Chen, Z. Yu, H. Zhang, B. Yang, X. Pang, M. Jiang, and Y. Cheng, "Multibeam antenna technologies for 5G wireless communications," *IEEE Transactions on Antennas and Propagation*, vol. 65, pp. 6231-6249, 2017.

[5] A. Aziz, M. A. Qureshi, M. J. Iqbal, S. Z. A. Zaidi, U. Farooq, and U. Ahmad, "Performance and quality analysis of adaptive beamforming algorithms (LMS, CMA, RLS & CGM) for smart antennas," *International Conference on Computer and Electrical Engineering*, vol. 6, pp. 302-306, 2010.

[6] J. A. Encinar and J. A. Zornoza, "Broadband design of three-layer printed reflectarrays," *IEEE Transactions on Antennas and Propagation*, vol. 51, pp. 1662-1664, 2003.

[7] M. E. Bialkowski and K. H. Sayidmarie, "Investigations into phase characteristics of a single-layer reflectarray employing patch or ring elements of variable size," *IEEE Transactions on Antennas and Propagation*, vol. 56, pp. 3366-3372, 2008.

[8] H. Rajagopalan, X. Shenheng, and Y. Rahmat-Samii, "On understanding the radiation mechanism of reflectarray antennas: An insightful and illustrative approach," *IEEE Antennas and Propagation Magazine*, vol. 54, pp. 14-38, 2012.

[9] M. H. Dahri, M. H. Jamaluddin, M. I. Abbasi, and M. R. Kamarudin, "A review of wideband reflectarray antennas for 5G communication systems," *IEEE Access*, vol. 5, pp. 17803-15, 2017.

[10] E. C. Choi and S. Nam, "W-band low phase sensitivity reflectarray antennas with wideband characteristics considering the effect of angle of incidence," *IEEE Access*, vol. 8, pp. 111064-111073, 2020.

[11] P. Nayeri, F. Yang, and A. Z. Elsherbeni, *Reflectarray Antennas: Theory, Designs and Applications*. Wiley-IEEE Press, 2018.

[12] J. Wu, X. Da, B. Lin, J. Zhao, and K. Wu, "Circularly polarized low-cost wide band reflectarray antenna constructed with subwavelength elements," *International Journal of RF and Microwave Computer Aided Engineering*, vol. 28, pp. 21277, 2018.

[13] J. Shaker, M. R. Chaharmir, and J. Ethier, *Reflectarray Antennas: Analysis, Design, Fabrication, and Measurement*. *Artech House*, 2013.

[14] A. K. Bhattacharyya, *Phased Array Antennas: Floquet Analysis, Synthesis, BFNs, and Active Array Systems*. John Wiley & Sons, 2006.

[15] P. Hannan and M. Balfour, "Simulation of a phased-array antenna in waveguide," *IEEE Transaction on Antennas and Propagation*, vol. 13, pp. 342-353, 1965.

[16] T. B. A. Senior and J. L. Volakis, *Approximate Boundary Conditions in Electromagnetics*. Institute of Electrical Engineers, Bookcraft Ltd., 1995.

[17] M. Bozzi, S. Germani, and L. Perregrini, "Performance comparison of different element shapes used in printed reflectarrays," *IEEE Antennas and Wireless Propagation Letters*, vol. 2, pp. 219-222, 2003.

[18] M. A. Sheikh and S. A. Khan, "Performance optimization of unit-cell reflectarray antenna for future 5G communications," *International Journal of Computer Applications*, vol. 975, pp. 68-73, 2017.

[19] S. Finich, N. A. Touhami, and A. Farkhsi, "Design and analysis of different shapes for unit-cell reflectarray antenna," *Procedia Engineering*, vol. 181, pp. 526-530, 2017.

[20] T. Abdennour Ben, M. Nedil, K. Hettak, and J. Shaker, "Reflectarray antenna design using hexagonal shape unit cells for 5G application," *IEEE International Symposium on Antennas and Propagation*, pp. 1639-1640, 2018.

[21] L. Cai, Z. H. Jiang, and W. Hong, "Evaluation of reconfigurable reflectarray antenna element at 19 GHz based on highly anisotropic liquid crystal material," *IEEE International Conference on Computational Electromagnetics*, pp. 1-3, 2019.

[22] J. Huang, R. Zhang, R. Xie, S. Shi, J. Ding, and G. Zhai, "Beam-Steerable reflectarray antenna for C-Band radar," *IEEE International Conference on Computational Electromagnetics*, pp. 1-3, 2019.

[23] K. Q. Henderson and N. Ghalichechian, "Steerable reflectarray using tunable height dielectric for high-power applications," *IEEE 14th European Conference on Antennas and Propagation*, pp. 1-4, 2020.

[24] M. Inam and M. Y. Ismail, "Design and analysis of Ku-band unit cells for reflectarray antennas," *IEEE International Conference on UK-China Emerging Technologies*, pp. 1-4, 2020.

[25] S. Spatola, J. S. Gomez-Diaz, and E. Carrasco, "Time modulated reflectarray unit-cells with non-reciprocal polarization control," *IEEE 14th European Conference on Antennas and Propagation*, pp. 1-4, 2020.

[26] H. Bodur and S. Çimen, "Reflectarray antenna design with double cutted ring element for X-band applications," *Microwave and Optical Technology*

Letters, vol. 62, pp. 3248-3254, 2020.
[27] S. Costanzo, F. Venneri, A. Borgia, and G. Di Massa, "A single-layer dual-band reflectarray cell for 5G communication systems," *International Journal of Antennas and Propagation*, vol. 2019, pp. 1-9, 2019.
[28] M. Ismail and A. Kiyani, "Investigation of reflection area on strategic reflectarray resonant elements," *IEEE Symposium on Wireless Technology & Applications*, pp. 363-367, 2013.
[29] S. Finich, N. Touhami, and A. Farkhsi, "Comparison and analysis of unit-cell environment behavior of reflectarray antenna," *ARPN Journal of Engineering and Applied Sciences*, vol. 11, pp. 1421-1424, 2016.
[30] H. Xiong, Q. Shen, and T. B Long, "Broadband terahertz absorber based on Dirac semimetal with tunable working bandwidth," *Results in Physics*, pp. 2211-3797, 2020.
[31] A. Kiyani and M. Ismail, "Design and analysis of high performance reflectarray resonant elements," *Procedia Engineering*, vol. 53, pp. 248-254, 2013.

Tahir Bashir received his B.Sc. degree in Telecommunication from Islamia University Bahawalpur, Pakistan in 2018 and M.S. degree in Electronics and Communication Engineering from Chongqing University China in 2020. His current research interest includes metamaterial absorbers, antenna and reflectarray design.

Han Xiong received the M.Sc. degree from Yunnan Normal University, Kunming, China, in 2010, and the Ph.D. degree in Radio Physics from the University of Electronic Science and Technology of China, Chengdu, China, in 2014. He is now an Associate Professor in Chongqing University, Chongqing, China. His research interests include antenna, absorber and metamaterials technology.

Abdul Aziz is working as Assistant Professor in Telecommunication Engineering Department, Islamia University of Bahawalpur, Pakistan since 2009. He received his B.S. degree in Electrical Engineering from Bahauddin Zakariya University, Multan, Pakistan in 2003 and the M.S. degree in Telecommunication Engineering from University of Engineering & Technology, Peshawar, Pakistan in 2008. He completed his Ph.D. from Electronic Engineering Department, Tsinghua University, Beijing, China in 2019. His research interests include design of transmissive and reflective metasurfaces for satellite communications, antenna theory and applied electromagnetics.

Muhammad Ali Qureshi received his B.Sc. in Electrical Engineering from UET Lahore in 2000 and M.Sc. in Telecommunication Engineering from NWFP-UET Peshawar in 2008. He completed his Ph.D. in Electrical Engineering from KFUPM, Saudi Arabia in 2017. He is working as Associate Professor and Chairman at the Department of Telecommunication Engineering at The Islamia University of Bahawalpur, Pakistan. His research interests include image and video processing, image forensics, image quality assessment, and wireless communication. He is a Senior Member of IEEE and Chair, IEEE Bahawalpur Subsection Region 10.

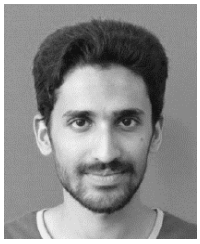

Haroon Ahmed received his B.Sc. degree in Electronics Engineering from Comsats Institute of Technology, Abbottabad, Pakistan in 2015 and M.S in Electronics and Communication Engineering from Chongqing University, Chongqing, China in 2019. Currently, he is pursuing Ph.D. in Information and Communication Engineering from Chongqing University, China. His research interest includes MIMO Antennas and systems for 5G communication.

Abdul Wahab received his B.Sc. degree in Telecommunication from the University of Science and Technology, KPK, Pakistan in 2018 and M.S. degree in Electronics and Communication Engineering from Chongqing University China in 2020. His research interest includes signal processing, MIMO Radars, SAR radars and remote sensing.

Muhammad Umaid received the B.Sc. degree in Telecommunication from The Islamia University Bahawalpur, Pakistan in 2018 and M.S. degree in Electrical Engineering from Chongqing University China in 2020. His current research interest includes reflectarray antenna design and control of renewable energy.

Electromagnetic Response Prediction of Reflectarray Antenna Elements Based on Support Vector Regression

Liping Shi, Qinghe Zhang, Shihui Zhang, Chao Yi, and Guangxu Liu

College of Computer and Information
China Three Gorges University, Yichang, 443002, China
1593735417@qq.com, zqh@ctgu.edu.cn

Abstract ─ In this letter, support vector regression (SVR) is used to predict the electromagnetic (EM) response of a complex shaped reflectarray (RA) unit cell. The calculation of the scattering coefficients of passive RA elements with periodic intervals is firstly transformed into a regression estimation problem, and then an analysis model is established by SVR to quickly predict the EM response of the unit cells. To this end, the full-wave (FW) simulation software is used to obtain a set of random samples of the scattering coefficient matrix of the RA antenna unit cell, which is used for SVR training. Under the same conditions, the radial basis function network (RBFN) is also used to predict the EM response of the elements, and the comparison results show the effectiveness and accuracy of the proposed method.

Index Terms ─ Electromagnetic response, reflectarray antenna elements, scattering matrix, support vector regression.

I. INTRODUCTION

Microstrip reflectarray (RA) antennas have replaced traditional parabolic reflectors and array antennas with advantages such as simple structure, easy manufacturing and transportation, and low manufacturing cost [1,2].

An important step in synthesizing such a high-performance RA antenna is to analyze its electromagnetic (EM) response. There are many different methods for the analysis of RA antennas. Considering the periodic characteristics of such antennas, the most commonly used method is the full-wave (FW) simulation which assumes the local periodicity [3,4]. Traditionally, a wide range of EM simulation software, such as High Frequency Structure Simulator (HFSS) and CST Microwave Studio [5], which used to calculate the RA unit cells' scattering matrix and establish *scattering matrix-versus-descriptors* lookup tables (LUTs) [6,7]. As we all know, the main disadvantage of establishing a database is that it requires a large number of samples and uses interpolation techniques [8], and the standard interpolation method cannot be used for EM prediction because of the high nonlinearity between the descriptor (frequency, angle of incidence, geometry, etc.) of the unit cell and the corresponding EM response [1,7,9]. Since the number of LUTs items increase exponentially with the degrees of freedom (DoFs) of the unit cells [6], involving a large amount of memory and computation time. In addition, parametric scanning is usually required to analyze the design of each possible cell, which is also very time-consuming [9]. Therefore, the FW method is rarely used in actual antenna synthesis [6].

The rapid development of machine learning methods has made it widely used in the field of antennas and electromagnetics. At present, there have been many successful applications including antenna diagnosis [10], modeling [11] and parameter reconstruction [12]. Several papers have used machine learning methods to design and analyze antennas. In [5,13], ANNs were used to design and analyze RA antenna and to predict magnitude, but the results were limited and overfitting problems may be encountered. In [7], Salucci, *et al* used the ordinary kriging (OK) based on statistical learning method to quickly predict the EM response of RA antenna. Inspired by this, support vector regression (SVR) has a large number of kernel functions that can be used compared to other regression methods, has a more solid mathematical theoretical foundation, and has the advantages of strong generalization ability and good robustness. Therefore, this paper intends to use SVR algorithm to predict the magnitude and phase response of RA antenna unit cells with complex shapes under different polarization states (i.e., co-polarization and cross-polarization), so as to overcome the problems of calculation time and memory of traditional FW simulation and the accuracy of ANNs.

The evaluation of the scattering coefficient of a typical RA antenna element characterized by arbitrary DoFs is first recast as a vectorial regression problem. Then, CST is used to simulate different RA antennas to obtain a set of data for SVR training and establish a substitute model. Finally, the results of SVR training are compared with the FW simulation results and the radial basis function network (RBFN), to prove the superiority

Submitted On: December 5, 2019
Accepted On: August 9, 2020
https://doi.org/10.47037/2020.ACES.J.351210

1054-4887 © ACES

of the proposed method.

II. OVERVIEW OF RA ANALYSIS

Microstrip RA antenna comprises a planar reflective surface and a feeder that illuminates a passive array of microstrip patches and produces an induced current, which in turn properly focuses the reflected beam by controlling the scattering properties of the RA surface [2].

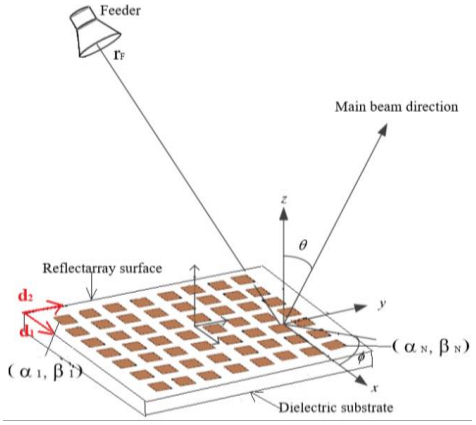

Fig. 1. Sketch of the RA antenna.

A microstrip RA consists of a planar array of $N\times N$ patches that are periodically arranged on a grounded single-layer dielectric substrate (Fig. 1). Each nth $(n=1,...,N^2)$ array element is described by I DoFs $\mathbf{L}(n)\triangleq\{L^{(i)}(n); i=1,...,I\}$. The field radiated by the RA, $\mathbf{E}(\theta,\varphi;\ f)$, is given by [7,14,15]:

$$\mathbf{E}(\theta,\varphi;\ f)=\sum_{n=1}^{N^2}\{[\mathcal{R}(\theta_n,\varphi_n;\ f)+\mathcal{S}(\theta_n,\varphi_n;\ f,\mathbf{L}(n))]\cdot\mathbf{E}_F(\theta_n,\varphi_n;\ f)\exp(jk_0\mathbf{r}_n\cdot\hat{\mathbf{r}})\},\quad(1)$$

where f is the working frequency, $\hat{\mathbf{r}}\triangleq(\sin\theta\cos\varphi,\ \sin\theta\sin\varphi,\cos\theta)$, $\mathbf{r}_n=(\alpha_n,\beta_n,0)$ is the location of the nth patch element, $k_0=(2\pi c_0)/f$ is the free-space wavenumber (c_0 being the speed of light), and (θ_n,φ_n) are the elevation angle and the azimuth one of the direction of incidence from the feed to the nth element, $\mathcal{R}(\theta_n,\varphi_n;\ f)=\{R_{xy}(\theta_n,\varphi_n;\ f);\ x,y=\{\theta,\varphi\}\}$ is the plane wave reflection matrix, $\mathcal{S}(\theta_n,\varphi_n;\ f,\mathbf{L}(n))=\{S_{xy}(\theta_n,\varphi_n;\ f,\mathbf{L}(n));\ x,y=\{\theta,\varphi\}\}$ is the scattering matrix, respectively, while,

$$\mathbf{E}_F(\theta_n,\varphi_n;\ f)=\frac{|\mathbf{r}_F|}{|\mathbf{r}_n-\mathbf{r}_F|}\frac{E_F(\theta_n,\varphi_n;\ f)}{E_F(0,0;\ f)}\times\exp(jk_0|\mathbf{r}_n-\mathbf{r}_F|-|\mathbf{r}_F|)[\cos\varphi_n\boldsymbol{\theta}+\sin\varphi_n\boldsymbol{\varphi}],\quad(2)$$

is the field pattern radiated by the feed on the nth element, $\mathbf{r}_F$ and $E_F(\theta,\varphi,f)$ being the feeder position and the element factor, respectively. We can see that the scattering matrix $\mathcal{S}(\theta_n,\varphi_n;\ f,\mathbf{L}(n))$ is largely dependent on the shape of the RA cells, exhibits a high degree of nonlinearity, and has no closed-form expression [15] that can be directly utilized. In this case, we need to find an evaluation function $\tilde{S}(\boldsymbol{z})$, that maps the input space $\mathbb{Z}$ to a high-dimensional space in which the linear function $\mathcal{S}(\mathbf{z})$ can be used to accurately perform the regression. To be exact, it is to find an evaluation function such that $\tilde{S}(\boldsymbol{z})\approx S(\boldsymbol{z})$, $\mathbf{z}\in\mathbb{Z}$, where $\mathbf{z}$ is the input vector of I+3 dimension which is defined by the incidence angles θ and φ, the working frequency f and the geometric parameters of I DoFs. The definition of input space $\mathbb{Z}$ is as follows:

$$\mathbb{Z}\triangleq\{\theta\in[\theta_{\min},\theta_{\max}];\varphi\in[\varphi_{\min},\varphi_{\max}];\ f\in[f_{\min},f_{\max}];\ L^{(i)}\in[L^{(i)}_{\min},L^{(i)}_{\max}]\}\ (i=1,...,I).\quad(3)$$

III. RESPONSE PREDICTION OF UNIT CELL BASED ON SVR

In this work, SVR is applied to find a surrogate model [16] to accommodate the inputs of the RA antenna unit cells. In order to find the mapping between the input $\mathbf{z}$ and the EM response output function $\tilde{S}(\boldsymbol{z})$, the elevation θ, the azimuth φ, the working frequency f, and the I DoFs of the array element are first discretized in A $[\theta_a=\theta_{\min}+(a-1)\Delta\theta;\ a=1,\ldots,A;\ \Delta\theta=(\theta_{\max}-\theta_{\min})/(A-1)]$, B $[\varphi_b=\varphi_{\min}+(b-1)\Delta\varphi;\ b=1,...,B;\ \Delta\varphi=(\varphi_{\max}-\varphi_{\min})/(B-1)]$, C $[f_c=f_{\min}+(c-1)\Delta f;\ c=1,\ldots,C;\ \Delta f=(f_{\max}-f_{\min})/(C-1)]$, and D $[L^{(i)}_{l_i}=L^{(i)}_{\min}+(d_i-1)\Delta L^{(i)},\ d_i=1,...,D_i;\ i=1,...,I;\Delta L^{(i)}=(L^{(i)}_{\max}-L^{(i)}_{\min})/(D_i-1)]$ quantized values, respectively (D indicates the total number of patch geometric shapes after removing the overlapping part of the ring patch). In this way, an FW simulation is performed for each mth $(m=1,...,M,\ M=A\times B\times C\times D)$ unit cell. Given an input $\mathbf{z}_m$ $[\mathbf{z}_m\triangleq[\theta_a,\varphi_b,f_c,\mathbf{L}_d]$, corresponding output $\mathcal{S}(\mathbf{z}_m)$ will be obtained, aiming at establishing the *sample set* $\mathcal{Q}\triangleq\{\mathbf{z}_m,\mathcal{S}(\mathbf{z}_m)\ ;\ m=1,...,M\}$ required for SVR training model. Although FW simulation can be used to calculate function $\mathcal{S}(\mathbf{z})$ simply and accurately, since the number of LUTs increases exponentially with the increase of DoFs [6], it is necessary to consider the storage and calculation time $T^{\mathrm{FW}}_{\mathrm{all}}$ of the simulation of unit cells with complex shapes ($T^{\mathrm{FW}}_{\mathrm{all}}\triangleq M\times T^{\mathrm{FW}}_{\mathrm{sin}}$, $T^{\mathrm{FW}}_{\mathrm{sin}}$ is the time taken to calculate a single $\mathcal{S}$ matrix).

To solve the problem of database storage and computing time, the machine learning method based on SVR is proposed in this paper. Getting an accurate prediction of the output $\tilde{S}(\boldsymbol{z})$, a certain number of samples should be randomly selected from the *sample set* simulated by FW for SVR learning, which is called

the *training set* $\mathcal{T} \triangleq \{\mathbf{z}_k, \mathrm{S}(\mathbf{z}_k); k = 1,...,K\}$. After the corresponding relationship between input and output is established by SVR, the EM response of the RA can be obtained quickly and accurately given any test data that is not in the training sample.

In the next section, the performance of the RA EM response estimation problem is also evaluated from the aspects of calculation error and time saved. The matrix norm error Ξ_1 and the phase mean squared error Ξ_2 are given by [7,17]:

$$\Xi_1 \triangleq \frac{1}{R}\sum_{r=1}^{R}\frac{\left\|\mathcal{S}^{\mathrm{SVR}}(\mathbf{z}_r)-\mathcal{S}(\mathbf{z}_r)\right\|^2}{\left\|\mathcal{S}(\mathbf{z}_r)\right\|^2}, \tag{4}$$

where $\mathcal{S}$ denotes the exact FW-computed scattering matrix, $\|\cdot\|$ being ℓ_2-norm, $R = M - K (r = 1,...,R)$ indicates the number of samples in the *testing set*, and,

$$\Xi_2 = \frac{1}{4R}\sum_{r=1}^{R}\sum_{\{x,y\}=\{\theta,\varphi\}}\left|\frac{1}{\pi}\arg\left[\frac{\mathcal{S}_{\mathrm{xx}}^{\mathrm{SVR}}(\mathbf{z}_r)}{\mathcal{S}_{\mathrm{xx}}(\mathbf{z}_r)}\right]\right|^2, \tag{5}$$

where the π normalization accounts for the fact that the phase is expressed in radians, whereas the coefficient 1/4 refers to the four entries of the scattering matrix. These metrics can quantitatively evaluate the prediction accuracy of method (4) and its reliability in estimating the phase of the scattering matrix (5) [7,17]. Another noteworthy evaluation factor is the computational efficiency, that is, the time saved by SVR compared to the FW simulation, given by:

$$\Delta T \triangleq 1 - \left|\frac{T_{\mathrm{train}}^{\mathrm{SVR}} + T_{\mathrm{test}}^{\mathrm{SVR}}}{T_{\mathrm{set}}^{\mathrm{FW}}}\right|, \tag{6}$$

where $T_{\mathrm{set}}^{\mathrm{FW}} \triangleq R \times T_{\mathrm{sin}}^{\mathrm{FW}}$ is the time for FW-computing the R items of *testing set*, $T_{\mathrm{train}}^{\mathrm{SVR}}$ is the time for the SVR training process, and $T_{\mathrm{test}}^{\mathrm{SVR}}$ (can be ignored) is the time for the SVR testing process.

Plus, two important evaluation indicators used for regression analysis, the determination coefficient (R^2) and the root mean square error (RMSE) are defined as follows:

$$R^2 = 1 - \frac{\sum_r^R \left(S^{\mathrm{SVR}}(\mathbf{z}_r) - S(\mathbf{z}_r)\right)^2}{\sum_r^R \left(S(\mathbf{z}_r) - \mathrm{mean}(S(\mathbf{z}_r))\right)^2}, \tag{7}$$

$$\mathrm{RMSE} = \sqrt{\frac{1}{R}\sum_r^R \left(S^{\mathrm{SVR}}(\mathbf{z}_r) - S(\mathbf{z}_r)\right)^2}, \tag{8}$$

where mean(·) represents the average.

IV. NUMERICAL RESULTS

In this paper, the scattering matrix of a RA element printed on a single-layer dielectric substrate with lattice period is studied, in which the thickness of the dielectric substrate is 1.524*mm*, the complex relative permittivity is $\varepsilon_r = 2.2 - j1.98\times10^{-2}$ ($\mathbf{d}_1 = (\lambda_0/3)\mathbf{x}$, $\mathbf{d}_2 = (\lambda_0/3)\mathbf{y}$ [see Fig. 2], λ_0 being the wavelength at the central frequency f_0), and the patch shape is multiple concentric square metal slots [i.e., the "Squared Phoenix" cell] [1,9,18]. The EM response calculation of the RA characterized by I = 4 DoFs is first discretized according to the following steps — $\theta_{\min} = 0$ [deg], $\theta_{\max} = 40$ [deg], $A = 5, \varphi_{\min} = 0$ [deg], $\varphi_{\max} = 45$ [deg], $B = 4$, $f_{\min} = 0.9 f_0$, $f_{\max}$ =1.1f_0, $C = 3$, $L_{\min}^{(1)} = 0.10\lambda_0$, $L_{\max}^{(1)} = 0.30\lambda_0$, $L_{\min}^{(2)} = 0.09\lambda_0$, $L_{\max}^{(2)} = 0.25\lambda_0$, $L_{\min}^{(3)} = 0.04\lambda_0$, $L_{\max}^{(3)} = 0.2\lambda_0$, $L_{\min}^{(4)} = 0.03\lambda_0$, $L_{\max}^{(4)} = 0.15\lambda_0$, $D_i = 5$ ($i = 1,...,I$). Excluding the overlapping parts of the concentric metal slots, the total number of geometric shapes is D = 120. The training samples required for the SVR are obtained by CST simulation modeling. Through CST simulation modeling, the total number of items in the *sample set* $\mathcal{Q}$ is M=7200.

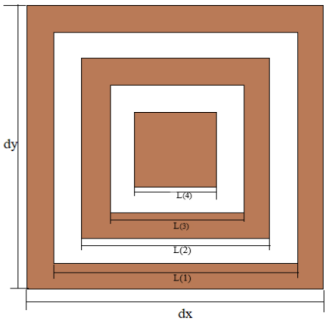

Fig. 2. Geometry of I=4 "Square Phoenix" unit cell.

The 7200 data generated by the FW simulation were divided into two subsets: a *training set* consisting of 6000 samples and a *testing set* which consists of 1200 samples. The inputs of SVR are the elevation θ_a, the azimuth φ_b, the frequency f_c, and I DoFs of geometric shapes, and the outputs are the magnitude, the phase, the real part and the imaginary part of the co-polarization $S_{\theta\theta}(\mathbf{z})$ and cross-polarization $S_{\theta\varphi}(\mathbf{z})$, respectively. The LIBSVM library [19] with the Gaussian kernel is used to get the SVR model. Two important parameters involved in SVR strategy—the penalty factor C and γ (γ is the parameter that comes with the kernel function), can be obtained by cross-validation and mesh parameter optimization [20], as shown in Table 1.

Table 1: The penalt factor C and $1/\gamma$ of SVR obtained by cross-validation

	Co-polarization		Cross-polarization	
	C	$1/\gamma$	C	$1/\gamma$
Magnitude	18	0.707	816	1.212
Phase	724	0.128	924	2.507
Real part	141	0.500	544	0.771
Imaginary part	364	0.911	512	0.354

Under the same conditions, the RBF method with simple network topology and fast learning speed is used as a comparison to illustrate the effectiveness of the proposed method. This paper calls the NEWRB toolbox function built in MATLAB to predict the EM response of RA antenna unit cell. Given that RBF and SVR are modeled under the same conditions, the maximum number of neural units in the RBF hidden layer is the total number of training data sets.

For verifying the validity of the proposed method, a sample that is not belong to $\mathcal{T}$ is randomly selected for numerical verification. Figures 3 (a) and 3 (b) show the plots of the magnitude and phase of $S_{\theta\theta}(\mathbf{z})$ versus the elevation θ when $f = f_0$ and φ=45 [deg], $L^{(1)} = 0.19\lambda_0$, $L^{(2)} = 0.16\lambda_0$, $L^{(3)} = 0.07\lambda_0$, $L^{(4)} = 0.05\lambda_0$. We can observe from the plot, compared with the RBF prediction method, as the elevation angle changes, the SVR is closer to the true value in predicting the scattering magnitude and phase.

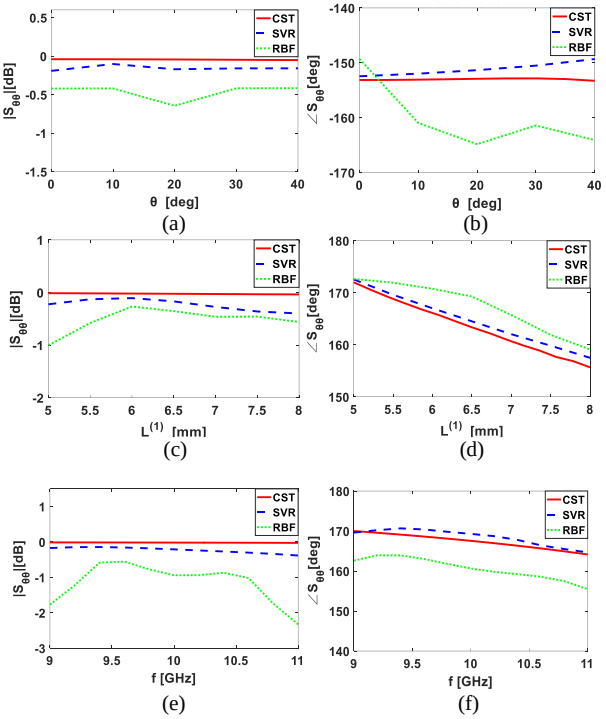

Fig. 3. Behavior of (a), (c), and (e) magnitude and (b), (d), and (f) phase of $S_{\theta\theta}(\mathbf{z})$ versus changes in (a) and (b) elevation angle θ, (c) and (d) element size [i.e., $L^{(1)}$], and (e) and (f) frequency.

The same consideration is given to the magnitude and phase of the EM response vary with the cell size [Figs. 3 (c), (d)] and frequency [Figs. 3 (e), (f)] of the element (where θ is 0 [deg]), we can see from the plots that the prediction results of SVR are also more accurate than that of RBF. As we expected, in these comparisons, using SVR to predict the EM response of a RA antenna element with a complex shape is significantly better than the predicted value of RBF in terms of prediction accuracy.

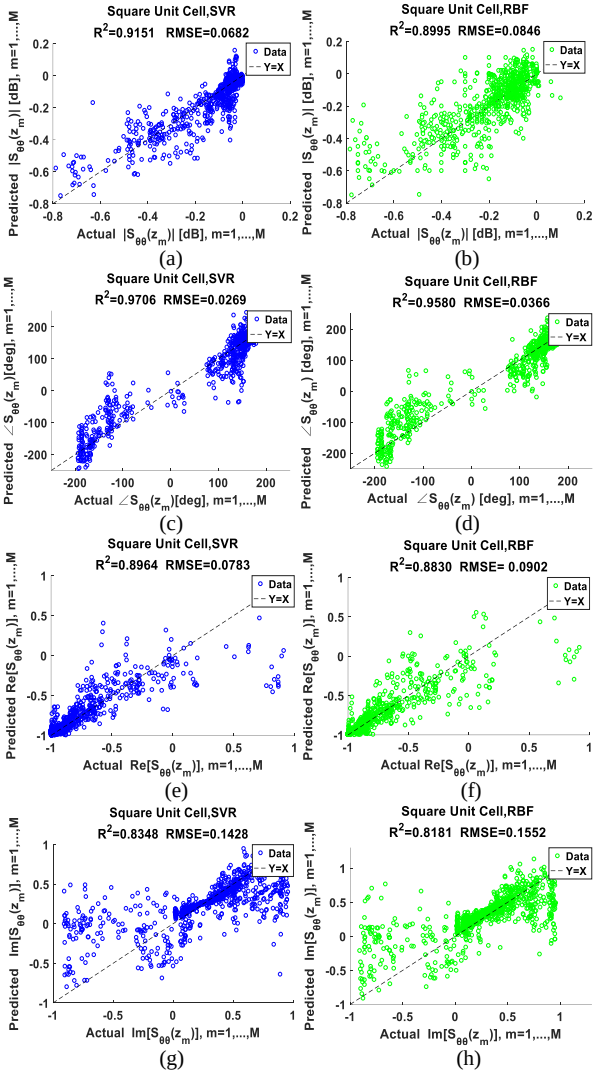

Fig. 4. Actual versus estimated values of (a) and (b) $|S_{\theta\theta}(\mathbf{z}_m)|$, (c) and (d) $\angle S_{\theta\theta}(\mathbf{z}_m)$, (e) and (f) $\mathrm{Re}[S_{\theta\theta}(\mathbf{z}_m)]$, and (g) and (h) $\mathrm{Im}[S_{\theta\theta}(\mathbf{z}_m)], m = 1,\ldots,M$, when using (a), (c), (e), and (g) SVR and (b), (d), (f), and (h) RBF prediction method.

Owing to the scattering coefficient is a complex number, the magnitude and phase of the scattering coefficient can be directly obtained from the real part and the imaginary part. Therefore, with purpose of further evaluating the enthusiasm of the SVR, it is also necessary to establish a training model of the real part and the imaginary part of the scattering coefficient by using SVR. Figure 4 shows the scatter plots of the magnitude [Figs. 4 (a), (b)], the phase [Figs. 4 (c), (d)],

the real part [Figs. 4 (e), (f)], and the imaginary part [Figs. 4 (g), (h)] of $S_{\theta\theta}(\mathbf{z}_m), m=1,...,M$, with the line Y = X representing the ideal bisector. The more concentrated the scatter is on the ideal bisector, the higher the accuracy predicted. From the scatter distribution in Fig. 4 and the determination coefficient R^2 and RMSE calculated by formulas (7) and (8), we can see that the SVR can accurately predict the EM response of RA antenna element with complex shapes, which are closer to the ideal bisector than the RBF ones [Figs. 4 (b), (d), (f), and (h)]. In addition, $\Xi_1^{\mathrm{SVR}}=0.0788$ and $\Xi_2^{\mathrm{SVR}}=0.0223$ versus $\Xi_1^{\mathrm{RBF}}=0.0862$ and $\Xi_2^{\mathrm{RBF}}=0.0477$, calculated by formulas (4) and (5) can be more explained. It is worth mentioning that SVR greatly improves the calculation efficiency of the EM response of the RA, $\Delta T^{\mathrm{SVR}}=0.15$ ($T_{\mathrm{sin}}^{\mathrm{FW}}\approx 1.20\times 10^{2}[\mathrm{s}]$) can be obtained from formula (6), that is to say, 15% time is saved compared with FW simulation. Similarly, time savings using the RBF method can also be obtained, $\Delta T^{\mathrm{RBF}}=0.70$, 70% time is saved (The training time of RBF is $T_{\mathrm{train}}^{\mathrm{RBF}}\approx 4.32\times 10^{4}[\mathrm{s}]$). From the perspective of quantitative indicators, in terms of time savings, there is no doubt that the SVR is more time-saving than the FW simulation in predicting EM response of the RA, but it is slightly inferior to the RBF, because the SVR needs to use mesh parameter optimization and cross-validation to find the optimal values of C and γ , while RBF is not needed.

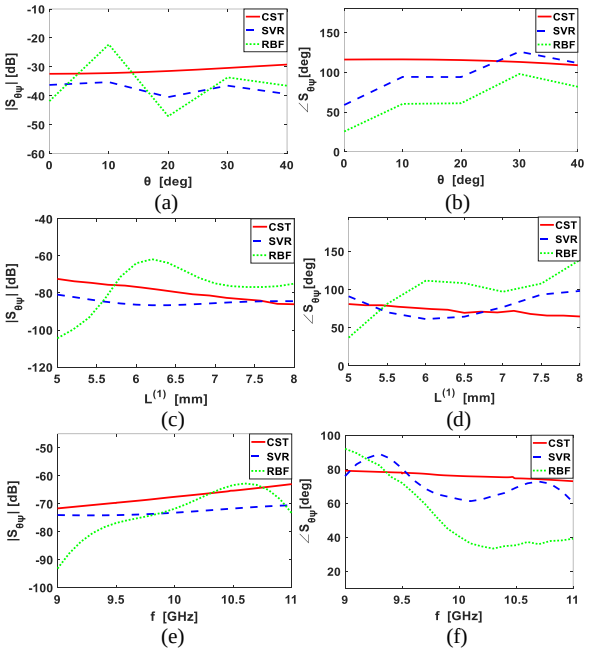

Fig. 5. Behavior of (a), (c), and (e) magnitude and (b), (d), and (f) phase of $S_{\theta\varphi}(\mathbf{z})$ versus changes in (a) and (b) incidence angle θ, (c) and (d) element size [i.e., $L^{(1)}$], and (e) and (f) frequency.

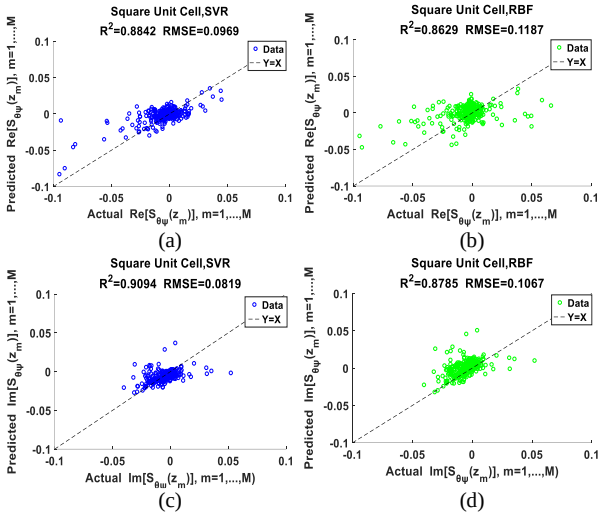

Fig. 6. Actual versus estimated values of (a) and (b) $\mathrm{Re}[S_{\theta\varphi}(\mathbf{z}_m)]$, and (c) and (d) $\mathrm{Im}[S_{\theta\varphi}(\mathbf{z}_m)], m=1,...,M$, when using (a) and (c) SVR, and (b) and (d) RBF prediction method.

Cross-polarization component $S_{\theta\varphi}(\mathbf{z}_m), m=1,...,M$ is also very important for the performance analysis of RA antenna. We can clearly see from the Figs. (5) and (6) that the RBF results deviate significantly from the ideal curve for both the curve that varies with a single input variable (Fig. 5) or the scatter cloud (Fig. 6), and the proposed method is significantly better than the predicted value of RBF. Similarly, the corresponding prediction errors of $S_{\theta\varphi}(\mathbf{z}_m), m=1,...,M$ can be obtained from formulas (4) and (5), namely $\Xi_1^{\mathrm{SVR}}=0.1021$ and $\Xi_2^{\mathrm{SVR}}=0.1764$ versus $\Xi_1^{\mathrm{RBF}}=0.1288$ and $\Xi_2^{\mathrm{RBF}}=0.1953$. Although the cross-polarization scattering characteristics of the "*Square Phoenix*" unit cells are weaker than the co-polarization scattering characteristics [18], from these quantitative indicators and Fig. 5 and Fig. 6, it is sufficient to prove the applicability of the proposed method to the EM response prediction of complex RA antenna elements.

V. CONCLUSION

In this letter, an effective and accurate prediction methodology, a machine learning method based on SVR is proposed to predict the EM response of complex RA antenna elements. The original arbitrary number of DoFs passive EM scattering problems is transformed into a regression estimation problem, and scattering model is established by using SVR through appropriate offline training, which overcomes the problems of traditional FW simulation and database. The calculation of the magnitude and phase of the scattering coefficient shows that the SVR and the FW simulation results are in good agreement (see Fig. 3), even for the cross-coefficient (see

Fig. 5), although they are highly nonlinear, which is very difficult to model. Through the quantitative calculation of equations (4) and (5), it is strongly demonstrated that compared with the ANNs algorithm based on RBFN, the EM response of complex RA antennas can be predicted more accurately by SVR. Although the time saved by SVR is second to RBFN, it is also more efficient than the FW simulation algorithm. With flexible tradeoff accuracy and computational efficiency, SVR can provide reliable, accurate and fast estimation of EM response, and providing an effective way to solve EM scattering problems.

ACKNOWLEDGMENT

This work was supported by the National Natural Science Foundation of China under Grant 61771008.

REFERENCES

[1] R. Deng, F. Yang, S. Xu, and M. Li, "A low-cost metal-only reflectarray using modified slot-type Phoenix element with 360◦ phase coverage," *IEEE Trans. Antennas Propag*., vol. 64, no. 4, pp. 1556-1560, Apr. 2016.

[2] J. Huang and J. A. Encinar, *Reflectarray Antennas*. Piscataway, NJ, USA: Wiley, 2008.

[3] D. R. Prado, M. Arrebola, M. R. Pino, R. Florencio, R. R. Boix, J. A. Encinar, and F. Las-Heras, "Efficient crosspolar optimization of shaped- beam dual-polarized reflectarrays using full-wave analysis for the antenna element characterization," *IEEE Transactions on Antennas and Propagation*, vol. 65, no. 2, pp. 623-635, 2017.

[4] R. Florencio, R. R. Boix, and J. A. Encinar, "Enhanced MoM analysis of the scattering by periodic strip gratings in multilayered substrates," *IEEE Trans. Antennas Propag*., vol. 61, no. 10, pp. 5088-5099, Oct. 2013.

[5] F. Gunes, S. Nesil, and S. Demirel, "Design and analysis of Minkowski reflectarray antenna using 3-D CST Microwave Studio-based neural network model with particle swarm optimization," *Int. J. RF Microw. Comput. Eng*., vol. 23, no. 2, pp. 272-284, Mar. 2013.

[6] L. Marnat, R. Loison, R. Gillard, D. Bresciani, and H. Legay, "Accurate synthesis of a dual linearly polarized reflectarray," in Proc. *3rd Eur. Conf. Antennas Propag. (EuCAP)*, Berlin, Germany, pp. 2523-2526, 2009.

[7] M. Salucci, L. Tenuti, G. Oliveri, and A. Massa, "Efficient prediction of the EM response of reflectarray antenna elements by an advanced statistical learning method," *IEEE Trans. Antennas Propag.*, vol. 66, no. 8, pp. 3995-4007, Aug. 2018.

[8] M. de Berg, O. Cheong, M. van Kreveld, and M. Overmars, *Computational Geometry: Algorithms and Applications*. Santa Clara, CA, USA: Springer-Verlag, 2008.

[9] R. Deng, S. Xu, F. Yang, and M. Li, "Single-layer dual-band reflectarray antennas with wide frequency ratios and high aperture efficiencies using Phoenix elements," *IEEE Trans. Antennas Propag*., vol. 65, no. 2, pp. 612-622, Feb. 2017.

[10] C. Shan, X. Chen, H. Yin, W. Wang, G. Wei, and Y. Zhang, "Diagnosis of calibration state for massive antenna array via deep learning," *IEEE Wireless Communications Letters*, vol. 8, no. 5, pp. 1431-1434, Oct. 2019.

[11] J. Cai, C. Yu, J. Xia, L. Sun, S. Chen, B. Pan, J. Su, and J. Liu, "Support Vector Regression Based Behavioral Model for Load Mismatched PAs," *2019 IEEE International Symposium on Radio-Frequency Integration Technology (RFIT)*, Nanjing, China, pp. 1-3, 2019.

[12] H. M. Yao, W. E. I. Sha, and L. Jiang, "Two-step enhanced deep learning approach for electromagnetic inverse scattering problems," *IEEE Antennas and Wireless Propagation Letters*, vol. 18, no. 11, pp. 2254-2258, Nov. 2019.

[13] V. Richard, R. Loison, R. Gillard, H. Legay, and M. Romier, "Loss analysis of a reflectarray cell using ANNs with accurate magnitude prediction," in *11th European Conference on Antennas and Propagation (EuCAP)*, Paris, France, pp. 2402-2405, Mar. 2017.

[14] D. M. Pozar, S. D. Targonski, and H. D. Syrigos, "Design of millimeter wave microstrip reflectarrays," *IEEE Trans. Antennas Propag.*, vol. 45, no. 2, pp. 287-296, Feb. 1997.

[15] P. Rocca, L. Poli, N. Anselmi, M. Salucci, and A. Massa, "Predicting antenna pattern degradations in microstrip reflectarrays through interval arithmetic," *IET Microw., Antennas Propag*., vol. 10, no. 8, pp. 817-826, Mar. 2016.

[16] A. I. J. Forrester, A. Sóbester, and A. J. Keane, *Engineering Design via Surrogate Modelling: A Practical Guide*. New York, NY, USA: Wiley, 2008.

[17] Y. Mao, S. Xu, F. Yang, and A. Z. Elsherbeni, "A novel phase synthesis approach for wideband reflectarray design," *IEEE Trans. Antennas Propag*., vol. 63, no. 9, pp. 4189-4193, Sep. 2015.

[18] L. Moustafa, R. Gillard, F. Peris, R. Loison, H. Legay, and E. Girard, "The Phoenix cell: A new reflectarray cell with large bandwidth and rebirth capabilities," *IEEE Antennas Wireless Propag. Lett.*, vol. 10, pp. 71-74, Jan. 2011.

[19] C.-C. Chang and C.-J. Lin, "LIBSVM: A library for support vector machines," *ACM Trans. Intell. Syst. Technol*., vol. 2, no. 3, pp. 27:1-27:27, Apr. 2011, software available at http://www.csie.ntu.edu.tw/_cjlin/libsvm

[20] G. C. Cawley and N. L. C. Talbot, "Efficient leave-one-out cross-validation of Kernel fisher discriminant classifiers," [J]. *Pattern Recognition*, vol. 11, 2003.

Performance and Analysis of UWB Aesthetic Pattern Textile Antenna for WBAN Applications

T. Annalakshmi [1] and S. Ramesh [2]

[1] Department of Electronics and Communication Engineering
New Prince Shri Bhavani College of Engineering and Technology, Chennai – 600074, Tamil Nadu, India
lakshmishanmu15@gmail.com

[2] Department of Electronics and Communication Engineering
SRM Valliammai Engineering College, Kattankulathur, Chennai - 603203, Tamil Nadu, India
rameshs.ece@valliammai.co.in

Abstract ─ This article proposes a new aesthetic pattern-three petal flower patch antenna that operates at Ultra Wide Band (UWB) for Wireless Body Area Network (WBAN) applications. The flower structure consists of three petals and a center circle patch with the partial ground plane at the bottom. A double-sided copper-coated conductive fabric, which is 0.08 mm thick, having a surface resistivity of 0.05 Ω/square, serves as the antenna patch and ground material. This conductive patch is placed in a denim jeans material with 1mm thick that forms the substrate. The utilization of a two-layer substrate and partial ground method enhances the impedance bandwidth of the antenna. The size of the antenna is 60 mm × 60 mm × 2.16 mm. The reflection coefficient, gain, efficiency, radiation pattern, and effects of bending were the various parameters analyzed for the flower antenna. The antenna radiates from 3 to 12 GHz, which covers the entire UWB frequency range from 3.1 to 10.6 GHz assigned by Federal Communications Commission (FCC). The measurement results validate the performance of a flower patch antenna.

Index Terms ─ Aesthetic pattern, laser-cut fabrication, partial ground, thick substrate, UWB, WBAN.

I. INTRODUCTION

The Market revenue of wearable devices is expected to leap at quadruple pace and reach $150 bn by the year 2026. Smart clothing segment, within wearable devices, have dynamic development, with fitness and fashion collaborating to create unique applications and trends within this segment [1, 2]. Ease in the availability of data, IoT, and acceptance at large wearable devices further boost this segment's growth. Wearable devices need to be of an adept design and created with ease; they need to be in-vogue, be captivating and irresistible and need to deliver the intent. Flexibility and breaking the norm on geometric patterns of the underlying technology of wearable devices is the way to enable them to be designed and created to be appealing to the masses across age groups and geography. This paper intends to prove that the fabrication of the antenna can be customized and designed to adapt to work in the UWB frequency range. It is most adapted for the fast-developing WBAN applications while retaining technical capabilities and reliability [3, 4].

Several kinds of research have been undertaken on enhancing the bandwidth of antenna for wearable applications. Some of the essential and noteworthy investigations have been cited below for reference: in [5], to cover the ultra-wideband, a Y shaped monopole antenna with the etched inverted bell-shaped slot in the partial ground was proposed. In [6], devoted a wearable antenna operates from 3.2-16.3 GHz. They introduced a Co- Planner Waveguide (CPW) structure with slots on the ground plane to increase bandwidth. In [7, 8], to improve the bandwidth, multiple resonators and slots were used. In [9], a multi-stacked patch is used with CPW feed to increase the bandwidth. In [10], combinations of parasitic patches are used for broadening the frequency range. In [11], the broadband was realized by combining the zeroth-order resonator (ZOR) structure with a micro strip patch. In [12], making edge truncation in the radiator and partial ground plane wideband is achieved. A rectangular slot antenna with reduced ground size and offset feeding is proposed to enhance the bandwidth [13]. A fractal antenna with a partially modified elliptical ground was designed to cover frequency from 1.4 to 20 GHz [14]. In [15], dual-band is achieved by the reactive loading in the form of a shorting pin and two arc-shaped slots introduced in the patch. In [16], to cover the UWB range, a lengthy slot, and the partial ground was used. In [17], the flower-shaped patch antenna designed with CPW feeding to achieve wideband impedance matching. Several kinds of patch and slot antennas were reported for UWB application in recent years [18-20].

Submitted On: May 25, 2020
Accepted On: October 20, 2020
https://doi.org/10.47037/2020.ACES.J.351211

1054-4887 © ACES

Based on these various cited studies and its results, the new aesthetic pattern-three petal flower patch antenna with the partial ground in a thick substrate with low dielectric constant material that operates at UWB has been introduced. It can be used in real-time wearable WBAN applications such as health monitoring, physical training, and navigation. This antenna has been designed using wearable technology to be applied to cloth, which will easily reach the masses. This article consists of four sections. Section II elaborates on the antenna geometry and fabrication method. In Section III, discussed the antenna result and its performance. Section IV presents the conclusion.

II. ANTENNA DESIGN

A. Antenna geometry

Figures 1 (a) and (b) depict the three petals flower textile antenna geometry and side view and simulated using CST Microwave Studio to utilize the finite integration technique. Using a three-point spline curve method, the flower shape antenna is formed, which is available in the CST-microwave studio 16 software.

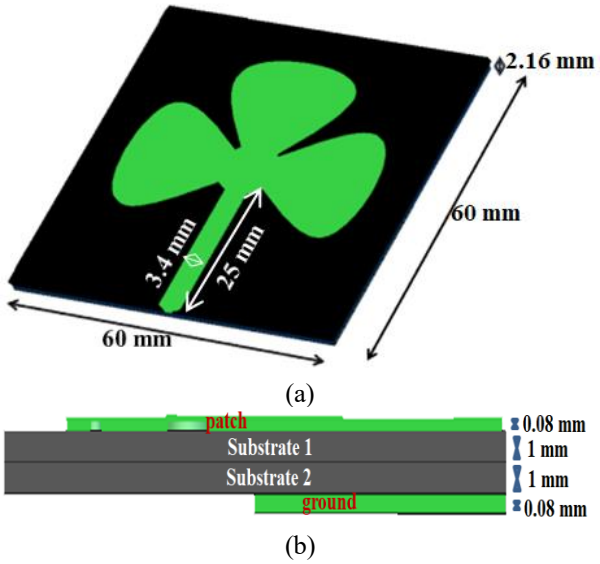

Fig. 1. (a) Antenna geometry and (b) side view of the proposed antenna.

The top layer of the antenna acts as a patch, consisting of three petals, a circle at the center, and a feed line. Table 1 gives the dimension of the flower patch. The X and Y-axis represent the orientation of every petal. The radius of the center circle is 5 mm, and the length and width of the feed line are 25 mm, 3.4 mm, respectively. The patch is made up of double-sided copper conductive fabric. The surface resistivity of the conductive fabric is 0.05 Ω/square. Its base material is polyester and coated with copper and nickel, while the thickness is 0.08 mm.

Table 1: The dimension of petals

	Xmin	Xmax	Ymin	Ymax
	Dimensions in mm			
Petal1	-10.84	10.84	34	52.89
Petal2	-22.89	-4	19.15	40.84
Petal3	4	22.89	19.15	40.84

Table 2: Component of conductive fabric

Component	Composition (%)
Polyester	70 ± 3
Copper	16± 5
Nickel	14 ± 2

Table 2 depicts the material basis and content of the conductive fabric. As the microstrip antenna has inherent narrow band characteristics, two methods have been explored to increase the bandwidth. In the first method, there is an increase in the substrate thickness with lower dielectric constant material. Thick substrates with a smaller range of dielectric constant are the most desired as they provide higher bandwidth and efficiency [21]. In general, the dielectric constant of textiles material has low value and reduces the surface wave losses. Here a denim jean material is used as a substrate with dielectric constant of 1.7, loss tangent of 0.025 with a thickness of 1mm [22]. The thickness of the denim jeans material is measured using a vernier caliper. To increase the thickness, two layers are sandwiched and serve as a thick intermediate substrate. The dimension of the substrate is 60 × 60 mm. In the second method, there is a reduction in ground size in half of the substrate size for bandwidth improvement. The bottom layer serves as a ground. The dimension of the ground is 60 × 30 mm in length and width. It is made up of copper coated fabric, which is the same as patch material.

B. Fabrication method

The antenna has been fabricated using flexible copper fabric material and shaped using a laser cutting machine [23]. Laser cutting is suitable for metal, plastic, paper, and fabric. The conductive fabric is cut to appropriate dimensions at the bottom and top layer to make the antenna resonate at the corresponding band using the laser machine SENFNNG –SF1610. A laser cutting machine works by focusing a beam of laser light on a piece of material. The laser light is highly powered when it is focused, and it raises the temperature of the material to be cut high enough to melt it in the small area where the beam is focused. The laser's head is moved using some form of the gantry to position the beam to cut shapes over the material. The laser cutting process uses a contactless beam to generate heat, causing the fabric to melt and vaporize the workspace. The weakening and removal of

the affected area of the material form the desired cut without causing any damages. The advantages of laser cutting are extreme accuracy, clean cuts, and sealed fabric edges to prevent fraying. The precisely cut flower pattern fabric and ground fabric are attached to a denim substrate using fabric glue. This antenna will be produced to custom specification and shipped to the cloth manufacturing unit, where it can be attached to the cloth by simple sewing method.

Front and back view of the fabricated antenna shown in Figs. 2 (a) and (b). A microstrip feed line is used to excite the flower patch using a 50 Ω SMA connector. In real-time scenarios, the existing microstrip line in the cloth and a flexible co-axial cable connects to the radio equipment, which acts as the transceiver [24]. Simple snaps used across the clothing industry can be used as the connector between the microstrip line and co-axial cable [25]. This will ease the work of the end-user creating a simple fastener to make or break the connection as required. The advantages of the snaps are cheap, easy to fix, and withstand wear and tear due to washing.

(a) (b)

Fig. 2. The fabricated antenna: (a) front view and (b) back view

III. RESULT AND DISCUSSIONS

The antenna was exposed to free space and near the human body environment to study the following parameters such as reflection coefficient, radiation pattern, gain, efficiency, and bending performance. The Gustav Voxel model available in the CST software was used for the simulation of an on-body environment [22]. Fig. 3 depicts the picture of on body model where the antenna is placed on the chest.

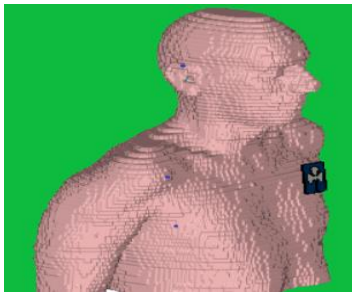

Fig. 3. Antenna placed on the chest of Gustav Voxel model.

A. Reflection coefficient

The measurement of reflection coefficient (S11) obtained using a vector network analyzer (VNA) in the frequency range of 0 to 22 GHz. A connection of VNA to a PC with interfacing software calibrates the S11 in short-open load through (SOLT) standards. Figure 4 shows the reflection coefficient characteristics of the antenna measured on free space and the on-body simulated environment when plotted against free space simulation. In the simulation, the antenna produces the impedance bandwidth of 9 GHz from 3 to 12 GHz frequency range, which covers the entire UWB band. On the other hand, the measured and on-body simulated result shows the same bandwidth with a slight variation in the level of reflection coefficient. The difference between simulation and measurements were observed in the found result. The difference in the reflection coefficient in the free space environment may be due to errors during the fabrication as the prototype is flexible, losses in SMA connector used, and due to the cable losses and connection repeatability with the feeding cable. Similarly, in the on-body simulation, the loss could be due to an on-body structure. The simulation and the measured result show that the antenna fulfills the bandwidth requirement of the UWB band.

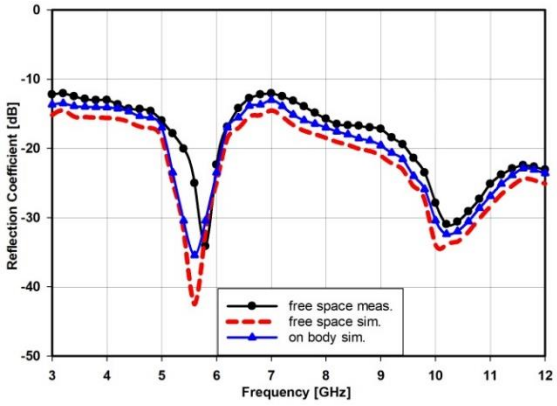

Fig. 4. Reflection coefficient comparison for simulation and measurement values.

B. Gain and efficiency

The gain and efficiency response of the proposed antenna is shown in Fig. 5. From the graph, we observe that the gain varies in the range of -1.29 dB (3 GHz) to 2.35 dB (12 GHz) whereas the measured gain lies in the range of -2.22 dB (3 GHz) to 1.35 dB (12 GHz) over the operating frequency band. In real measurement, antenna gain is calculated using the anechoic chamber. It uses the pyramidal horn as the transmitting antenna, which produces 15 dB gain in the frequency range of 600 MHz to 18 GHz. The proposed antenna acts as a receiver antenna kept with a distance of 5.7 m from the transmitter antenna. Similarly, in the on-body simulation the gain

value varies from -1.79 dB (3 GHz) to 1.8 dB (12 GHz). The gain of the flower antenna measured from the chamber and on-body simulations are in good agreement with free space simulated gain over the entire operating band. Besides, it is observed that the simulated radiation efficiency in free space lies in the range of 0.69 to 0.76 and 0.65 to 0.71 in on-body simulation over the entire operating frequency range.

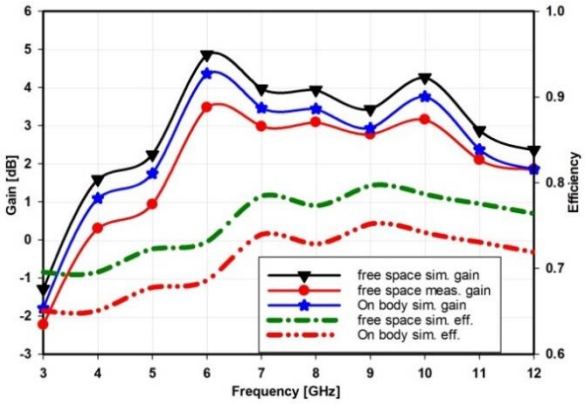

Fig. 5. The gain and efficiency response of the proposed antenna.

C. Radiation pattern

Figure 6 shows the radiation pattern measurement setup in E-plane and H-plane directions using the fully shielded anechoic chamber. The chamber's working frequency ranges from 700 MHz to 18 GHz with a dimension of 5.7 m × 3.5 m × 3 m. The study of the radiation pattern of the proposed antenna in the H plane and E plane directions at 4, 7, and 10 GHz is shown in Figs. 7 (a), (b) and (c). The value of phi is 0° for all theta values to arrive at the radiation pattern in the E plane. Similarly, to attain the H plane's radiation pattern, phi has been set as 90° for all theta's values. In all the specified frequencies, the H-plane pattern shows that the radiation pattern is bidirectional. In E-plane, the radiation is omnidirectional. It is observed that in both planes, there is a proper matching between free space. On-body simulation, and measured patterns in the predetermined frequencies.

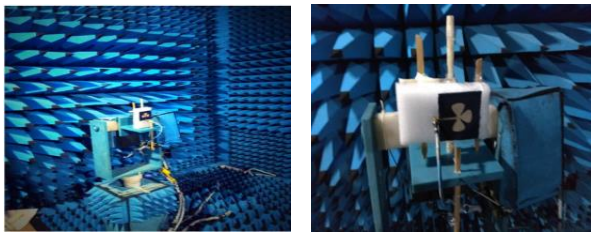

(a) (b)

Fig. 6. Radiation pattern setup in chamber: (a) H-plane direction and (b) E-plane direction.

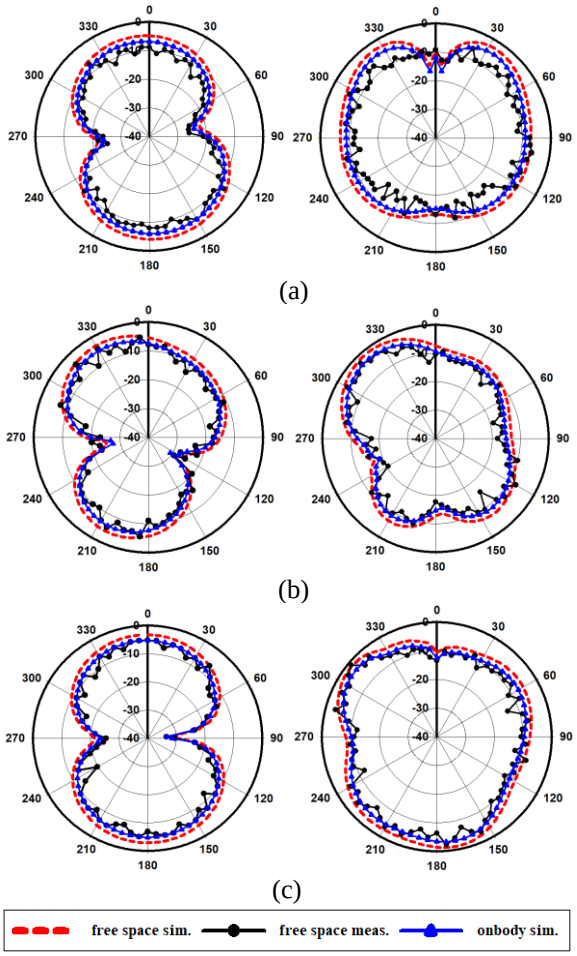

Fig. 7. Simulated and measured radiated pattern in H-plane direction (left) and E-plane direction (right) for: (a) 4 GHz, (b) 7 GHz, and (c) 10 GHz.

D. Bending performance

WBAN applications should have the inherent capacity to retain their technical features even when they are bent, as they expect to align with the body movement of the person who would be wearing them.

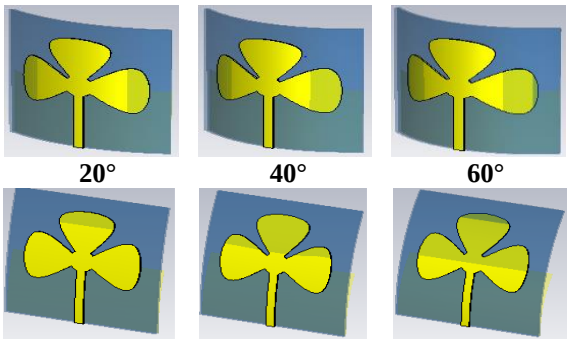

Fig. 8. Antenna bending at E-plane direction (top row), H-plane direction (bottom row) in various angle.

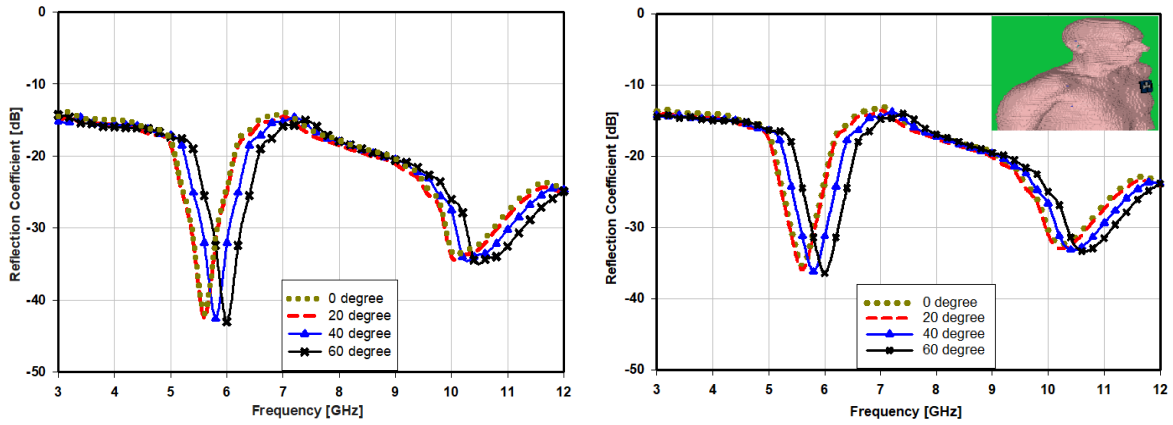

Fig. 9. Bending performance at E-plane direction: (a) free space simulation and (b) on-body simulation.

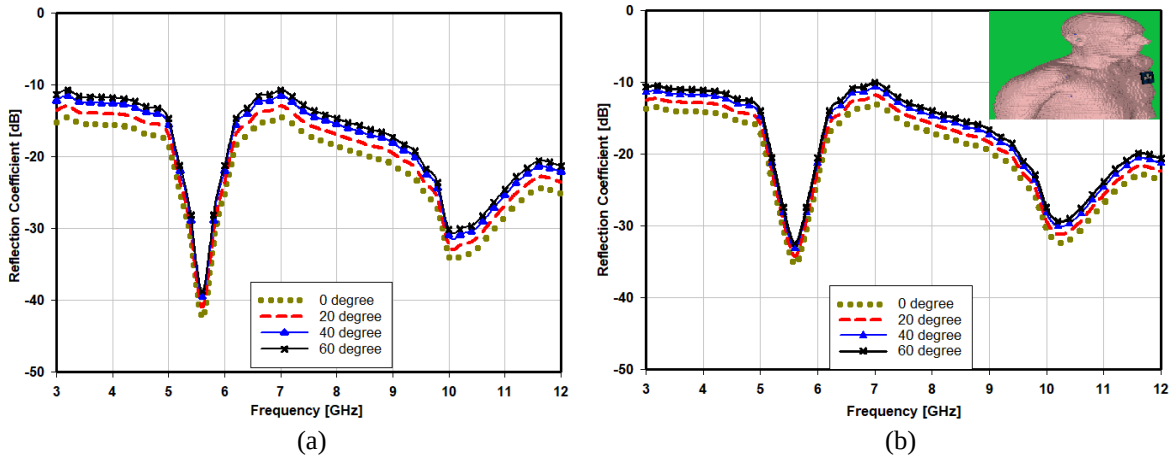

Fig. 10. Bending performance at H-plane direction: (a) free space simulation and (b) on-body simulation.

There were three bending angles considered for the study in E and H-plane direction. Figure 8 shows antenna bending in E-plane and H-plane direction at 20°, 40°, and 60° angles. In Figs. 9 and 10 the simulated reflection coefficient characteristics of the antenna is studied at various angles on both free space and on body simulation environment. The reflection coefficient of flower antenna with different angles was compared with 0° angle (flat antenna) in E-plane and H-plane directions. In both bending directions for 20°, 40°, and 60°, the antenna provides the required bandwidth from 3 to 12 GHz in free space and on-body environment. From the results, we can say that the proposed antenna is working as expected in all bending conditions, and the reflection coefficient was found identical for all angles compared to the flat antenna. Only a small fluctuation was found at a higher bending angle of 60° in both directions due to the impedance transition direction.

E. Surface current

Figure 11 depicts the surface currents of the proposed flower antenna. The surface current shows the actual electric current that is induced by an applied electromagnetic field. From the figure, we see that the current distribution is equal in all the three petals, the maximum surface current is 31.3 A/m. From the direction of current distribution, we observe that the antenna is vertically polarized.

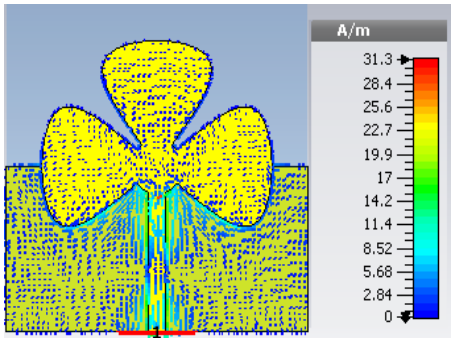

Fig. 11. The surface current of proposed antenna.

IV. CONCLUSION

The Aesthetic pattern patch antenna has been designed to operate at UWB frequency, which supports WBAN application. This antenna has been fabricated with commonly available daily wear jean material as a substrate using a simple fabrication technique, which makes it very cost-effective and robust. The patch and ground are also made using copper fabric. Both materials are very flexible and more comfortable for regular wearable purposes. The attractive flower shape patch inspires the people to wear. The proposed antenna provides sufficient reflection coefficient, gain, and efficiency in the operating band.

Furthermore, it produced excellent radiation characteristics in simulation and measurements. The radiation pattern of the proposed antenna in the H-plane is bidirectional, and in E-plane, it provides an omni-directional pattern. Also, the antenna works well in E and H-plane bending direction. These features make the antenna aptly suited for real-time wearable WBAN applications such as health monitoring, physical training, and navigation. The application of this antenna can range from simple day to day applications to sophisticated medical devices and military applications with the explosion of IoT.

ACKNOWLEDGMENT

The authors wish to acknowledge DST-FIST supporting facilities in the department of Electronics and Communication Engineering, SRM Valliammai Engineering College, Chennai, Tamil Nadu, India.

REFERENCES

[1] J. Tak and J. Choi, "An all textile Louis Vuitton logo antenna," *IEEE Antennas and Wireless Propagation Letters*, vol. 14, pp. 1211-1214, 2015.

[2] G. W. Whittow and M. J. Rigelsford, "Performance and radiation patterns of aesthetic and asymmetric logo-based patch antennas," *Journal of Electromagnetic Waves and Applications*, vol. 28, pp. 848-860, 2014.

[3] A. Mersani, L. Osmman, and I.-M. Ribero, "Flexible UWB AMC antenna for early stage skin cancer identification," *Progress in Electromagnetics Research*, vol. 80, pp. 71-81, 2019.

[4] R. Bala, R. Singh, A. Marwaha, and S. Marwaha, "Wearable graphene based curved patch antenna for medical telemetry applications," *ACES Journal*, vol. 31, no. 5, pp. 543-550, May 2016.

[5] P. Sambandam, M. Kanagasabai, S. Ramadoss, R. Natarajan, M. G. N. Alsath, S. Shanmuganathan, M. Sindhadevi, and S. K. Palaniswamy, "Compact monopole antenna backed with fork slotted EBG for wearable applications," *IEEE Antennas and Wireless Propagation Letters*, vol.19, pp. 228-232, 2020.

[6] S. M. H. Varkiani and M. Afsahi, "Compact and ultra-wideband CPW-fed square slot antenna for wearable applications," *AEÜ International Journal of Electronics and Communications*, vol. 106, pp. 108-115, 2019.

[7] B. V. B. R. Simorangkir, A. Kiourti, and P. K. Esselle, "UWB wearable antenna with full ground plane based on PDMS embedded conductive fabric," *IEEE Antennas and Wireless Propagation Letters*, vol. 17, pp. 493-496, 2018.

[8] W. Yao, H. Yang, X. Huang, and Z. Yu, "A four-leaf clover shape MIMO antenna for UWB applications," *ACES Journal*, vol. 31, no. 12, pp. 1421-1425, Dec. 2016.

[9] A. L. Y. Poffelie, P. J. Soh, S. Yan, and A. E G. Vandenbosch, "A high fidelity all-textile UWB antenna with low back radiation for off-body WBAN applications," *IEEE Transactions on Antennas and Propagation*, vol. 64, no. 2, pp. 757-760, 2016.

[10] B. P. Samal, P. J. Soh, and A. E. G. Vandenbosch, "UWB all-textile antenna with full ground plane for off-body WBAN communications," *IEEE Transactions on Antennas and Propagation*, vol. 62, no. 1, pp. 102-107, 2014.

[11] K. Sun, L. Peng, Q. Li, X. Li, and X. Jiang, "Compact Zeroth-order resonance loaded microstrip antenna with enhanced bandwidth for wireless body area networks/brain activity detection," *ACES Journal*, vol. 33, no. 6, pp. 631-640, June 2018.

[12] S. Mohandoss, S. K. Palaniswamy, R. R. Thipparaju, M. Kanagasabai, B. R. B. Naga, and S. Kumar, "On the bending and time domain analysis of compact wideband flexible monopole antennas," *AEÜ International Journal of Electronics and Communications*, vol. 101, pp. 168-181, 2019.

[13] K. Shafique, A. B. Khawaja, A. M. Tarar, M. B. Khan, M. Mustaqim, and A. Raza, "A wearable ultra-wideband antenna for wireless body area networks," *Microwave and Optical Technology Letters*, vol. 58, no. 7, pp. 1710-1715, 2016.

[14] M. Karimyian-Mohammadabadi, M. A. Dorostkar, F. Shokuohi, M. Shanbeh, and A. Torkan, "Super-wideband textile fractal antenna for wireless body area networks," *Journal of Electromagnetic Waves and Applications*, vol. 29, no. 13, pp. 1728-1740, 2015.

[15] B. V. B. R. Simorangkir, Y. Yang, L. Matekovits, and P. K. Esselle, "Dual-band dual-mode textile antenna on PDMS substrate for body-centric communications," *IEEE Antennas and Wireless Propagation Letters*, vol. 16, pp. 677-680, 2016.

[16] N. Chahat, M. Zhadobov, R. Sauleau, and K. Ito, "A compact UWB antenna for on-body

applications," *IEEE Transactions on Antennas and Propagation*, vol. 59, no. 4, pp. 1123-1131, Apr. 2011.
[17] S. R. Patre and P. S. Singh, "CPW-fed flower-shaped patch antenna for broadband applications," *Microwave and Optical Technology Letters*, vol. 57, no. 12, pp. 2908-2913, 2015.
[18] M. NejatiJahromi, M. N. Jahromi, and M. Rahman, "A new compact planar antenna for switching between UWB, narrow band and UWB with tunable-notch behaviors for UWB and WLAN applications," *ACES Journal*, vol. 33, no. 4, pp. 400-406, Apr. 2018.
[19] Z.-L. Song, Z.-J. Zhu, and L. Cao, "High isolation UWB-MIMO compact micro-strip antenna," *ACES Journal*, vol. 33, no. 3, pp. 293-297, Mar. 2018.
[20] S. Ramesh and J. Jayalakshmi, "Compact fractal wearable antenna for wireless body area communication," *Telecommunication and Radio Engineering*, vol. 79, no. 1, pp. 71-80, 2020.
[21] A. C. Balanis, *Antenna Theory, Analysis and Design*. John Wiley and Sons Inc., New York, 1997.
[22] I. Gil and R. Fernández-García, "Wearable PIFA antenna implemented on jean substrate for wireless body area network," *Journal of Electromagnetic Waves and Applications*, vol. 31, pp. 1194-1204, 2017.
[23] N. Chahat, M. Zhadobov, S. A. Muhammad, L. L. Coq, and R. Sauleau, "60-GHz textile antenna array for body-centric communications," *IEEE Transactions on Antennas and Propagation*, vol. 61, no. 4, pp. 1816-1824, Apr. 2013.
[24] A. Sabban, "Active compact wearable body area networks for wireless communication, medical and IoT applications," *Applied System Innovation*, vol. 1, no. 46, 2018.
[25] T. Kellomaki, "Snaps to connect coaxial and microstrip lines in wearable systems," *International Journal of Antenna and Propagation*, vol. 2012, 10 pages, 2012.

T. Annalakshmi received her B. Tech. in Electronics and Communication Engineering from Pondicherry University in the year of 2002, M.E. in Communication Systems from Anna University in the year of 2011, and currently pursuing her Ph.D. in the Department of Electronics and Communication Engineering, SRM Valliammai Engineering College, Chennai. Her research interest includes Antennas & Propagation and Wireless Communications. She is currently working as an Associate Professor in the Department of Electronics and Communication Engineering, New Prince Shri Bhavani College of Engineering and Technology, Chennai with 13 years of experience. She is life time member in ISTE and ISRD.

S. Ramesh received his B.E. in Electronics and Communication Engineering from University of Madras, M.Tech. in Communication Engineering from VIT University, Vellore and received his Ph.D. degree on from SRM University, Chennai, in 2001, 2004 & 2015 respectively. He is currently working as an Associate Professor in the Department of Electronics and Communication Engineering, SRM Valliammai Engineering College, Chennai with experience of 16 years. He is a senior member (S'10-M'17-SM'18) of IEEE Antennas & Propagation Society, Life member in IETE, ISTE, SEMCE, BES. He authored papers in reputed journals and international/national conferences. His area of interest includes Antennas & Propagation and Wireless Communications. He is guiding research scholars in the field of antennas & RF Filter under Anna University, Chennai. He is associated with IEEE AP-S Madras chapter as a member in executive committee during 2018-2019 and IEEE MTT-S Madras Chapter for the year 2017.

Design of Frequency Reconfigurable Patch Antenna for Sensing and Tracking Communications

Priya Anumuthu[*1], Kaja Mohideen Sultan [1], Manavalan Saravanan [3], Mohd Tarmizi Ali [4], Manikandan Kandadai Venkatesh [1], Mohammad Ghouse Khaderbasha Saleem [1], and Imaduddeen Valathoor Nizamuddeen [1]

[1] Department of Electronics and Communication Engineering
B.S. Abdur Rahman Crescent Institute of Science and Technology, Chennai, India
priyamarish@crescent.education, kajamohideen@crescent.education,
manikandankv.92@gmail.com, mdghouse.hbk@gmail.com, er.imaduddeen@gmail.com

[3] Department of Electronics and Communication Engineering
Vel Tech Rangarajan Dr. Sagunthala R&D Institute of Science and Technology, Chennai, India
msarawins@ieee.org

[4] Fakulti Kejuruteraan Elektrik,Universiti Teknologi MARA, Shah Alam, Malaysia
mizi732002@salam.uitm.edu.my

Abstract ─ This paper presents a front-end structure of a reconfigurable patch antenna for cognitive radio systems. The antenna structure consists of an Ultra-wideband (UWB) sensing antenna and an array of frequency reconfigurable antennas incorporated on the same substrate. The UWB and reconfigurable antennas are fed by co-planar waveguides (CPW). The reconfigurability is achieved by rotating the series of patch antennas through a certain angle and the rotation is controlled by mechanical means using an Arduino microcontroller. The rotational reconfigurability has been preferred over MEMS switches, PIN diodes, and other lumped elements because the latter requires the need for bias lines. The entire structure is designed using High Frequency Structure Simulator (HFSS) software and the prototype is fabricated over FR-4 substrate having a thickness of 1.6mm and measurements are carried out. This antenna achieves a wideband frequency from 2 GHz to 12 GHz and distinct narrow band of frequencies by reconfigurability using single antenna consisting of different shapes spaced accurately to ensure isolation between adjacent frequency bands and each antenna element working for a bandwidth of 2 GHz for frequency from 2 GHz to 12 GHz upon a single substrate and the reconfigurable elements are controlled using a low cost Arduino microcontroller connected directly to the antenna which ensures accurate controlling of the rotation and fast switching between the antenna elements. The measured results agree with the simulated results and have less than 10 dB impedance bandwidth.

Index Terms ─ CPW feed, mechanical control, reconfigurable antenna, sensing applications, tracking applications, UWB antenna.

I. INTRODUCTION

Cognitive radio (CR) is touted as the future of RF communication systems. It can be the perfect solution for spectrum scarcity and spectral traffic. According to the Federal Communications Commission (FCC), "a cognitive radio is a radio that can change its transmitter parameters based on interaction with the environment in which it operates." In order to change the transmission parameters, an antenna should have the ability to sense its vicinity. Hence a more generalized architecture for the CR system involves the use of a UWB sensing antenna and frequency reconfigurable antenna arrays. The UWB sensing antenna continuously monitors the spectrum to identify the spectrum with the least traffic (white spaces) and adjusts its transmission parameters to communicate in that spectrum. This dependency on the reconfigurable antennas has made it one of the hot topics for research. A large amount of work has been carried out in designing antenna structure for cognitive radio systems. The proposed design is inspired by [1] in which a CR system is implemented by incorporating both UWB sensing and reconfigurable antennas on the same substrate. The reconfigurability is achieved through the rotation. The proposed design varies extensively in terms of the design, material used and the technique of controlling the rotational movement. The antenna is

Submitted On: June 10, 2020
Accepted On: September 26, 2020
https://doi.org/10.47037/2020.ACES.J.351212

1054-4887 © ACES

designed over an FR-4 substrate with a CPW feeding structure. This was preferred over a microstrip feed line as presented in [1] to enhance the bandwidth response considering a low-cost substrate material. Detailing of different types of reconfigurable antennas and different methods to achieve reconfiguration has been explained in [2]. Achieving frequency reconfigurability by providing DC bias through a RLC coupled DC line circuit is exploited in [3]. A polarization and frequency reconfigurable patch antenna in which the reconfigurability is achieved through mechanical rotation of the radiating element is explained in [4] and a frequency reconfigurable antenna achieved through rotation with 4 different shapes in [5].The challenges involved in designing a CR system and the general architecture of a CR system has been described in [6]. An Insight on the design approaches for a CR system is also presented. In [7], a combination of wideband and narrowband antennas designed over the same substrate is presented. The wideband antenna is a CPW fed printed hour-glass shaped monopole which operates from 3 to 11GHz. The narrowband antenna is a microstrip patch printed on the reverse side of the substrate and connected to the wideband antenna via a shorting pin and designed to operate from 5.15 to 5.35 GHz. Reconfigurability in frequency can be obtained either by making uses of switches (MEMS, LASER diodes) or by rotational motion. Many works have been carried out in both of these categories. In [8] the authors have used MEMS switches to switch on parts of the antenna structure enabling it to tune to frequencies between 5 and 7 GHz. [9] takes another approach by rotating the reconfigurable antennas by 180° enabling it to work in 4 GHz and 6.65 GHz. Saravanan and Rangachar [10-11], demonstrated reconfigurable antenna using pin diodes operating at S-band. Lin and Wong [12] presented a polarization reconfigurable antenna by reconfiguring feeding network through sequential excitation by means of pin diodes in the feed network. A most common method of achieving polarization reconfiguration is by etching a slot on radiating element and reconfiguring it by means of pin diodes [13]. Polarization diversity by bridging the slot gap with diode switches is achieved in [14].

II. ANTENNA STRUCTURE

The antenna is designed over an FR-4 substrate of dimension 100 × 60 × 1.6 mm^3 with a dielectric constant of 4.4. The antenna structure is shown in Fig. 1. It can be divided into two separate modules. The first being a UWB sensing antenna present at the left of the substrate and the next is an array of patch antennas placed inside a circle of radius 24 mm.

A. Wideband sensing antenna structure

The sensing antenna is a UWB sensing antenna fed by a CPW feed line. The UWB antenna takes the shape of a planar INVERTED C Antenna (PICA) as shown in Fig. 2. It uses a CPW feed having width of 4 mm and a gap of 0.3 mm between the microstrip line and the ground plane. This feed line ensures impedance matching at the ports (50Ω). The UWB sensing antenna has a bandwidth of about 10 GHz enabling it to scan an entire spectrum from 2─12 GHz.

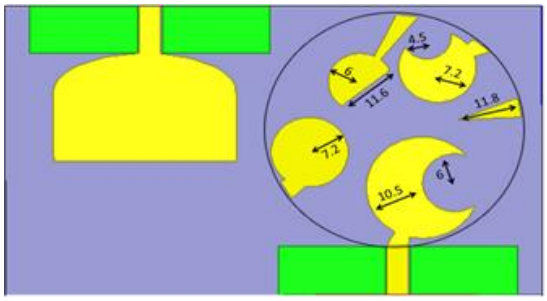

Fig. 1. Antenna structure.

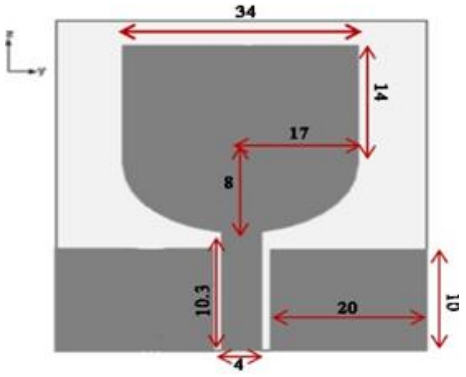

Fig. 2. UWB antenna structure (dimensions in mm).

B. Reconfigurable antenna structure

The reconfigurable antenna structure is designed to the right of the sensing antenna as shown in Fig. 1. It is sufficiently isolated from the sensing antenna by placing the input ports diagonally opposite to each other thereby minimizing the coupling between the two ports. The reconfigurable antenna was designed with proper tuning and spacing between each antenna element to ensure complete isolation and reduced coupling to avoid adjacent band interference. The arrays of patch antennas are placed inside a circle of radius 24 mm. The various patch antennas when rotated by a certain angle gets excited by the feeding system. Each patch resonates at certain frequency spanning across the entire spectrum as defined by the sensing antenna. A thick conductive lead is soldered to the feed line. The Arduino is programmed in such a way that the particular structure comes in contact with the feed for the respective angle of rotation. Initially the conductive element represented as shape 1 is at 0° which then rotated to an angle of 37° so that the shape 2 conductive patch comes in contact with the

feed. Further by moving shape 2 by 37° using arduino microcontroller the shape 3 conductive element comes in contact with the feed point and start radiating. The Shape 4 conductive patch comes in contact with the feeding system by further rotation of shape 3 by 99° and the shape 5 comes into contact with feed after moving shape 4 at an angle of 60°. The initial position of shape 1 can be regained by further moving shape 5 at an angle of 127°. The various reconfigurable shapes with its angular positions are shown in Fig. 3.

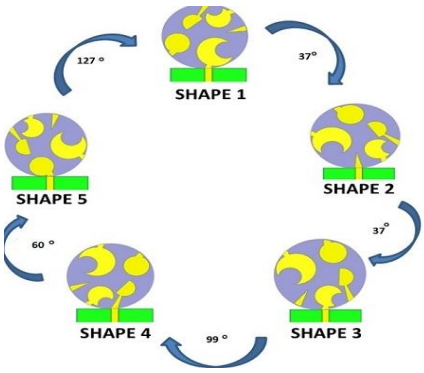

Fig. 3. Reconfigurable positions.

III. RESULTS AND DISCUSSION

The design is modelled and simulated in HFSS. The simulation results and its implication are discussed in this section.

A. Wideband sensing antenna

The UWB sensing antenna is designed as shown in Fig. 2. The performance of the UWB antenna is unaltered for any given position of the reconfigurable antenna. This is due to the fact that the antennas are sufficiently isolated by feeding them diagonally opposite to each other. The S_{11} curve of the wideband sensing antenna is measured using N3916A VNA and the measurement setup is shown below in Fig. 4. It is observed from the return loss plot shown in Fig. 5 that the UWB antenna operates from 2─12 GHz with a bandwidth of about 10 GHz.

Fig. 4. Measurement setup of UWB antenna.

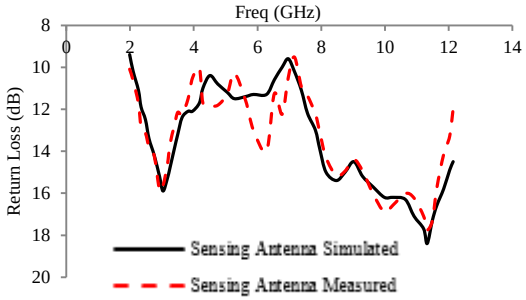

Fig. 5. Return loss - UWB sensing antenna.

The simulated radiation pattern of the UWB antenna for 6 GHz, 8 GHz, and 10 GHz in E-Plane are shown in Fig. 6. The radiation pattern is near omnidirectional over the entire spectrum.

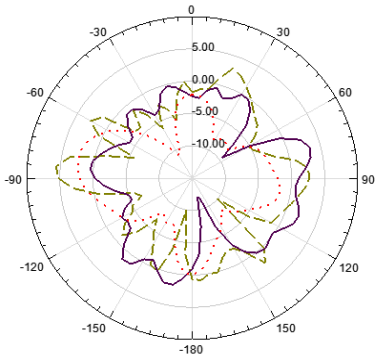

Fig. 6. Simulated UWB antenna radiation pattern at f = 6 GHz (dotted line), f = 8GHz (solid line), f = 10 GHz (dashed line).

The results in Fig. 7 show the measured 3D radiation pattern of the sensing antenna. Figure 7 (a) shows the measured radiation pattern at 6 GHz. Figure 7 (b) shows the radiation pattern measured at 8 GHz and Fig. 7 (c) shows the measured radiation pattern at 10 GHz.

B. Reconfigurable antenna

The simulated and measured return loss with respect to the frequency of the reconfigurable antennas is shown in Fig. 8 (a) and Fig. 8 (b). It is observed from Fig. 8 that, each shape of the reconfigurable antenna corresponds to specific parts of the spectrum adding up to span across the entire UWB. The simulated and measured return loss characteristics shown in Figs. 8 (a) and 8 (b) shows a 10dB impedance bandwidth for all the frequency bands.

Figure 3 shows the various reconfigurable positions. Reconfigurability through rotation was preferred mainly because it doesn't need any external bias or optical pumping as in MEMS switches and laser diodes which are used conventionally. In the simulation, the reconfigurable antenna structure is rotated for the

specified angle as mentioned in Fig. 3. The simulated and measured radiation pattern for the reconfigurable antennas is shown in Fig. 9 and Fig. 10 respectively. Table 1 gives the details, entailing each shape along with the gain of the reconfigurable antennas. Fig. 11 gives gain of the sensing antenna along the entire bandwidth.

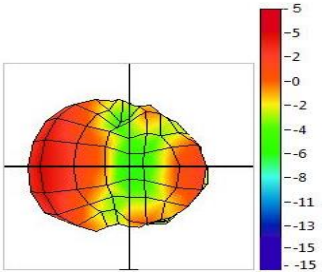

(a) 6 GHz

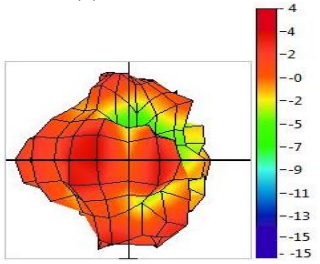

(b) 8 GHz

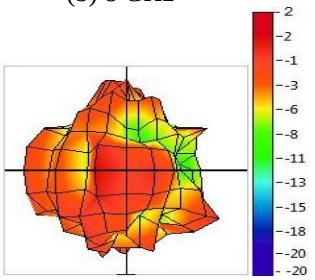

(c) 10 GHz

Fig. 7. 3D measured radiation pattern (UWB sensing antenna).

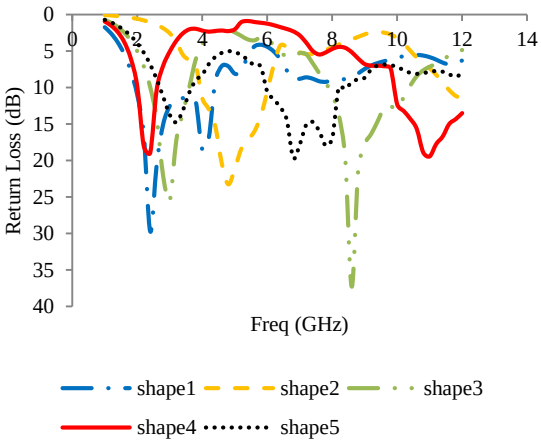

(a) Simulated return loss (dB)

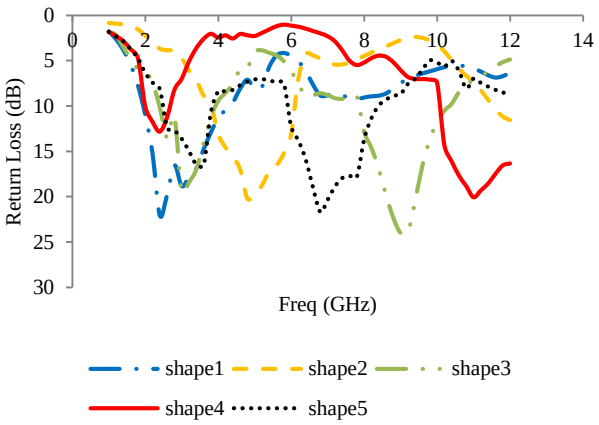

(b) Measured return loss (dB)

Fig. 8. Return loss (dB) at different antenna shapes.

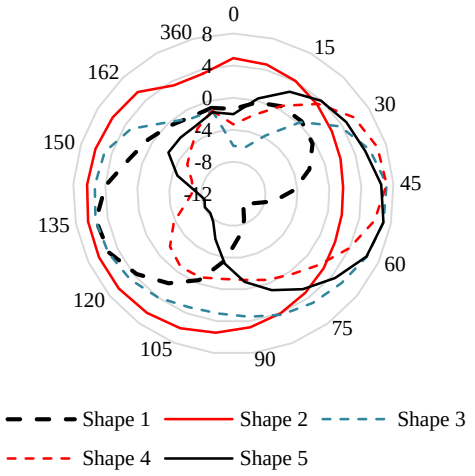

Fig. 9. Simulated 2D radiation pattern of reconfigurable antennas.

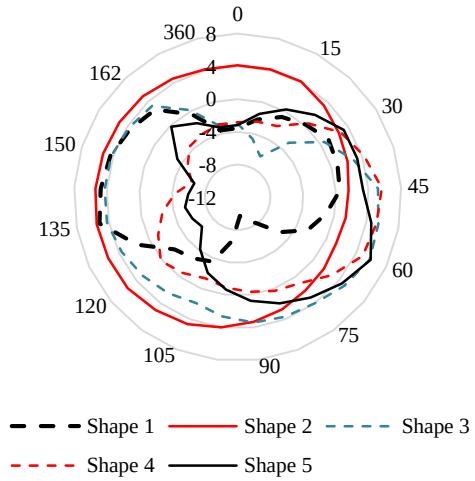

Fig. 10. Measured 2D radiation pattern of reconfigurable antennas.

Table 1: Performance comparison at different shapes

Shapes	Freq Range (GHz)	Bandwidth (GHz)	Simulated Gain (dB)	Measured Gain (dB)
Shape 1	2-4	2	5.2	4.31
Shape 2	4-6	2	6	5.53
Shape 3	8-10	2	7	5.83
Shape 4	10-12	2	5.1	5.23
Shape 5	6-8	2	6.8	5.93

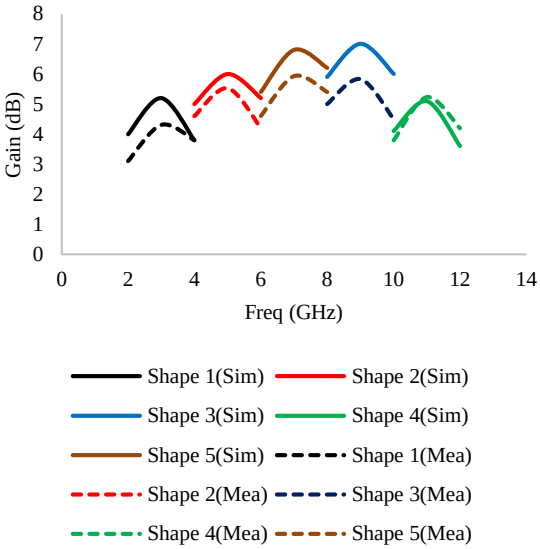

Fig. 11. Gain of the sensing antenna.

The simulated and measured efficiency with respect to the operating band is given in Fig. 12. It is observed that the antenna achieves nearly flat efficiency characteristics over the operating band with a maximum efficiency of 78%.

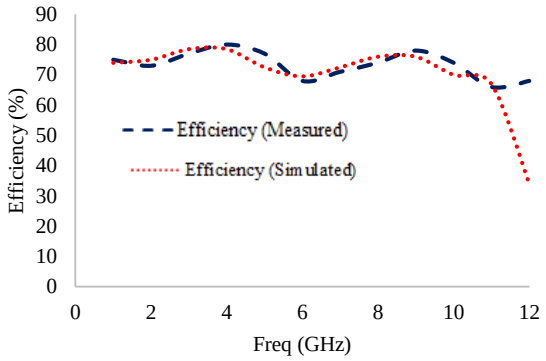

Fig. 12. Efficiency plot.

C. Radiation pattern of the reconfigurable antenna

The radiation pattern measurement is taken in the Anechoic Chamber at the Antenna Research Center (ARC), UiTM, Shah Alam, Malaysia, and the setup is shown in Fig. 13. The prototype is fabricated by rotating the shapes in the simulation. Each prototype has a U shaped wideband sensing antenna along with one reconfigurable antenna connected to the coplanar feed.

All the five reconfigurable shaped prototypes have been tested in the anechoic chamber and one such setup is presented below as an example. It can be noted that the shapes tries to radiate with minimal loss in gain. This is of vital importance to the considered design and its application in cognitive radios.

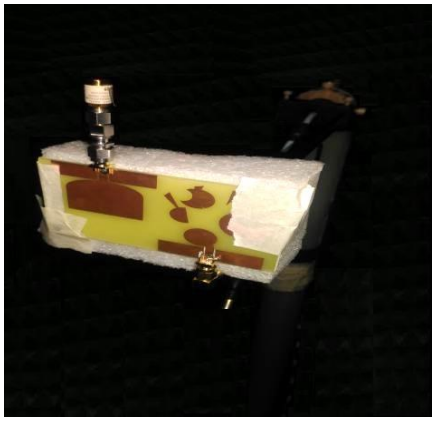

Fig. 13. Radiation pattern measurement setup at ARC, UiTM, Shah Alam, Malaysia.

D. Coupling between the two antenna modules

Since the sensing and the reconfigurable antennas are placed on the same substrate it is essential to avoid interference and minimize the coupling between them. The mutual coupling between the two ports would affect the transmission parameters and hence care has to be taken to keep the coupling at its minimum. As shown in Fig. 14, shows coupling isolation of 15dB was achieved with a peak coupling isolation of 40dB. The min/max coupling between the various shapes of the reconfigurable antenna and the sensing antenna is given in Table 2. The proposed antenna design is compared with other existing antenna designs and the performance comparison is tabulated in Table 3. The proposed antenna structure has a sensing antenna and tracking antenna on a single substrate having Omni-directional pattern for sensing antenna and directional pattern for reconfigurable antennas. The reconfigurable antennas are carefully spaced to avoid interference between one another and hence capable of tracking the white spaces.

E. Reconfigurability through rotation controlled using Arduino Microcontroller

In order to practically realize and to achieve the reconfigurability through the rotation, the prototype antenna is controlled directly using Arduino

Microcontroller which can be easily programmable as per the requirements. The reconfigurable antenna section is connected with the Servo Motor sg90 along with the Servo Motor Shield L293D and it is powered with 5v supply. The servo motor can be rotated to 180° clockwise as well as 180° anticlockwise. The trigger pin is used to control the rotation of servo motor ON/OFF state based on the given input angle. The antenna is mounted in an acrylic platform and the rotating part is mounted in the blades of the servo motor. The experimental setup of rotational reconfigurability is shown in Fig. 15. Initially, the position of the servo motor is in zero degree position. As per the design calculations of the antenna, angular position for the each antenna is known. The Microcontroller has been programmed to rotate in steps based on the angle of separation between the shapes. The antenna position is initially considered as origin angle that is zero degree. The servo motor is fed with the input angle of 37° for the following antenna in the clockwise direction. The servo motor stops the rotation when the feed and the antenna is in contact based on the input angle. After the second antenna it will rotate another 37° to cover the third antenna. After that it will rotate 99° to reach the fourth antenna in the clockwise direction. After that it will come to the initial position and rotate 127° in the anti-clockwise direction to reach the 5th antenna. The servo motor after moving for a certain angle corresponding to a particular reconfigurable antenna stops at a position where the feed and the antenna are in contact. The metal contact has been established between the feed and the reconfigurable shape. The duration of pause between the consecutive antennas is configurable as per the requirement of operation by modifying the delay parameter between each trigger. The time for which the antenna has to be in contact with the feed line is programmed by applying a delay to the servo motor. Since this rotatable antenna does not need any additional software and computer to control the rotational motion of the motor the switching between the antenna elements is faster and hence tracking is faster .The operation continues for the rest of the shapes and the result obtained through rotation is measured using Vector Network analyzer.

Table 2: Coupling isolation between the two modules

Shapes	Max (dB)	Min (dB)
Shape 1	27	15
Shape 2	28	16
Shape 3	35	17
Shape 4	31	15
Shape 5	40	15

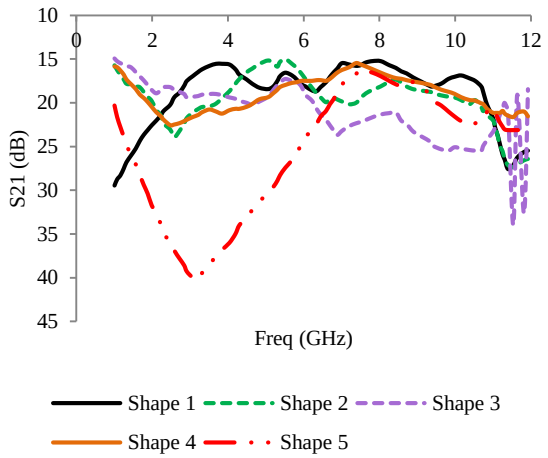

Fig. 14. Coupling isolation between the input ports (S_{21}).

Table 3: Comparison with existing designs

Ref.	Dimension (mm)	Operating Frequency (GHz)	Peak Gain (dB)
[1]	70× 50 × 1.6	2-10	8.45
[3]	50× 60 × 1.6	0.9-2.5	4.742
[4]	30× 30 × 1.6	4.7-5.03	2.73
[5]	50 × 50 × 1.6	2-7	5.9
Proposed work	100 × 60 ×1.6	2-12	5.83

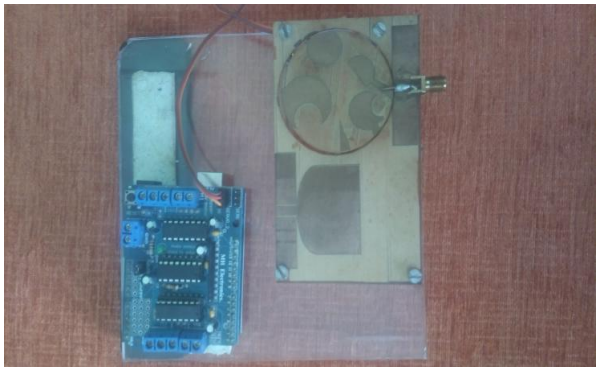

Fig. 15. Experimental setup of rotational reconfigurability using Arduino Microcontroller.

IV. CONCLUSIONS

This paper provides an insight towards designing a rotatable reconfigurable antenna and how it can be used as an RF transceiver for cognitive radio applications. As discussed above a UWB sensing antenna is designed which is operational from 2-12 GHz along with reconfigurable antennas serving the entire spectrum of

UWB. A significant coupling isolation of 15dB is achieved which provides sufficient isolation between the two ports enabling it to function together without performance degradation. Given the obtained results, the proposed structure holds good to serve as a transceiver for a CR system for sensing and tracking applications. In future by adding a GSM module the antenna can be controlled using mobile application.

REFERENCES

[1] Y. Tawk, J. Costantine, K. Avery and C. G. Christodoulou, "Implementation of a cognitive radio front-end using rotatable controlled reconfigurable antennas," *IEEE Transactions on Antennas and Propagation*, vol. 59, no. 5, pp. 1773-1778, May 2011.

[2] C. G. Christodoulou, Y. Tawk, S. A. Lane, and S. R. Erwin, "Reconfigurable antennas for wireless and space applications," in *Proceedings of the IEEE*, vol. 100, no. 7, pp. 2250-2261, July 2012.

[3] H. T. Chattha, M. Hanif, X. Yang, I. E. Rana, and Q. H. Abbasi, "Frequency reconfigurable patch antenna for 4G LTE applications," *Progress in Electromagnetics Research M*, vol. 69, pp. 1-13, 2018.

[4] H. Li, Z. Gong, J. Zhang, J. Ding, and C. Guo, "Dual-layered polarization and frequency reconfigurable microstrip antenna by rotating breach-truncated circular radiator," *International Journal of Microwave and Wireless Technologies*, vol. 9, no. 8, pp. 1705-1712, 2017.

[5] Y. Tawk, J. Costantine, and C. G. Christodoulou, "A frequency reconfigurable rotatable microstrip antenna design," *IEEE Antennas and Propagation Society International Symposium*, pp. 1-4, 2010.

[6] P. Gardner, M. R. Hamid, P. S. Hall, J. Kelly, F. Glianem, and E. Ebrahimi, "Reconfigurable antennas for cognitive radio: Requirements and potential design approaches," *2008 Institution of Engineering and Technology Seminar on Wideband, Multiband Antennas and Arrays for Defense or Civil Applications*, pp. 89-94,2008.

[7] E. Ebrahimi and P. S. Hall, "A dual port wide-narrowband antenna for cognitive radio," *2009 3rd European Conference on Antennas and Propagation*, pp. 809-812, 2009.

[8] H. A. Tarboush, S. Khan, R. Nilavan, H. S. Al-Raweshidy, and D. Budimir, "Reconfigurable wideband patch antenna for cognitive radio," *2009 Loughborough Antennas and propagation Conf.*, pp. 141-144, 2009.

[9] Y. Tawk and C. G. Christodoulou, "A new reconfigurable antenna design for cognitive radio," *IEEE Antennas and Wireless Propagation Letter*s, vol. 8, pp. 1378-1381, 2009.

[10] M. Saravanan and M. J. S. Rangachar, "Circular ring shaped polarization reconfigurable antenna for wireless communications," *Progress in Electromagnetics Research M*, vol. 74, pp. 105-113, 2018.

[11] M. Saravanan and M. J. S. Rangachar, "Polarization reconfigurable square patch antenna for wireless communications," *Advanced Electromagnetics*, vol. 7, no. 4, pp. 103-108, 2018.

[12] W. Lin and H. Wong, "Wideband circular polarization reconfigurable antenna," *IEEE Trans. Antennas Propag.*, vol. 63, no. 12, pp. 5938-5944, 2015.

[13] B. Anantha, L. Merugu, and P. S. Rao, "A novel single feed frequency and polarization reconfigureable microstrip patch antenna," AEU - *International Journal of Electronics and Communications*, vol. 72, pp. 8-16, 2017.

[14] M. Saravanan and M. J. S. Rangachar, "Design of pin loaded reconfigurable patch antenna for wireless communications," *Applied Computational Electromagnetics Society Journal*, vol. 34, no. 10, pp. 1535-1541, 2019.

A Metamaterial Inspired Compact Miniaturized Triple-band Near Field Resonant Parasitic Antenna for WLAN/WiMAX Applications

Si Li [1], Atef Z. Elsherbeni [2], Zhenfeng Ding [3], and Yunlong Mao [1]

[1] School of Electronics and Information
Jiangsu University of Science and Technology, Zhenjiang, Jiangsu 212003, China
lisi0511@just.edu.cn, maoyunlong0511@just.edu.cn

[2] Electrical Engineering Department
Colorado School of Mines, CO 80401 USA
aelsherb@mines.edu

[3] Research Institute of Petroleum Exploration and Development
PetroChina Company Limited, Beijing 100083, China
815703534@qq.com

Abstract ─ This paper presents a metamaterial-inspired triple-band antenna specified for WLAN and WiMAX applications with a compact size of 24mm × 18mm × 1mm (at 2.4 GHz). It consists of a dual-band left-handed metamaterial (LHM) unit surrounded by a G-style monopole antenna. The LHM is first designed and analyzed with equivalent circuits and simulations. A loop antenna based on the LHM unit is designed and simulated to investigate the radiating performance of the LHM unit structure. We also ran simulations for the G-style monopole. Later, the LHM unit is employed as a near-field resonant parasitic (NFRP) element that surrounded by the G-style monopole. A prototype of this antenna is fabricated. Simulations and measurements were carried out and the results match well, identifying good omni-directional radiating performance. Radiation comparisons with the loop antenna and the G-style monopole indicate that due to NFRP, the G-style monopole's pass bands are shifted to lower frequencies to satisfy 2.45 GHz and 5.5 GHz bands requirements, meanwhile the LHM unit structure operates a third pass band of 3.5 GHz. The compact size and good radiation properties of the antenna render it suitable for WLAN/ WiMAX applications.

Index Terms ─ Left-handed metamaterial, miniaturized antenna, WLAN/WiMAX.

I. INTRODUCTION

With the rapid development of wireless communications, the demand for antennas with compact size and multiband property has greatly increased. A lot of investigations were conducted to satisfy the wireless local area network (WLAN) standard of 2.4 GHz to 2.484 GHz / 5.15 GHz to 5.35 GHz / 5.75 GHz to 5.825 GHz, and the World Wide Interoperability for Microwave Access (WiMAX) standard of 3.4 GHz to 3.69 GHz / 5.25 GHz to 5.85 GHz requirements. Various types of miniaturized WLAN / WiMAX antennas have been reported, among which printed monopole antennas have been widely used because of their low cost, light weight and good performance. Such that in [1], F shaped slots were etched on the rectangular radiating patch and a circular disc printed on the other side of the substrate, achieving wide band coverage and good radiating performance; in [2], a high gain dual-band slot antenna was presented based on an ultra wide band slot radiating element.

Recently, metamaterials (MTMs) have arouse great attentions due to their unique properties in antenna designs [3]. Efforts to miniaturize and compactify antennas have employed composite right/left handed transmission lines (CRLH-TLs) and multiple electrically small near-field resonant parasitic (NFRP) elements. However, even though CRLH-TL may brought higher level miniaturization since its zeroth resonance is independent with size, high quality factors make the corresponding operating bands extremely narrow [4-8]. Comparably, NFRP elements can be designed and adjusted independently, thereby offering additional degree of freedom in antenna designs [9, 10]. The operating principle of NFRP is illustrated in Fig. 1. In general, NFRP elements can be divided into 2 categories, i.e., electric-driven and magnetic-driven NFRP [11], depending on how they coupled to antennas. Meander lines [11] and split ring resonators (SRR) [12] are representative NFRP elements reported and significant miniaturization were achieved [13, 14]. Besides, good

Submitted On: July 2, 2020
Accepted On: November 30, 2020
https://doi.org/10.47037/2020.ACES.J.351213

1054-4887 © ACES

radiating performance can also be obtained with improved impedance matching due to NFRP coupling [15].

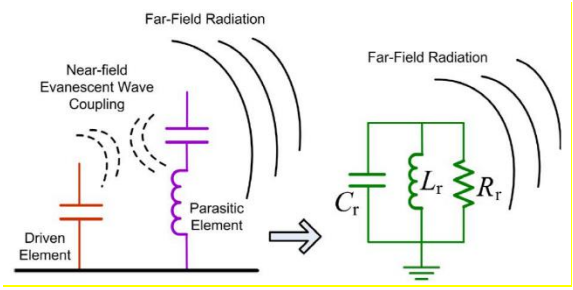

Fig. 1. Illustration of NFRP.

In this paper, a metamaterial-inspired compact miniaturized triple-band NFRP antenna for WLAN/ WiMAX applications is presented. A dual-band left-handed metamaterial (LHM) is first designed and analyzed with equivalent circuits and full-wave simulations. Then this LHM unit is employed as NFRP element that surrounded by a G-style monopole antenna. We investigated the radiating performance of the G-style monopole, a loop antenna based on the designed LHM unit and the final proposed NFRP antenna, figured out that the near-field resonate coupling makes the working bands of the G-style monopole shift to lower frequencies to meet 2.4GHz and 5.5 GHz WLAN/WiMAX requirements, while the LHM unit itself operates additional frequency band from 3.40 GHz to 3.69 GHz. A prototype of the proposed antenna is fabricated and measured, the results match well to the simulated ones, indicating good omni-directional radiating performance at WLAN / WiMAX frequency ranges.

II. LHM DESIGN AND ANALYSIS

A. LHM design

A novel LHM unit is designed, as illustrated in Fig. 2, where metallic strips are printed on a 1 mm-thick FR4 whose relative permittivity is 4.4. Optimized parameters are a = 10 mm, b = 8.3 mm, c = 0.5 mm, w = 1 mm, and the gap g = 0.2mm.

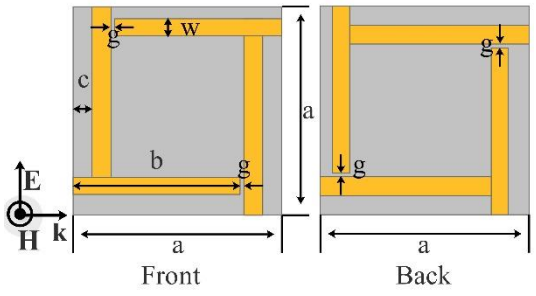

Fig. 2. Structure of the designed LHM unit.

B. Equivalent circuit analysis

The designed LHM is at least capable of generating two magnetic resonances and two electric resonances from its metallic structure [16]. The first magnetic resonance comes from the rectangular loop of the metallic structure. Its equivalent circuit is illustrated in Fig. 3, where L_1 is the self-inductance of each strip, C_g is the gap capacitance, and C_s is the surface capacitance.

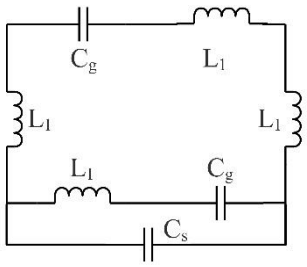

Fig. 3. Equivalent circuit of the first magnetic resonance.

According to the strip line theory [17], the inductance of a strip line can be calculated using:

$$L = 2\times10^{-4} l\left[ln\left(\frac{l}{w+t}\right)+1.193+0.2235\frac{w+t}{l}\right]. \quad (1)$$

Where *l* is the length, *w* is the width, and *t* is the thickness of the strip line. For convenience, we define a function to represent the calculation of the inductance of (1) as *Cal_induc(w, l, t)*.

The capacitance per unit length of the paralleled strip lines, C_{pul}, is calculated using:

$$C_{pul} = \varepsilon_0 \varepsilon_e F(k). \quad (2)$$

Where ε_0 is the permittivity of free space, ε_e and *F(k)* are given as:

$$\varepsilon_e = 1+(\varepsilon_r - 1)F(k)/2F(k1), \quad (3)$$

$$F(k) = \begin{cases} \frac{1}{\pi}\ln(2\frac{1+\sqrt{k'}}{1-\sqrt{k'}}), & 0 < k \le \frac{1}{\sqrt{2}} \\ \pi\ln(2\frac{1+\sqrt{k}}{1-\sqrt{k}})^{-1}, & \frac{1}{\sqrt{2}} < k \le 1 \end{cases} \quad (4)$$

where

$$\begin{cases} a_e = g/2, b_e = a_e + w, \\ k = a_e / b_e \\ k1 = \dfrac{\sinh(\pi a_e / 2h)}{\sinh(\pi b_e / 2h)}, \\ k' = \sqrt{1-k^2} \end{cases} \quad (5)$$

and *g* is the gap width between two strips, *w* is the width of each strip, h is the thickness of the substrate, and ε_r is the relative permittivity. For convenience, we define a function $Cal\_cap(w, g, h, \varepsilon_r)$ to represent capacitance of (2).

For the case when the strips are on different sides of the substrate, the capacitance can be calculated using:

$$C = \frac{\varepsilon_r \varepsilon_0 S}{d}, \tag{6}$$

where S is the paralleled area, d is the distance between the strips.

When the gap capacitance C_g is too small, the surface capacitance should be taken into consideration. The calculation for surface capacitance is simplified as the summation of the paralleled strips together.

Accordingly, we obtain:

$$\begin{cases} L_1 = Cal\_induc(w,b,t) \approx 5.51nH \\ C_g = w \times Cal\_cap(w, a-b-c-w, h, \varepsilon_r) \approx 0.05\,pF \\ C_s = 2 \times (b-c-w) \times Cal\_cap(w, a-2(c+w), h, \varepsilon_r) \\ \quad \approx 0.2\,pF \end{cases}. \tag{7}$$

Therefore, the first magnetic resonant frequency is:

$$f_{m1} = \frac{1}{2\pi\sqrt{4L_1 \times \left(C_s + C_g/2\right)}} \approx 2.25GHz. \tag{8}$$

The second magnetic resonance mainly comes from the mutual coupling between the metallic structures on different sides of the substrate. Before the equivalent circuit analysis, the capacitance constitution under this situation should be introduced.

Figure 4 displayed the capacitance constitution. Unlike the single sided cases, both plane-parallel coupling and surface coupling contributes to the calculations of equivalent capacitance. It should also be noticed that the equivalent surface capacitance and gap capacitance only include the coupling through the air.

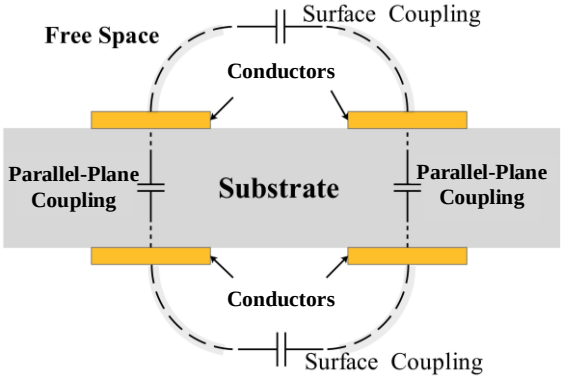

Fig. 4. Capacitance constitution illustration.

Since the proposed structure in Fig. 2 is symmetrical, it can be divided into 4 identical parts, of whom each part is composed of two paralleled metallic strips separated by the substrate. Hence, we built the equivalent circuit for each part first, and then connect them together as shown in Fig. 5. The surface capacitance are also equally distributed to each branch. Therefore, the equivalent circuit for the second magnetic resonance are obtained as illustrated in Fig. 5, where C_1 refers to the plane-parallel capacitor of the two paralleled strips on different sides of the substrate, C'_g and C'_s refer to the gap and surface capacitors, respectively.

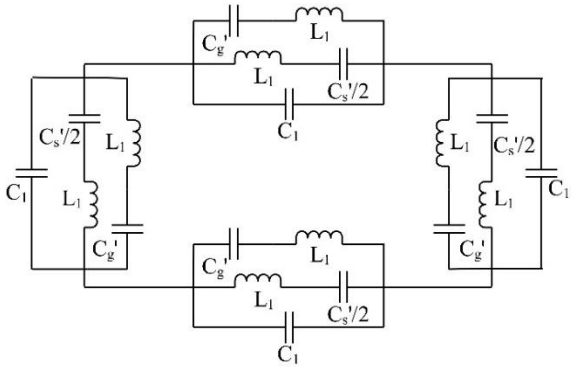

Fig. 5. Equivalent circuit for the second magnetic resonance.

According to the previous setup, we can obtain that:

$$\begin{cases} C_g' = \frac{1}{2} \times w \times Cal\_cap(w, a-b-c-w, h, \varepsilon_r = 1) \\ \quad \approx 0.01\,pF \\ C_s' = \frac{1}{2} \times 2(b-c-w) \times Cal\_cap(w, a-2(w+c)h, \varepsilon_r = 1) \\ \quad \approx 0.05\,pF \\ C_1 = \frac{\varepsilon_0 \varepsilon_r bw}{h} \approx 0.32\,pF. \end{cases} \tag{9}$$

Therefore, the second magnetic resonant frequency is:

$$f_{m2} = \frac{1}{2\pi\sqrt{2L_1 \times \left(C_1 + C'_g + C'_s/2\right)/4}} \approx 5.05GHz. \tag{10}$$

The analysis for the electric resonators is quite different. Vertically polarized electric field will activate vertical currents on the strips as illustrated in Fig. 6. For the first electric resonance whose equivalent circuit is also displayed in Fig. 6.

In this figure, C_2 refer to capacitance of two vertical neighboring strips of the upper and lower units, which is approximated as:

$$C_2 = (a-2c) \times Cal\_cap(w, 2c, h, \varepsilon_r) \approx 0.29\,pF. \tag{11}$$

Therefore, the first electric resonant frequency is:

$$f_{e1} = \frac{1}{2\pi\sqrt{3L_1 \times C_2}} \approx 2.30GHz. \tag{12}$$

Similarly, the equivalent circuit for the second electric resonator of a double sided units as illustrated in Fig. 7.

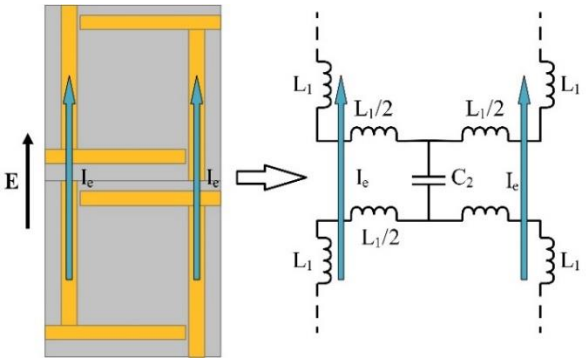

Fig. 6. Two LHM vertically position units and their equivalent circuit of the first electric resonator.

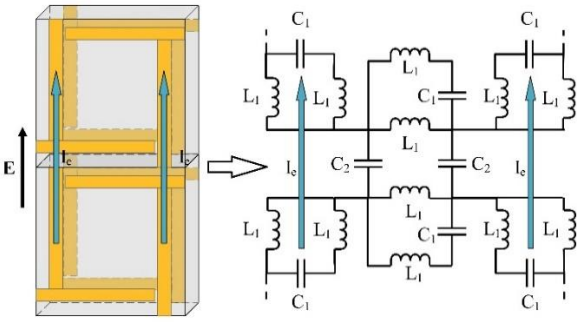

Fig. 7. Equivalent circuit of the second electric resonator.

Hence it is concluded that the equivalent inductance L_e and the equivalent capacitance C_e should be:

$$\begin{cases} L_e = L_1 \\ C_e = 2C_1 \,\|\, C_2 \approx 0.2\,pF \end{cases}. \tag{13}$$

Therefore, the second electric resonant frequency is obtained:

$$f_{e2} = \frac{1}{2\pi\sqrt{L_e \times C_e}} \approx 4.80GHz. \tag{14}$$

C. Simulation and analysis

Simulations were operated using HFSS to get the S parameters. The magnitude of S_{11} and S_{21} are displayed in Fig. 8. Due to the high loss of the substrate, passing band property of this LHM is not very good.

The effective permeability and permittivity are retrieved with the help of 'S parameter retrieval' method in [18]. Figure 9 displayed the real part of effective permeability μ_{eff}, permittivity ε_{eff} and refractive index n of the LHM. It is observed that double negative properties are from 2.12 to 2.45 GHz, 4.84 to 5.08 GHz, and 5.19 to 5.42 GHz, respectively. The first and second negative bands match well with our analysis. The third one needs further investigation and will not be discussed here. These LHM bands are very close to the WLAN/ WiMAX bands.

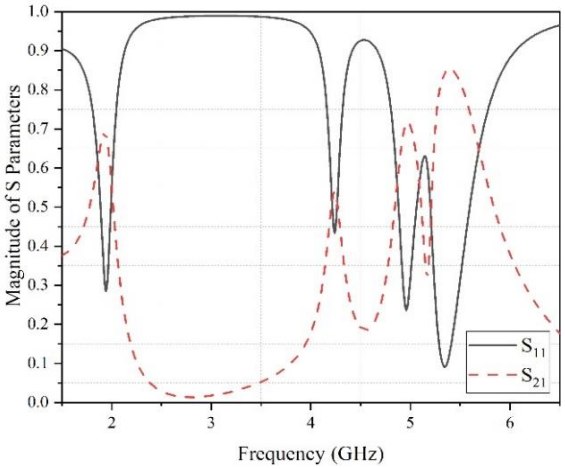

Fig. 8. Magnitude of simulated S parameters of the proposed LHM.

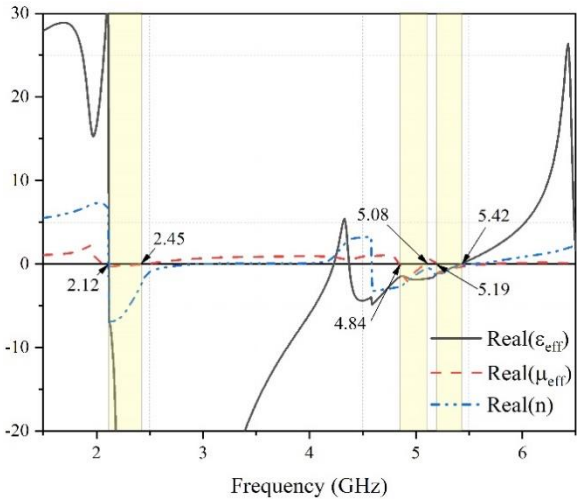

Fig. 9. Retrieved effective parameters of the proposed LHM.

III. LHM INSPIRED ANTENNA: DESIGN AND ANALYSIS

A. Analysis of a loop antenna using the LHM unit

Since we want to use the LHM unit not only for NFRP, but also as a loop antenna, it is essential to discuss the radiating property of this LHM unit with proper feed to serve as a loop antenna. The structure is displayed in Fig. 10. Parameters are L_s = 24mm, W_s = 18mm, L_g = 8.5mm, L_f = 11mm, W_f = 3mm, W_2=6mm, and W_g =7.2mm. This antenna is printed on a FR4 substrate with a thickness of 1mm.

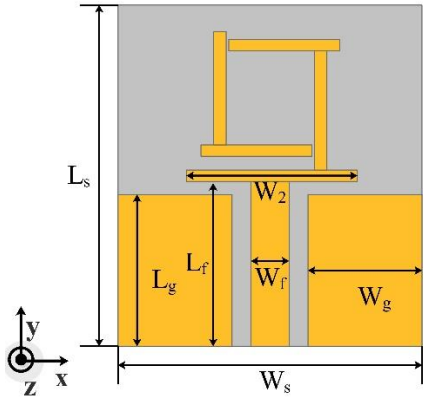

(a) Front view

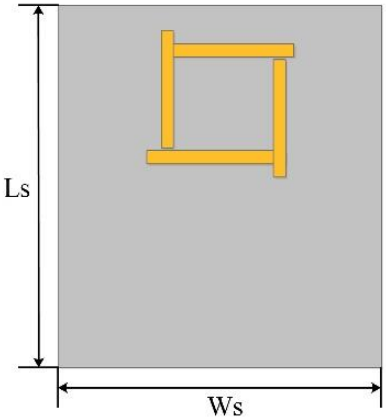

(b) Back view

Fig. 10. Structure of the proposed antenna: (a) front view and (b) back view.

The simulated S_{11} is displayed in Fig. 11. There are two pass bands as observed, of which one is from 2.49 GHz to 2.58 GHz, and the other one is from 3.71 GHz to 4.34 GHz. The 2 resonant frequencies are 2.54 GHz and 4 GHz, respectively.

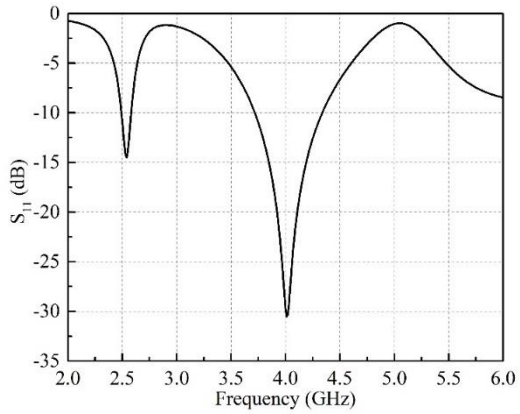

Fig. 11. Simulated S parameter of the LHM antenna.

B. Analysis of G-style monopole antenna

A G-style monopole antenna is designed as displayed in Fig. 12 with parameters listed in Table 1.

Table 1: Parameters for G-style monopole (Unit: mm)

Parameters	L_1	L_2	L_3	L_f	L_g	L_s
Length	4.7	12.4	7	11	8.5	24
Parameters	W_1	W_2	W_3	W_f	W_g	W_s
Length	1	10.4	2	3	7.2	18

This antenna is a normal dual-band monopole. It is obvious that the lengths of the two branches decide its operating bands. We ran simulations for this antenna, and the results are shown in Fig. 13. It is observed that the first passing band is ranging from 2.76 GHz to 3.03 GHz, while the second passing band is ranging from 5.2 GHz to 7.68 GHz.

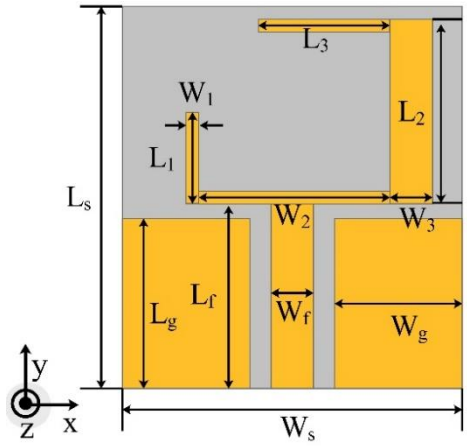

Fig. 12. Structure of the G-style monopole antenna.

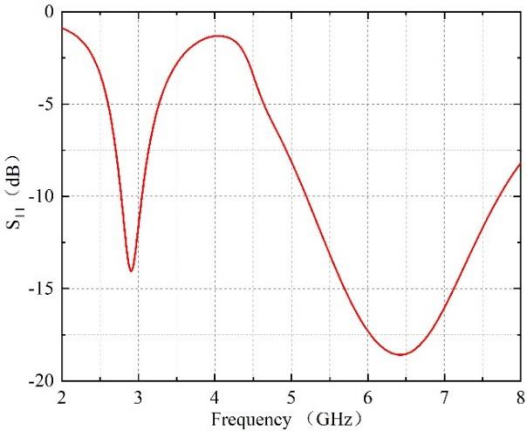

Fig. 13. Simulated S_{11} of the G-style antenna.

C. LHM inspired antenna

The G-style monopole antenna is then used to surround the designed LHM unit, as illustrated in Fig.

14. The lengths of the parameters are exactly the same as listed previously in Table 1. The gap between the LHM unit and the G-style monopole g_1 = 0.5mm.

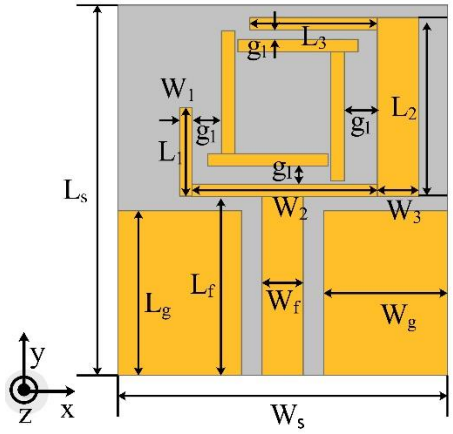

(a) Front view

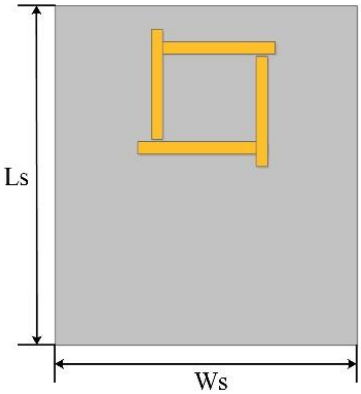

(b) Back view

Fig. 14. Structure of the LHM inspired antenna.

We ran simulations with HFSS and CST for the LHM inspired antenna, respectively. Furthermore, a prototype of the antenna is fabricated and its radiating performance are measured in a microwave chamber as displayed in Fig. 15.

The simulated and measured S_{11} for the LHM inspired antenna are displayed in Fig. 16. It is observed that there are 3 pass bands, of whom the first one is from 2.4 GHz to 2.52 GHz, the second one is from 3.4 GHz to 3.69 GHz, and the third one is from 4.47 GHz to 6 GHz, covering the requirements of WLAN and WiMAX. The measured S_{11} matches well with the simulated one.

The peak gain and efficiency of the LHM inspired antenna at different frequencies are displayed in Fig. 17. It is observed that at the frequencies of 2.4 GHz to 2.5 GHz, the simulated peak gain is ranging from 0.73 dBi to 1.11 dBi, and the efficiency is ranging from 71.5% to 81.3%; at 3.4 GHz to 3.69 GHz, the peak gain is ranging from 1.25 dBi to 1.54 dBi, and the efficiency is ranging from 78.2% to 88.5%; at 5.15 GHz to 5.85 GHz, the peak gain is ranging from 2.45 dBi to 3 dBi, and the efficiency is ranging from 93.9% to 95.4%.

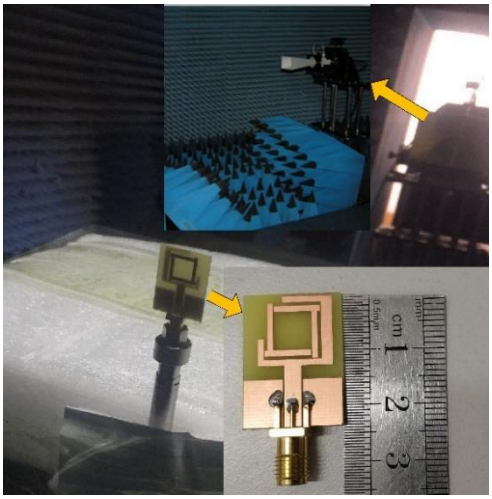

Fig. 15. A Fabricated prototype and measurement facilities.

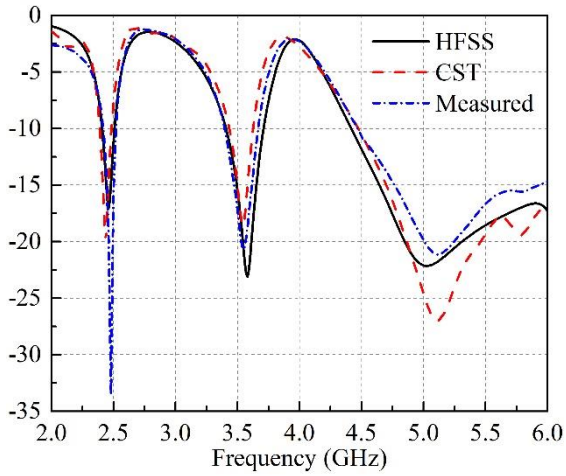

Fig. 16. Simulated and measured S_{11} of the LHM inspired antenna.

Radiation patterns of the proposed antenna are also simulated and measured. Due to the facility limitation, only normalized pattern is measured. Figures 18 (a) to (f) displayed the simulated (dashed lines) and measured (solid lines) normalized radiation pattern of the LHM inspired antenna on YOZ plane (black) and XOZ plane (red) at 2.45 GHz, 3.5 GHz, 3.6 GHz, 5.2 GHz, 5.5 GHz, and 5.8 GHz, respectively. As observed, the proposed antenna exhibits good omni-directional performance at all the discussed frequencies.

Therefore, the gain, efficiency and radiation patterns of the LHM inspired antenna indicate that this antenna exhibits good radiation performance for WLAN/WiMAX applications.

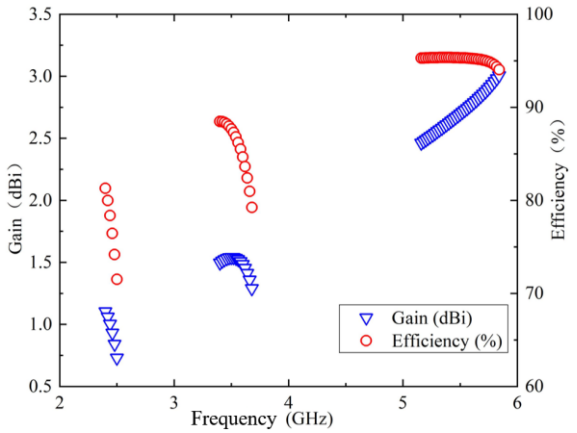

Fig. 17. Simulated gain and efficiency at frequency ranges of 2.4 to 2.5 GHz, 3.4 to 3.69 GHz, 5.15 to 5.85 GHz.

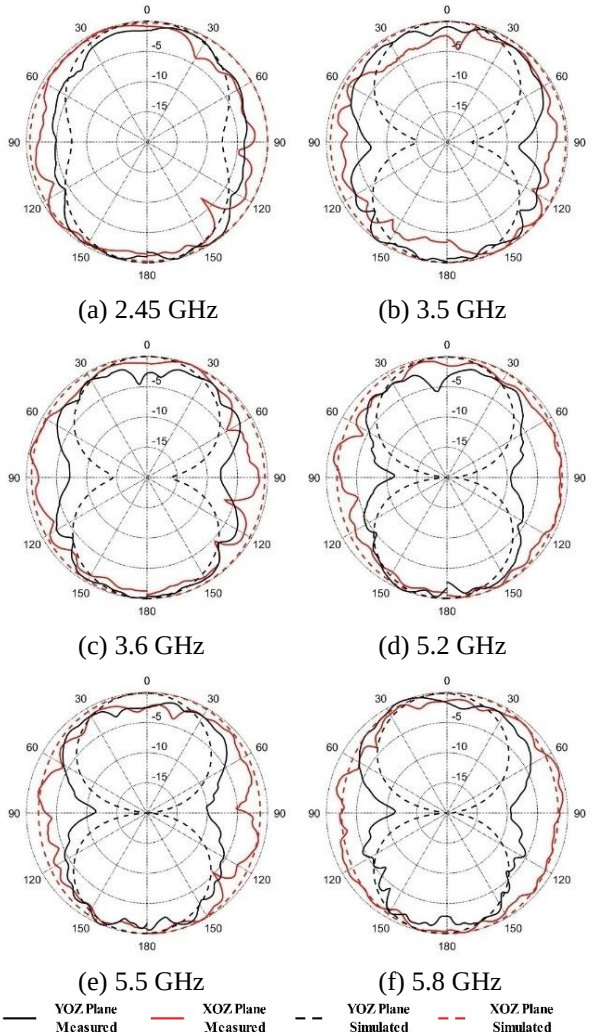

Fig. 18. Simulated (dashed lines) and Measured (solid lines) normalized radiation patterns of the LHM loaded antenna at: (a) 2.45 GHz, (b) 3.5 GHz, (c) 3.6 GHz, (d) 5.2 GHz, (e) 5.5 GHz, and (f) 5.8 GHz.

D. Discussions of electric current distributions

To further investigate the radiating property, surface current distributions of this LHM inspired NFRP antenna at 2.45 GHz, 3.5 GHz and 5.5 GHz are displayed in Figs. 19 (a) to (c), respectively.

At 2.45 GHz, the longer arm of the G-style structure is the main radiating element. Remarkable induced current is observed around the LHM unit structure. Therefore, near-field resonant coupling between the LHM unit and the G-style monopole played an important role to make the resonant frequencies shift to meet 2.45 GHz band requirement.

At 3.5 GHz, Strongest current is observed flowing around the LHM unit, identifying that the LHM unit is now turned to a loop radiator that fed through the coupling with the G-style structure.

At 5.5 GHz, the shorter arm of the G-style structure becomes the main radiator. Induced current is also observed flowing around the LHM unit, identifying that for this case, near-field resonant coupling will still serve as a parasitic element, shifting the resonant frequencies to meet the 5.5 GHz band requirement.

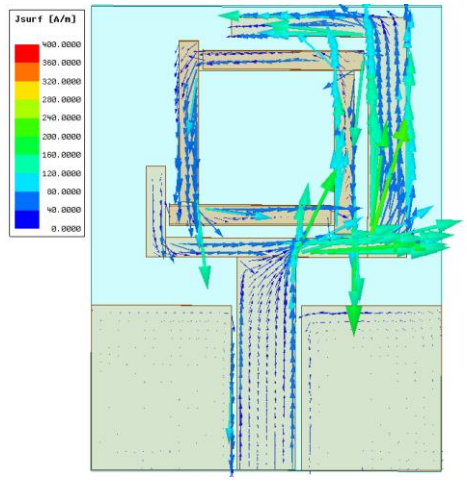

(a) 2.45 GHz

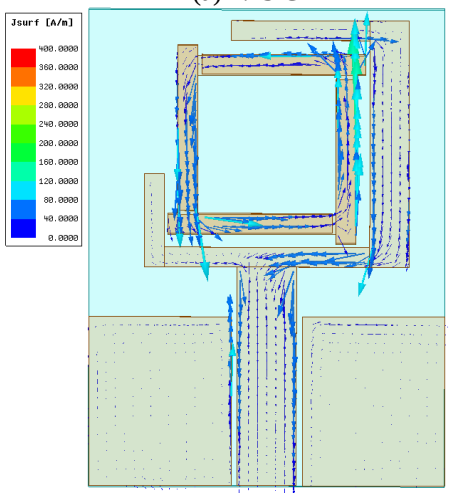

(b) 3.5 GHz

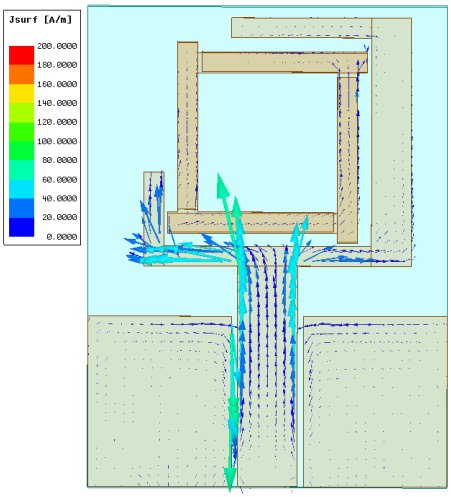

(c) 5.5 GHz

Fig. 19. Surface current distribution of the LHM inspired antenna at: (a) 2.45 GHz, (b) 3.5 GHz, and (d) 5.5 GHz.

Table 2 listed the comparisons of size and frequency coverage of the proposed antenna with some recently reported WLAN/WiMAX antennas.

Table 2: Comparison of sizes and operating frequency ranges with the proposed antenna

Ref. (year)	Size (mm^2)	Frequencies (GHz)		
		WLAN 2.4-2.484	WiMAX 3.4-3.69	WLAN & WiMAX 5.15-5.85
[1] (2016)	19×25	2.00-2.76	3.04-4.00	5.20-6.00
[19] (2016)	34×30	1.92-2.17	3.40-3.60	5.15-5.35
[20] (2016)	40×40	2.20-2.80	Not cover	5.20-7.00
[21] (2016)	28×32	2.29-2.88	3.26-3.88	4.17-6.07
[22] (2016)	24×22.5	2.39-2.52	3.34-3.67	4.43-5.97
[23] (2017)	26×29.4	2.23-2.89	3.21-4.45	5.32-5.85
[24] (2017)	22×45	2.12-3.06	Not cover	5.06-5.28
[6] (2018)	70×44	2.22-2.79	Not cover	5.42-6.04
[25] (2018)	23×17	0.48-6.5		
[26] (2019)	32×37.2	2.22-2.52	3.42-3.68	5.30-5.65
Proposed	24×18	2.40-2.52	3.40-3.69	4.47-6.00

From this table, it is drawn that the proposed antenna has a relatively small size while also provide a whole coverage of WLAN/WiMAX frequency ranges.

IV. CONCLUSION

This paper presents a metamaterial inspired miniaturized triple-band antenna with a compact size of $24 \times 18 \times 1$ mm^3 (at 2.4 GHz). A LHM is designed and analyzed with equivalent circuit and simulations. It is then employed as NFRP element that surrounded by a G-style monopole. To investigate the operating principle, we also ran simulations for the G-style monopole antenna, a loop antenna based on the LHM unit. The results indicate that the LHM unit made the operating bands correspond to the G-style monopole to lower frequencies, while the LHM unit itself is operating an additional passing band. A prototype of the proposed antenna is fabricated and measured. The results were in good agreement with the simulated ones, validating good radiating performance of the proposed metamaterial inspired antenna. Hence, the proposed antenna is a good candidate for WLAN/WiMAX applications.

ACKNOWLEDGMENT

This paper is supported by the Natural Science Foundation of Jiangsu province of China (BK20190956).

REFERENCES

[1] A. K. Gautam, L. Kumar, B. K. Kanaujia, and K. Rambabu, "Design of compact F-shaped slot triple-band antenna for WLAN/WiMAX applications," *IEEE Trans. Antennas Propag*., vol. 64, no. 3, pp. 1101-1105, 2016.

[2] M. V. Rooyen, J. W. Odendaal, and J. Joubert, "High-gain directional antenna for WLAN and WiMAX applications," *IEEE Antennas and Wireless Propagation Letters*, vol. 16, no. 99, pp. 286-289, 2017.

[3] A. D. Tadesse, O. P. Acharya, and S. Sahu, "Application of metamaterials for performance enhancement of planar antennas: A review," *International Journal of RF and Microwave Computer-Aided Engineering*, p. e22154, 2020. doi: 10.1002/mmce.22154.

[4] S. Yan and G. Vandenbosch, "Low-profile dual-band pattern diversity patch antenna based on composite right/left-handed transmission line," *IEEE Trans. Antennas Propag*., vol. PP, no. 99, pp. 1-1, 2017.

[5] C. Zhang, J. Gong, Y. Li, and Y. Wang, "Zeroth-order-mode circular microstrip antenna with patch-like radiation pattern," *IEEE Antennas and Wireless Propagation Letters*, vol. 17, no. 3, pp. 446-449, 2018.

[6] K. Sun, S. Han, J. Choi, and J. K. Lee, "Miniaturized active metamaterial resonant antenna with improved radiation performance based on negative-resistance-enhanced CRLH transmission lines," *IEEE Antennas and Wireless Propagation*

Letters, vol. 17, no. 7, pp. 1162-1165, 2018.

[7] G. Xiang, T. Jackson, and P. Gardner, "Multiband open-ended resonant antenna based on one ECRLH unit cell structure," *IEEE Antennas and Wireless Propagation Letters*, vol. 16, no. 99, pp. 1-1, 2017.

[8] Z. Wu, L. Li, X. Chen, and K. Li, "Dual-band antenna integrating with rectangular mushroom-like superstrate for WLAN applications," *IEEE Antennas & Wireless Propagation Letters*, vol. 15, pp. 1269-1272, 2016.

[9] A. Erentok and R. W. Ziolkowski, "Metamaterial-inspired efficient electrically small antennas," *IEEE Trans. Antennas Propag.*, vol. 56, no. 3, pp. 691-707, 2008.

[10] Y. Dong and T. Itoh, "Metamaterial-based antennas," *Proc. IEEE*, vol. 100, no. 7, pp. 2271-2285, 2012.

[11] T. Dong, X. Zhu, M. Li, Y. Zhang, B. Zhou, H. Zeng, and M.-C. Tang, "Design of electrically small Hilbert fractal NFRP magnetic monopole antennas," *Journal of Electromagnetic Waves and Applications*, vol. 33, no. 4, pp. 454-464, 2019.

[12] P. Pokkunuri, B. T. P. Madhav, and M. Venkateswararao, "Metamaterial inspired reconfigurable fractal monopole antenna for multi-band applications," *Int. J. Intell. Eng. Syst.*, vol. 12, pp. 53-61, 2019.

[13] M.-C. Tang, Y. Duan, Z. Wu, X. Chen, M. Li, and R. W. Ziolkowski, "Pattern reconfigurable, vertically polarized, low-profile, compact, near-field resonant parasitic antenna," *IEEE Trans. Antennas Propag.*, vol. 67, no. 3, pp. 1467-1475, 2018.

[14] K. E. Kedze, H. Wang, and I. Park, "Compact broadband omnidirectional radiation pattern printed dipole antenna incorporated with split-ring resonators," *IEEE Access*, vol. 6, pp. 49537-49545, 2018.

[15] M.-C. Tang, Y. Chen, and R. W. Ziolkowski, "Experimentally validated, planar, wideband, electrically small, monopole filtennas based on capacitively loaded loop resonators," *IEEE Trans. Antennas Propag.*, vol. 64, no. 8, pp. 3353-3360, 2016.

[16] S. Li, W. Yu, A. Z. Elsherbeni, W. Li, and Y. J. I. J. O. A. Mao, "A novel dual-band left-handed metamaterial design method," *International Journal of Antennas and Propagation*, vol. 2017, 2017.

[17] I. Bahl and P. Bhartia, *Microwave Solid State Circuit Design*. Wiley, 2003.

[18] X. Chen, T. M. Grzegorczyk, B. I. Wu, P. J. Jr, and J. A. Kong, "Robust method to retrieve the constitutive effective parameters of metamaterials," *Phys. Rev. E*, vol. 70, no. 1, pt. 2, pp. 811-811, 2004.

[19] A. R. Jalali, J. Ahamdi- Shokouh, and S. R. Emadian, "Compact multiband monopole antenna for UMTS, WiMAX, and WLAN applications," *Microwave & Optical Technology Letters*, vol. 58, no. 4, pp. 844-847, 2016.

[20] A. Pirooj, M. Naser-Moghadasi, and F. B. Zarrabi, "Design of compact slot antenna based on split ring resonator for 2.45/5 GHz WLAN applications with circular polarization," *Microwave & Optical Technology Letters*, vol. 58, no. 1, pp. 12-16, 2016.

[21] G. Liu, Y. Liu, and S. Gong, "Compact tri-band wide-slot monopole antenna with dual- ring resonator for WLAN/WiMAX applications," *Microwave & Optical Technology Letters*, vol. 58, no. 5, pp. 1097-1101, 2016.

[22] S. Imaculate Rosaline and S. Raghavan, "Meta-material inspired monopole antenna for WLAN/ WiMAX applications," *Microwave & Optical Technology Letters*, vol. 58, no. 4, pp. 936-939, 2016.

[23] R. S. Daniel, R. Pandeeswari, and S. Raghavan, "Design and analysis of metamaterial inspired open complementary split ring resonators for multiband operation," *Progress In Electromagnetics Research C*, vol. 78, pp. 173-182, 2017.

[24] A. S. M. Alqadami, M. F. Jamlos, J. S. Ping, S. K. A. Rahim, G. A. E. Vandenbosch, and A. Narbudowicz, "Miniaturized dual-band antenna array with double-negative (DNG) metamaterial for wireless applications," *Appl. Phys. A*, vol. 123, no. 1, p. 22, 2017.

[25] M. Alibakhshikenari, B. Virdee, A. Ali, and E. Limiti, "Miniaturized planar-patch antenna based on metamaterial L-shaped unit-cells for broadband portable microwave devices and multiband wireless communication systems," *IET Microwaves Antennas and Propagation*, vol. 12, no. 7, pp. 1080-1086, 2018.

[26] U. Patel and T. K. Upadhyaya, "Design and analysis of compact μ-negative material loaded wideband electrically compact antenna for WLAN/ WiMAX applications," *Progress In Electromagnetics Research*, vol. 79, pp. 11-22, 2019.

A Third-Order Bandpass Three-Dimensional Frequency Selective Surface with Multiple Transmission Zeros

Zhengyong Yu[*1, 2] and Wanchun Tang[2]

[1] School of Computer and Communication Engineering
Huai'an Vocational College of Information Technology, Huai'an, 223003, China
yonglly@sina.com

[2] School of Physics and Technology
Nanjing Normal University, Nanjing, 210023, China
eewctang@njnu.edu.cn

Abstract ─ We present a third-order bandpass three-dimensional frequency selective surface (3D FSS) with multiple transmission zeros in this paper. The unit cell of the proposed 3D FSS consists of an air-filled square waveguide and a cuboid dielectric block with three concentric metallic square loops. Due to its inner electromagnetic coupling in the unit cell, this FSS provides a flat passband with three transmission poles, a wide out-of-band rejection with three transmission zeros, and high frequency selectivity. In order to explain the working principle, an equivalent circuit model is established and investigated. Finally, an FSS prototype is fabricated and measured, and the results exhibit good stability for both TE and TM polarizations under incident angles from 0° to 50°. Besides, this FSS has a relatively compact unit cell.

Index Terms ─ Bandpass, dual polarizations, frequency selective surface (FSS), third-order, transmission zeros.

I. INTRODUCTION

During the past decade, frequency selective surfaces (FSSs) have been widely studied due to their superior spatial filtering characteristics for some practical applications, including radar cross section reduction, electromagnetic interference shielding and so on [1-5]. Recently, FSSs are also used as partially reflecting surfaces with aperture antenna to drastically improve their radiation patterns and antennas performance [6]. Typical FSSs are usually two-dimensional (2D) arrays assembled by periodically arranged planar unit cells, which can exhibit bandpass or bandstop filtering responses. For the bandpass FSS, it requires flat transmission response with low insertion loss within the passband, as well as fast roll-off and wide rejection out of the passband. Besides, it should also have dual polarizations, good angular stability and compact unit cell.

To meet these above requirements, many second-order bandpass FSSs have been reported [7-12]. A bandpass FSS with second-order response is proposed by inserting the capped dielectric in the perforated metallic plate [7]. However, this FSS suffers from slow roll-off out of the passband without any transmission zero, resulting in poor frequency selectivity. To achieve fast roll-off filtering performance, a bandpass FSS is designed by using vertically cascaded substrate integrated waveguide (SIW) cavities [8]. In such an FSS, two transmission zeros located near the edges of the passband are generated by the coupling between multiple resonant modes in these SIW cavities. However, the angular stability deteriorates due to its large electrical size. Then, a quasi-elliptic bandpass FSS is presented based on the hybrid array of double square loops and gridded square loops, but its electrical size and thickness are also large [9]. Moreover, three-dimensional (3D) FSSs can provide 3D resonant cavities to achieve a desired response [10-12], as an alternative method. For example, two bandpass 3D FSSs with the quasi-elliptic responses are presented, taking advantage of the shielded microstrip lines [10-11]. Unfortunately, these two designs only operate under a single polarization. Later, the authors in [12] propose a dual-polarized bandpass 3D FSS with fast both sides roll-off by the combination of the metal cylindrical pipes and disks. Nevertheless, this 3D FSS has a large electrical size and the angular stability is also needed to be improved.

For the third-order or high-order bandpass FSSs, several design approaches of these FSSs are investigated [13-19]. Two FSSs with third- and fourth-order bandpass responses are realized by using the arrays of sub-wavelength periodic structures with non-resonant elements [13]. A multilayered third-order bandpass FSS

Submitted On: April 20, 2020
Accepted On: October 20, 2020
https://doi.org/10.47037/2020.ACES.J.351214

1054-4887 © ACES

is obtained according to the coupled matrix theory [14]. Another FSS is achieved by the two capacitive patch layers and a slot layer, exhibiting wide-passband performance [15]. However, these designs in [13-15] do not have any transmission zero, so the frequency selectivity is unsatisfactory. Then, one transmission zero located at the right side of the passband is produced for high frequency selectivity [16-18]. In [16], one FSS structure is presented by a hybrid resonator to realize a third-order bandpass response with one transmission zero. In [17-18], similar frequency selective performances are achieved based on the two capacitive patch resonators and one hybrid resonator. Additionally, one FSS with an additional transmission zero located at the left side of the passband is designed to provide a stable, highly-selective, and wide-passband response [19]. However, this design has a larger unit cell size and a poor out-of-band rejection performance. Thus, there is a challenge for the FSS design to realize flat passband, high frequency selectivity, wide out-of-band rejection, good angular stability, dual polarizations, and compact unit cell simultaneously. In addition to the above FSSs composed of printed microwave substrates, the FSSs can also be made of all-dielectric materials [20], printed surfaces [21], all-metal structures [22], and artificial magnetic conductor [23]. Besides, one new approach in designing bandpass FSSs is proposed by using artificial intelligence in conjunction with an electromagnetic simulator [24].

In this paper, a dual-polarized bandpass 3D FSS is presented to obtain these performances simultaneously. The unit cell of the proposed 3D FSS is composed of an air-filled square waveguide and a cuboid dielectric block with three concentric metallic square loops. By the inner electromagnetic coupling in the unit cell, this FSS realizes a third-order bandpass response with wide out-of-band rejection and high frequency selectivity. Meanwhile, its frequency selectivity is further improved by the high quality factor (Q-factor) of the square waveguide cavity. An equivalent circuit model is established and analyzed to explain its working principle. At last, a prototype of the proposed 3D FSS is fabricated and measured, and its simulated results are coincided with experimental ones.

II. UNIT CELL DESIGN AND SIMULATION

As depicted in Fig. 1 (a), the unit cell of the proposed 3D FSS consists of an air-filled square waveguide, and a cuboid dielectric block with three concentric metallic square loops is inserted in the square waveguide. As shown in Fig. 1 (b), the gridded square loop (GSL) structures can be observed on both the top and bottom layers of the unit cell. The periods of the unit cell along the *x*- and *y*-axes are denoted as *p*. The wall thickness and height of the square waveguide are *t* and *h*. These two metallic square loops etched on the top and bottom layers have the same geometrical parameters with the size l_1 and width w_1. The size and width of the square loop in the middle layer are l_2 and w_2. The relative dielectric constant of the cuboid dielectric block is expressed as ε_r.

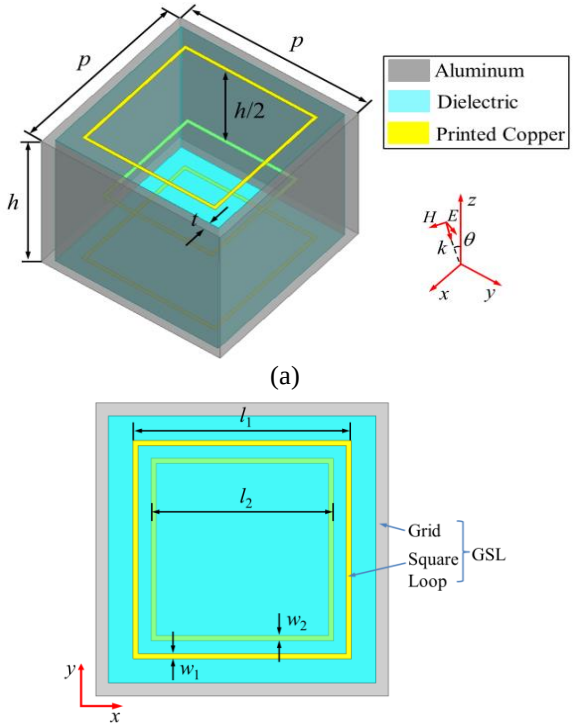

Fig. 1. Unit cell of the proposed 3D FSS. (a) Perspective view and (b) top view.

Figure 2 gives the simulated frequency responses of the proposed 3D FSS under normal incidence by the commercial ANSYS HFSS Simulation Software. The design parameters of the proposed 3D FSS are listed in Table 1. It can be observed from Fig. 2 a third-order bandpass response with wide out-of-band rejection and high frequency selectivity is achieved, including three transmission poles f_{p1}=5.46 GHz, f_{p2}=5.74 GHz and f_{p3}=5.87 GHz in the passband, and three transmission zeros f_{z1}=6.08 GHz, f_{z2}=6.35 GHz and f_{z3}=7.1 GHz in the upper stopband. The master and slave boundary conditions are applied for the unit cell simulations with Floquet ports, as depicted in Fig. 3.

For expressing the fractional bandwidths of the passband and the upper stopband, FBW_{3dB} and FBW_{20dB} are defined as follows:

$$FBW_{3dB} = \frac{Bandwidth\ of\ |S_{21}| \geq -3dB}{Center\ frequency\ of\ the\ passband\ (f_1)} \times 100\%, \quad (1)$$

$$FBW_{20dB} = \frac{Bandwidth\ of\ |S_{21}| \leq -20dB}{Center\ frequency\ of\ the\ upper\ stopband\ (f_2)} \times 100\%. \quad (2)$$

The simulated 3 dB bandwidth of the passband is 0.61 GHz (5.3-5.91 GHz), and the center frequency of the passband (f_1) is 5.605 GHz. The simulated 20 dB bandwidth of the upper stopband is 2.7 GHz (5.99-8.69 GHz), and the center frequency of the upper stopband (f_2) is 7.34 GHz. Therefore, FBW_{3dB} and FBW_{20dB} are 10.9% and 36.8%, respectively.

Table 1: Design parameters of the proposed 3D FSS

p	l_1	l_2	w_1
11.4 mm	8.5 mm	7.1 mm	0.2 mm
w_2	h	t	ε_r
0.2 mm	10 mm	0.5 mm	3.5

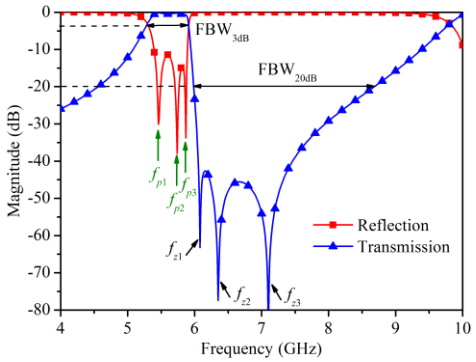

Fig. 2. Simulated frequency responses of the proposed 3D FSS by HFSS.

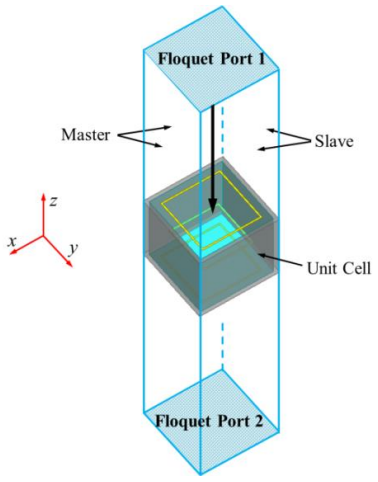

Fig. 3. Periodic boundary conditions of the unit cell.

III. EQUIVALENT CIRCUIT MODEL

In order to explain the working principle of the proposed 3D FSS, an equivalent circuit model is established under the normal incidence and depicted in Fig. 4. The equivalent circuit model consists of five parts, including three *LC* resonators separated by the two square waveguides. These three *LC* resonators represent the GSLs at the top/bottom layers and the square loop in the middle layer. These three *LC* resonators are denoted as R_1, R_2 and R_3, as shown in Fig. 4 (a). The square waveguide is modeled as the transmission line with the frequency-depended characteristic impedance $Z(f)$ and electrical length $\theta/2$ under the dominant mode TE_{10}. The inductors L_0 and L_1 are the self-inductance of the grid and square loop of the GSLs, respectively, and the inductor L_2 is the self-inductance of the square loop in the middle layer. The capacitor C_1 is the gap capacitance between the square loop and the grid for the GSL. The capacitor C_2 is the gap capacitance between the square loop and waveguide inner wall, which is located in the middle layer. The electrical and magnetic couplings between R_1 and R_2 are represented by the mutual capacitance C_m and the mutual inductance L_m, whereas the electrical and magnetic couplings between the R_3 and R_1/R_2 are denoted by the mutual capacitance C_{m1} and the mutual inductance L_{m1}. For the equivalent circuit modeling, the losses are not considered and included.

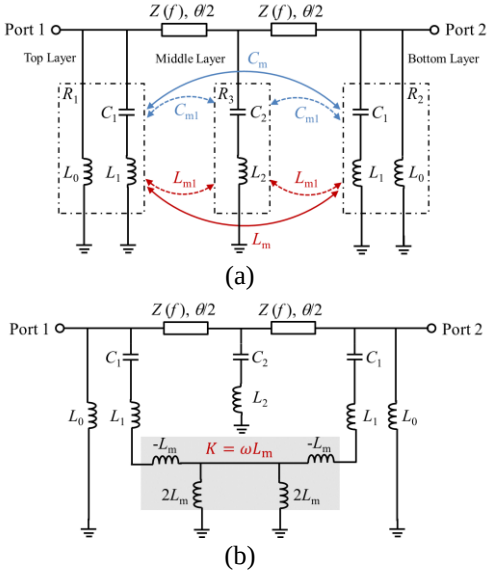

Fig. 4. Equivalent circuit model of the proposed 3D FSS. (a) General model and (b) simplified model.

For simplicity, only the magnetic coupling (L_m) between R_1 and R_2 is considered in our equivalent circuit modeling. The mutual inductance L_m can be denoted by an impedance inverter $K=\omega L_m$ [25]. Thus, a simplified circuit model is obtain and shown in Fig. 4 (b). It is observed that two propagation paths, including the coupling path through mutual inductance (L_m) and the

signal path directly through the square waveguide cavity ($Z(f)$, θ), are constructed. The electromagnetic waves are combined out-of-phase by these two paths, resulting in multiple transmission zeros at finite frequencies. The initial circuit values of the electrical parameters L_0, L_1, L_2, C_1 and C_2 can be calculated by using the given formulas in [26], and the final parameter values of the equivalent circuit model are extracted by the curve-fitting method [27], as shown in Table 2. The free space at the top and bottom layers of the unit cell can be modeled as a transmission line with the characteristic impedance of Z_0=377 Ω.

Table 2: Final parameter values of the equivalent circuit model

L_0	L_1	L_2
4.43 nH	5.36 nH	13.01 nH
L_m	C_1	C_2
-0.0015 nH	0.1 pF	0.0494 pF

In view of the symmetry of the equivalent circuit model shown in Fig. 4 (b), symmetric network theory is adopted to simplify the analysis of this circuit, as depicted in Fig. 5 (a). The even- and odd-mode equivalent circuits are given in Fig. 5 (b) and Fig. 5 (c) by applying an ideal magnetic wall (an open circuit) or an ideal electrical wall (a short circuit) at the symmetry plane T-T', respectively.

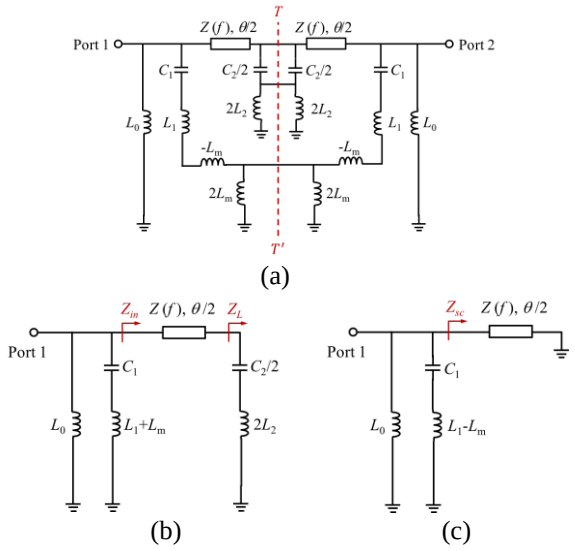

Fig. 5. Even- and odd-mode analysis method. (a) Symmetry plane T-T', (b) even-mode circuit, and (c) odd-mode circuit.

The characteristic impedance $Z(f)$ and electrical length θ of the square waveguide transmission line are defined as [28]:

$$Z(f)=\frac{\pi^2}{8}\sqrt{\frac{\mu_0}{\varepsilon_0\varepsilon_r}}\frac{1}{\sqrt{1-\left(\frac{\lambda(f)}{2(p-2t)}\right)^2}}, \tag{3}$$

$$\lambda(f)=\frac{1}{f\sqrt{\mu_0\varepsilon_0\varepsilon_r}}, \tag{4}$$

$$\theta=h\sqrt{(2\pi f)^2\mu_0\varepsilon_0\varepsilon_r-\left(\frac{\pi}{p-2t}\right)^2}, \tag{5}$$

where μ_0 is the magnetic permeability of free space, and ε_0 is the electric permittivity of free space.

From Fig. 5 (b), the load impedance Z_L of the square waveguide transmission line ($Z(f)$, $\theta/2$) is calculated by:

$$Z_L=j\omega(2L_2)+\frac{1}{j\omega\left(\frac{C_2}{2}\right)}. \tag{6}$$

Then, the corresponding input impedance Z_{in} can be expressed as:

$$Z_{in}=Z(f)\frac{Z_L+jZ(f)\tan(\theta/2)}{Z(f)+jZ_L\tan(\theta/2)}. \tag{7}$$

Consequently, the even-mode input admittance Y_{even} is represented as:

$$Y_{even}=\frac{1}{j\omega L_0}+\frac{1}{\frac{1}{j\omega C_1}+j\omega(L_1+L_m)}+\frac{1}{Z_{in}}. \tag{8}$$

Similarly, the odd-mode input admittance Y_{odd} can be deduced from Fig. 5 (c) as follows:

$$Y_{odd}=\frac{1}{j\omega L_0}+\frac{1}{\frac{1}{j\omega C_1}+j\omega(L_1-L_m)}+\frac{1}{Z_{sc}}, \tag{9}$$

$$Z_{sc}=jZ(f)\tan(\theta/2), \tag{10}$$

where Z_{sc} is the input impedance of the waveguide transmission line ($Z(f)$, $\theta/2$) under a short circuit.

Finally, the scattering matrix parameters of the proposed 3D FSS can be calculated by using the following equations [25]:

$$S_{11}=S_{22}=\frac{1/Z_0{}^2-Y_{even}Y_{odd}}{(1/Z_0+Y_{even})(1/Z_0+Y_{odd})}, \tag{11}$$

$$S_{21}=S_{12}=\frac{1/Z_0(Y_{odd}-Y_{even})}{(1/Z_0+Y_{even})(1/Z_0+Y_{odd})}. \tag{12}$$

Figure 6 compares the reflection and transmission coefficients obtained from HFSS and equivalent circuit model, and there is a good agreement. There is a relative difference at the upper stopband from 6 to 10 GHz, because the couplings (C_m, C_{m1}, L_{m1}) are ignored in the equivalent circuit model. Besides, the square waveguide is analyzed under the dominant mode TE_{10} without considering the effect of the higher modes. However, the established equivalent circuit model can give a view of

the working mechanism of the proposed 3D FSS.

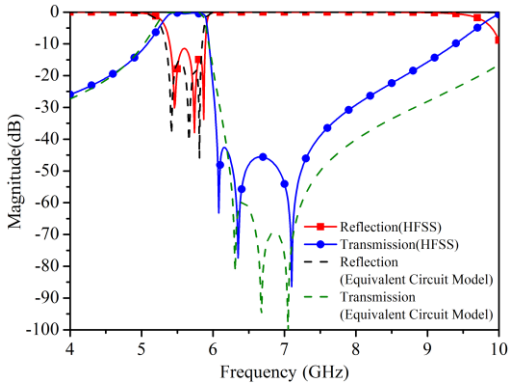

Fig. 6. Comparison of the reflection and transmission coefficients by HFSS and equivalent circuit model.

IV. FABRICATION AND MEASUREMENT

To verify the performances of the proposed 3D FSS, the prototype is fabricated. It consists of two building parts and their geometrical dimensions are given in Fig. 7 (a). The building part I is one piece of aluminium plate with a thickness of 1.0 mm, and 27 slots are periodically cut halfway along the plate. The building part II is one cuboid dielectric block with a thickness of 10 mm, and it is fabricated by using multi-layer PCB technology. The material of the dielectric block is F4B and its relative dielectric constant is 3.5 with the loss tangent of 0.005. For assembly, the pieces (building part I) are cross-joined together through the opening slots to construct an aluminium frame, which achieves the periodic square waveguides. Then, the cuboid dielectric blocks (building part II) are inserted, one by one, into the constructed frame. Finally, the size of the fabricated 3D FSS is 317.4 mm×317.4 mm with 26×26 unit cells, as shown in Fig. 7 (b). The electrical size of the unit cell $p\times p\times h$ is $0.21\lambda_0\times0.21\lambda_0\times0.187\lambda_0$, where λ_0 is the free-space wavelength at f_1.

The frequency responses of the proposed 3D FSS are measured by the free-space method, and its measurement environment is given in Fig. 7 (c). There are two wideband horn antennas (operating from 1 to 18 GHz), the FSS prototype, and the rotatable screen covered by absorbers. The FSS prototype is placed within the rectangular through-hole window in the center of the rotatable screen for measurement of incident stability. A pair of horn antennas are located about 1.2 m apart from each side of the centered rotatable screen, so that a uniform plane wave striking upon the FSS. The two horn antennas are connected by the vector network analyzer. Besides, the measurement device is surrounded by using the absorbing screens. For the transmission coefficients measurement, the propagation loss is firstly eliminated by the normalization of the measured results without the FSS prototype, and the environment noise is eliminated by the measured results of an identically-sized metallic plate. Then, the frequency responses of proposed 3D FSS can be obtained. Besides, the time-domain gating function of the vector network analyzer is also applied to calibrate the measured results for considering the multipath effects.

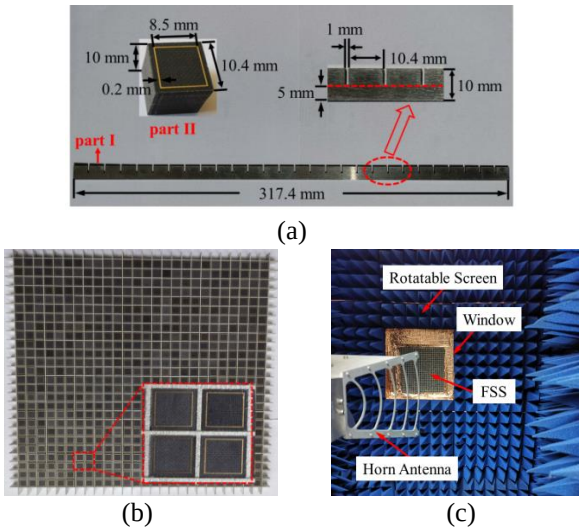

Fig. 7. Fabricated 3D FSS. (a) Building parts and dimensions, (b) photograph of the fabricated FSS prototype, and (c) measurement setup.

The measured results under different incident angles and polarizations are demonstrated in Fig. 8 compared with the simulated ones. It is clear that the transmission coefficients keep very stable versus variable incident angles up to 50° for transverse electric (TE) and transverse magnetic (TM) polarizations. The insertion loss within passband gradually becomes larger as the incident angle increases, which is mainly caused by the variation of wave impedance of the incident wave. The measured insertion loss (1.1 dB) is larger than the simulated one (0.7 dB) under the normal incidence. In addition, due to the decrease of the Q-factor for the fabricated 3D FSS, the measured 3dB bandwidth of the passband is widened. The discrepancies between the measurement and simulation result from fabrication tolerance, assembly tolerance and measurement error. Table 3 provides the comparison between the presented 3D FSS and previously reported designs with similar frequency responses, and our proposed 3D FSS exhibits good angular stability, dual polarizations, and small electrical size. However, compared with 2D FSSs composed of PCB, our designed 3D FSS suffers from the assembly process on account of a large number of building blocks.

Table 3: Comparison of the FSS designs with similar responses

Ref.	Order	TZs Num.	Unit Cell Size and Thickness	Insertion Loss/Return Loss at f_1 (dB)	Upper Out-of-Band Rejection (dB)	Polarization	Angular Stability (TE/TM)
[7]	2	0	$0.42\lambda_0\times0.42\lambda_0\times0.14\lambda_0$	0.5/11.5	-	Dual	40°/40°
[8]	2	2	$0.72\lambda_0\times0.72\lambda_0\times0.085\lambda_0$	2.5/-	18	Dual	20°/20°
[9]	2	3	$0.3\lambda_0\times0.3\lambda_0\times0.217\lambda_0$	0.5/18	35	Dual	40°/40°
[10]	2	3	$0.16\lambda_0\times0.15\lambda_0\times0.287\lambda_0$	1.2/23	33	Single	40°
[11]	2	2	$0.32\lambda_0\times0.21\lambda_0\times0.167\lambda_0$	1.2/19	50	Single	20°
[12]	2	3	$0.65\lambda_0\times0.65\lambda_0\times0.268\lambda_0$	2.2/7.5	14	Dual	-/20°
[13]	3	0	$0.13\lambda_0\times0.13\lambda_0\times0.094\lambda_0$	0.8/14	-	Dual	45°/45°
[17]	3	1	$0.23\lambda_0\times0.23\lambda_0\times0.035\lambda_0$	0.9/-	17.5	Dual	50°/50°
[19]	3	2	$0.32\lambda_0\times0.32\lambda_0\times0.128\lambda_0$	0.72/14	25	Dual	40°/40°
This work	**3**	**3**	$\mathbf{0.21\lambda_0\times0.21\lambda_0\times0.187\lambda_0}$	**1.1/12**	**43**	**Dual**	**50°/50°**

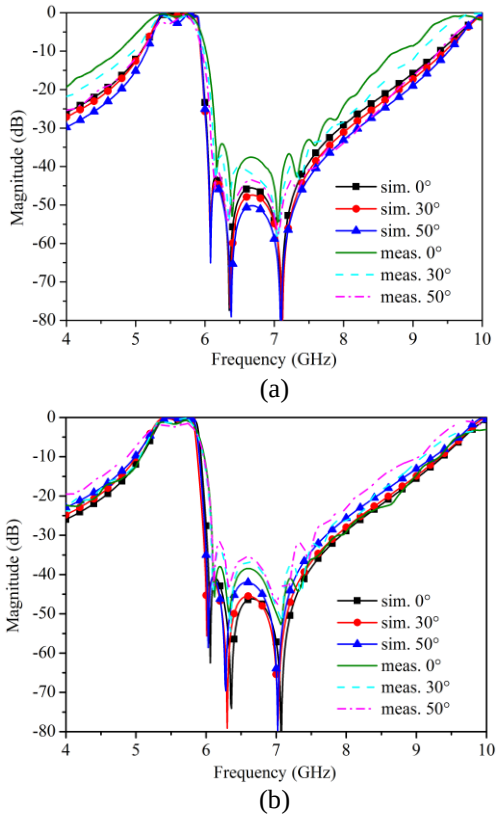

Fig. 8. Measured and simulated transmission coefficients of the proposed 3D FSS under oblique incidence for (a) TE polarization and (b) TM polarization.

V. CONCLUSION

A dual-polarized 3D FSS has been presented in this paper, which provides a third-order bandpass response with three transmission zeros. By inserting a cuboid dielectric block with three concentric metallic square loops into an air-filled square waveguide, the unit cell of the proposed 3D FSS is constructed. Due to the inner electromagnetic coupling in the unit cell, this FSS can achieve a flat passband response with wide out-of-band rejection and high frequency selectivity. The selectivity can be further improved by the high Q-factor of square waveguide cavity. An equivalent circuit model successfully demonstrates the working principle. The measured results show high consistency with the simulated ones, which verifies the performances of the proposed 3D FSS.

ACKNOWLEDGMENT

This work was supported by Doctor Studio Project, Qing Lan Project, "333 Project" Research Funding Project of Jiangsu Province (No. BRA2018315), Natural Science Foundation of the Jiangsu Higher Education Institutions of China (No. 19KJB510002), and National Natural Science Foundation of China (No. 61571232), Huai'an Innovation Service Capacity Construction Project (HAP201904).

REFERENCES

[1] B. A. Munk, *Frequency Selective Surfaces: Theory and Design.* New York, NY, USA: Wiley, 2000.

[2] H. Huang and Z. Shen, "Low-RCS reflectarray with phase controllable absorptive frequency-selective reflector," *IEEE Trans. Antennas Propag.*, vol. 67, no. 1, pp. 190-198, 2019.

[3] H. Huang, Z. Shen, and A. A. Omar, "3-D absorptive frequency selective reflector for antenna radar cross section reduction," *IEEE Trans. Antennas Propag.*, vol. 65, no. 11, pp. 5908-5917, 2017.

[4] D. Li, T. W. Li, E. P. Li, and Y. J. Zhang, "A 2.5-D angularly stable frequency selective surface using via-based structure for 5G EMI shielding," *IEEE Trans. Electromagn. Compat.*, vol. 60, no. 3,

pp. 768-775, 2018.

[5] M. Idrees, S. Buzdar, S. Khalid, and M. A. Khalid, "A miniaturized polarization independent frequency selective surface with stepped profile for shielding applications," *Applied Computational Electromagnetics Society Journal*, vol. 31, no. 5, pp. 531-536, 2016.

[6] A. Lalbakhsh, M. U. Afzal, K. P. Esselle, S. L. Smith, and B. A. Zeb, "Single-dielectric wideband partially reflecting surface with variable reflection components for realization of a compact high-gain resonant cavity antenna," *IEEE Trans. Antennas Propag.*, vol. 67, no. 3, pp. 1916-1921, 2019.

[7] C. Jin, Q. H. Lv, J. L. Wang, and Y. Li, "Capped dielectric inserted perforated metallic plate bandpass frequency selective surface," *IEEE Trans. Antennas Propag*., vol. 65, no. 12, pp. 7129-7136, 2017.

[8] G. Q. Luo, W. Hong, Q. H. Lai, K. Wu, and L. L. Sun, "Design and experimental verification of compact frequency-selective surface with quasi-elliptic bandpass response," *IEEE Trans. Microw. Theory Tech*., vol. 55, no. 12, pp. 2481-2487, 2007.

[9] B. Li and Z. Shen, "Synthesis of quasi-elliptic bandpass frequency-selective surface using cascaded loop arrays," *IEEE Trans. Antennas Propag*., vol. 61, no. 6, pp. 3053-3059, 2013.

[10] B. Li and Z. Shen, "Three-dimensional bandpass frequency-selective structures with multiple transmission zeros," *IEEE Trans. Microw. Theory Tech*., vol. 61, no. 10, pp. 3578-3589, 2013.

[11] A. K. Rashid, Z. Shen, and B. Li, "An elliptical bandpass frequency selective structure based on microstrip lines," *IEEE Trans. Antennas Propag*., vol. 60, no. 10, pp. 4661-4669, 2012.

[12] Z. Z. Zhao, A. X. Zhang, X. M. Chen, G. T. Peng, J. X. Li, H. Y. Shi, and A. A. Kishk, "Bandpass FSS with zeros adjustable quasi-elliptic response," *IEEE Antennas Wireless Propag. Lett*., vol. 18, no. 6, pp. 1184-1188, 2019.

[13] M. A. Al-Joumayly and N. Behdad, "A generalized method for synthesizing low-profile, band-pass frequency selective surfaces with non-resonant constituting elements," *IEEE Trans. Antennas Propag*., vol. 58, no. 12, pp. 4033-4041, 2010.

[14] K. Payne, K. Xu, and J. H. Choi, "Generalized synthesized technique for the design of thickness customizable high-order bandpass frequency-selective surface," *IEEE Trans. Microw. Theory Tech*., vol. 66, no. 11, pp. 4783-4793, 2018.

[15] Z. Z. Zhao, W. Li, X. M. Chen, J. Z. Chen, H. Y. Shi, J. X. Li, S. T. Zhu, and A. X. Zhang, "Broadband angle insensitive frequency-selective surface with multiple resonant modes," *Microw. Opt. Technol. Lett*., vol. 60, pp. 2660-2664, 2018.

[16] M. Gao, S. M. A. M. H. Abadi, and N. Behdad, "A hybrid miniaturized-element frequency selective surface with a third-order bandpass response," *IEEE Antennas Wireless Propag. Lett*., vol. 16, pp. 708-711, 2016.

[17] M. Li and N. Behdad, "A third-order bandpass frequency selective surface with a tunable transmission null," *IEEE Trans. Antennas Propag*., vol. 60, no. 4, pp. 2109-2113, 2012.

[18] N. Behdad, M. Al-Joumayly, and M. Salehi, "A low-profile third-order bandpass frequency selective surface," *IEEE Trans. Antennas Propag*., vol. 57, no. 2, pp. 460-466, 2009.

[19] Q. H. Lv, C. Jin, B. C. Zhang, and R. Mittra, "Wide-passband dual-polarized elliptic frequency selective surface," *IEEE Access*, vol. 7, pp. 55833-55840, 2019.

[20] M. U. Afzal, A. Lalbakhsh, and K. P. Esselle, "Electromagnetic-wave beam-scanning antenna using near-field rotatable graded-dielectric plates," *Journal of Applied Physics*, vol. 124, no. 23, pp. 234901, 2018.

[21] A. Lalbakhsh, M. U. Afzal, and K. P. Esselle, "Multiobjective particle swarm optimization to design a time-delay equalizer metasurface for an electromagnetic band-gap resonator antenna," *IEEE Antennas Wireless Propag. Lett.*, vol. 16, pp. 912-915, 2017.

[22] A. Lalbakhsh, M. U. Afzal, K. P. Esselle, and S. L. Smith, "Low-cost nonuniform metallic lattice for rectifying aperture near-field of electromagnetic bandgap resonator antennas," *IEEE Trans. Antennas Propag*., vol. 68, no. 5, pp. 3328-3335, 2020.

[23] A. Lalbakhsh, M. U. Afzal, K. P. Esselle, and S. Smith, "Design of an artificial magnetic conductor surface using an evolutionary algorithm," *International Conference on Electromagnetics in Advanced Applications (ICEAA)*, pp. 885-887, 2017.

[24] A. Lalbakhsh, M. U. Afzal, K. P. Esselle, and B. A. Zeb, "Multi-objective particle swarm optimization for the realization of a low profile bandpass frequency selective surface," *International Symposium on Antennas and Propagation (ISAP)*, pp. 1-4, 2015.

[25] J. S. Hong and M. J. Lancaster, *Microstrip Filters for RF/Microwave Application*. New York, NY, USA: Wiley, 2001.

[26] D. Ferreira, R. F. S. Caldeirinha, I. Cuinas, and T. R. Fernandes, "Square loop and slot frequency selective surfaces study for equivalent circuit model optimization," *IEEE Trans. Antennas Propag*., vol. 63, no. 9, pp. 3947-3955, 2015.

[27] D. S. Wang, W. Q. Che, Y. M. Chang, K. S. Chin, and Y. L. Chow, "A low-profile frequency selective surface with controllable triband characteristics," *IEEE Antennas Wireless Propag. Lett.*, vol. 12, pp. 468-471, 2013.

[28] D. M. Pozar. *Microwave Engineering*. 3rd ed., New York, NY, USA: Wiley, 2009.

Zhengyong Yu was born in Huaian, China, in 1982. He received the B.S. degree from the Huaiyin Institute of Technology, Huaian, China, in 2006, the M.S. degree from the Nanjing University of Science and Technology, Nanjing, China, in 2008, and the Ph.D. degree from Nanjing Normal University, in 2020.

He is currently an Associate Professor and Senior Engineer in Huaian Vocational College of Information Technology. He is Jiangsu Province 333 project personnel training object, and Jiangsu Province Qing Lan project academic leader. His current research interests include fundamental electromagnetic theory, frequency selective surfaces and near-field antennas.

Wanchun Tang was born in China in 1967. He received the B.S. degree from Tsinghua University, Beijing, China, in 1990, the M.S. degree from the Nanjing University of Science and Technology, Nanjing, China, in 1995, and the Ph.D. degree from the City University of Hong Kong, Hong Kong, in 2003, all in Electrical Engineering.

He was a Full Professor with the Department of Communication Engineering, NJUST, and is currently a Specially Invited Full Professor with the Jiangsu Key Laboratory on Optoelectronic Technology, School of Physics and Technology, Nanjing Normal University, Nanjing. He has authored or coauthored over 100 journal and conference papers. His current research interests include modeling and optimization of RFIC, antennas, signal integrity, and power integrity design in package.

Radiated Susceptibility Analysis of Multiconductor Transmission Lines Based on Polynomial Chaos

Tianhao Wang [1], Quanyi Yu [1], Xianli Yu [2], Le Gao [1], and Huanyu Zhao [1*]

[1] College of Instrumentation and Electrical Engineering
Jilin University, Changchun, 220000, 130061 China
wangtianhao@jlu.edu.cn, yqy17@mails.jlu.edu.cn, gaole@jlu.edu.cn, zhaohyjlu@jlu.edu.cn*

[2] College of Geo-Exploration Science and Technology
Jilin University, Changchun, 220000, 130061 China
yuxianli@jlu.edu.cn

Abstract **–** To address the uncertainties of the radiated susceptibility of multiconductor transmission lines (MTLs), a surrogate model of the MTLs radiated susceptibility is established based on generalized polynomial chaos (gPC), and the gPC is made sparser by combining the adaptive hyperbolic truncation (AHT) scheme and the least angle regression (LAR) method. The uncertainties of the radiated susceptibility of transmission lines are calculated using the adaptive-sparse polynomial chaos (AS-PC) scheme. The parameters related to the incident field, such as elevation angle θ, azimuth angle ψ, polarization angle η, and field amplitude E, are inevitably random. Therefore, these four variables are taken as random input variables, and each of them is subject to different variable distributions. The MTLs model with infinite ground as the reference conductor is adopted, different impedances are used and the AS-PC scheme is combined with transmission line theory to calculate the average, standard deviation and probability distribution of the radiated susceptibility of MTLs. Sobol global sensitivity analysis based on variance decomposition is adopted to calculate the influence of random input variables on the MTLs radiated susceptibility model. The calculation results are compared with the results of the Monte Carlo (MC) method, proving that the proposed method is correct and feasible.

Index Terms **–** Adaptive Hyperbolic Truncation (AHT), Least Angle Regression (LAR), Multiconductor Transmission Lines (MTLs), polynomial chaos, radiated susceptibility.

I. INTRODUCTION

The electromagnetic compatibility problem caused by the complex electromagnetic environment has attracted more and more attention of researchers. Transmission lines, as the carrier of power and signal, are an indispensable part of electrical and electronic equipment. As an important problem in electromagnetic compatibility, MTLs radiated susceptibility has received increasing research attention. By combining the transmission line equation, the solution of the double-conductor transmission lines radiated susceptibility equation is obtained when the relevant parameters of the incident field are determined [1]. Then, the double-conductor transmission line model is extended to a more complex MTLs model, and the frequency-domain response of the radiated susceptibility of MTLs is obtained by [2,3].

Due to the complexity of the electromagnetic environment and the possible position change of the electronic equipment, the relevant parameters of the incident field (such as elevation angle θ, azimuth angle ψ, polarization angle η, and field amplitude E) will inevitably have uncertainties. In the past decades, the uncertainties of transmission line radiated susceptibility have been studied. Researches used stochastic reduced-order models to analyze the uncertainties of induced current generated by MTLs radiated by random plane wave [4]. The probability immunity method was used to analyze the radiated susceptibility of a double-conductor electric short transmission line incident by a random plane wave [5], and the statistical characteristics of the response current of MTLs excited by a random plane wave were analyzed [6]. [7] studied the simulations of uniform and non-uniform transmission lines and compared the results of the two. The time domain model of MTLs in the ordinary differential equation form was used in reference [8] to analyze the fast response of MTLs in the field line coupling situation, and the BLT (Beam-Liu-Tesche) equation [9] was used to calculate the frequency-domain response of lossless MTLs under plane wave radiation. A PCB radiated electromagnetic compatibility model [10] is established, which can accurately reproduce the NFS signals emitted by electronic circuits with transient excitation of nanoseconds duration. For the uncertainties of electromagnetic coupling of

Submitted On: May 4, 2020
Accepted On: August 9, 2020

https://doi.org/10.47037/2020.ACES.J.351215

1054-4887 © ACES

MTLs, the probability distribution model of the electromagnetic coupling of MTLs is established by combining the full-factor numerical integration, sparse-grid numerical integration, and maximum entropy methods [11]. Polynomial chaos [12] was used to analyze the uncertainties of the electromagnetic coupling of a naval ship harness. Similarly, [13-15] combined with the gPC analyzed the uncertainties of radiated susceptibility. In order to predict the model more efficiently, least angle regression method [16] is proposed, and on this basis, a sparse chaos polynomial is proposed [17], which is used to solve the engineering probability problem. In view of different transmission line types, the frequency-domain response of the twisted pair transmission lines radiated susceptibility with ground as the reference conductor was analyzed [18]. Analogously, the twisted pair transmission lines radiated susceptibility model [19] was established by using the variable distance function and the moment method. The uncertainties of the radiated susceptibility of the randomly wound transmission line model with ground as the reference conductor was calculated and analyzed [20].

Quantify the uncertainties of the model output is at the heart of uncertainty analysis. Therefore, global sensitivity analysis which can quantitatively analyze the impact of the interaction between multiple input variables on the model outputs is necessary. The global sensitivity analysis method mainly includes the Sobol method based on variance decomposition [21]. First-and second-order reliability methods are used to analyze the reliability and global sensitivity of the radiated susceptibility of MTLs [22].

On the basis of the gPC, this paper proposes an AS-PC method that combines the AHT scheme with the LAR to analyze the uncertainties of the radiated susceptibility of MTLs with different impedances and combines it with the Sobol global sensitivity analysis method based on variance decomposition to calculate the global sensitivity of the input variables of the radiated susceptibility of MTLs. Finally, the total and first-order sensitivity indices are obtained, and the influence degree of different input variables on the transmission line radiated susceptibility model is analyzed quantitatively. The calculation results are compared with the results of 20000 MC realizations to verify the correctness and efficiency of this method.

II. ADAPTIVE SPARSE POLYNOMIAL CHAOS

The polynomial chaos from the homogeneous function [23,24] in Wiener theory has a solid mathematical foundation and can accurately describe the randomness of variables in any form of distribution. Wiener first used Hermite orthogonal polynomials based on Gaussian random variables to establish polynomial chaos. Later, Xu and Karniadakis extended them to more traditional random variable distribution types through the Askey scheme and obtained a gPC with a wider range of application [25]. The orthogonal polynomials corresponding to the distribution types of the traditional random input variables are shown in Table 1.

Let the original model be $Y = y(\xi)$ and expand it with the gPC scheme. The result is as follows:

$$\begin{aligned} Y &= c_0 I_0 + \sum_{i_1=1}^{\infty} c_{i_1} I_1\left(\xi_{i_1}\right) + \sum_{i_1=1}^{\infty}\sum_{i_2=1}^{i_1} c_{i_1 i_2} I_2\left(\xi_{i_1},\xi_{i_2}\right) + \\ &\quad \sum_{i_1=1}^{\infty}\sum_{i_2=1}^{i_1}\sum_{i_3=1}^{i_2} c_{i_1 i_2 i_3} I_3\left(\xi_{i_1},\xi_{i_2},\xi_{i_3}\right) + \cdots \\ &= \sum_{i=0}^{\infty} \hat{c}_i \Phi_i(\boldsymbol{\xi}). \end{aligned} \tag{1}$$

Table 1: Orthogonal polynomials corresponding to distribution types

Distribution Type	Probability Density Function	Orthogonal Polynomial	Weight Function	Variable Range
Normal	$\frac{1}{\sqrt{2\pi}} e^{-x^2/2}$	Hermite $H_n(x)$	$e^{-x^2/2}$	$[-\infty,+\infty]$
uniform	$\frac{1}{\sqrt{2\pi}} e^{-x^2/2}$ 1/2	Legendre $P_n(x)$	1	[-1,1]
β	$\frac{(1-x)^{\alpha}(1+x)\beta}{2^{\alpha+\beta+1}B(\alpha+1,\beta+1)} e^{-x}$	Jacobi $P_n^{(\alpha,\beta)}(x)$	$(1-x)^{\alpha}(1+x)\beta$	[-1,1]
exponential	e^{-x}	Laguerre $L_n(x)$	e^{-x}	$[0,+\infty]$

In (1), $I_n\left(\xi_{i_1},\cdots,\xi_{i_n}\right)$ represents a mixed orthogonal polynomial of *n* order, which is a function of multi-dimensional standard random variables $\left[\xi_{i_1},\cdots,\xi_{i_n}\right]$. $\hat{c}_i$ and Φ_i correspond to $c_{i_1 i_2 \cdots i_p}$ and $I_n\left(\xi_{i_1},\ldots,\xi_{i_n}\right)$ in (1), respectively. Polynomial chaos expansion $\Phi_i(\boldsymbol{\xi})$ is the product of the one-dimensional orthogonal polynomial basis function corresponding to each random variable. The number of terms in the expansion of gPC is theoretically infinite. To calculate the coefficients of the

gPC expansion, the traditional method must select the highest order P of the polynomial and truncate it at the P order, and the obtained polynomial chaos expansion is:

$$Y = \sum_{i=0}^{P} \hat{c}_i \Phi_i(\boldsymbol{\xi}). \tag{2}$$

When the dimension of the input variables of the model is n, the number of truncated polynomial chaos expansion terms (N) is:

$$N = \frac{(P+n)!}{P!n!}. \tag{3}$$

One of the core functions of the gPC method is solving the expansion term coefficient ($\hat{c}_i$), which is generally calculated by the regression or projection method. (3) indicates that the number of terms of the expansion increases with the dimension of the input variables and the truncation order of the gPC scheme, resulting in a dimension problem and reducing the coefficient calculation efficiency of the expansion term of the gPC scheme. If the truncation order is reduced, then the solution accuracy of the expansion coefficient cannot be guaranteed. Therefore, the key to solving the problem is to use an appropriate truncation method and the sparse method to reduce the polynomial, which is not very important in the expansion term of gPC.

A. Adaptive hyperbolic truncation

According to the effect sparsity and ordering principles of the model [26], the lower-order effect in the model is more important than the higher-order effect, and focus should be on the "important few" rather than the "unimportant many." The hyperbolic truncation scheme can effectively reduce the high-order effect factors among the variables in the model [27]. Let p_i be the highest order of Φ_i, and the order of the k-th dimension random variable is l_k when the traditional truncation scheme is adopted:

$$p_i = \sum_{k=1}^{n} l_k = l_1 + l_2 + \cdots + l_n. \tag{4}$$

Given that the concept of norm is used in the hyperbolic truncation scheme, and q refers to the norm, then (4) is redefined as:

$$p_i = \left(\sum_{k=1}^{n} (l_k)^q \right)^{1/q} \le P, 0 < q \le 1. \tag{5}$$

(5) shows that when q = 1, $P_{\max} = P$, the truncation scheme is the traditional truncation scheme. Meanwhile, the hyperbolic truncation scheme parses the high-order effect of the model on the basis of the traditional truncation scheme. When q <1, all the remaining polynomials are located under the hyperbolic curve or surface. To intuitively show the truncation effect of the hyperbola, two-dimensional input variables are taken as examples, as shown in Fig. 1.

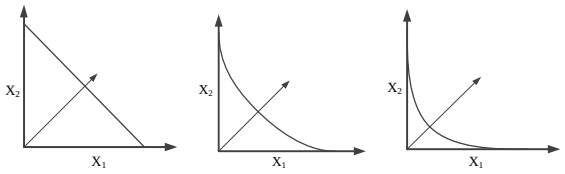

n=2, *q*=1 *n*=2, *q*=0.75 *n*=2, *q*=0.5

Fig. 1. Hyperbolic truncation diagram of different dimension input variables and q norms.

Figure 1 shows that for input variables of different dimensions, the hyperbolic truncation scheme can effectively reduce the high-order effect of the model and maintain the low-order effect below the curve. In Fig. 1, when q = 1, the hyperbola is a straight line, as shown in a; when q < 1, the straight line becomes a hyperbola, as shown in b and c. With the decrease of q, the penalty of the hyperbolic truncation scheme for the high-order effect of the model is more obvious. The traditional truncation order (P = 5) and the input variable dimension (n = 2) are taken as examples, as shown in Fig. 2.

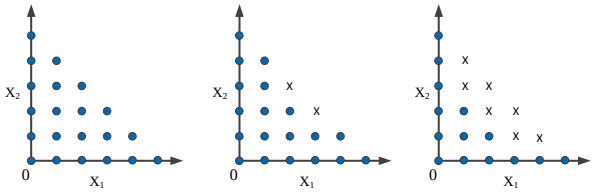

P=5, *q*=1 *P*=5, *q*=0.75 *P*=5, *q*=0.5

Fig. 2. Truncation effect of hyperbolic truncation when P=5, n = 2.

To show the influence of the related sparse processing method on the model, let g be the sparse coefficient:

$$g = N'/N. \tag{6}$$

In the above equation, N' is the number of polynomial expansion terms after sparse processing, and N is the number of polynomial expansion terms without sparse processing. For the model with n = 4 (input variables) and q = 0.8 (hyperbolic truncation norm), the sparse coefficients generated by different truncations are shown in Table 2.

Table 2: Comparison of the number of polynomial terms of the traditional and hyperbolic truncation schemes with different truncation orders

	Traditional	q=0.8	*g*
P=5	126	61	48.4%
P=10	1001	408	40.8%
P=15	3876	1476	38.1%

Table 2 shows that the hyperbolic truncation scheme can effectively reduce the number of polynomial terms, and the sparse coefficients decrease with the increase in the truncation order. Thus, the hyperbolic truncation scheme can effectively perform the preliminary sparse processing of the model. In practical calculation and analysis, the choice of hyperbolic truncation norm q is important. When the value of norm q is extremely low, although many high-order effects are removed, the low-order effects of the model are also affected, resulting in an extremely large error in the final calculation results of the model. In view of the selection of the hyperbolic truncation norm q, an adaptive method is proposed to select the appropriate hyperbolic truncation norm q, which takes the leave-one-out (*LOO*)verification error as the criterion.

The LOO cross-validation error uses cross-validation to overcome the overfitting problem caused by the normalized empirical error, which is a technology developed in statistical learning. Let the *LOO* cross-validation error be ε_{LOO}. m metamodels are established, with each based on the simplified experimental design, and their predictions are compared at the exclusion point with the true value ε_{LOO} can be expressed as follows:

$$\varepsilon_{LOO} = \frac{\sum_{i=1}^{m}\left(M\left(x^{(i)}\right) - M^{PC\backslash i}\left(x^{(i)}\right)\right)^2}{\sum_{i=1}^{N}\left(M\left(x^{(i)}\right) - \hat{\mu}Y\right)^2}. \tag{7}$$

In (7), $M(x^{(i)})$ is the response value of the model at point $x^{(i)}$ of the ith metamodel, $M^{PC\backslash i}(x^{(i)})$ is the response value of the polynomial chaos model at point $x^{(i)}$ of the ith metamodel, and $\hat{\mu}$ is the mean value.

The main steps of the selection algorithm of AHT norm q with ε_{LOO} as the criterion are as follows:

(1) Set the selection range of hyperbolic truncation norm q to [a, b] and the step size to s.
(2) Set threshold of ε_{LOO}.
(3) When ε_{LOO} is less than the set threshold or exceeds the maximum selection range, the program stops, and the obtained g value is the final selection result.

B. Least angle regression

The AHT can effectively reduce the influence of high-order effects among variables in the model. Table 2 shows that although the number of polynomial terms after hyperbolic truncation is reduced by more than half compared with the traditional gPC, some space remains for the sparse processing of the number of polynomial terms after the AHT due to the large number of basic terms of the polynomials. LAR is an important sparse algorithm that can effectively make the model sparser. Therefore, on the basis of the AHT, LAR is used to sparse the hyperbolic truncation polynomials to further sparse the number of terms of the polynomial chaos. In 2004, Efron proposed a variable selection method similar to forward stepwise regression [16]. The main idea of LAR is as follows:

The model is represented as $Y = X\theta$, using the cosine similarity method to select the most relevant independent variable (X_j) with dependent variable Y. The residual (γ) of Y and X_j is calculated, moving in the direction of X_j until another variable X_t appears. The correlation between X_t and residual γ is equal to that between X_j and residual γ, that is, residual γ is located on the angle bisector of X_j and X_t and then continues to move forward along the angle bisector until the next independent variable that is most related to the residual appears. In short, we are constantly looking for variables that are most relevant to the current residual. Taking the two-dimensional input variables as an example, the schematic of LAR is shown in Fig. 3. The main steps of LAR are as follows:

(1) Let all polynomial coefficients be 0, and the initial residual γ be the observation vector.
(2) Find the most relevant variable (X_1) with dependent variable Y by cosine similarity.
(3) Let variable X_1 move in the current direction until X_1 and X_2 can be divided equally, that is, until the correlation between X_2 and the residual is the same as that between X_1 and residual γ. At this time, residual γ is located on the angular bisector of X_1 and X_2.
(4) Similar to Step 2, continue to move in the direction of the angular bisector obtained in Step 2 until a new independent variable (X_3) appears with the same degree of correlation as residual γ.
(5) Update the coefficients and move eligible arguments from the candidate set to the active set.
(6) Repeat the above steps until all variables are iterated.

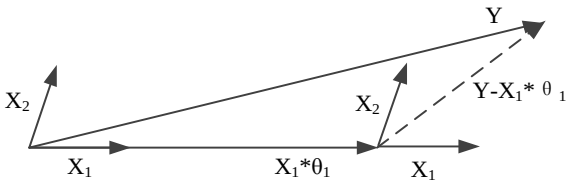

Fig. 3. LAR of two-dimensional input variables.

C. Global sensitivity analysis based on polynomial chaos

The Sobol method is the most classical among the global sensitivity analysis methods. In this method, the interaction between single and multiple input variables is ANOVA, and their contribution to the model output variance is calculated to analyze the influence degree of different single or multiple variables' interaction on the

output model, that is, the idea of ANOVA. With the use of the Sobol method, the output model is decomposed into the sum of 2^n increasing terms:

$$Y(\boldsymbol{\xi}) = y_0 + \sum_{i=1}^{n} y_i(\xi_i) + \sum_{1\le i\le j\le n} y_{ij}(\xi_i,\xi_j) + y_{1,2,\ldots,n}(\xi_1,\xi_2,\ldots,\xi_n). \quad (8)$$

In (8), ξ represents the *n*-dimensional input variables [ξ_1, ξ_2, …, ξ_n], y_0 is the mean value of Y (ξ), and the decomposition terms have an orthogonal relationship. The coefficients of each decomposition term in (8) can be obtained by recursively calculating the sum of the expansion terms through an integral. To obtain the variance decomposition formula, the variance is taken from both sides of (8):

$$Var\left[Y(\xi)\right] = D = \sum_{i=1}^{n} D_i + \sum_{1\le i<j\le n} D_{ij} + \cdots + D_{1,2,\ldots,n} \quad (9)$$

The different decomposition terms in (9) represent the influence of different input variables and the interaction between variables on the output response variance. The Sobol sensitivity indices are defined as:

$$S_{i_1,\ldots,i_s} = \frac{D_{i_1,\ldots,i_s}}{D}, 1\le i_1<\ldots<i_s\le n; s=1,\ldots,n. \quad (10)$$

S_i refers to the first-order sensitivity indices, which represent the contribution of a single input to the output response variance. The sum of the first-order sensitivity indices of each input variable and the sensitivity indices of the interaction between each variable is defined as the total sensitivity indices

$$S_i^T = S_i + \sum_{j<i} S_{j,k,i} + \cdots + S_{1,2,\cdots,n}. \quad (11)$$

In the early days of the Sobol method, the total sensitivity indices and the sensitivity indices of each order were calculated by MC. However, MC has a high calculation cost and a low calculation efficiency. Therefore, this paper combines AS-PC and the Sobol method to calculate the total sensitivity indices and the sensitivity indices of each order [28]:

$$Y(\xi) = c_0 + \sum_{i=1}^{n}\sum_{\alpha\in I_i} c_\alpha\Phi_\alpha(\xi_\alpha) + \sum_{1\le i_1<i_2\le n}\sum_{\alpha\in I_{i_1,i_2}} c_\alpha\Phi_\alpha(\xi_{i_1},\xi_{i_2}) + \cdots + \sum_{1\le i_1<\cdots<n}\sum_{\alpha\in I_{i_1,\cdots,i_s}} c_\alpha\Phi_\alpha(\xi_{i_1},\cdots,\xi_{i_s}) + \sum_{\alpha\in I_{1,\ldots,n}} c_\alpha\Phi_\alpha(\xi_1,\cdots,\xi_n). \quad (12)$$

In (12),

$$I_{i_1,\ldots,i_s} = \left\{\begin{matrix}\alpha\in(\alpha_1,\alpha_2,\cdots,\alpha_n):\alpha_k=0;\\ k\notin(i_1,\cdots,i_s),\forall k=1,\cdots,n\end{matrix}\right\}. \quad (13)$$

$Y(\xi)$ can be calculated:

$$Y(\xi) = \sum_{\alpha\in I_{i_1,\cdots,i_s}} c_\alpha\Phi_\alpha(\xi_{i_1},\ldots,\xi_{i_s}). \quad (14)$$

According to the orthogonality of the basis functions of polynomial chaos,

$$D_{i_1,\ldots,i_s} = \sum_{\alpha\in I_{i_1,\cdots,i_s}} c_\alpha^2. \quad (15)$$

The global sensitivity indices of Sobol based on AS-PC, including the first-order and total sensitivity indices, can be obtained by combining (10) and (11).

III. NUMERICAL EXAMPLE

This paper focuses on the research and analysis of the uniform lossless MTLs with ground as the reference conductor. In real life, all kinds of electrical and electronic equipment and large-scale systems are exposed to complex electromagnetic environment, and the uncertainty factors that lead to the electromagnetic compatibility radiated susceptibility of transmission lines in all kinds of equipment and systems are mainly concentrated in the incident field generated by the external electromagnetic environment. The elevation angle (θ), azimuth angle (ψ), polarization angle (η), and level amplitude (E) of the incident plane wave of the MTLs system with the ground as the reference conductor is shown in Fig. 4.

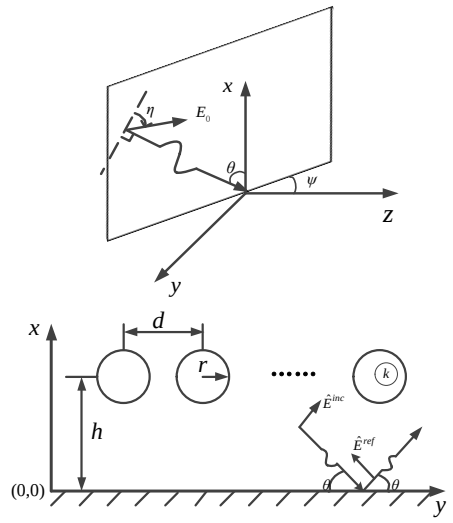

Fig. 4. Relationship between plane incident wave and transmission line position.

Where *d* is the distance between transmission lines, *h* is the height of the transmission lines from the ground,

r is the radius of the transmission lines, θ is the elevation angle, ψ is the azimuth angle, η is the polarization angle and E_0 is the level amplitude of the incident plane wave.

In this section, the gPC model of the radiated susceptibility of MTLs is established. The random input variables of MTLs radiated susceptibility are θ, ψ, η, and the E_0. According to the distribution type of each variable, the corresponding orthogonal substrate can be determined and the gPC proxy model can be established.

The number of transmission lines is 3, and a (3+1) MTLs model with the ground as the reference conductor is established. As shown in Fig. 5, the length of the transmission lines is l = 1m, the radius is r = 0.4mm, the distance between transmission lines is 1cm, the height (h) from the ground is 2cm. The impedance of the source end and the load end of the transmission line are set as low impedance and high impedance respectively. The radiated susceptibility under different impedance conditions is compared and analyzed.

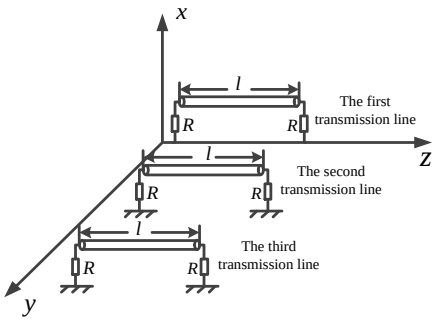

Fig. 5. (3+1) MTLs system.

The random input variables in the example are the elevation angle (θ), azimuth angle (ψ), polarization angle (η), and level amplitude (E) of the incident plane wave. Elevation angle θ is subject to uniform distribution on the interval [0,0.5π], azimuth angle ψ is subject to uniform distribution on the interval [- π, π], polarization angle η is subject to uniform distribution on the interval [0,2π], and level amplitude E is subject to normal distribution with a mean value of 1 V/M and a standard deviation of 0.2v/m. According to the different distributions of random input variables, the corresponding orthogonal basis is selected to build the gPC model. In the traditional truncation scheme, taking the remote induced current (I_{R2}) of the second transmission line in Fig. 5 as an example, truncation orders (P) 5, 10, 15, and 20 are used. In the case of low impedance and high impedance respectively, the mean value and standard deviation of the gPC model of MTLs radiated susceptibility are calculated, the low impedance is 50Ω, and the high impedance is 10kΩ. The frequency range of the incident field is set to [10MHz, 1GHz], and the calculated mean value and the standard deviation are combined with the calculation of 20000 MC runs. The results are shown in Fig. 6.

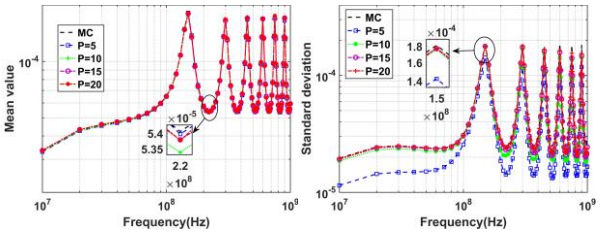

(a) Comparison of mean value and standard deviation of low impedance

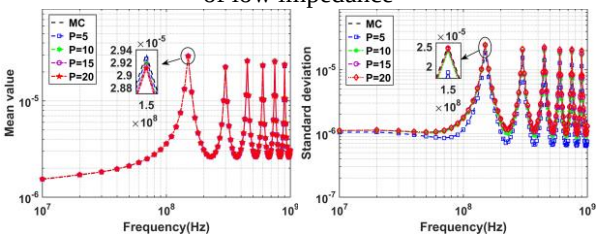

(b) Comparison of mean value and standard deviation of high impedance

Fig. 6. Comparison between the mean value and standard deviation of traditional gPC with different truncation orders and the 20000 MC realizations.

According to the comparison results in Fig. 6, for the mean value and standard deviation of the radiated susceptibility induced current (I_{R2}) of the MTLs, the calculation results of the standard deviation of the low-order truncation are poor under the traditional truncation scheme, but the calculation results of the mean value and standard deviation approach the calculation results of MC as the truncation order increased. Next, for different truncation orders (P), we select ε_{LOO} at three frequency points (i.e., 50, 80, and 100MHz) for comparison, as shown in Fig. 7. Figure 7 shows that the lower-order truncation, such as the 5th and 10th order truncations, is relatively large, and the calculation results are not ideal, whereas the ε_{LOO} of the 15th and the 20th order truncations are relatively low and basically consistent. Therefore, the calculation accuracy increases with the truncation order (P), indicating that the 15th-order truncation can achieve a high accuracy in the traditional truncation.

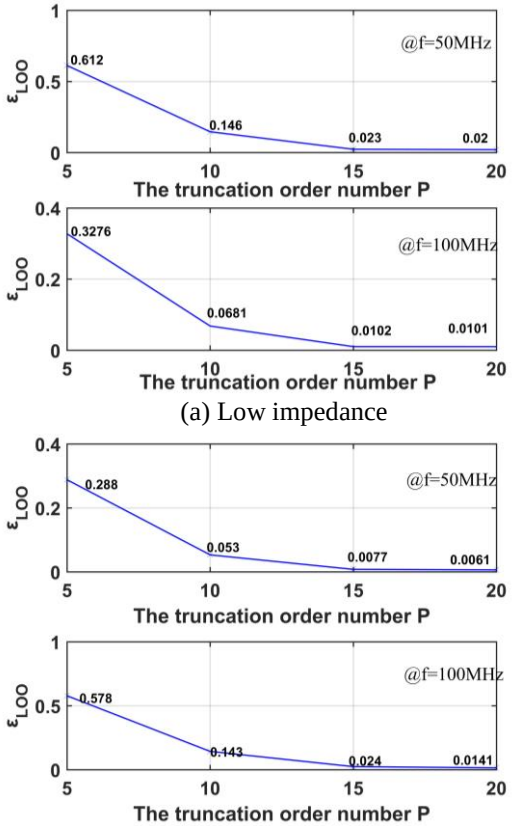

(a) Low impedance

(b) High impedance

Fig. 7. ε_{LOO} comparison between different frequency points and different truncation order.

According to (3), 3876 expansions of gPC exist in the traditional truncation scheme of order 15.A large sparse processing space remains in gPC. To further reduce the calculation cost and improve the calculation efficiency, the AHT scheme introduced earlier is used to deal with the polynomials. Taking the induced current (I_{R2}) at 50MHz as an example, the selection interval of hyperbolic truncation norm q is [0.5,1], the step s is 0.05, and the threshold value is 0.05. It is also calculated for low impedance and high impedance respectively.

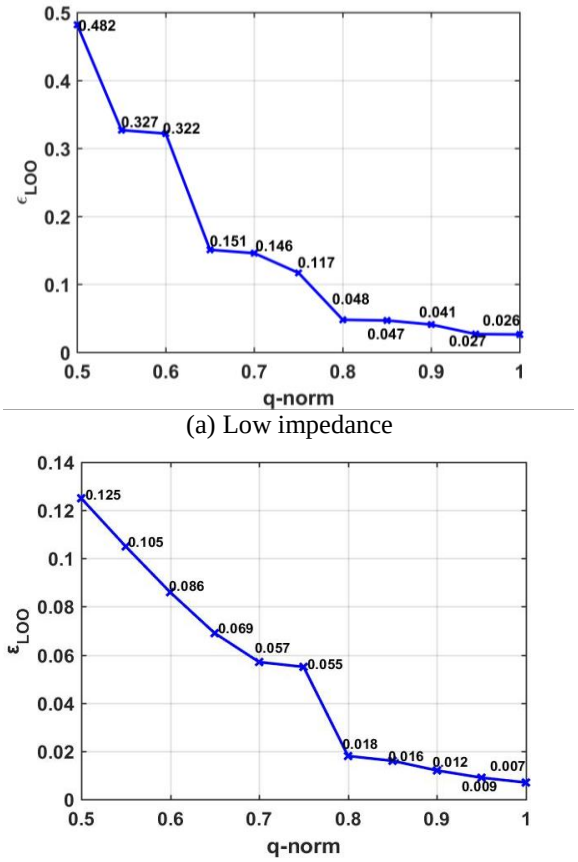

(a) Low impedance

(b) High impedance

Fig. 8. ε_{LOO} curve of different q norm.

Table 3: Comparison of sparse coefficient g with different q norm when P=15

q	0.5	0.55	0.6	0.65	0.7	0.75	0.8	0.85	0.9	0.95	1
N'	263	358	480	662	873	1133	1476	1893	2404	3095	3876
g	6.79%	9.24%	12.4%	17.1%	22.5%	29.2%	38.1%	48.8%	62.0%	79.9%	1

According to Fig. 8, when q = 0.8, ε_{LOO} reaches the threshold value, and when q >0.8, ε_{LOO} changes slightly. Combined with the sparse coefficient (g) in Table 3, compared with q >0.8, when ε_{LOO} is nearly the same, sparse coefficient q = 0.8 is the smallest, and the calculation cost is the lowest. Therefore, q = 0.8 satisfies the expectation of this work and can complete the initial sparse processing of polynomials. q is set to 0.8 for further analysis. After completing the selection of hyperbolic truncation norm q, the LAR introduced in the previous paper, that is, AS-PC, is combined for a more intensive sparse processing of the model. The previous study proved that under the traditional truncation scheme, P = 15 can achieve good accuracy. To verify that P = 15 can also achieve ideal accuracy when using the AS-PC, the induced current at 50, 80, and 100MHz is also selected as an example to compare the different truncation orders, as shown in Fig. 9.

Figure 9 indicates that when q = 0.8, compared with the calculation result of low-order truncation, the different of ε_{LOO} between P = 15 and P = 20 is small and basically consistent, indicating that the proposed model can achieve

the ideal precision when q = 0.8 and P = 15. Therefore we take the P=15 as the truncation order for the following study. To further verify the accuracy of AS-PC, the probability distribution of the radiated susceptibility induced current of the MTLs at the frequency points of 50, 80, and 100MHz is calculated. The probability distribution curve of the radiated susceptibility induced current of the MTLs is calculated by combining with AS-PC, as shown in Fig. 10.

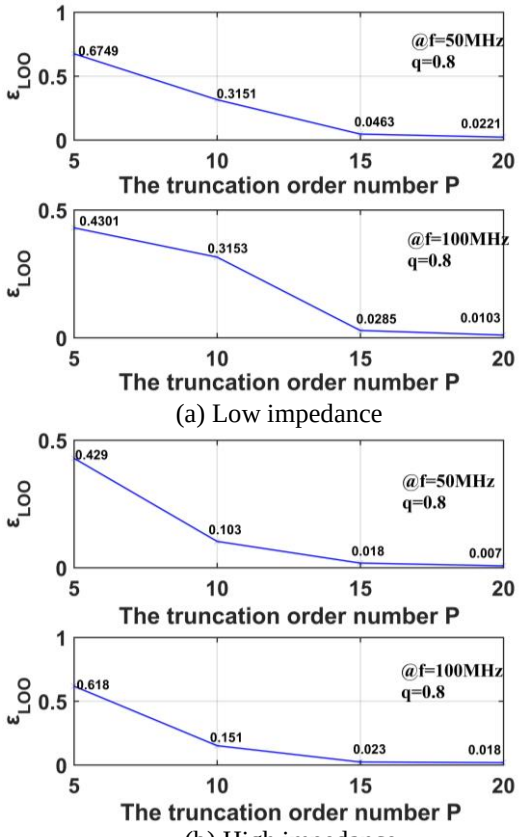

(a) Low impedance

(b) High impedance

Fig. 9. Comparison of different truncation order ε_{LOO} at different frequency points when q = 0.8 and P = 15.

The comparison of the results of the probability distribution curve in Fig. 10 shows that AS-PC can effectively calculate the probability distribution of induced current I_{R2} at different frequency points on the premise of ensuring the calculation accuracy, and we can see that in the case of low impedance, the induced current is smaller than that in the case of high impedance, which shows that increasing the load impedance of transmission line can effectively reduce the induced current when the transmission line is radiated. Take the case of low impedance, further analysis can be made by combining the calculation times of AS-PC and gPC and the sparse coefficient g, as shown in Table 4.

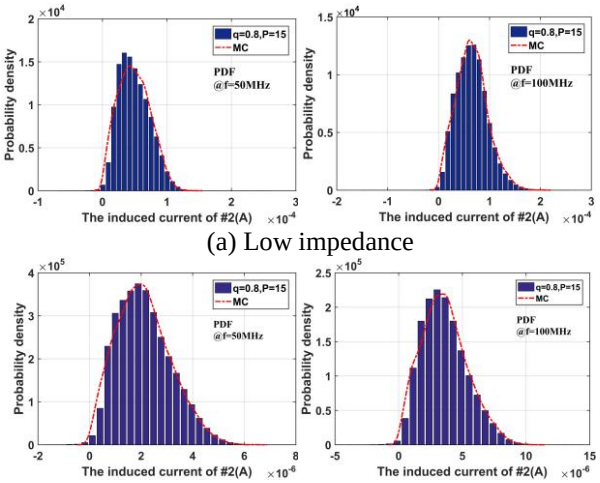

(a) Low impedance

(b) High impedance

Fig. 10. Comparison of induced current probability distribution of AS-PC calculated #2 transmission line at different frequency points.

Table 4: Computing time comparison between AS-PC and gPC

	Computing time (s)	g
AS-PC	6.39	3.25%
gPC	13.69	100%
20000 MC	2001.54	nan

The main frequency of the CPU used is 2.3GHz, and the RAM is 8GB. Table 4 shows that compared with the calculation time of 20000 MC realizations, the calculation time of gPC decreased greatly. However, AS-PC further compresses the calculation time effectively, saving calculation costs and improving the calculation efficiency while ensuring the calculation accuracy. On the basis of the above calculation results, AS-PC can effectively sparse gPC and accurately calculate the induced current probability distribution of the radiated susceptibility of MTLs at different frequency points.

The above calculation and analysis show that the AS-PC method can quickly and accurately calculate the relevant statistical characteristic parameters (such as the mean standard deviation probability distribution) in the uncertainties of the radiated susceptibility of MTLs on the premise of ensuring the calculation accuracy. Next, to further analyze the influence of different input variables on the model in the MTLs radiated susceptibility system, the global sensitivity calculation method introduced in the previous paper was studied.

The global sensitivity indices of each input variable are calculated by combining (10) and (11) and the expansion coefficients of AS-PC. Taking the response current at 50MHz at the right end of #2 transmission lines as an example, under different impedance conditions,

the total and first-order sensitivity indices of each input variable are calculated as follows.

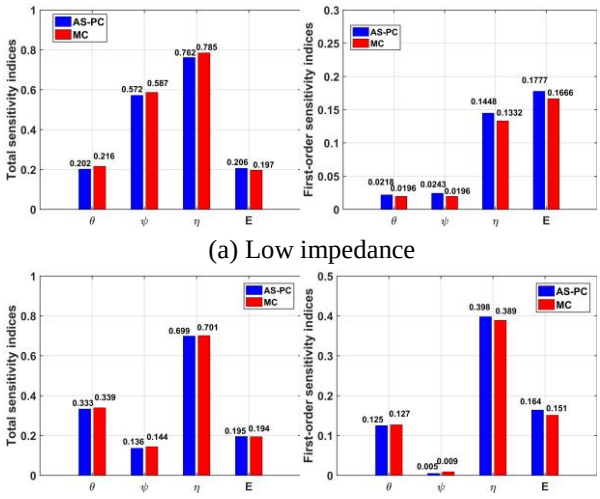

(a) Low impedance

(b) High impedance

Fig. 11. Comparison between the total and first-order sensitivity indices.

Figure 11 shows that the total and first-order sensitivity indices calculated based on the proposed method are basically the same as those calculated by the 20000 MC realizations, and the influence degree of various input variables on the model is also the same. The total sensitivity indices and the first-order sensitivity indices of the polarization angle η are both kept at a high level in the case of low impedance and high impedance, which is an important factor affecting the radiated susceptibility of the MTLs at this frequency point. However, in the case of low impedance, the sensitivity indices of elevation angle θ is low, which has little influence on the whole model. In the case of high impedance, the sensitivity indices of azimuth angle ψ is at a low level, which has less influence on the model than that of polarization angle η. On the basis of the above analysis, the proposed method is faster and more efficient and is thus effective in calculating the total sensitivity index and the first-order sensitivity indices of the radiated susceptibility of MTLs.

To more intuitively show the influence degree of different random variables at different frequency points on the whole model, the total sensitivity indices of the influence degree of each parameter on the radiated susceptibility of MTLs in the frequency band [10MHz, 1GHz] is calculated as shown in Fig. 12.

It can be seen from the analysis of Fig. 12 that no matter in the case of low impedance or high impedance, in the frequency band [10MHz, 1GHz], the influence degree of level amplitude E is maintained at a low level, which has little influence on the model as a whole. Although the influence is increased in the higher frequency band, such as [900MHz, 1GHz], the influence degree of polarization angle η at the same frequency band is far greater than level amplitude E, and when the frequency is higher than 200MHz, the influence degree of elevation angle θ on the model is also far greater. In the case of low impedance, azimuth ψ becomes an important factor affecting the model at about 200MHz, but the influence degree is greatly reduced at the high frequency, while in the case of high impedance, the influence of azimuth ψ is very weak at the low frequency. On the basis of the above analysis, when the location and frequency range of the radiation source in the surrounding environment are known in the practical engineering application, when designing the electrical system in this environment, attention should be paid to the polarization angle of the radiation source, and the position distribution of the transmission line should be adjusted reasonably and effectively to avoid unnecessary electromagnetic compatibility problems.

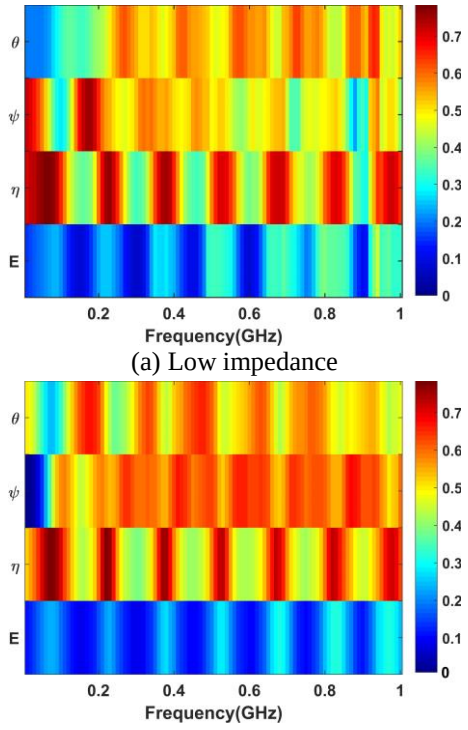

(a) Low impedance

(b) High impedance

Fig 12. [10MHz, 1GHz] influence of parameters on radiated susceptibility of MTLs.

IV. CONCLUSION

The uncertainties of the radiated susceptibility of MTLs with infinite ground as the reference conductor are studied. The elevation (θ), azimuth (ψ), polarization angle (η),and level amplitude (E) of the incident plane wave of the random input variables related to the radiated susceptibility of the MTLs are respectively subject to the

corresponding random distribution type. A surrogate model is established by gPC. On this basis, an AS-PC that combines the AHT with the LAR is proposed, and the gPC is sparsed and calculated to obtain the transmission lines-induced current (voltage)-related statistical information with different impedances, such as the mean value, the standard deviation, and the probability distribution. The comparison of the calculated results with 20000 MC realizations shows that the proposed method can effectively analyze the uncertainties of the radiated susceptibility of MTLs. Compared with the MC and gPC methods, AS-PC greatly improves the calculation efficiency and achieves fast calculation of the statistical characteristics of the radiated susceptibility of MTLs. Combined with the Sobol global sensitivity analysis method, the total and first-order sensitivity indices of the related random input variables in the radiated susceptibility model of MTLs are calculated, and the calculation results are compared with those of 20000 MC realizations. The comparison result proves that the proposed method can effectively calculate the influence degree of relevant parameters on the radiated susceptibility model of transmission lines. Therefore, the uncertainty analysis method for the radiated susceptibility of MTLs adopted in this paper can be used as a theoretical basis and reference for EMC design and rectification of relevant system cables.

ACKNOWLEDGMENT

This work was supported in part by the National Natural Science Foundation of China under Grant 51707080, and in part by the Jilin Scientific and Technological Development Program under Grant 20180101032JC, Grant 20190103055JH and Grant 20190303097SF.

REFERENCES

[1] C. Taylor, R. Satterwhite and C. Harrison, "The response of a terminated two-wire transmission line excited by a nonuniform electromagnetic field," *IEEE Trans. Antennas Propagat*., vol. 13, no. 6, pp. 987-989, Nov. 1965.

[2] C. R. Paul, "Frequency response of multiconductor transmission lines illuminated by an electromagnetic field," *IEEE Trans. on Electromagn. Compat.*, vol. EMC-18, no. 4, pp. 183-190, Nov. 1976.

[3] C. R. Paul, *Analysis of Multiconductor Transmission Lines*, 2nd ed., New York, NY, USA: Wiley, 2008.

[4] Z. Fei, Y. Huang, J. Zhou, and C. Song, "Numerical analysis of a transmission line illuminated by a random plane-wave field using stochastic reduced order models," *IEEE Access*, vol. 5, pp. 8741-8751, 2017.

[5] D. Bellan and S. Pignari, "A probabilistic model for the response of an electrically short two-conductor transmission line driven by a random plane wave field," *IEEE Trans. on Electromagn. Compat.*, vol. 43, no. 2, pp. 130-139, May 2001.

[6] S. Pignari and D. Bellan, "Statistical characterization of multiconductor transmission lines illuminated by a random plane-wave field," *IEEE International Symposium on Electromagnetic Compatibility Symposium Record*, Washington, DC, vol. 2, pp. 605-609, 2000.

[7] M. Omid, Y. Kami, and M. Hayakawa, "Field coupling to nonuniform and uniform transmission lines," *IEEE Trans. on Electromagn. Compat.*, vol. 39, no. 3, pp. 201-211, Aug. 1997.

[8] G. S. Shinh, N. M. Nakhla, R. Achar, M. S. Nakhla, A. Dounavis, and I. Erdin, "Fast transient analysis of incident field coupling to multiconductor transmission lines," *IEEE Trans. on Electromagn. Compat.*, vol. 48, no. 1, pp. 57-73, Feb. 2006.

[9] X. Zhang, Z. Zhao, Y. Qin, J. Luo, and G. Ni, "Transient analytic solutions of lossless multiconductor transmission line excited by plane-wave," *Proceedings of the 9th International Symposium on Antennas, Propagation and EM Theory*, Guangzhou, pp. 1073-1076, 2010.

[10] B. Ravelo, Y. Liu, and A. K. Jastrzebski, "PCB near-field transient emission time-domain model," *IEEE Trans. Electromagn. Compat.*, vol. 57, no. 6, pp. 1320-1328, Dec. 2015.

[11] L. Gao, Q. Yu, D. Wu, T. Wang, X. Yu, Y. Chi, and T. Zhang, "Probabilistic distribution modeling of crosstalk in multi-conductor transmission lines via maximum entropy method," in *IEEE Access*, vol. 7, pp. 103650-103661, 2019.

[12] Y. Chi, B. Li, X. Yang, T. Wang. K. Yang, and Y. Gao, "Research on the statistical characteristics of crosstalk in naval ships wiring harness based on polynomial chaos expansion method," *Nephron. Clin. Pract*., vol. 24, no. s2, pp. 205-214, 2017.

[13] P. Manfredi and F. G. Canavero, "Polynomial chaos representation of transmission-line response to random plane waves," *International Symposium on Electromagnetic Compatibility - EMC Europe*, Rome, pp. 1-6, 2012.

[14] P. Manfredi and F. G. Canavero, "Polynomial Chaos for Random Field Coupling to Transmission Lines," in *IEEE Trans. Electromagn. Compat.*, vol. 54, no. 3, pp. 677-680, June 2012.

[15] T. Bdour and A. Reineix, "Global sensitivity analysis and uncertainty quantification of radiated susceptibility in PCB using nonintrusive polynomial chaos expansions," *IEEE Trans. Electromagn. Compat.*, vol. 58. no. 3, pp. 939-942, June 2016.

[16] B. Efron, T. Hastie, I. Johnstone, and R. Tibshirani, "Least angle regression," *The Annals of Statistics*, vol. 32, no. 2, pp. 407-451, 2004.

[17] G. Blatman and B. Sudret, "Adaptive sparse

polynomial chaos expansion based on least angle regression," *J. Comput. Phys.*, vol. 230, no. 6, pp. 2345-2367, Dec. 2011.

[18] G. Spadacini, F. Grassi, F. Marliani, and S. A. Pignari, "Transmission-line model for field-to-wire coupling in bundles of twisted-wire pairs above ground," *IEEE Trans. Electromagn. Compat.*, vol. 56, no. 6, pp. 1682-1690, Dec. 2014.

[19] G. Spadacini and S. A. Pignari, "Numerical assessment of radiated susceptibility of twisted-wire pairs with random nonuniform twisting," *IEEE Trans. Electromagn. Compat.*, vol. 55, no. 5, pp. 956-964, Oct. 2013.

[20] H. Y. Xie, Y. Li, and H. L. Qiao, "Analysis of field coupling to transmission lines with random rotation over the ground," *Chin. Phys. B.*, vol. 24, no. 6, pp. 171-176, Apr. 2015.

[21] I. M. Sobol, "Global sensitivity indices for nonlinear mathematical models and their Monte Carlo estimates," *Math. Comput. Simul.*, vol. 55, no. 1-3, pp. 271-280, 2001.

[22] A. Kouassi, J. Bourinet, S. Lalléchère, P. Bonnet, and M. Fogli, "Reliability and sensitivity analysis of transmission lines in a probabilistic EMC context," *IEEE Trans. Electromagn. Compat.*, vol. 58, no. 2, pp. 561-572, Apr. 2016.

[23] N. Wiener, "The homogeneous chaos," *Am. J. Math*., vol. 60, pp. 897-936, 1938.

[24] N. Wiener, *Nonlinear Problems in Random Theory*. MIT Technology Press and John Wiley and Sons, 1958.

[25] D. Xiu and G. E. Karniadakis, "Modeling uncertainty in flow simulations via generalized polynomial chaos," *J. Comput. Phys.*, vol. 187, no. 1, pp. 137-167, 2003.

[26] R. Mukerjee and C. F. J. Wu, *A Modern Theory of Factorial Designs*. *Springer New York*, 2006.

[27] M. Larbi, I. S. Stievano, F. G. Canavero, and P. Besnier, "Identification of main factors of uncertainty in a microstrip line network," *Prog. Electromagn. Res*., vol. 162, pp. 61-72, 2018.

[28] B. Sudret, "Global sensitivity analysis using polynomial chaos expansions," *Reliability Engineering and System Safety*, vol. 93, no. 7, pp. 964-979, Apr. 2008.